Université de Liège

Faculté des Sciences

Département d'Astrophysique, de Géophysique et d'Océanographie

Energetic study of solar-like oscillations in red giants

Mathieu Grosjean

PhD Thesis

October 2015

Jury members :

- Pr. Pierre Magain (President)
- Pr. Marc-Antoine Dupret (Supervisor)
- Dr. Kevin Belkacem (Supervisor)
- Dr. Valérie Van Grootel
- Pr. Arlette Noels
- Pr. Benoit Mosser
- Dr. Andréa Miglio

Abstract

Observations of solar-like oscillations by CoRoT and *Kepler* space-borne telescopes, have opened new opportunities for the energetic modelling of these oscillations. In particular, oscillations propagating in both the convective envelope and the radiative core of evolved low-mass stars, called mixed-modes, have been detected, allowing us to investigate various physical processes acting on oscillations in these two regions. Theoretical predictions for the linewidths and the amplitudes of solar-like oscillations, as obtained and discussed in this thesis, strongly depend on the treatment of the interaction between convection and oscillations. Observed properties of solar-like oscillations thus gives us the opportunity to test and constrain this treatment.
The comparisons between observed and theoretical linewidths of main-sequence stars allow us to constrain the parameters of the time-dependent treatment of convection and to produce more accurate results. The remaining discrepancies will give us new clues for the improvement of the treatment of the interaction between convection and oscillations.
The modelling of the energetic aspects of solar-like oscillations in red giants allows us to derive a detectability limit for mixed-modes. These results are in overall good agreement with typical red-giant observed power spectra.
A detailed comparison between an observed subgiant and the corresponding theoretical predictions confirms that the main aspects of the observed energetic properties of solar-like oscillations are well reproduced by the theoretical modelling. Discrepancies between observed and theoretical linewidths of quadrupole mixed-modes lead us to invoke the existence of a new damping mechanism in the core of this star.

Resumé

L'observation d'oscillations de type solaire, dans de nombreuses étoiles de faible masse, par les satellites CoRoT et *Kepler* a ouvert de nouvelles possibilités pour la modélisation des aspects énergétiques de ces oscillations. En particulier, la détection de modes mixtes, se propageant dans l'enveloppe convective et dans le coeur radiatif des géantes rouges, nous permet d'étudier les processus physiques à l'origine des propriétés énergétiques des modes dans ces deux régions. Les prédictions théoriques pour les largeurs et les amplitudes des oscillations de type solaire, telles qu'obtenues et discutées dans cette thèse, dépendent fortement du traitement des processus d'interaction entre la convection et les oscillations. La détermination observationnelle des largeurs et amplitudes des modes nous donne donc l'opportunité de tester et contraindre un tel traitement.
Les comparaisons des largeurs observées et théoriques pour des étoiles de séquence principale nous permet de contraindre précisément les paramètres du traitement de la convection dépendante du temps et ainsi de produire des résultats bien plus réalistes. Les différences restantes entre largeurs observées et théoriques apportent de nouvelles pistes pour une amélioration du traitement de l'interaction entre la convection et les oscillations.
La modélisation des aspects énergétiques des oscillations de type solaire dans les géantes rouges nous permet d'établir une limite de détectabilité des modes mixtes. Il apparait que les résultats de cette modélisation sont globalement en accord avec les observations.
Une comparaison détaillée des propriétés énergétiques des modes observés dans une sous-géante et prédites par une modélisation théorique de cette étoile, montre que la plupart des aspects énergétiques des oscillations de type solaire sont bien reproduits par les modèles théoriques. Les différences entre les observations et les prédictions théoriques des largeurs et amplitudes des modes mixtes quadripolaires nous amènent à l'hypothèse qu'un nouveau mécanisme d'amortissement est à l'oeuvre dans le coeur de cette étoile.

Merci !!

Au moment de finir cette thèse, je souhaite remercier celles et ceux qui ont contribué à cette aventure.

Tout d'abord, un grand merci à Marc-Antoine et Kevin pour m'avoir guidé dans ce parcours scientifique. Leur aide, leurs conseils et leurs avis dans mes recherches et dans la rédaction de cette thèse, m'ont été très précieux.
Merci également à Réza, Richard, Josefina, Arlette, Benoit, Othman et Sébastien pour leurs conseils, leur disponibilité, leur aide et pour les outils qu'ils ont mis à ma disposition.
Merci aux membres du jury, d'avoir accepté de prendre le temps de lire cette thèse.
Je remercie aussi le F.R.I.A. pour m'avoir permis d'effectuer ce doctorat.
Un merci tout particulier à Angela, pour son aide dans la production de cette thèse ainsi que tout au long de mon doctorat.
Je remercie toutes les personnes du département d'astrophysique et plus particulièrement celles du B5c +1 pour leur accueil.

Un tout grand merci à tous mes amis, qui m'ont soutenu, encouragé, parfois supporté tout au long de ces 4 années de thèse.
Un merci tout particulier à Lionel avec lequel j'ai découvert beaucoup de choses. Merci également pour m'avoir aidé à garder toute la forme et l'énergie nécessaires pour avancer dans cette thèse.
A Xavier, pour son grand soutien et pour les recharges en énergie autour d'un thé toujours très constructif.
Un big merci à Vivien et à Quentin, partenaires indéfectibles de mon doctorat et de toutes les activités gravitant autour.
Merci à Gregory, Jérémy, Ludo pour avoir joué les parfaits supports.
Aux étudiants du bachelier en sciences physiques pour l'enthousiasme qu'ils ont manifesté pour mes recherches ainsi que pour l'animation qu'ils apportent.

Enfin, je souhaite remercier ma famille qui m'a toujours soutenu et encouragé durant tout mon parcours universitaire.

Contents

Chapter 1

Introduction

When looking at the night sky, the stars generally seem to be quiet, stable, unchanging,... Reality is more complex: stars were born, will die and, undergo a lot of changes. As a "sphere of gases", a star is the scene of various complex physical processes. Some of them are of interest in this thesis and concern the structural changes occurring from the birth to the death of a star.

We can sort out the stars into some groups according to their surface properties (effective temperature and luminosity), which is the so called Hertzsprung-Russell diagram (hereafter HRD, see Fig. 1.1). The theory of stellar structure and evolution describes the internal constitution of stars and how this structure evolves with time. This evolution is mainly driven by nuclear reactions inside the star that transform hydrogen (the fundamental constituent of stars) into more massive elements. This theory also describes the different physical processes at work inside a star. It allows one to understand the different stars as a function of their mass and age. The general theory of stellar structure and evolution, will be introduced in Chap. 2 and applied to low-mass stars (i.e. stars with masses of the order of the solar one).
Among these different groups in the HRD, main-sequence stars, red-giant stars, and white dwarfs correspond to the subsequent evolutionary sequences undergone by low-mass stars (the evolutionary path of a 1 $M_{\odot}$ star is also represented in Fig. 1.1). Main-sequence stars are burning hydrogen into helium in their core. For low-mass stars, when an appreciable part of the hydrogen is exhausted (around 10% of the stellar mass), the hydrogen burning continues in a shell above an inert helium core until the central burning of helium into carbon starts. These latter phases correspond, for low-mass stars, to the red-giant phase. When nuclear burning ceases, a low-mass star joins the white dwarfs branch where it will cool down.

The theory of stellar structure and evolution has succeeded to describe the different types of stars as well as their evolution, reproducing the observed surface properties. However, to test this theory further, one needs to confront the structure of stellar models with the observations. The problem of accessing the inner structure of astrophysical objects, has been mentioned by Sir Arthur Eddington in the first sentences of his book " *The Internal Constitution of the Stars*" in 1926:

> *"At first sight it would seem that the deep interior of the Sun and stars is less accessible to scientific investigation than any other region of the universe. Our telescopes may probe farther and farther into the depths of space; but how can we ever obtain certain knowledge of that which is hidden behind substantial barriers? What appliance can pierce through the outer layers of a star and test the conditions within?"*

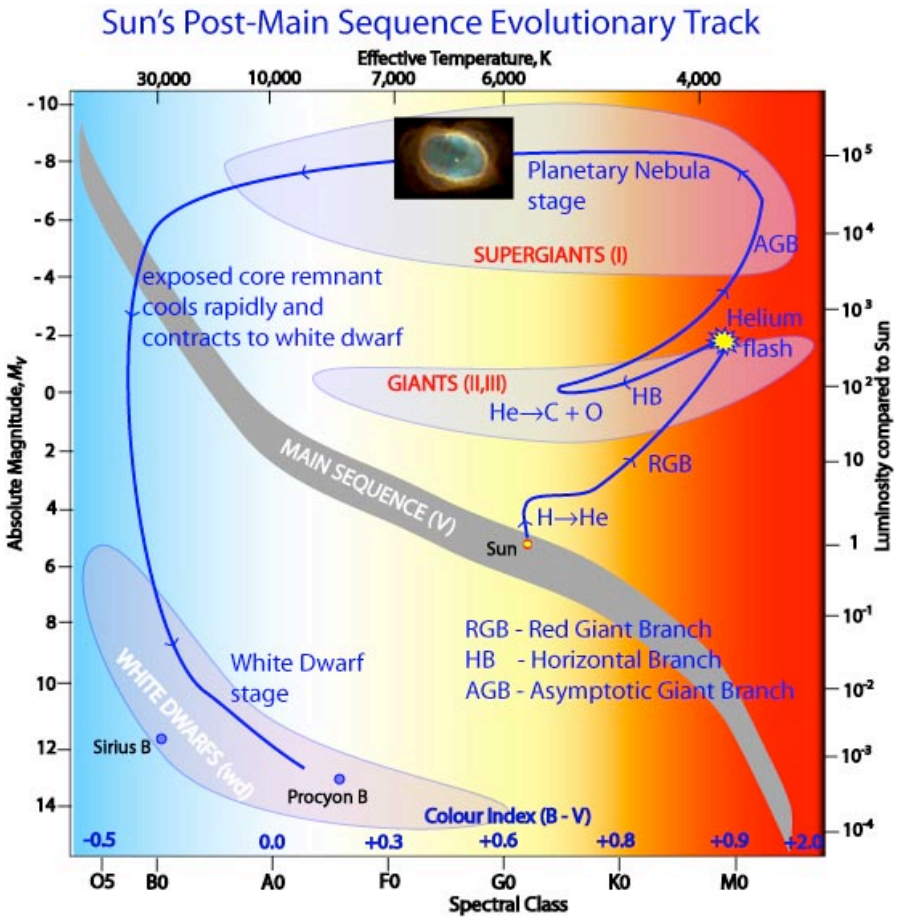

Figure 1.1: Schematic Hertzsprung-Russell diagram with the evolutionary track of a $1M_\odot$ star (from CSIRO webpage, Australia Telescope National Facility: http://www.atnf.csiro.au).

Indeed, stars are opaque and the information we receive as photons comes only from their surface layers, i.e. the photosphere. A similar situation exists for the Earth for which only the near surface layers are directly accessible to observation. Nonetheless, the study of the propagation of seismic waves inside our planet allows geophysicists to draw a realistic picture of the hidden Earth internal structure.

The solution to the stellar interior problem is also to use waves propagating inside the object of interest (the study of such waves is called Helioseismology for the Sun and Asteroseismology for other stars). Inside a star, different mechanisms can lead to the generation of waves. Adding some boundary conditions for the propagation of such waves, resonant modes arise. These modes create periodic changes of the radius, effective temperature (and therefore luminosity) of the star. These variations are detectable near the photosphere and allow the observer to determine the periods (or frequencies) of the oscillation modes of a star, from which one can infer information on the stellar structure. The theory of stellar oscillations (and its application to low-mass stars) and how one can link oscillation properties to the stellar structure will be introduced in Chap. 3.

These last decades, asteroseismology has proved to be a unique and powerful tool to access the inner structure of stars. Since many stars oscillate, we can obtain information on the inner properties of a large variety of stars and on stellar evolution. In this thesis, we are mainly interested by low-mass red-giant stars, which correspond to evolved solar-type stars. These stars are "cool" stars (with surface temperatures around 5000 K), more luminous and much larger than our Sun (with luminosities between 10 and 10^3 $L_\odot$ and radii between 5 and 100 $R_\odot$). In this thesis, I will investigate stars from the main sequence to the red giant phase (with particular emphasis on the latter), between 1 and 2 $M_\odot$ and up to no more than $20R_\odot$.

1.1 Historical context of solar-like oscillations

As their name suggest it, solar-like oscillations have been first discovered in the Sun. We provide in Sect. 1.1.1 some key events in the course of their discovery, their observations, and their interpretations (a more detailed review can be found in e.g. Christensen-Dalsgaard 2002; Kosovichev 2011, and references within). We then move in Sect. 1.1.2 to other stars and the recent contributions of the space-borne telescopes CoRoT and *Kepler* in the study of solar-like oscillations (with a particular interest for evolved low-mass stars).

1.1.1 Oscillations of the Sun

Some decades after Sir Arthur Eddington's remark, Leighton (1960) discovered oscillations in dopplergrams of the Sun with periods of about 5 min and amplitudes around 0.4 $km.s^{-1}$. Mein (1966) computed a theoretical solar oscillation power spectrum. He concluded that the oscillations are acoustic waves and suggested that some of their properties may be determined by the convective zone just below the surface. We will have to wait almost ten years and the first longer observations runs of the Sun (3 hours sets instead of 30-40 min) to clearly confirm the nature of the 5 min oscillation modes (Deubner 1975).

Information from the solar oscillation frequencies

Additional observations by Rhodes et al. (1975) led to the first use of the solar oscillations to probe the inner structure of the Sun. Indeed, the comparison of their observations with the frequencies computed from different theoretical solar models allowed them to put some limits on the depth of the solar convective envelope. With longer duration of observations, new breakthroughs occurred and laid down firm bases for the wide diagnostic power of solar-like oscillations. Claverie et al. (1979) measured the equidistant frequency separation in the solar power spectrum (the large separation, as predicted by Vandakurov 1968) and Grec et al. (1980) resolved the fine structure of the frequency pattern and provided the value of the solar small separation. These parameters have, since their discovery, led to very important results for various solar problems (see e.g. Iben 1976; Christensen-Dalsgaard et al. 1979; Christensen-Dalsgaard, Gough 1981) and are now widely used to infer basic properties of distant stars (see Sect. 3.5 on current asteroseismic techniques). The clear identification of the observed radial and non-radial modes led to the development of helioseismic techniques based on various comparisons between theoretical predictions and observations. One of these predictions concerned the impact of rotation on mode frequencies called rotational frequency splitting (an effect similar to the Doppler splitting). This effect has been observationally confirmed by Rhodes et al. (1979); Ulrich et al. (1979); Deubner et al. (1979) with long continuous observations. Their measures gave a first evidence and, later, a first determination of the Sun internal differential rotation profile.

Analyses of more and more precise data on solar oscillations have produced these last decades a lot of interesting results on the inner solar structure and on some physical processes within (see e.g. the review of Christensen-Dalsgaard 2002). Among them, we may cite the development of inversion techniques (see Sect. 3.5.3) to determine the sound speed profile inside the Sun (Christensen-Dalsgaard et al. 1985) and the helium abundance of the solar convective envelope (see e.g. Vorontsov et al. 1991; Kosovichev et al. 1992; Antia, Basu 1994).
Our knowledge of the rotation profile of the Sun has also been improved by inversion techniques which have provided the radial and latitudinal dependence of the rotation rate (see e.g. Brown 1985; Schou et al. 1998). Goode (1991) determined that the solar rotation profile presents a latitudinal dependence of the angular velocity in almost all the convective envelope and then changes sharply toward a solid body rotation in the radiative interior. Spiegel, Zahn (1992) interpreted this transition region as a tachochline.
Concerning the solar core, Noerdlinger (1977) has highlighted the importance of diffusion and gravitational settling of chemical elements. These processes are now included in almost all solar models (see e.g. Cox et al. 1989; Proffitt 1994; Gabriel, Carlier 1997; Morel et al. 1997).
Finally, with the possibility to observe the wave field in a given region of the solar surface one can also investigate the local properties of the subsurface region. Local helioseismology gives access to the three dimensional structure and to the flows below the surface, such as large scale convective flow patterns, meridional flows,... (see e.g. Duvall 2000; Haber et al. 2002) bringing valuable information on the dynamic of the convective envelope.

Information from energetic aspects of solar oscillations

All these results mainly focused on the frequencies of the modes. The interpretation of the amplitudes of these modes is more challenging because they are the result of a balance between driving and damping processes. From a theoretical point of view, Ando, Osaki (1977) determined that the mode driving is concentrated close to the surface. We note for further use that this region is the location of highly turbulent convective motions, which represent the main difficulty for a realistic modelling of solar-like oscillations. The question of the excitation of the modes is linked to their stability: did their amplitude grow until a saturation mechanism takes place (unstable modes) or did it naturally decrease (stable modes)?
This question for the solar oscillations has been investigated by various authors (see e.g. Ando, Osaki 1975; Balmforth 1992b). Numerical computations taking into account only the κ mechanism (excitation and damping due to opacities; see Sect. 3.1.4) gave results inconsistent with the observed amplitudes. Ando, Osaki (1975) found that only some of the observed modes were unstable, the other being predicted stable. It would have implied clear amplitude differences between stable and unstable modes, which is not the case. By taking into account additional sources of damping (due to the radiative and convective fluxes, as well as turbulent pressure; see Sect. 3.2.7), Balmforth, Gough (1990) and Balmforth (1992b) showed that the damping due to the turbulent pressure stabilises all solar modes.
An additional argument favouring stable modes comes from the observed shape of individual modes in the power spectrum. With a high enough frequency resolution, the modes appear in the power spectrum with a Lorentzian profile, from which we can measure the linewidths and amplitudes (see e.g. Libbrecht 1988; Chaplin et al. 1998). A Lorentzian shape in the Fourier frequency space is characteristic of an exponential behaviour in the time space. Thus, an exponential damping is favoured. Indeed, if modes were unstable, a saturation mechanisms should take place and from this moment their amplitude behaviour will no longer be exponential. Moreover, observations of other stars which present unstable modes show that such modes reach much higher amplitudes than in the Sun. It would have thus required a very efficient saturation mech-

anism if solar modes were to be unstable. It has thus been concluded that solar modes are stable (intrinsically damped). The damping mechanism for solar-like oscillations will be presented in details in Sect. 3.2.

Solar oscillations being damped, a new excitation mechanism is needed to explain their existence and amplitudes (the classical κ mechanism is not able to excite these modes). Since the discovery of the solar oscillations, Stein, Leibacher (1974) have suggested that these oscillations could be excited by turbulent motions in the convective envelope. Lighthill (1967) had already shown that a part of the convective energy is transformed into acoustic noise by the turbulence. Goldreich, Keeley (1977) proposed the first theoretical estimate of the amplitudes of stable solar modes. The model developed by Balmforth (1992a) allowed them, by adjusting various free parameters to solar observations, to reproduce the amplitudes of the observed modes. More recently, Samadi et al. (2003a), based on the theory developed by Samadi, Goupil (2001) (which generalise the theory of Goldreich, Keeley 1977), reproduced the solar mode amplitudes, without adjustments of free parameters to the observations, by constraining the convection using 3D hydrodynamic simulations. This formalism is adopted in this thesis and will be presented in Sect. 3.4. Improvements of this theory have been made in the description of the turbulence (Belkacem et al. 2006a,b, 2010) and the treatment of non-radial oscillations (Belkacem et al. 2008).

We thus define **solar-like oscillations as intrinsically damped oscillations excited by turbulent motions in the upper convective layers of a star**. We thus expect to observe such oscillations in stars with a convective envelope, i.e. low-mass stars on the main-sequence and in the red-giant phase (see Sect. 2.3.2 for a description on the occurrence of convective envelopes depending on the stellar mass and evolutionary state). From an observational point of view, solar-like oscillations can be identified in other stars thanks to equidistant spacings in the frequency pattern (large and small frequency separations, see Sect. 3.1.3). Moreover, the heights of the peaks in the power spectrum follow a characteristic bell shape (see for example Fig. 1.2) which is theoretically explained by the contributions of turbulent eddies of different characteristics as a function of the oscillation frequency (see details in Sect. 3.4.3).

1.1.2 From the Sun to solar-like oscillators

From ground-based observations, detections of solar-like oscillations in main-sequence stars were a few and difficult to confirm. Procyon is the first star suspected to present solar-like oscillations (α CMi, Brown et al. 1991) based on the shape of the power excess in its spectrum. The nature of these oscillations was clearly established almost ten years later (Martić et al. 1999; Barban et al. 1999). Thanks to high precision spectroscopy, Kjeldsen et al. (1995) detected for the first time individual frequencies of solar-like oscillations in another star (η Boo). For this star, Brown et al. (1997) could not confirm the detection of solar-like oscillations and the clear confirmation came only later by Kjeldsen et al. (2003) and Carrier et al. (2005). In addition, β Hyi (Bedding et al. 2001) and α Cen (a solar twin) also presented signs of solar-like oscillations (see Bouchy, Carrier 2001). For this last star, the very high quality of observations have allowed Miglio, Montalbán (2005) and De Meulenaer et al. (2010) to exclude the existence of a convective core. These four stars were the only main-sequence ones in which we have detected or suspected solar-like oscillations, from the ground, prior to the CoRoT and *Kepler* era.

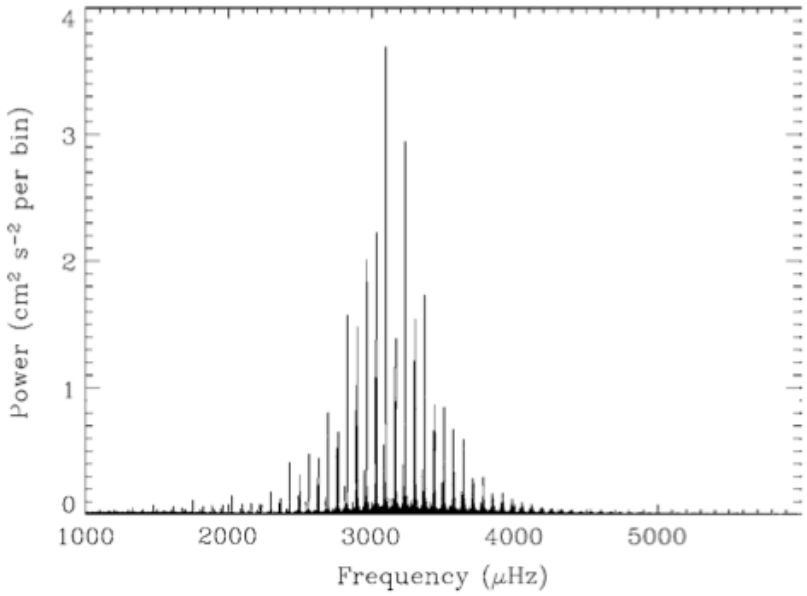

Figure 1.2: Power spectrum of the Sun: Oscillations radial velocity as a function of the frequency (from Aerts et al. 2010).

At this time, the situation for more evolved stars was even less clear. When only ground based observations were available, the detection of non-radial modes was a pending issue. On one hand, observations of α UMa (Buzasi et al. 2000) and their theoretical analysis by Dziembowski et al. (2001) led them to infer that the inner radiative damping is too strong to have observable non-radial oscillations. Radial velocity observations of ξ Hydrae and ϵ Ophiuchi seemed to confirm these results (Frandsen et al. 2002; Stello et al. 2006; De Ridder et al. 2006; Mazumdar et al. 2009). On the other hand, Hekker et al. (2006) concluded from spectral-lines analyses of three red giants (ξ Hydrae, ϵ Ophiuchi, η Serpentis) and a subgiant (δ Eridani) that non-radial oscillations could be detectable in some cases.

All these results motivated the development of space-borne missions, that now give to the asteroseismic community new exciting results and challenges for the understanding of the physics of stars.

The breakthrough of CoRoT and *Kepler* space-borne telescopes

The CoRoT mission (Baglin et al. 2006) was designed to discover exoplanets of super-earth radii and to study the internal structure of stars (mainly linked to stellar convection and rotation issues). Launched in December 2006, it has gathered data till November 2012. The observations covered different regions of the sky with an observation duration ranging between 20-30 and 150 days. The *Kepler* mission (Borucki et al. 2008) was designed to detect earth-size exoplanets. Since its launch in 2009 it has observed the same field of view (with about 150 000 stars). It thus gives us access to observations covering a very long period (around 4 years of observations were gathered when two reaction wheels failed in May 2013). This represents an unprecedented follow-up of many stars, which, coupled with the high photometric precision, allows one to iden-

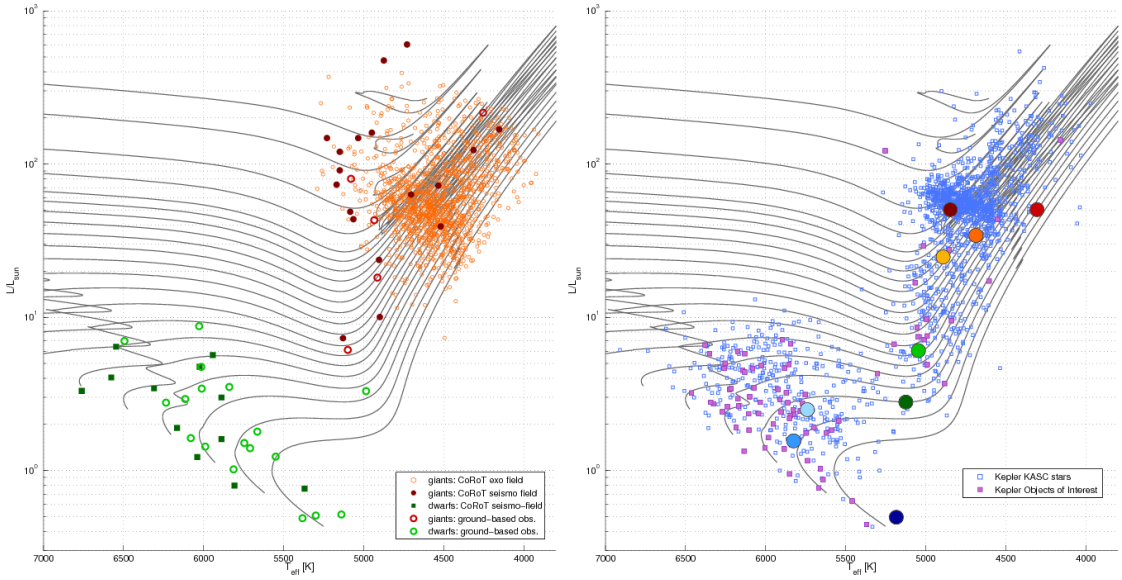

Figure 1.3: From Chaplin, Miglio (2013): HRD of stars confirmed to display solar-like oscillations. Contributions of the CoRoT (left) and *Kepler* (right) missions.

tify the mode parameters (frequencies, linewidths and amplitudes) with an excellent precision (Gilliland et al. 2010). We can have a glimpse of the contribution of CoRoT and *Kepler* in the area of solar-like oscillations with the very high number of observed targets confirmed to be solar-like pulsators as illustrated in Fig. 1.3.

One of the major achievements, and surprise of the CoRoT mission is the discovery of non-radial solar-like oscillations in red giants (De Ridder et al. 2009). The detectability of these pressure dominated non-radial modes in red giants was theoretically predicted by Dupret et al. (2009) who also predicted that gravity-dominated mixed modes should be detectable in red giants (depending on the evolutionary stage).

As already mentioned, solar oscillations are acoustic modes, trapped in the convective envelope, and giving us information only on superficial layers. Gravity modes, trapped in the radiative core of the Sun, (see Sect. 3.1.3 for the specificities of these two types of modes) do not reach the surface with detectable amplitudes (see e.g. Appourchaux et al. 2010). The situation is similar for other low-mass stars on the main sequence.

For evolved low-mass stars, the stellar evolution leads to a quite different, and complex, situation. Due to the contraction of the core and the expansion of the envelope (see Sect. 2.5), the typical frequency ranges of acoustic and gravity modes approach each other and finally overlap. As a consequence, both types of modes interact, which leads to oscillations that can propagate both in the convective envelope (with an acoustic mode behaviour) and in the radiative core (with a gravity mode behaviour) of the star. Such modes are named mixed-modes (see Sect. 3.1.3). This phenomenon was first theoretically suggested by Scuflaire (1974) and Dziembowski (1977). These mixed-modes can be described as a resonant interaction (also called an avoided crossing) between a gravity and an acoustic mode (see e.g. Aizenman et al. 1977; Deheuvels, Michel 2010). When the star is still close to the main sequence, only a few modes are concerned, but they may

reach high enough amplitude at the surface to be detected. In that case, new peaks appear in the power spectrum. It is expected that these peaks present distinct characteristics from acoustic modes, depending on their relative trapping between the core and the envelope. As the star evolves in the red-giant phase, the number of mixed-modes between two acoustic modes increases (more and more modes undergo avoided crossings), which leads to a very rich and complex power spectrum. A lot of gravity-dominated mixed-modes create peaks in the power spectra that are no longer equally spaced in frequency but are almost equally spaced in period (see Sect. 3.1.3). Providing we can distinguish these modes in a power spectrum (and identify them), they give us a direct access to the inner structure of the star because they propagate both in the central and superficial layers of the star.

The detection of non-radial mixed-modes (De Ridder et al. 2009) thus represents an opportunity to probe the inner structure of evolved low-mass stars, and has already led to a lot of interesting results (the interested reader could find in e.g. Chaplin, Miglio 2013, a review of the recent results in asteroseismology of solar-like oscillations). Observations of gravity-dominated mixed-modes, which are almost equally spaced in periods, allow us to distinguish between stars with very close surface properties but different core densities. In particular, this allows us to distinguish stars on the red-giant branch and in the central helium burning phase (see e.g. Bedding et al. 2011; Mosser et al. 2011, and Sect. 3.5.1). The high frequency resolution of the observations allows one to distinguish rotational multiplets in the power spectrum of gravity- and acoustic- dominated mixed-modes from which one can extract the rotation rate of the centre and of the surface of the stars (see e.g. Beck et al. 2012; Deheuvels et al. 2012; Mosser et al. 2012b; Deheuvels et al. 2014). The major conclusion of these studies is that red-giant cores spin slower, by about two orders of magnitude, than what one expects from the current stellar evolutionary models including transport of angular momentum by meridional circulation and shear instabilities (Eggenberger et al. 2012; Marques et al. 2013; Ceillier et al. 2013). This calls for a new mechanism able to transport angular momentum from the core to the envelope. Cantiello et al. (2014) added the effect of magnetic field and reached the same conclusion. Recently, Rüdiger et al. (2015) have shown that a toroidal magnetic field could transport angular momentum from the core to the envelope in subgiants and early red giants. The impact of internal gravity waves (e.g. Press 1981) in the transport of angular momentum for red giants has still to be investigated (but see Fuller et al. 2014). Belkacem et al. (2015a,b) suggested and demonstrated that mixed-modes can effectively transport angular momentum in evolved red giants.

Energetic aspects of solar-like oscillations in red giants

The energetic aspects of solar-like oscillations determine the linewidths and heights of the peaks in the power spectrum. Indeed, these observables are directly related to the lifetimes and amplitudes of the modes (see Sect. 4.4.2). Investigating these effects requires a non-adiabatic approach of the oscillations (i.e. including energy exchanges between the oscillation and the surrounding medium). Since solar-like oscillations excitation and damping are directly related to convection, it is necessary to also model the interaction between convection and oscillations (for both their damping and their excitation).
Simultaneously with the first detections of mixed-modes in red giants, Dupret et al. (2009) provided the first theoretical explanation for the different visibilities of these modes in red giants. Their theoretical models treat the interaction between convection and oscillations for the damping (with a non-local time-dependent treatment of convection, Grigahcène et al. 2005, see also Sect. 3.2) and the driving of the modes (with a stochastic excitation model, Samadi, Goupil 2001, see also Sect. 3.4). They concluded that gravity-dominated mixed-modes should be visible

in red-giant power spectra until the radiative damping, which increases during the evolution of the star, becomes too important. Moreover, they show that different strengths of the radiative damping lead to various structures in power spectra.

On the observational side, the study of these effects suffers from the difficulty to precisely determine the linewidths and amplitudes of the modes. First, linewidths and heights determined from the observed power spectrum are strongly correlated (Chaplin et al. 1998). Second, it requires long times of observations (typically larger than 10 times the lifetime of the mode) to fully resolve the Lorentzian profile of the peak. If this condition can now be easily satisfied for pressure-dominated modes (with lifetimes between 1-10 days on the main sequence and 10-100 days on the red-giant branch, see e.g. Belkacem et al. 2012), it is rarely the case for gravity-dominated modes, which can reach much longer lifetimes (up to a factor 100, see Chap. 6).

Mode linewidths and heights have recently been considered more thoroughly for radial modes both on the observational side (e.g. Baudin et al. 2011; Corsaro et al. 2012; Appourchaux et al. 2012; Corsaro et al. 2013; Appourchaux et al. 2014) and on the theoretical side (e.g. Chaplin et al. 2009b; Belkacem et al. 2011; Belkacem et al. 2012) because they are important for the estimate of mode detectability, as well as for constraining the interaction between oscillations and turbulent convection. Note that with the very large number of observed stars displaying solar-like oscillations, it is now possible to perform ensemble analyses (see Sect. 3.5.1) also on the global energetic properties of these oscillations (mainly for radial modes). Based on measures of linewidths and amplitudes of radial modes (around the frequency of maximum power), it is possible to extract global tendencies linking linewidths and amplitudes to basic stellar parameters.
Prior to the detection of solar-like oscillations in stars other than the Sun, theoretical considerations led to think that acoustic mode amplitudes should vary as L/M (Kjeldsen, Bedding 1995, with L the luminosity and M the mass of the star). Such scaling relation was recently adjusted by Samadi et al. (2012).

Measurements of the observed linewidths of radial modes around the frequency of maximum power led Chaplin et al. (2009b); Baudin et al. (2011) to exhibit a strong dependence between the linewidths Γ of radial modes and the effective temperature $T_{\rm eff}$ of the star, on the main sequence and in the red-giant phase (with possibly a different $\Gamma - T_{\rm eff}$ relation between the two evolutionary phases). This relation was theoretically investigated by Belkacem et al. (2012a) who predicted a unique scaling relation from main-sequence to red-giant phase and confirmed the strong dependence of the linewidths to the effective temperature.
Belkacem et al. (2012a) also proposed a theoretical explanation for the plateau of the linewidths (well known in the Sun) and showed how the position of the plateau is linked to the frequency of maximum power.

Nevertheless, literature is more tenuous about the amplitudes and lifetimes of mixed modes. Only very recently have mixed-mode linewidths and amplitudes been measured for subgiant stars (Benomar et al. 2013; Benomar et al. 2014), mainly because of the complexity of individually fit all modes for power spectra including mixed modes.

1.2 Problematic and organisation of the manuscript

Motivated by all these recent results, the goal of my thesis is to investigate in details the energetic properties of solar-like oscillations (the linewidths, amplitudes and heights of the peaks in power spectra) from a theoretical point of view. These properties determine the shape and the complexity of the power spectrum. I will thus study the physical processes driving and damping solar-like oscillations and investigate how they can lead to different morphologies in power spectra. A major goal of this work is to establish the links between the morphologies of red-giant power spectra and their internal structure. Comparisons between theoretical and observed linewidths and amplitudes will allow me to put some constraints on the interaction between convection and oscillations, which is at the basis of the energetic aspects of solar-like oscillations; and on the physical conditions and damping in the stellar cores.

The typical questions I will address are:

- Given the characteristics (the mass, the evolutionary stage) of red giants, and accounting for the duration of the observations, which modes can be detected?
- Which information on the inner structure do they hold (on the trapping of mixed-modes, the physical conditions in the central layers, the interaction between turbulence and oscillations, ...)?
- How theoretical predictions (especially for mode lifetimes and amplitudes) compare with observations?
- Which information on the accuracy, strengths, and limits of the models can be derived?
- Which theoretical uncertainties/parameters most affect the predictions and how can they be constrained from observations?

The first step is to clearly understand the theories involved (their current successes and their assumptions) in any attempt to model the energetic aspects of solar-like oscillations. Thus, the first part of this thesis will be dedicated to the description of the theoretical background on solar-like oscillations, with a particular emphasis on red giants and on the energetic modelling of the oscillations.
The theoretical study starts with the modelling of the object of interest. I will present in Chap. 2 the theory of stellar structure and evolution, focusing on low-mass evolved stars and on the physical processes acting in such stars. A particular attention will be devoted to the convection (in Sect. 2.4) which plays an important role for solar-like oscillations.
This will permit us to introduce solar-like oscillations in Chap. 3, where the theory of stellar oscillations (as a perturbation of the stellar equilibrium structure) will be presented in Sect 3.1. I will then focus on the properties of solar-like oscillations. We will first look at the frequency pattern and at the trapping of oscillation modes (including the specificities of mixed modes) in Sect. 3.1.3. Then, I will present the theories enabling us to model their energetic properties, namely their damping with the time-dependent treatment of convection (hereafter TDC) in Sect. 3.2 and their excitation with a stochastic excitation model in Sect. 3.4. I will then describe the different ways we can use the observed oscillations properties to access the internal stellar structure and to understand the physical processes that give their characteristics to the oscillations in Sect. 3.5.

The second part of this manuscript is dedicated to my own developments and results.

As a preamble for the presentation of my results, I discuss in Chap. 4 the general method adopted in this thesis for the modelling of solar-like oscillations and of theoretical power spectra. In particular, I will discuss some difficulties in the modelling, due to the very specific physical characteristics of red giants, and the adopted solutions

A well known issue in the modelling of solar-like oscillations concerns the interaction between convection and oscillations. The time dependent treatment of convection involves significant assumptions and free parameters. In Chap. 5, I will test the effects of the different parameters of the TDC on theoretical radial modes linewidths in order to identify their impact on theoretical predictions. I will also present how the theoretical results compare with observations, and how observed linewidths can help us to constrain the TDC parameters for a better understanding of the interaction between convection and oscillations.

Observed red-giant power spectra display a large variety of complexity in the number and the relative amplitudes of mixed-modes peaks (see e.g. Fig 4 in Chaplin, Miglio 2013). To understand these different types of power spectra we need to identify the key parameter(s) for the detectability of the modes. I will address this question in Chap. 6 with theoretical modellings of series of red-giant power spectra. In Sect. 6.1, I will first present simple theoretical considerations that will allow us to understand the combined impact of trapping, damping and driving on the morphology of the power spectrum (mainly on the different heights of the peaks). Then, I will investigate the physical process inside the star that limits the amplitudes of g-dominated mixed-modes and that can prevent their detection. I will then search what are the common characteristics of models with similar detectability of mixed-modes. This will allow me to extend the results on the theoretical detectability of mixed-modes to a wide range of masses (representative of CoRoT and *Kepler* observations) in Sect. 6.2. I will finally present a specific behaviour of a red-clump stellar model that creates a pattern in the power spectrum for which one has to be very careful in its interpretation (Sect. 6.4).

Finally, in Chap. 7, I will present a full non-adiabatic analysis of an observed subgiant star. I will first present the specificities of the modelling of a star with mixed-modes in Sect. 7.2. Then I will compare the theoretical lifetimes and amplitudes of the modes to the observed ones in Sect. 7.3. Finally, in Sect. 7.4, I will discuss the accuracy of theoretical predictions with a new analysis of the same star with a longer duration of observation. This will allow me to discuss the potential diagnostic provided by the observation of additional mixed-modes.

Part I

Theoretical background on low-mass stars and solar-like oscillations

Chapter 2

Structure and evolution of low-mass stars

A star is, in first approximation, a self-gravitating sphere of gas governed by the laws of hydrodynamics. By low-mass stars, we denote stars that develop an electron degenerate core after the main sequence and then ignite the helium nuclear burning during an He-flash (see Sect. 2.5 for the description of these evolutionary phases). Standard evolutionary models show that such stars exist in a limited mass range ($M/M_\odot \in [0.45; 2.5]$). Objects below $M \simeq 0.45 M_\odot$ do not perform core helium burning, while stars beyond $M \simeq 2 - 2.5 M_\odot$ do not develop an electron degenerate core and start helium burning in a quiescent way.

In this chapter, I will describe the general theory of stellar structure and evolution. This includes a presentation of the characteristic time scales associated with the main physical processes occurring inside a star in Sect. 2.1. I will then discuss the basic equations as well as the physical inputs and processes needed to understand and to compute the equilibrium structure of a star as well as its evolution in Sect. 2.2. In Sect. 2.3, I will focus on the specificities of energy transport inside the star. Since convection is a very important process for low-mass stars (as stated for the Sun in Sect. 1.1.1 and as we will see later in this chapter and the in following one), I will develop the commonly adopted formalism for the modelling of convective layers in Sect. 2.4. With all these developments, we will be able to understand the evolutionary path of a low-mass star as pictured in Sect. 2.5. Finally, I will present in Sect. 2.6 some major current issues and prospects in stellar modelling.

2.1 Time scales of stellar dynamics

From their birth to their death, stars undergo a lot of structural changes, associated with various physical processes acting on very different time scales. I give here a brief overview of these time scales, related to different equilibriums inside the star.

- The dynamical time scale represents the time needed for a star to respond to a sudden perturbation of the hydrostatic equilibrium. Suppressing one of the two opposite forces acting on this equilibrium (the pressure gradient against the gravity force), we find

$$t_{\rm dyn} = \sqrt{\frac{R^3}{GM}} \simeq \frac{1}{\sqrt{G\rho_\star}}, \tag{2.1}$$

with G the gravitational constant, R and M the total radius and mass of the star and $\rho_\star$ its mean density. For further use, we note that the period of the fundamental radial pulsation mode is of the order of the dynamical time scale.

- The Helmholtz-Kelvin time scale is linked to the thermal equilibrium between the star's production and loss of energy. The Virial theorem states that, before the appearance of nuclear reactions, half of the gravitational potential energy released by the contraction of the star leads to an increase of its internal energy while the other half is radiated. Assuming a cut-off of the nuclear reactions, the luminosity of the star will come from its internal energy and its gravitational potential energy. This time scale is therefore an estimate of the cooling time of the star. It is defined as

$$t_{\rm HK} = \frac{GM^2}{2RL}, \tag{2.2}$$

  with L the total luminosity of the star.

- Since nuclear reactions drive stellar evolution, the typical evolution time scale is associated with the nuclear time scale given by

$$t_{\rm nuc} = \frac{E_{\rm nuc}}{L}, \tag{2.3}$$

  where $E_{\rm nuc}$ is the nuclear energy produced inside the star, from the beginning to the end of a given nuclear burning phase. It represents the time needed for the nuclear reactions to significantly modify the chemical composition of the star. For main-sequence stars, it corresponds to the time needed for the star to burn about 10% of its hydrogen at a given luminosity.

In a star, we have almost always between these global time scales $t_{\rm dyn} \ll t_{\rm HK} \ll t_{\rm nuc}$. For example, for the Sun $t_{\rm dyn} = 26$ min $\ll t_{\rm HK} = 3.1 \times 10^7$ years $\ll t_{\rm nuc} = 9.8 \times 10^9$ years and for a red giant (of 1.5 $M_\odot$ and 12 $R_\odot$) $t_{\rm dyn} \simeq 39$ h $\ll t_{\rm HK} \simeq 3.5 \times 10^4$ years $\ll t_{\rm nuc} \simeq 9.10^6$ years. These relations between the different time scales will allow us to make some simplifications in the development of the equations of the stellar structure (Sect. 2.2.2) and in the oscillation equations (see Chap. 3). The hierarchy $t_{\rm dyn} \ll t_{\rm HK} \ll t_{\rm nuc}$ involves that it is not necessary to consider changes of chemical composition in the study of thermal or dynamical processes. From this relation, we can also make the hypothesis that in almost all evolutionary phases, the star is at thermal and hydrostatic equilibrium. As we will see in Chap. 3, $t_{\rm dyn} \ll t_{\rm HK}$ means that oscillations can be considered as adiabatic almost everywhere in the star.

2.2 Basic equations of stellar structure and evolution

I describe here the case of a single star without magnetic field and for which the classical Newton gravitational law can be used (which is almost always the case except for very compact objects such as neutron stars). After a short presentation of the two possible points of view to describe a fluid, I give in Sect. 2.2.1 the general hydrodynamics equations and apply them to the stellar case (using some simplifications) in Sect. 2.2.2.

In the **Lagrangian description**, one follows the evolution of an infinitesimal mass element. A physical quantity X is given as a function of a vector $\mathbf{a}$ attached to the fluid element and of the

time t. In this thesis the partial time derivative of $X(\mathbf{a}, t)$ in the Lagrangian description, i.e. following the movement of a given mass element, will be noted dX/dt.

The **Eulerian description** consists in analysing the fluid at a fixed spatial point. A local physical quantity X is given as a function of the position $\mathbf{r}$ and the time. In the Eulerian description, the partial derivation of $X(\mathbf{r}, t)$ with respect to the time will be noted $\partial X/\partial t$.

These two formalisms are linked through their temporal derivatives as follows,

$$\frac{dX}{dt} = \frac{\partial X}{\partial t} + \mathbf{v} \cdot \nabla X, \tag{2.4}$$

where $\mathbf{v}$ is the fluid velocity (i.e. the Lagrangian derivative of the position: $d\mathbf{r}/dt$).

2.2.1 General equations of hydrodynamics

The four basic fluid equations are:

- The continuity equation, that describes the mass conservation:

$$\frac{d\rho}{dt} + \rho \nabla \cdot \mathbf{v} = \frac{\partial \rho}{\partial t} + \nabla \cdot (\rho \mathbf{v}) = 0, \tag{2.5}$$

  where ρ and $\mathbf{v}$ are the local density and velocity vector.

- The motion equation describes momentum conservation. Neglecting the viscosity (because the Reynolds number is very high in stars, see Sect. 2.4) and also neglecting the Lorentz force due to the magnetic field, it reads:

$$\frac{d\mathbf{v}}{dt} = \frac{\partial \mathbf{v}}{\partial t} + \mathbf{v} \cdot \nabla \mathbf{v} = -\nabla \psi - \frac{\nabla P}{\rho}, \tag{2.6}$$

  where ψ is the gravitational potential and P the total pressure (taking into account the contribution of gas and radiation).

- The equation of energy conservation:

$$T \frac{dS}{dt} = \epsilon - \frac{\nabla \cdot \mathbf{F}}{\rho}, \tag{2.7}$$

  where T is the temperature, S the entropy, ϵ the energy generation rate and $\mathbf{F}$ the energy flux.

- The Poisson equation, that describes the behaviour of the gravitational potential:

$$\nabla^2 \psi = 4\pi G \rho, \tag{2.8}$$

To these equations, one must add an energy transport equation to determine the energy flux in Eq. 2.7.

2.2.2 The four equilibrium equations

During the main part of the life of a star, its evolution results from changes of chemical composition due to nuclear reactions. Given the time scales of the different dynamical processes (Sect. 2.1), we can almost always assume that the star is in hydrostatic equilibrium at each given time. For low-rotating or non-rotating stars, we can assume that stellar models have a spherical symmetry and neglect the Coriolis force. Given the spherical symmetry, we can rewrite all the physical quantities as a function of the radial coordinate r. This allows one to simplify the structure equations 2.5 to 2.8 as follows:

The mass of a shell

$$\frac{dm}{dr} = 4\pi r^2 \rho. \tag{2.9}$$

with $m(r)$ the mass inside a sphere of radius r ($m(R) = M$).

The hydrostatic equilibrium

$$\frac{dP}{dr} = -\frac{Gm\rho}{r^2}. \tag{2.10}$$

The energy conservation

$$\frac{dL}{dr} = 4\pi r^2 \rho \epsilon. \tag{2.11}$$

The energy transport

$$\frac{dT}{dr} = -\frac{Gm\rho T}{r^2 P}\nabla \qquad \text{with} \qquad \nabla = \frac{d\ln T}{d\ln P}, \tag{2.12}$$

The first two equations determine the mechanical profile, while the last two determine the energetic profile inside the star. They are coupled through the density. Additionally to these equations, one needs a theory of energy transport (as detailed in Sect 2.3) to determine ∇ in Eq. 2.12, which is a-priori unknown. Even with a theory for the energy transport, this set of equations is not complete and one also needs boundary conditions in order to solve it. The following points present the additional requirements needed in order to obtain a complete set of equations for the computation of an evolutionary stellar model.

Equation of state: Since we have now four equations for five unknown quantities (m, ρ, P, L, T), we need an additional equation to provide the behaviour of one thermodynamic quantity depending on the others. This is given by equations of state (for example, $P = P(\rho, T, \mu)$ where μ is the mean molecular weight i.e., the mean mass of particles in atomic mass unit).

In the case of a **non-degenerate gas**, the pressure can be decomposed into gas pressure ($P_{\rm gas}$) and radiative pressure ($P_{\rm rad}$). Assuming the matter is formed of nuclei and free electrons, the equation of state of a perfect gas is given by

$$P_{\rm gas} = \frac{k\rho T}{\mu m_u} \tag{2.13}$$

where k is the Boltzmann's constant and $m_u \equiv 1/N_A$ with N_A the Avogadro's number.
The radiative pressure is given by

$$P_{\rm rad} = \frac{1}{3} a T^4 \tag{2.14}$$

with a the radiation density constant.
In the **non-degenerate case**, summing Eqs. 2.13 and 2.14, the equation of state for the total pressure writes:

$$P = \frac{k\rho T}{\mu m_u} + \frac{1}{3}aT^4 \tag{2.15}$$

The equation of state 2.15 is no longer valid when the density is so high that electrons are in a degenerate state, which happens, for example (at least partially), in the core of red-giant stars. For a **non-relativistic complete degeneracy** the equation of state gives the electrons pressure:

$$P_e = \frac{8\pi}{15h^3 m_e}\left(\frac{3h^3}{8\pi m_u}\right)^{2/3}\left(\frac{\rho}{\mu_e}\right)^{5/3}. \tag{2.16}$$

where h is the Planck's constant, m_e the mass of an electron, m_u the atomic mass unit and μ_e the mean mass by free electron. Thus, in degenerate conditions, the pressure is independent of the temperature. This will have an important consequence on low-mass stars evolution as we will see in Sect. 2.5.

Chemical composition: To fulfil the equations, the last requirement is a description of the chemical composition of the star to obtain the molecular weight. The chemical composition changes during the evolution of the star mainly due to nuclear reactions. Transport mechanisms and mixing processes (such as diffusion and convection) can also contribute to change the chemical composition. One can write the local variation of the abundance $X_{\rm i}$ of an element i as

$$\frac{dX_{\rm i}}{dt} = \sum_{\rm j} R_{\rm ij} - \frac{1}{\rho r^2}\frac{\partial}{\partial r}(r^2 \rho w_{\rm i} X_{\rm i}) \tag{2.17}$$

with $\sum_{\rm j} R_{\rm ij}$ the contributions of all nuclear reactions involving the element i and $w_{\rm i}$ the diffusion velocity of the element i. Note that in a convective region the mixing speed is so fast that we can always consider the region as homogeneous.
The chemical composition is usually described by the mass fraction of hydrogen (X), helium (Y) and metals (Z) (such that $X + Y + Z = 1$). In stellar models, the metals composition is given by the metallicity $[Fe/H] = \log(Z/X) - \log(Z/X)_\odot$ where (Z/X) is the ratio at the stellar surface and $(Z/X)_\odot$ corresponds to the ratio obtained for the Sun. The amount of individual metals is generally described by the solar mixture of heavy elements which mainly comes from the spectroscopic analyses of the Sun from Grevesse, Noels (1993) (GN93, solar metallicity $(Z/X)_\odot = 0.0244$), Asplund et al. (2005) (AGS05, $(Z/X)_\odot = 0.0165$) and Asplund et al. (2009) (AGSS09, $(Z/X)_\odot = 0.0181$) [1].

Boundary conditions: To be able to solve this set of equations, we need boundary conditions. The conditions at the centre of the star are simply given by $r(m = 0) = 0$ and $L(m = 0) = 0$. For the "surface" of the star, the boundary conditions are more challenging. One needs to know the temperature and pressure profiles in the very outer layers of the star. This had to be based on atmosphere models that provide the variation of these quantities with the optical depth.

[1] these are the three principal stellar mixtures used in stellar evolutionary codes.

Atmosphere model: Ideally, the outer boundary conditions should be fixed with a realistic atmosphere model. Such procedure presents some practical difficulties and the matching with the equilibrium model is not always ensured (see e.g. Montalbán, Dupret 2007). Thus, one generally uses a simple Eddington's grey atmosphere. Another possibility is to use semi-empirical relations between the temperature and the optical depth (see e.g. Krishna Swamy 1966).
The transition from the optically thick interior to the optically thin atmosphere is marked by the photosphere defined by $L(R) = 4\pi R^2 \sigma T(R)^4$, with σ the Stefan-Boltzmann's constant. In the case of an Eddington's grey atmosphere (as used throughout this work), this limit occurs at an optical depth $\tau = 2/3$. This relation also defines the effective temperature $T_{\rm eff} = T(R)$, which corresponds to the temperature of a black body emitting the same amount of energy as the star.

2.3 Energy transport mechanisms

The existence of a temperature gradient between the centre and the surface of the star requires a steady flow of energy from the core to the surface. This heat transfer involves the exchange of some particles (photons, electrons, matter), corresponding to different mechanisms that can transport this energy, depending on local thermodynamical properties. Thus, we can replace ∇ in Eq. 2.12 by the appropriate temperature gradient depending on the nature of the transport mechanism. Heat transfers through photons and electrons (radiation and conduction) are treated in a similar way (see Sect. 2.3.1). Heat transfer through matter exchanges (convection) requires a specific treatment. We give in Sect. 2.3.2 the criteria for the onset of convection in stellar interiors before developing the formalism in more details in Sect. 2.4. In all cases, we briefly discuss the stellar regions concerned by these different mechanisms.

2.3.1 Radiation and conduction

Radiation: In the interior of the star, the mean free path of a photon is negligible compared to the distance over which the energy transport extends (the stellar radius). One can thus describe in a very good approximation the radiative transfer by a diffusion equation, which gives the radiative flux:

$$\mathbf{F}_{\rm rad} = -\frac{4ac}{3}\frac{T^3}{\kappa\rho}\frac{\partial T}{\partial r}, \tag{2.18}$$

with a the radiation density constant, c the light speed an κ the opacity (see below, Eq. 2.20). Eq. 2.18 can be recast to give

$$\frac{dT}{dr} = -\frac{3\kappa\rho L_{\rm rad}}{16\pi r^2 acT^3}, \tag{2.19}$$

where $L_{\rm rad} \equiv 4\pi r^2 F_{\rm rad}$ is the radiative luminosity and κ is the mean Rossland opacity based on the monochromatic opacities κ_ν following

$$\frac{1}{\kappa} = \frac{\int_0^\infty \frac{1}{\kappa_\nu}\frac{\partial B_\nu}{\partial T}d\nu}{\int_0^\infty \frac{\partial B_\nu}{\partial T}d\nu}, \tag{2.20}$$

where B_ν is the Planck function at the frequency ν.
In the presence of convection, replacing the radiative luminosity by the total luminosity $L = L_{\rm rad} + L_{\rm conv}$ (with $L_{\rm conv}$ the luminosity transported by convection) in Eq. 2.19, we define the radiative gradient as:

$$\nabla_{\rm rad} \equiv \frac{3\kappa PL}{16\pi acGmT^4} \tag{2.21}$$

which is the (fictive) gradient that the medium should have to transport all the energy by radiation.
The opacity coefficient represents how the matter interacts with photons. One has to account for all the processes that can prevent the photon from moving freely in the matter to compute such a coefficient[2]. In practice, the opacity coefficients (for a given temperature, density and chemical composition) are most of the time interpolated in tables from OPAL (Iglesias, Rogers 1996) and OP (Mendoza 1992) groups. In the study of low-mass stars, these opacity tables are generally completed with the Ferguson et al. (2005) tables at low temperatures and with the conductive opacities from Potekhin et al. (1999).

Conduction: Transport of energy by conduction is due to collisions of particles in random thermal motions. In the general stellar case, given the high temperatures involved, the free paths of electrons and nuclei are much smaller than those of photons and conductive heat transport is negligible. However, in degenerate environments (such as in the core of evolved low-mass stars, see e.g. Iben 1968) the mean free path of electrons is considerably increased and conduction becomes an efficient heat transport mechanism. This mean free path remains very small compared to the radius of the star, so conductive transport of energy can also be treated as a diffusion process. Thus, one can add conductive energy transport to the radiative one by replacing $1/\kappa$ by $1/\kappa_{\rm rad} + 1/\kappa_{\rm cond}$ in Eq. 2.21 (with the appropriate definition of $\kappa_{\rm cond}$). In the latter, we will always assume that $\mathbf{F}_{\rm rad}$ and $\nabla_{\rm rad}$ take into account both radiative and conductive transports. This is to simplify the notations and to separate the contribution of convection to those of radiation and conduction.

2.3.2 Convection

In some cases, the radiation cannot transport all the energy from the centre to the surface of the star and this transport is thus carried out by convective motions. We recall here the criteria for the onset of convection in stars.

To derive such a criterion, we study the adjustment of the medium to a perturbation. We assume that a small element of matter is lifted up over a small distance (i.e. a displacement toward lower density regions). During this operation, the pressure equilibrium between the element and its surrounding is maintained (justified by the assumption that the dynamical time scale is smaller than the convective time scale). After this small displacement, the density of the element (which can change during its motion) is in general different from the one of the surrounding matter. It then undergoes a buoyancy force $\mathbf{F} = -\mathbf{g}\Delta\rho$ where $\mathbf{g}$ is the acceleration of the gravity and $\Delta\rho$ the density difference between the element (e) and it surrounding (s).

If $\Delta\rho < 0$, the element continues to go further in less dense regions. Thus, the situation is clearly unstable and the initial perturbation is increased. On the other hand, if $\Delta\rho > 0$, the element will go back to its original position, the layer is stable. These two situations depend on the change of the element density during its travel and on the gradient of density of the surrounding medium between the original and final position of the element. Such conditions on the gradient of density can be transformed into conditions on temperature gradients after simple algebra. The condition required for instability (i.e. for convection to take place) can be written as

$$\nabla > \nabla_{\rm e} - \left(\frac{\partial \ln \rho}{\partial \ln \mu}\right)\left(\frac{\partial \ln T}{\partial \ln \rho}\right)\nabla_{\mu}, \tag{2.22}$$

[2]This involves a huge amount of quantum mechanics computations to take into account all the possible interactions between an atom and a photon.

where $\nabla \equiv (d\ln T/d\ln P)_{\rm s}$ and $\nabla_\mu \equiv (d\ln \mu/d\ln P)_{\rm s}$ describe the variation of temperature and of molecular weight in the surrounding and $\nabla_e \equiv (d\ln T/d\ln P)_{\rm e}$ describes the variation of temperature of the element. Such criterion is in practice not very useful since we do not know a-priori ∇ and ∇_e.

If the convective element moves adiabaticaly, we should have $\nabla_e = \nabla_{\rm ad}$. Where we have defined $\nabla_{\rm ad} = \partial \ln T/\partial \ln P|_S$. In stars, the convective element will always experience some radiative losses such that we have $\nabla_e > \nabla_{\rm ad}$. In the same time, convective heat transport will decrease the temperature gradient of the surrounding such that $\nabla < \nabla_{\rm rad}$. Finally in unstable situations, we have the relation:

$$\nabla_{\rm ad} < \nabla_e < \nabla < \nabla_{\rm rad}. \tag{2.23}$$

We can now rewrite the instability criterion given in Eq. 2.22 in a more convenient way as

$$\nabla_{\rm rad} > \nabla_{\rm ad} - \left(\frac{\partial \ln \rho}{\partial \ln \mu}\right)\left(\frac{\partial \ln T}{\partial \ln \rho}\right)\nabla_\mu \tag{2.24}$$

in which all the quantities can be easily determined. This is the so-called Ledoux criterion, which reduces to the Schwarzschild criterion if the chemical composition is homogeneous ($\nabla_\mu = 0$):

$$\nabla_{\rm rad} > \nabla_{\rm ad} \tag{2.25}$$

From Eq. 2.21, we see that $\nabla_{\rm rad} \propto \kappa_{\rm rad} L/m$. According to the Schwarzschild criterion, convection will be favoured when the radiative gradient takes large values, which can happen either if $\kappa_{\rm rad}$ or L/m are large. In stars, these situations are mainly encountered in two cases (see also Sect. 2.5 for a description of the occurrence of convective zones during stellar evolution):

- **Convective cores:** When the nuclear energy rate strongly depends on the temperature (for example in the CNO nuclear cycle), the ratio L/m (in the central regions) is large and then favours the apparition of a convective core. This occurs, for example, on the main sequence for stars with $M \geqslant 1.3 M_\odot$, and during the core helium burning phase of low-mass stars.

- **Convective envelopes:** In cool stars envelopes ($T_{\rm eff} \lesssim 7500K$), the opacity $\kappa_{\rm rad}$ is large leading to a large radiative gradient which favours the onset of convection. This occurs in all low-mass stars ($M < 2M_\odot$) and in massive stars in post main-sequence stages.

Since low-mass stars are all characterised by a convective envelope, and since it is of prime importance for the study of solar-like oscillations, I will describe in the next section the simple way to model convection in stellar interiors in the frame of the mixing-length theory (hereafter MLT).

2.4 The convective treatment in stellar interior.

In fluid dynamics, dimensionless numbers are very useful to characterise a fluid. The Reynolds number, Re, which characterises the ratio between the advection and the viscosity, is given by (e.g. Landau, Lifshitz 1959):

$$Re = \frac{UL}{\nu}, \tag{2.26}$$

where, for the Sun (at the top of the convective zone), we have the typical length scale $L \sim 10^8$ cm, the typical velocity $U \sim 10^5\ cm.s^{-1}$ and a very small viscosity $\nu \sim 1\ cm^2.s^{-1}$ so $Re \sim 10^{13}$. The Reynolds number, in stellar conditions, is thus very large; much larger than the critical number beyond which turbulence occurs ($Re_{\rm crit} \simeq 2300$). In consequence, stellar convection is highly turbulent, involving a wide range of eddy scales (energetic, temporal and spatial). An important consequence of this turbulence is that convection mixes stellar matter very efficiently and rapidly.
Turbulent convective motions in stars transport a huge amount of energy in a very compressible stratified gas with variation of physical quantities over many orders of magnitude.
Because stellar convection is highly turbulent, its modelling is very complex and requires a specific treatment. The mixing-length theory is the one traditionally used to model convection in stars. Given the importance of convection for solar-like oscillations, I will develop in the next sections how the equations describing convection under the mixing-length approximation are obtained.

I first present in Sect. 2.4.1 the main ideas and hypotheses behind the mixing-length theory. The main goal of such a theory is to obtain the convective flux and the temperature gradient inside a convective zone. To do this, I develop the general expressions for the convective flux (in Sect. 2.4.2) and of the temperature gradient (in Sect. 2.4.3). After the definition of the convective efficiency, we will be able to obtain a cubic equation for this quantity (in Sect. 2.4.4). From the solution of this equation, it is then easy to make the developments backward in order to obtain the desired quantities. The derivation of the MLT formalism presented here is mainly based on the one developed and discussed in the textbooks of Cox (1968); Böhm-Vitense (1992); Kippenhahn et al. (2012).

2.4.1 The approximations of the MLT

The traditional way to model convective motions in stars uses the formalism of the mixing-length theory (Böhm-Vitense 1958). By analogy with the molecular heat transfer, Prandtl (1925) proposed a simple picture of the convection. Macroscopic elements (blobs or bubbles), moved by buoyancy forces, transport heat over a mean free path (called the mixing length) before dissolving.
This picture implies 5 main approximations:

- The whole spectrum of eddies is reduced to a single representative bubble (all convective elements have the same size but their precise shape is not given).
- This bubble travels radially over a distance ℓ_m (i.e. the mixing length) before dissolving and releasing their energy.
- Convection is treated as a perturbation of the mean structure and second-order terms in convective quantities are neglected.
- The bubble keeps the pressure equilibrium with the surrounding environment during its travel[3]
- The properties of convective elements depend only on local conditions (i.e. all elements have the same physical properties at a given distance r from the centre of the star)

[3]It is the Boussinesq approximation for which we assume that the pressure scale height is large compared to the size of the convective elements. This approximation is not strictly valid since the mixing length, obtained for example in solar calibrated models, appears to be of the same order than the pressure scale height.

We often assume that the mixing length ℓ_m can be expressed as a fraction α of the pressure scale height $H_p = P/|\nabla P| = P/\rho g$ such as $\ell_m = \alpha H_p$. We also assume that the free mixing-length parameter α is constant inside the convective region.
Moreover, we assume that the convection is time independent. A theory of time-dependent convection will be introduced later in this manuscript (in Sect. 3.2) to treat the interaction between convection and oscillations. I will also return on the local hypothesis and present a non-local approach of convection in Sect. 3.3.
In the MLT framework, the turbulence and the various involved scales are not considered. Another formalism to treat stellar convection, taking into account various spatial scales, namely the Full Spectrum of Turbulence theory, has been developed by Canuto, Mazzitelli (1991). This theory also suffers from being local and involving a free parameter similar to α. We will not further develop this theory since all the stellar models studied in this thesis (and the associated oscillation calculations) have been obtained using the MLT. In Sects. 3.2 and 3.4 we will consider in more details the interaction between turbulent convection and stellar oscillations.
Despite these "strong" approximations and the very simple picture, the MLT has been able to give a good account of the global characteristics of stars (e.g. their location in the HR diagram). In the extreme cases, when convection is very efficient or inefficient the mixing-length theory provides a valid estimate of the temperature gradient (see Sect. 2.4.4). When comparing physical quantities (such as the convective flux, convective efficiency, ...) derived from the MLT and from 3D simulations we see that they are not much different (see e.g. Dupret et al. 2006a). The remaining discrepancies need further improvements (such as a non-local approach) to be reduced. It seems that the calibration of the mixing-length parameter α hides almost all the uncertainties of the theoretical model.

2.4.2 Derivation of the convective flux

The total energy flux is given by the sum of the radiative and convective fluxes ($F_{\rm rad} + F_{\rm c}$). This sum defines the temperature gradient $\nabla_{\rm rad}$ that would be necessary to transport all the flux by radiation such as,

$$F_{\rm rad} + F_{\rm c} = \frac{4acG}{3}\frac{T^4 m}{\kappa P r^2}\nabla_{\rm rad}. \tag{2.27}$$

When a part of the flux is transported by convection, the actual temperature gradient ∇ is different from $\nabla_{\rm rad}$ and the radiative flux is given by Eq. 2.18. As explained in the beginning of Sect. 2.3, the real temperature gradient is not a-priori known and should be derived from the modelling of the energy transport mechanisms.
In this section, I will derive the expression of the convective flux in the frame of the mixing-length theory. This will enable us to discuss the efficiency of convection and finally to obtain the temperature gradient in a convective environment under the approximations of the MLT.
In a specific layer (as schemed in Fig. 2.1), the convective energy flux is given by the balance between the downward (d) and upward (u) energy transports (thermal and kinetic energy):

$$F_{\rm c} = \rho_u v_u c_p T_u + \frac{1}{2}\rho_u v_u v_u^2 - \rho_d v_d c_p T_d - \frac{1}{2}\rho_d v_d v_d^2, \tag{2.28}$$

with c_p the average of the specific heat per unit mass at constant pressure (the averaging is made over a distance Δr). We first require no net mass transport which gives $\rho_u v_u = \rho_d v_d = \rho v_c$ with v_c the average radial velocity of convective elements. According to the basic approximations of the MLT, we also neglect terms in v^3 (so we neglect the flux of kinetic energy).
The average convective flux is thus given by

$$F_{\rm c} = \rho v_{\rm c} c_{\rm p} \Delta T, \tag{2.29}$$

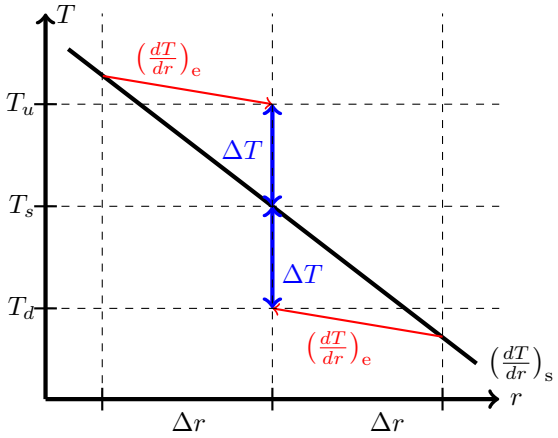

Figure 2.1: Adaptation of Fig 6.2 from Böhm-Vitense (1992). In black, the variation of temperature in the medium, in red the change of temperature in the convective element during its travel and in blue the difference of temperature between the convective element and the surrounding medium at the studied layer.

with $\Delta T \simeq [(\partial T/\partial r)_e - (\partial T/\partial r)_s]\,\Delta r$ as schemed in Fig 2.1. The subscript e refers to the convective element (the bubble or blob) and the subscript s to the average surrounding. ΔT is the excess of temperature of the convective element over the average of its surrounding after travelling a distance Δr.

With the pressure scale height $H_p = -dr/d\ln P$ and assuming that the convective element has traveled over a distance $\ell_m/2$, one can write

$$\frac{\Delta T}{T} = \frac{1}{H_p}(\nabla - \nabla_e)\frac{\ell_m}{2}. \tag{2.30}$$

And so, by inserting Eq. 2.30 into Eq. 2.29, the convective flux is given by

$$F_c = \rho v_c \frac{T}{H_p}(\nabla - \nabla_e)\frac{\ell_m}{2}. \tag{2.31}$$

We have now to get an expression for the average convective velocity v_c. To do this, we first express the resulting radial buoyancy force, per unit mass, f_A acting on the convective element.

$$f_A = -g\frac{\Delta\rho}{\rho},$$

where we have neglected the variation of the local gravity g over the distance traveled by the convective element. $\Delta\rho$ is the excess of density of the element after travelling a distance Δr. In the context of the MLT, we assume that the element travels a distance $\Delta r = \ell_m/2$, so the net work W, per unit mass, done on this element is given by

$$W = -\frac{1}{2}g\frac{\Delta\rho}{\rho}\frac{\ell_m}{2}, \tag{2.32}$$

where we have also assumed that the excess of density starts from zero and increases linearly with Δr (hence the mean $\Delta\rho$ is the half of the final one).

Following Cox (1968), we assume that half of the work is converted into kinetic energy ($E_{\rm kin} = 1/2 v_c^2$ per unit mass) and the other half is transmitted to the surrounding. Thus, we can write for the convective velocity,

$$v_c^2 = W = -\frac{\ell_m}{4} g \frac{\Delta\rho}{\rho} \tag{2.33}$$

With the equation of state

$$\frac{\Delta\rho}{\rho} = \left.\frac{\partial \ln\rho}{\partial \ln P}\right|_{\rm T,\mu} \frac{\Delta P}{P} + \left.\frac{\partial \ln\rho}{\partial \ln T}\right|_{\rm P,\mu} \frac{\Delta T}{T} + \left.\frac{\partial \ln\rho}{\partial \ln \mu}\right|_{\rm P,T} \frac{\Delta\mu}{\mu}. \tag{2.34}$$

Assuming $\Delta P = 0$ and $\Delta\mu = 0$, using Eq. 2.30 and with $\frac{1}{Q} = (\partial \ln\rho/\partial \ln T)_{\rm P,\mu}$ it becomes:

$$\frac{\Delta\rho}{\rho} = \frac{1}{Q}\frac{\Delta T}{T} = \frac{1}{Q}\frac{1}{H_p}(\nabla - \nabla_e)\frac{\ell_m}{2}. \tag{2.35}$$

We can now express the convective velocity in terms of temperature gradients.

$$v_c^2 = -\frac{1}{Q}(\nabla - \nabla_e)\frac{g\ell_m^2}{8H_p}. \tag{2.36}$$

Finally, inserting Eq. 2.36, into Eq. 2.31, the convective flux writes,

$$F_{\rm c} = -\frac{1}{4\sqrt{2}}\rho c_p T \sqrt{g\frac{1}{Q}}\ell_m^2 \left(\frac{\nabla - \nabla_e}{H_p}\right)^{3/2}. \tag{2.37}$$

Note that in this equation, the temperature gradients ∇ and ∇_e are still unknown. To go further, we need to consider the exchanges of energy between the convective element and the surrounding medium.

2.4.3 The temperature gradient

We consider here that the representative convective element is a blob of typical size d, surface S and volume V. We are interested by the radiative losses experienced by the blob which result in a temperature gradient larger than the adiabatic one.

A rising convective element, hotter than its surrounding, will lose heat during its travel. We consider an energy flux $f_{\rm rad}$ (directed from the centre of the bubble to its surface) due to the difference of temperature ΔT between the bubble and its environment. In a similar way to Eq. 2.18, we can write this energy flux as

$$f_{\rm rad} \simeq \frac{8ac}{3}\frac{T^3}{\kappa_{\rm rad}\rho}\frac{\Delta T}{d}, \tag{2.38}$$

where we have assumed that we have a spherical blob, such that the gradient of temperature along the normal of the blob's surface reduces to $2\Delta T/d$.
For the whole surface of the blob S, the radiative loss per unit time is given by

$$l_{\rm rad} = S f_{\rm rad} \simeq \frac{8acT^3}{3\kappa\rho}\Delta T\frac{S}{d}, \tag{2.39}$$

which represents the "luminosity of the blob". It also gives the rate at which the blob will exchange thermal energy with its environment:

$$-l_{\rm rad} \simeq \rho V c_p \frac{\partial \Delta T}{\partial t}. \tag{2.40}$$

Equalizing Eq 2.39 and 2.40 and assuming a spherical blob ($V/S \simeq d/6$), we obtain directly

$$\frac{\partial \Delta T}{\partial t} = -\frac{\Delta T}{\tau_{\rm rad}}, \tag{2.41}$$

with $\tau_{\rm rad}$ the time scale of thermal adjustment

$$\tau_{\rm rad} = \frac{\kappa_{\rm rad}\rho^2 c_p d^2}{16acT^3} = \rho V c_p \frac{\Delta T}{l_{\rm rad}}. \tag{2.42}$$

Thus, $\tau_{\rm rad}$ represents the excess of thermal energy divided by the luminosity, which is to the blob what the Kelvin-Helmholtz time scale is to the whole star.

Due to radiative losses, the temperature change of the convective element deviates from the adiabatic case by

$$\left(\frac{\partial T}{\partial r}\right)_e - \left(\frac{\partial T}{\partial r}\right)_{\rm ad} = -\frac{l_{\rm rad}}{\rho V c_p v_c}, \tag{2.43}$$

where the right-hand term of this equation represents the decrease of temperature per unit length over which the element rises for a total energy loss $l_{\rm rad}$. Expressing this equation with temperature gradients we obtain:

$$(\nabla_e - \nabla_{\rm ad}) = \frac{l_{\rm rad} H_p}{\rho V c_p T v_c}. \tag{2.44}$$

Finally, replacing $l_{\rm rad}$ by Eq. 2.39 with the average value of ΔT given by Eq. 2.30, we obtain

$$\frac{\nabla_e - \nabla_{\rm ad}}{\nabla - \nabla_e} = \frac{4acT^3}{3\kappa_{\rm rad}\rho^2 c_p}\left(\frac{S\ell_m}{dV}\right)\frac{1}{v_c}. \tag{2.45}$$

$S\ell_m/dV$ represents the "form factor" of the bubble. For a sphere of diameter ℓ_m we have $S\ell_m/dV = \frac{9/2}{\ell_m}$.

We define the **convective efficiency** Γ as

$$\Gamma \equiv \frac{\nabla - \nabla_e}{\nabla_e - \nabla_{\rm ad}} \simeq \frac{4}{9}\frac{F_c S}{l_{\rm rad}} \tag{2.46}$$

where for the last equality we have used F_c given by Eq. 2.31, $l_{\rm rad}$ given by Eq. 2.44, and assumed that the bubble is a sphere of diameter ℓ_m. With the last term of this equation, we see that Γ represents the ratio between the energy transported by the convection and the radiative energy loss, justifying the appellation of "convective efficiency".
With the definition of the thermal adjustment time scale in Eq. 2.42 and defining the lifetime of a bubble $\tau_c \equiv \ell_m/v_c$ we can also write $\Gamma = 2\tau_{\rm rad}/\tau_c$.

We have now expressed all the equations describing the convective region. We only need some algebra to obtain an equation that can be easily solved to finally determine the temperature gradient.

2.4.4 The cubic MLT equation

With the expressions for Γ (using Eq. 2.45), v_c given by Eq. 2.36 and $H_p = P/(\rho g)$ one can rewrite Γ as

$$\Gamma = \mathcal{A}(\nabla - \nabla_e)^{1/2}, \tag{2.47}$$

with

$$\mathcal{A} \equiv -\frac{c_p}{12\sqrt{2}acQ^{-1/2}} \frac{\kappa_{\rm rad} g \rho^{5/2}}{P^{1/2}T^3} \ell_m^2. \tag{2.48}$$

From the energy conservation equation, the total energy flux is given by

$$F = \frac{4ac}{3}\frac{T^4 g}{P\kappa_{\rm rad}}\nabla_{\rm rad} = \frac{4ac}{3}\frac{T^4 g}{P\kappa_{\rm rad}}\nabla + F_c. \tag{2.49}$$

Inserting F_c from Eq. 2.37 into Eq. 2.49, we obtain the relation between the gradients

$$\nabla_{\rm rad} - \nabla = a_0 \mathcal{A}(\nabla - \nabla_e)^{3/2}, \tag{2.50}$$

where we have replaced the factor 9/4 in Eq. 2.46 by a general form factor a_0. Using the expression obtained for Γ in Eq. 2.47, we can write

$$\nabla_{\rm rad} - \nabla = a_0 \Gamma(\nabla - \nabla_e). \tag{2.51}$$

Defining ζ, one can see after few manipulations that

$$\zeta \equiv \frac{\nabla_{\rm rad} - \nabla}{\nabla_{\rm rad} - \nabla_{\rm ad}} = \frac{a_0\Gamma^2}{1 + \Gamma(1 + a_0\Gamma)}. \tag{2.52}$$

Isolating $\nabla - \nabla_{\rm ad}$ in this equation we obtain

$$\nabla - \nabla_{\rm ad} = (1-\zeta)(\nabla_{\rm rad} - \nabla_{\rm ad}) = \left(\frac{1+\Gamma}{a_0\Gamma^2}\right)\zeta(\nabla_{\rm rad} - \nabla_{\rm ad}) = \frac{1+\Gamma}{a_0\Gamma^2}(\nabla_{\rm rad} - \nabla). \tag{2.53}$$

Combining Eq. 2.47, 2.53 and Eq. 2.53, gives

$$\Gamma(\Gamma + 1) = \mathcal{A}^2(\nabla - \nabla_{\rm ad}). \tag{2.54}$$

Adding $a_0\Gamma^3$ (from Eq.2.47 and using Eq. 2.50) to Eq. 2.54, we have finally:

$$\boxed{a_0\Gamma^3 + \Gamma^2 + \Gamma = \mathcal{A}^2(\nabla_{\rm rad} - \nabla_{\rm ad})} \tag{2.55}$$

which is the classical cubic MLT equation. $\nabla_{\rm rad}$ and $\nabla_{\rm ad}$ are known so, in practice, one solves this last equation for Γ and then comes back to the different expressions presented in this section to obtain ∇, v_c and F_c

For very large or very small Γ, it is possible to develop Taylor expansions of the above equations to obtain more easily the convective behaviour in these cases, as it is done in e.g. Cox (1968); Kippenhahn et al. (2012). **In the very deep interior**, because of the high density and temperature, $\Gamma \gg 1$, there is only small radiative losses and the convection is very efficient. In this case we find that the temperature gradient approaches the adiabatic one (but never equals it).

In the superficial layers of outer convective zones (near the photosphere of the star), radiative losses are large, $\Gamma \ll 1$, so the convection is inefficient and the temperature gradient is close to the radiative one. When going deeper, the density and the mixing length become larger, the efficiency of the convection increases and the temperature gradient departs from the radiative one to tend to the adiabatic one. Thus, the gradient of temperature is reduced by the presence of convective energy transport.

When none of the above limiting cases apply, the resolution of the mixing length equations leads to a temperature gradient between the adiabatic and radiative one. This is, for example, the case in the upper part of outer convective envelopes when convection is said to be **superadiabatic** ($\Gamma \sim 1$).

2.5 The evolution path of low-mass stars

We have now all the elements to compute and follow the evolution of a stellar model. The method to solve the structure equations is well described in several textbooks (e.g Kippenhahn et al. 2012; Maeder 2009). We describe here the evolution of low-mass stars, and the different typical characteristics of their structures according to their mass and/or their evolutionary stage. The elements presented here come either from numerical computations of stellar evolution or from simple theoretical relations. This story of low-mass stars is mainly inspired from the lecture notes of Kippenhahn et al. (2012). We can follow the evolution of a low-mass star in a Hertzsprung-Russell diagram (Fig. 2.2). We also present in Fig. 2.3 a schematic view of the evolution of the internal structure of a star (a $1M_\odot$ star, corresponding to the HRD of Fig. 2.2). In these figures, circled red numbers indicate particular moments of the stellar evolution as listed thereafter.

1. The birth of a star begins with the **collapse of a homogeneous cloud of gas** due to a gravitational instability. The Jeans criterion (Jeans 1902) allows one to estimate the size and mass of an initial perturbation leading to a collapse of the molecular cloud. This criterion shows that only clouds of mass higher than around $10^5 M_\odot$, much larger than the stellar mass, will collapse. It is therefore expected that the cloud will undergo some fragmentation and that most of the fragments form low-mass stars. In the first moments, the cloud is optically thin and the collapse is isothermal (with a cloud temperature around 10 K).

2. After around 10^5 years, the central part of the cloud becomes optically thick. The collapse is now adiabatic, leading to an increase of the luminosity and of the temperature (to a lower extent) of the protostar. A core in hydrostatic equilibrium forms, surrounded by an accretion disk. We can now refer to this hydrostatic core as a **protostar**.

3. The first point in Fig. 2.2 corresponds to the moment when the protostar **photosphere becomes visible** which determines what one usually calls the onset of the pre-main-sequence phase (hereafter PMS). All the ages given in Figs. 2.2 and 2.3 are counted from this point. As long as the accretion phase lasts, the protostar stays on its birth line. When accretion stops, the protostar follows its evolution by descending along the **Hayashi track**: its luminosity decreases at an almost constant $T_{\rm eff}$.

   Note that the Hayashi line defines, for a given set of stellar parameters, the locus in the HRD of fully convective stars.

4. During the PMS, when the central temperature reaches about $10^6 K$ the **first nuclear burning** in the life of the star, the deuterium burning starts. The succession of nuclear burnings drives the evolution of the star. Whether a certain nuclear reaction will occur or not is mainly determined by the mass of the star. "Stars" less massive than $0.08 M_\odot$ cannot burn hydrogen quietly because of electron degeneracy. This mass limit draws a separation between stars and brown dwarfs. With the increase of the temperature, the stellar core becomes more transparent, thus the convection disappears starting from the central layers (the hotter ones). A convective envelope remains for low-mass stars (below $\sim 1.5 M_\odot$). This happens around the minimum of luminosity at the bottom of the Hayashi line.

5. When the core temperature is high enough, the star ignites hydrogen and nuclear reactions become the first source of energy. Before the equilibrium temperature of hydrogen burning is reached, some reactions of the CNO cycle or of the pp chain occur in the stellar core.

   For stars with $M \gtrsim 1.3 M_\odot$: The first reactions of the CNO cycle transform ^{12}C into ^{14}N bringing ^{12}C to its equilibrium value. Given the high dependency in temperature of this reaction, a convective core is formed. When the ^{12}C reaches its equilibrium value, the full CNO cycle takes place to transform hydrogen into helium. Since all the reactions of the CNO cycle have a strong dependence in the temperature, the convective core remains.

   For stars with $M \lesssim 1.3 M_\odot$: First reactions destroying ^3He (from the pp-chain) take place to bring it to its equilibrium value. The high dependence in temperature of these reactions also favours the formation of a convective core. When these components reach their equilibrium value the complete pp-chain becomes the dominant source of energy and the convective core disappears (the pp-chain is less dependent in the temperature).

   This change in the origin of the stellar luminosity (from gravitational energy to nuclear energy) indicates the arrival of the star on the **Zero Age Main Sequence**. It took around 5.10^7 years to a $1 M_\odot$ star to travel from the formation of the hydrostatic core to the ZAMS.

6. The star is now in full equilibrium (hydrostatic and thermal) and enters in the **main-sequence phase**. The evolution of the star is governed by nuclear reactions and accordingly the evolution in this phase takes place on the nuclear time scale (of the order of 10^{10} years for the Sun). It will spend the largest part of its life in this core hydrogen burning phase. The displacement of the star in the HRD is very slow. The burning of hydrogen leads to a slight increase of the temperature and luminosity of the star.

7. When the hydrogen at the centre of the star is exhausted, **the hydrogen burning process continues in a shell surrounding an inert helium core**. This leads to an increase of the mass M_c of the helium core that is quasi-isothermal. The helium core becomes degenerate (more precisely, the electrons inside the core are in degenerate conditions).

   The evolution in the subgiant phase is thus characterised by a progressive increase of the mass of an inert and partially degenerate helium core and a progressive expansion of the convective envelope. This induces a decrease of the effective temperature, at almost constant luminosity, marked by a displacement to the right in the HRD.

   The contraction of the core is accompanied by an expansion of the envelope above the shell. Because of the proximity to the Hayashi line (that cannot be crossed), the expansion of the envelope cannot lead the star to much lower effective temperatures. When the convective envelope becomes large enough, further expansion is only possible through an increase of its luminosity, as it will be detailed in the next point.

   The evolution of the core and of the hydrogen burning shell of red giants can be understood through homology relations because the pressure at the base of the envelope is negligible

compared to the pressure in the core and in the shell. We can then assume that physical quantities (such as density, temperature, ...) in the region of the shell simply depend on the mass M_c and radius R_c of the core. These relations (as detailed in e.g., Kippenhahn et al. 2012) show that when increasing the mass of the core, R_c will decrease and the luminosity will increase. From homology considerations, one can also derive that the temperature in the shell will increase as $T_c \propto \mu M_c/R_c$. Since the core is isothermal, the central temperature will also increase with the mass of the core. These predictions are supported by numerical simulations as soon as the core is sufficiently condensed.

8. The star will then evolve by climbing on a line almost parallel to the Hayashi track **the Red-Giant Branch** towards higher luminosities (and larger radii). Such stars have huge convective envelopes (we remind that the Hayashi track represents fully convective stars), occupying up to 70% of their total mass (see Fig. 2.3). On this branch, the luminosity of the star increases strongly.

9. At some point, the convective envelope penetrates deeply inside the star in layers partially processed by some reactions of the CNO cycle and pp chain (transforming for example ^{12}C in ^{14}N). Due to the convective motions, the material created by the nuclear reaction will be distributed in the whole envelope and will reach the surface. This phenomenon is called **the first dredge up**. It has taken to the star around 10^9 years to travel from the end of the main sequence to this dredge up. After the dredge up, the convective envelope begins to retreat while the mass of the inert and degenerate He core continues to increase.

10. The monotonic increase of the luminosity is stopped when the shell enters the region left by the maximal penetration of the convective envelope. At this point, the shell encounters a discontinuity of the molecular weight (between the homogeneous hydrogen-rich outer layers and the helium-enriched layers below). Again, with the help of homology relations (see point 7 here-above), it can be shown that a decrease of the molecular weight will lead to a decrease of the luminosity.

    When the shell has passed the discontinuity, the luminosity increases again with the increase of the core mass. Because of this "loop" in the HR diagram (the star passes three times in this region), one then expects to observe more stars in this part of the diagram called the **red-giant bump**.

11. The increasing luminosity (due to the increase of the core mass) leads to an increase of the growth rate of the helium core mass, which leads again to a higher increase of luminosity, and so on... The evolution of the star on the red-giant branch goes faster and faster as it climbs the red-giant branch toward higher luminosities.

12. Since the evolution of the stellar core is well described by homology relations (see points 7-8 above), independently of the total mass of the star, the temperature of helium ignition ($T_c \simeq 10^8 K$) is reached when $M_c \simeq 0.48 M_\odot$ whatever the total mass of the low-mass star (this value slightly depends on the metallicity).

    This onset of helium burning takes place inside a shell where the temperature is maximum (due to the loss of energy by neutrinos inside the core, the maximal temperature is reached in a layer slightly off the centre of the star).

Because the core is degenerate, the helium ignition creates a thermal runaway (because of the lack of pressure regulation) and the central temperature increases more and more leading to a huge overproduction of nuclear energy. Locally, the luminosity reaches, during few seconds, values of the order of $10^{11} L_\odot$ (near the centre). It is the **"Helium Flash"**. Note that almost nothing of this luminosity reaches the surface because of the high opacity of the envelope. This energy is progressively transformed into expansion work as the degeneracy level decreases.

13. The increase of temperature at an almost constant density finally **decreases the degeneracy level**, leading to an expansion of the concerning region.

    When degeneracy is lifted off, the pressure regulation mechanism acts, decreasing the temperature and density in the region where helium burning takes place. This turns off the nuclear reaction, and a new cycle of contraction-heating-onset of nuclear reactions begins. This sequence of secondary flashes brings the He-burning closer and closer to the centre and progressively lifts off degeneracy.

    The expansion of the core radius goes with a contraction of the envelope and a decrease of the luminosity. The central temperature finally decreases to a value allowing a quiescent, stable helium burning: The star has reached the **horizontal branch (hereafter HB)** (located near the Hayashi line, at $L \simeq 100 L_\odot$).

14. The horizontal branch is similar to a main sequence for core helium burning stars. The star will thus move slightly towards higher effective temperatures and luminosities during this phase. A convective core forms during this phase (favoured by the high temperature dependence of the 3α reaction). The opacity in the core will increase with the abundance of oxygen and carbon. At first, this leads to an increase of the mass of the convective core but after a while the radiative gradient presents a minimum in the convective core. If the convective core boundary is fixed such that this minimum is in convective neutrality in the convective side of the boundary, the layers surrounding the convective core are such that the Schwarzschild criterion for the onset of convection (Eq. 2.25) is verified while the Ledoux criterion (Eq. 2.24) is not. These layers become semi-convective. Currently, we do not have a clear and generally accepted description of what happen in this region (some authors proposed that a partial, slow mixing can occur in semi-convective layers).

15. After the exhaustion of helium in the core, the star climbs the **asymptotic giant branch (AGB)** while it burns helium and hydrogen in shells above an inert core of carbon and oxygen. A loop of extinction and restart of shell burning take place leading to thermal pulses (TP AGB). When the luminosity reaches a certain value, important part of the star envelope is ejected creating a planetary nebulae. Finally, only the carbon-oxygen core and a very thin envelope ($< 1\%$ of the stellar mass) remain, shell burnings definitively switch off and the star will **cool down on the white dwarfs branch**.

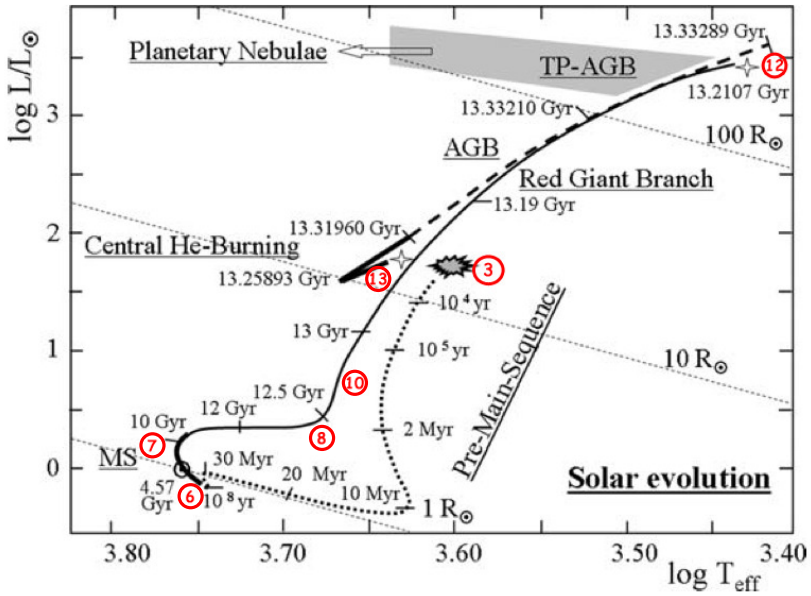

Figure 2.2: Fig. 25.11 from Maeder (2009): Evolution path of a $1M_{\odot}$ star in the Hertzsprung-Russell diagram.

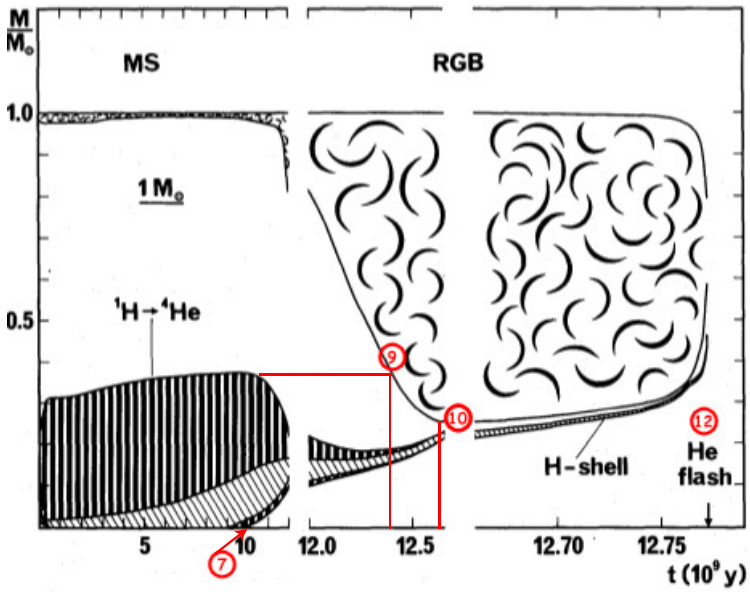

Figure 2.3: Fig. 25.10 from Maeder (2009): Evolution of the internal structure of a $1M_{\odot}$ star. Cloudy regions represent convective zones. Hatched regions represent the layers of the stars where nuclear reactions take place.

2.6 Beyond the standard model : problems and prospects

The main uncertainties in stellar structure and evolution emerge from difficulties in modelling several physical processes. In this section, I will discuss some limits of the current stellar standard models and prospects to overcome them. This presentation is not exhaustive and mainly focuses on issues that can affect low-mass stars. Among them, I will discuss the treatment of convection (Sect. 2.6.1), transport mechanisms (Sect. 2.6.2), rotation (Sect. 2.6.3), and mass loss (Sect. 2.6.3).

2.6.1 Convection

As mentioned in Sect. 2.4, convection is very difficult to model for mainly three reasons. It is a non-local phenomena; the state of a convective element depends on what happened to it below and/or above. The energetic, spatial and temporal scales of convection cover many orders of magnitude. And finally, stellar convection is highly turbulent.
In stellar cores, the high efficiency of convection leads to a quasi-adiabatic situation. There is therefore no major difficulties to compute the temperature gradient and the convective flux in a convective core. At the opposite, in the superadiabatic region (upper part of the convective envelope), current convection models are affected by large uncertainties. The standard modelling of these regions is based on analytical theories (the MLT or the FST) that simplify the real nature of convection (see Sect. 2.4.1). A third analytic approach, Reynolds-stress models (see e.g. Yang, Li 2007), treats the turbulence by splitting the physical quantities into an average and a fluctuating part. This theory takes explicitly the non-local nature of turbulence into account but suffers of practical issues for implementation in a stellar evolutionary code. A much more realistic modelling of convection is now accessible thanks to 3D hydrodynamical simulations. These simulations do not reach, by far, the very high values of stellar Reynolds numbers and the smallest scales of the turbulent cascade. Nonetheless, 3D simulations can be compared with analytical results to test the accuracy of the analytical models (see e.g. Dupret et al. 2006a). The main limit of such simulations is that they cannot be included in stellar evolution computations because of the time needed to compute the evolution of a convective zone over a short part of the star life. To obtain a more accurate description of the upper convective layers in stellar models (in particular for asteroseismology) the use of patched models seems to be promising. Such models (see e.g. Dupret et al. 2006a, for the way to patch the models) are made of a standard equilibrium model in which one replaces the upper layers by the outcome of a 3D simulation that can either be obtained directly or through interpolations in a grid of 3D simulations.

Apart from these general modelling issues, there exists also some uncertainties linked to the border of the convective zone. Beyond numerical problems in the determination of convective boundaries (see Gabriel et al. 2014, for a detail explanation on how to determinate convective boundaries), convective elements are likely to have enough inertia at the boundary to cross over and penetrate the stable layers. This phenomenon, generally referred as overshooting, obviously needs a non-local theory to be properly modelled. However, one usually parametrises the overshooting in term of the local pressure scale height (with a parameter similar, but not related, to α). For convective cores, overshooting leads to an increase of their size and of the time spent by the star in the concerned evolutionary phase (by increasing the amount of fuel available for nuclear reactions). Thus, this can significantly affect the evolutionary path of the star. For convective envelope, "undershooting" significantly affects the frequencies, and asteroseismology provides diagnosis tools of the extent of this process (see e.g. Lebreton, Goupil 2014).

2.6.2 Main transport mechanisms

I will discuss here three types of mechanisms that can transport chemical elements and hence modify the evolution of the star. The first one is linked to microscopic effects that affect different particles in different ways. The second is related to rotation and the third to internal waves.

In the stellar interior, microscopic particles are subject to two forces. The gravitational force that pushes down the heaviest ones, and radiative forces that push up the absorbing ones. This leads to diffusion processes which have to be accounted for in evolutionary codes. Helioseismology has emphasised the importance of diffusion for the computation of a realistic solar model (see e.g. Noerdlinger 1977). So, there are significant efforts made in the modelling of diffusion velocities. The adopted formalisms use a perturbative approach. The main difficulties is the calculations of the cross-sections representing the interactions between two particles or between a particle and a photon. This leads to important numerical difficulties given the time scales of diffusion and the important quantity of data needed.

Rotation affects radiative zone with two different transport mechanisms (e.g. Zahn 1991). First, in presence of rotation a meridional circulation is generated, that advects angular momentum toward the surface and mixes chemical elements. Second, differential rotation generates shear turbulence. The transport by turbulence is modelled as a diffusive mechanism, and the determination of the values of the turbulent diffusion coefficients that must be used to model this transport represents the major source of uncertainties (Mathis et al. 2014).

Some waves can also transport angular momentum (see e.g. Talon 2008, and references within). Transport by internal gravity waves have been proposed to explain the solid body rotation of the solar core. For more evolved stars, in the upper part of the red giant branch, Belkacem et al. (2015a) have shown that mixed-modes can also contribute to the transport of angular momentum (see also Sect. 1.1.2).

2.6.3 Other Physical mechanisms

We have already mentioned in Sect. 2.2.2, the issue in stellar structure modelling due to outer boundary conditions and atmosphere models. In the physics input of an equilibrium model, uncertainties linked to the description of the matter in stellar conditions (such as the computation of opacities, equation of state, ...) can also affect the evolutionary path. The chemical composition is obviously a key parameter for stellar evolution. The general assumption of a solar metal mixture in other star is probably not always valid (there are examples of stars with enhancement in α elements). Rotation also affects the structure of the star by breaking the spherical symmetry. One thus needs to compute 2D or 3D stellar equilibrium models (see e.g. Roxburgh 2006). The effects of the magnetic field on the stellar structure (mainly through transport mechanisms) are still subject to debate. An important issue in the evolution of low-mass stars is related to mass loss on the red giant branch. Several indicators, such as differences in masses between red-giant branch stars and horizontal-branch stars (see e.g. McDonald, Zijlstra 2015), indicate that red giants should experience some mass loss on the red-giant branch. The moment and the mechanisms of this mass loss is still unclear. Various analytical formulations (see e.g. Reimers 1975; Schröder, Cuntz 2005) have been proposed and lead to very different results, which have a strong impact on the predictions of the future evolution of a red-giant star.

Conclusion

We have introduced in this chapter the standard theory of stellar structure and evolution applied for low-mass stars. Despite various assumptions, this theory provides a solid background and explains the general observed trends. As observations reach higher and higher precisions, it becomes obvious that some processes are still misunderstood and missing in the standard model. The impact of these uncertainties on the theoretical predictions clearly appears when confronted with recent observations. To all these problems, we have now some hints from hydrodynamics simulations, from laboratory experiments and from asteroseismology. The study of waves, in the Sun and stars, has proven to be a unique, powerful tool to probe the inner stellar structure and physics. We have already mentioned in the introduction some results obtained thanks to helioseismology and asterseismology that brought a new light on current issues in stellar physics, as well as new constraints for the theories. This thesis focuses on the use of asteroseismology in red-giant stars, to better understand their physics and to constrain the current theories of solar-like oscillators, with a special emphasis on the energetic aspects of the oscillations strongly related to the interactions between oscillations and convection. The next chapter is thus dedicated to a presentation of the theory of stellar oscillations, applied to low-mass stars, including a description on the interactions between convection and oscillations (for both their damping and driving). The final part of Chap. 3 provides a brief overview of how asteroseismology allows us to draw some conclusions on the stellar structure and physics.

Chapter 3

Solar-like oscillations

Solar-like oscillations are of small amplitudes (around 5 ppm for the Sun) and it is only recently, thanks to the space-borne telescopes CoRoT (Baglin et al. 2006) and *Kepler* (Gilliland et al. 2010) that it has become possible to observe such oscillations in a wide number of stars, including evolved low-mass stars (the interested reader could find in Chaplin, Miglio 2013, and references within, an early review of the results obtained by these missions on solar-like oscillations).

In this chapter, I present the general theory of stellar oscillations in Sect. 3.1. I then describe the link between the oscillation frequencies and the inner structure of the stars (in Sect. 3.1.3). I also introduce the driving and damping of stellar oscillations (in Sect. 3.1.4). Energetic aspects of solar-like oscillations are directly linked to the interaction between convection and oscillations. Thus, I develop the theories for the damping (the time dependent treatment of convection in Sect. 3.2) and the excitation (the stochastic excitation process in Sect. 3.4) of these oscillations. In Sect. 3.5, I finally present the asteroseismic methods for the interpretation of observed mode frequencies in terms of stellar internal structure and physics.

3.1 Theory of stellar oscillations

We describe oscillations of a star in hydrostatic equilibrium, without rotation nor magnetic field, so that the spherical symmetry is maintained. Since the dynamical time scale is much lower than the nuclear time scale (see Sect. 2.1) we can assume that the chemical composition of the star does not change during a large number of oscillation cycles. We thus treat stellar oscillations as a perturbation of the equilibrium state.

I present in Sect. 3.1.1 the perturbative approach used to obtain in Sect. 3.1.2 the general equations of stellar oscillations. In Sect. 3.1.3, I discuss different types of modes that can exist inside a star, including mixed-modes of prime importance for evolved low-mass stars. I end this presentation of stellar oscillations with some energetic properties of oscillations in radiative zones in Sect. 3.1.4 (the case of convective zones being detailed Sects. 3.2 and 3.4).

3.1.1 Small perturbations approach

If X is a physical quantity and X_0 its equilibrium value,

- **The Lagrangian perturbation** of X is defined by

$$\delta X(\mathbf{a},t) \equiv X(\mathbf{a},t) - X_0(\mathbf{a}) \tag{3.1}$$

  with $\mathbf{a}$ a vector associated with a mass element. This description represents the variation of X (with the time t) following the mass element.

- **The Eulerian perturbation** of X is defined by

$$X'(\mathbf{r},t) \equiv X(\mathbf{r},t) - X_0(\mathbf{r}) \tag{3.2}$$

  which represents the variation of X at a given fixed position $\mathbf{r}$.

In general, the relative deviation of physical quantities to their equilibrium value is small. We can thus use Taylor developments limited to the first order around the equilibrium in a good approximation. Thus, the two perturbation formalisms are linked by

$$\delta X = X' + \nabla X_0 \cdot \delta\mathbf{r} \tag{3.3}$$

This linear approximation will be in use in all this manuscript.
Applying small perturbations to the structure equations (Eqs. 2.5 to 2.8), and the linear approximation, we obtain a system of linear equations describing the perturbations.

- the perturbed continuity equation reads:

$$\rho' + \nabla \cdot (\rho\delta\mathbf{r}) = 0 \tag{3.4}$$

- the perturbed equation of motion (momentum conservation):

$$\frac{\partial^2\delta\mathbf{r}}{\partial t^2} = -\nabla\psi' + \frac{\rho'}{\rho^2}\nabla P - \frac{1}{\rho}\nabla P' \tag{3.5}$$

- the perturbed Poisson equation:

$$\nabla^2\psi' = 4\pi G\rho' \tag{3.6}$$

- the perturbed energy equation:

$$T\frac{d\delta S}{dt} = T\left[\frac{\partial S'}{\partial t} + \mathbf{v}.\nabla S\right] = \epsilon' + \frac{\rho'}{\rho^2}\nabla\cdot\mathbf{F} - \frac{1}{\rho}\nabla\cdot\mathbf{F}' + \epsilon'_k \tag{3.7}$$

  where $\mathbf{v} = \partial\delta\mathbf{r}/\partial t$, ϵ_k correspond to the dissipation of kinetic energy into heat which appears in a time-dependent treatment of the convection (see Sect. 3.2) and $\mathbf{F} = \mathbf{F}_{\rm rad} + \mathbf{F}_{\rm conv}$.

- The perturbed radiative flux in the diffusion approximation reads:

$$\mathbf{F'}_{\rm rad} = \left[3\frac{T'}{T} - \frac{\kappa'}{\kappa} - \frac{\rho'}{\rho}\right]\mathbf{F}_{\rm rad} - \frac{4acT^3}{3\kappa\rho}\nabla T' \tag{3.8}$$

  The perturbation of the convective flux requires more developments and will be discussed in details in Sect. 3.2.

Assuming that the general form of the solutions is given by $\mathbf{X}(\mathbf{r},t) = \mathbf{X}(\mathbf{r})\exp(i\sigma t)$, where σ and X are complex[1], allows us to simplify the equations were temporal derivatives appears, i.e. the perturbation of the equation of motion and of the equation of energy conservation as

$$\sigma^2\delta\mathbf{r} = \nabla\psi' - \frac{\rho'}{\rho^2}\nabla P + \frac{1}{\rho}\nabla P', \tag{3.9}$$

$$i\sigma T\delta S = \epsilon' + \frac{\rho'}{\rho^2}\nabla\cdot\mathbf{F} - \frac{1}{\rho}\nabla\cdot\mathbf{F}' + \epsilon'_k. \tag{3.10}$$

To complete the above set of equations (Eqs. 3.4, 3.6, 3.9, and 3.10), one also has to **perturb the equations of state**. This allows one to obtain relations linking together the perturbations of the different thermodynamical quantities. We give here some of these relations, which will be useful in the following sections (a complete derivation of all the possible relations can be found in e.g. Unno et al. 1989).

$$\frac{\delta T}{T} = \frac{\delta S}{c_v} + (\Gamma_3 - 1)\frac{\delta\rho}{\rho} \tag{3.11}$$

$$\frac{\delta P}{P} = P_T\frac{\delta T}{T} + P_\rho\frac{\delta\rho}{\rho} = P_T\frac{\delta S}{c_v} + \Gamma_1\frac{\delta\rho}{\rho} \tag{3.12}$$

with

$$\Gamma_1 = \left.\frac{\partial\ln P}{\partial\ln\rho}\right|_S \ , \ \Gamma_3 - 1 = \left.\frac{\partial\ln T}{\partial\ln\rho}\right|_S \ , \ P_T = \left.\frac{\partial\ln P}{\partial\ln T}\right|_\rho \ , \ P_\rho = \left.\frac{\partial\ln P}{\partial\ln\rho}\right|_T \tag{3.13}$$

3.1.2 Non-adiabatic non-radial oscillations

In a spherical coordinate system (r,θ,ϕ) with an orthonormal basis $(\mathbf{e}_r,\mathbf{e}_\theta,\mathbf{e}_\phi)$, the displacement vector writes

$$\delta\mathbf{r} = \xi_r\mathbf{e}_r + \xi_\theta\mathbf{e}_\theta + \xi_\phi\mathbf{e}_\phi. \tag{3.14}$$

We also define the Legendre operator

$$\mathcal{L}^2 = -\frac{1}{\sin\theta}\frac{\partial}{\partial\theta}\left(\sin\theta\frac{\partial}{\partial\theta}\right) - \frac{1}{\sin^2\theta}\frac{\partial^2}{\partial\phi^2}. \tag{3.15}$$

Given the spherical symmetry of the equilibrium configuration, the three components of the perturbed equation of motion are given by,

$$\sigma^2\xi_r = \frac{\partial\psi'}{\partial r} + \frac{\rho'}{\rho}\frac{Gm}{r^2} + \frac{1}{\rho}\frac{\partial P'}{\partial r}, \tag{3.16}$$

$$\sigma^2\xi_\theta = \frac{1}{r}\frac{\partial}{\partial\theta}\left(\psi' + \frac{P'}{\rho}\right), \tag{3.17}$$

$$\sigma^2\xi_\phi = \frac{1}{r\sin\theta}\frac{\partial}{\partial\phi}\left(\psi' + \frac{P'}{\rho}\right). \tag{3.18}$$

[1]The complex form is useful to mathematically describe the oscillation problem. Physical quantities will be obtained by taking the real part of the eigenfunctions.

As for the term ϵ'_k in Eq. 3.10, we note that the interaction between turbulent convection and oscillations will introduce additional terms in the equation of motion (see Sect. 3.2).
From the perturbed equation of mass conservation (Eq. 3.4), using expressions of ξ_θ and ξ_ϕ given by Eqs. 3.17 and 3.18 and the definition of $\mathcal{L}^2$ given in Eq. 3.15, we obtain

$$\rho' + \xi_r + \rho\left[\frac{1}{r^2}\frac{\partial}{\partial r}(r^2\xi_r) - \frac{1}{\sigma^2 r^2}\mathcal{L}^2\left(\psi' + \frac{P'}{\rho}\right)\right] = 0, \tag{3.19}$$

and the perturbed Poisson equation (Eq. 3.6) becomes,

$$\frac{1}{r^2}\frac{\partial}{\partial r}\left(r^2\frac{\partial\psi'}{\partial r}\right) - \frac{1}{r^2}\mathcal{L}^2\psi' = 4\pi G\rho' \tag{3.20}$$

We see that the operator $\mathcal{L}^2$ appears in all the equations with partial derivative with respect to the angular coordinate (θ, ϕ). This allows one to separate the variables of the problem and search for solutions of the form $X(r, \theta, \phi) = X(r)f(\theta, \phi)$.

The function $f(\theta, \phi)$ must be an eigenfunction of the Legender operator. This is exactly what defines the spherical harmonics:

$$\mathcal{L}^2 Y_\ell^m(\theta, \phi) = \ell(\ell+1)Y_\ell^m(\theta, \phi) \tag{3.21}$$

Spherical harmonics form a complete set of orthogonal functions on the sphere, such as we can write the solutions of the equations as

$$\mathbf{X}'(r, \theta, \phi, t) = \sum_{\ell,\mathrm{m}} \mathbf{X}'_{\ell,\mathrm{m}}(r)Y_\ell^m(\theta, \phi)\exp(i\sigma t) \tag{3.22}$$

A solution of the form $\mathbf{X}'(r, \theta, \phi, t) = \mathbf{X}'(r)Y_\ell^m(\theta, \phi)\exp(i\sigma t)$ is called a mode of angular degree ℓ and azimuthal degree m. With solutions of this form, the angular frequency of the mode is given by the real part of σ. The imaginary part of σ gives the damping rate of the mode. If $\Im(\sigma) > 0$, the oscillation is a stable (damped) mode (i.e. its amplitude decays exponentially with time). On the opposite, if $\Im(\sigma) < 0$, the amplitude of the mode grows exponentially, the mode is unstable (i.e. oscillations are excited).
For ease of notations, we decompose the complex eigenvalue in its real and imaginary part:

$$\sigma = \omega + i\eta \tag{3.23}$$

where η represents the damping rate of the mode and ω the angular frequency (in rad/s) linked to the cyclic frequency ν by the relation $\nu = \omega/2\pi$ (in Hz).

Using the decomposition in spherical harmonics, the oscillation problem is reduced from a 3 dimensional (r, θ, ϕ) to a 1 dimensional problem (r).
The displacement vector is thus given by

$$\delta\mathbf{r} = \Re\left\{\left[\xi_r(r)Y_\ell^m(\theta, \phi)\mathbf{e}_r + \xi_h(r)\left(\frac{\partial Y_\ell^m}{\partial\theta}(\theta, \phi)\mathbf{e}_\theta + \frac{1}{\sin\theta}\frac{\partial Y_\ell^m}{\partial\phi}(\theta, \phi)\mathbf{e}_\phi\right)\right]e^{i\sigma t}\right\}, \tag{3.24}$$

with

$$\xi_h \equiv \frac{1}{r\sigma^2}(\delta\psi + \frac{\delta P}{\rho}). \tag{3.25}$$

Following this decomposition, we note the radial component of a vector with a subscript r and the horizontal component (in θ and ϕ) with a subscript h.

Using the equation for the horizontal motion (Eq. 3.25), the perturbed continuity equation becomes:

$$\frac{\delta\rho}{\rho} + \frac{1}{r^2}\frac{d}{dr}(r^2\xi_r) - \frac{\ell(\ell+1)}{\sigma^2 r^2}\left(\delta\psi + \frac{\delta P}{\rho}\right) = 0. \tag{3.26}$$

The perturbed Poisson equation reads:

$$\frac{1}{r^2}\frac{d}{dr}\left(r^2\frac{d\psi'}{dr}\right) - \frac{\ell(\ell+1)}{r^2}\psi' = 4\pi G\rho'. \tag{3.27}$$

For the perturbed energy equation we define

$$L = 4\pi r^2 F_r; \qquad L_{\rm rad} = 4\pi r^2 F_{\rm rad,r},; \qquad L_{\rm conv} = 4\pi r^2 F_{\rm conv,r} \tag{3.28}$$

so, the perturbations of Eqs. 3.28 with the help of Eq. 2.18 write

$$\frac{\delta L_{\rm rad}}{L_{\rm rad}} = 2\frac{\xi_r}{r} + 3\frac{\delta T}{T} - \frac{\delta\kappa}{\kappa} - \frac{\delta\rho}{\rho} + \frac{d\delta T/dr}{dT/dr} - \frac{d\xi_r}{dr}, \tag{3.29}$$

and

$$\frac{\delta L_{\rm conv}}{L_{\rm conv}} = 2\frac{\xi_r}{r} + \frac{\delta F_{\rm conv,r}}{F_{\rm conv,r}}. \tag{3.30}$$

Given the definitions of the different luminosities (Eq. 3.28) this decomposition (i.e. Eq. 3.30) is also applicable for the total and the radiative luminosity.

Using the decomposition of the solutions in spherical harmonics (Eq. 3.22) in the perturbed energy equation 3.7, we obtain:

$$\begin{aligned} i\sigma T\delta S = &- \frac{d\delta(L_{\rm conv}+L_{\rm rad})}{dm} + \epsilon\left[\frac{\delta\epsilon}{\epsilon} + \ell(\ell+1)\frac{\xi_h}{r}\right] \\ &+ \frac{\ell(\ell+1)}{4\pi r^3\rho}\left[L_{\rm rad}\left(\frac{\delta T}{r\left(\frac{dT}{dr}\right)} - \frac{\xi_r}{r}\right) - L_{\rm conv}\frac{\xi_h}{r}\right] \\ &+ \frac{\ell(\ell+1)}{\rho r}\delta F_{\rm conv,h} + \epsilon'_k. \end{aligned} \tag{3.31}$$

Note on spherical harmonics and mode classification:

Modes, which can be decomposed as the product of a radial function and a spherical function described by a spherical harmonic Y_ℓ^m, are characterised by three quantum numbers that determine the shape of the distortion created by the oscillation (as represented on Fig. 3.1):

- n: **the radial order** is approximately given by the number of nodes of the eigenfunction in the radial direction (from the centre to the surface of the star). For more details, see Takata (2012) where an approach to the exact classification of adiabatic eigenmodes of stars is presented.
- ℓ: **the angular degree** of the mode is the total number of nodal lines on the surface of the star;
- m: **the azimuthal order** corresponds to the number of meridional nodal lines on the stellar surface.

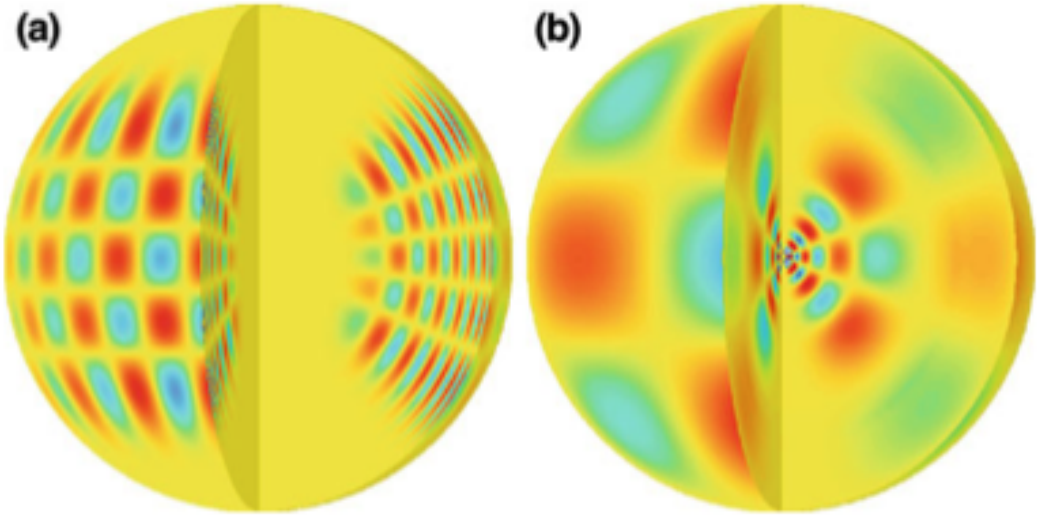

Figure 3.1: 3D representation of eigenfunctions of two solar mode. **a**: a p-mode ($\ell = 20$, $m = 16$, $n = 16$) and **b**: a g-mode ($\ell = 5$,$m = 3$,$n = 5$). The colors represent the values of the radial displacement ξ_r (> 0 in red and < 0 in blue). [Illustration from Rozelot, Neiner (2011)]

Given the properties of spherical harmonics with the Legendre operator, the resulting equations (Eqs. 3.24 to 3.31) are independent of m. For each value of ℓ there is $2\ell + 1$ possible values of m. The problem is thus degenerated (i.e. frequencies are independent of m). This is caused by the spherical symmetry of the problem. Any breaking of this symmetry (such as induced by rotation or magnetic field) will lift off this degeneracy.

3.1.3 Physical nature of modes

To obtain simple relations between oscillation properties and stellar interior characteristics, we make the **adiabatic approximation**. In the major part of the star, the thermal relaxation time is much larger than the pulsation period (of the order of the dynamical time scale, see Sect. 2.1). This means that because of the very high heat capacity, the entropy of the matter has not the time, during one pulsation cycle, to vary significantly. We should note that this is not true for the uppermost layers of the star where oscillations are highly non-adiabatic. We then assume that $\delta S = 0$ so we reduce the problem to three differential equations (Eqs. 3.24 to 3.27).
In this approximation, the perturbation of the equation of state links the perturbed density to the perturbed pressure and temperature as

$$\frac{\delta P}{P} = \Gamma_1 \frac{\delta \rho}{\rho} \qquad \text{and} \qquad \frac{\delta T}{T} = (\Gamma_3 - 1)\frac{\delta \rho}{\rho} \tag{3.32}$$

In the adiabatic case, the eigenfunctions are real and the eigenvalues are either pure real (dynamically stable modes, sinusoidal time dependence), or pure imaginary (dynamically unstable modes, exponential time dependence).

We also make the **Cowling approximation** (Cowling 1941) which consists in neglecting the Eulerian perturbation of the gravitational potential ($\psi' = 0$). This approximation is admissible in the case of modes with a large number of nodes or in the superficial layers where the local density is much smaller than the mean density of the star.

With these two approximations, the problem simply reduces to a single second-order equation. First, we can write the two remaining equations (the radial equation of motion and the equation for the perturbed density combined with the horizontal equation of motion) as

$$\frac{d\xi_r}{dr} = -\left(\frac{2}{r} - \frac{1}{\Gamma_1} H_P^{-1}\right)\xi_r + \frac{1}{\rho c_s^2}\left(\frac{L_\ell^2}{\omega^2} - 1\right) P', \tag{3.33}$$

$$\frac{dP'}{dr} = \rho(\omega^2 - N^2)\xi_r - \frac{1}{\Gamma_1} H_P^{-1} P', \tag{3.34}$$

with c_s the local sound speed and N^2 and L_ℓ^2 (defined below) two characteristic frequencies of the stellar structure. In these equations, the terms containing derivatives of equilibrium quantities are much smaller than the left hand side. In a very rough approximation, we neglect these terms (a similar result can be obtained in a more rigorous way with an appropriate change of variables following e.g. Gabriel, Scuflaire 1979; Unno et al. 1989), which leads to

$$\frac{d\xi_r}{dr} = \frac{1}{\rho c^2}\left(\frac{L_\ell^2}{\omega^2} - 1\right) P', \tag{3.35}$$

$$\frac{dP'}{dr} = \rho(\omega^2 - N^2)\xi_r. \tag{3.36}$$

Combining these two equations, we finally obtain as a rough description of the non-radial oscillation equation:

$$\frac{d^2\xi_r}{dr^2} = \frac{\omega^2}{c^2}\left(1 - \frac{N^2}{\omega^2}\right)\left(\frac{L_\ell^2}{\omega^2} - 1\right)\xi_r. \tag{3.37}$$

The two particular frequencies appearing in the above equations are :

- **the Lamb frequency**

$$L_\ell^2 = \frac{\ell(\ell+1)c^2}{r^2} \tag{3.38}$$

- **the Brunt-Vaisälä frequency**

$$N^2 = \left(\frac{1}{\Gamma_1}\frac{d\ln P}{dr} - \frac{d\ln\rho}{dr}\right) g \tag{3.39}$$

  Assuming a fully ionised ideal gas, and neglecting the radiation pressure, N^2 can be rewritten as

$$N^2 \simeq \frac{g^2\rho}{P}(\nabla_{\rm ad} - \nabla + \nabla_\mu), \tag{3.40}$$

  where we recognise in the right-hand side the Ledoux criterion for the onset of convection (Eq. 2.24). Hence, we will have $N^2 > 0$ in a radiative zone and $N^2 < 0$ in a convective zone.

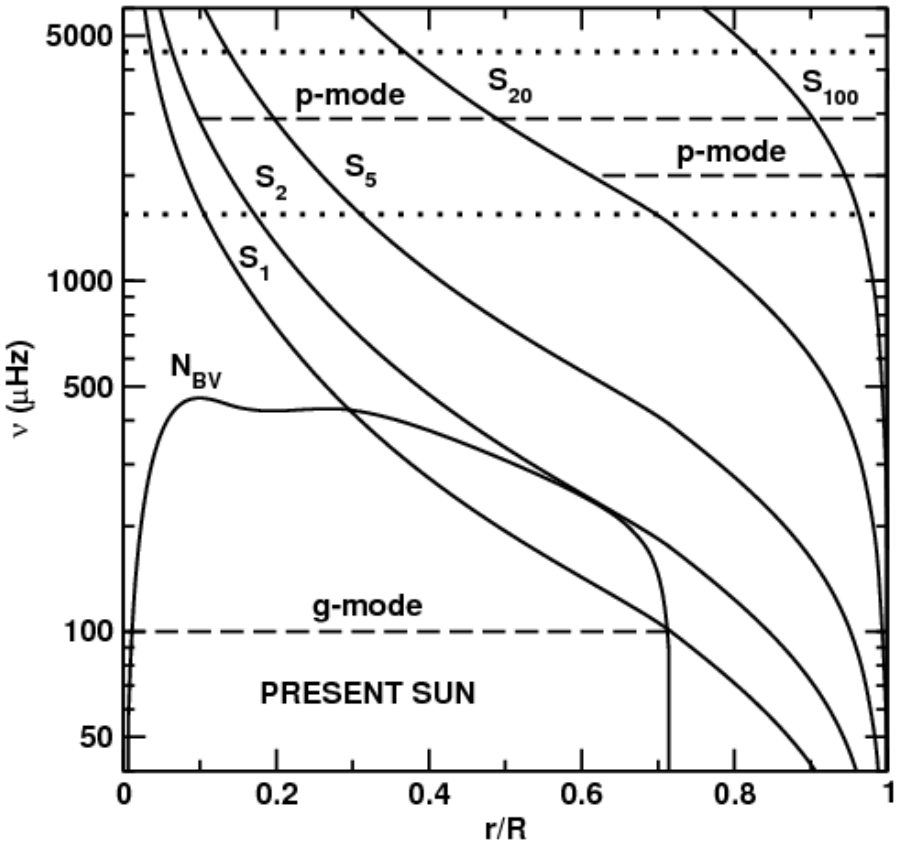

Figure 3.2: Propagation diagram: illustration of the Brunt-Vaisälä frequency ($N_{\rm BV}$) and the Lamb frequency (S_ℓ) for the Sun. Horizontal lines represent typical frequencies of p and g modes. [From Lebreton, Montalbán (2009).]

An illustration of the behaviour of these two frequencies is given in Fig. 3.2. A particular feature of the Brunt-Vaisälä frequency is related to the gradient of molecular weight. If originally present, the retreat of the convective core during the evolution on the main sequence leaves a sharp peak in ∇_μ and hence in N^2. In practice, the maximum in N^2 is often linked to an increase of μ in nuclear burning regions.
Let us now rewrite Eq. 3.37 as

$$\frac{d^2\xi_r}{dr^2} = -K(r)\xi_r, \tag{3.41}$$

with

$$K(r) = \frac{\omega^2}{c_s^2}\left(\frac{N^2}{\omega^2} - 1\right)\left(\frac{L_\ell^2}{\omega^2} - 1\right). \tag{3.42}$$

We directly see that this equation admits two type of solutions according to the sign of $K(r)$:

- **an evanescent solution** in the regions where $K(r) < 0$

$$\xi_r \sim \exp\left(\pm \int |K(r)|^{1/2} + \phi\right) \tag{3.43}$$

  i.e. if $N < \omega < L_\ell$ or $L_\ell < \omega < N$, with ϕ a phase term determined by boundary conditions.

- **an oscillatory solution** in the regions where $K(r) > 0$

$$\xi_r \sim \cos\left(\int K(r)^{1/2} + \phi\right) \tag{3.44}$$

  i.e. if $\omega > N, L_\ell$ or $\omega < N, L_\ell$. We expect that these conditions on the frequency will be realised separately by two different types of modes. Modes with high frequencies, satisfying the first condition, are labelled p modes. Modes with low frequencies, satisfying the second condition, are labelled g modes. Some details on the physical nature of these modes are given here-below.

In general, for a given mode (i.e. for a given frequency), we can have one or more regions that satisfy the oscillatory criterion separated by evanescent regions. In practice, a specific mode will have most of its energy in one of the propagation cavities. The mode is then said to be trapped in this cavity. The boundaries of the trapping cavities are generally at points with $K(r) = 0$, called turning points.

The propagation regions of p and g modes for typical main-sequence stars are illustrated in Fig. 3.2. In such stars, the trapping regions of p and g modes are clearly distinct. With the evolution of the star, the Brunt-Vaisälä frequency can take such large values that the criterion for g mode is satisfied even at high frequencies (see Fig. 3.4). As a consequence, the frequency ranges of p and g modes overlap. Thus, at a given frequency, a mode can be trapped in both p and g cavities. Such mode is called a **mixed-mode**, for it propagates in both cavities and thus presents both p and g mode characteristics. In the following paragraphs, I present separately some properties of p modes, g modes and mixed-modes.

An important quantity to characterise the trapping of oscillations is **the inertia of a mode**. It is given by the integral expression

$$I_k = \int_0^M \left(|\xi_r|^2 + \ell(\ell+1)|\xi_h|^2\right) dm. \tag{3.45}$$

We could note for further use that $1/2\omega^2 I_k$ gives the energy of the mode. It is useful to provide the dimensionless mode inertia

$$I = \frac{\int_0^M |\xi|^2 dm}{M|\xi_r(R)|^2} = \frac{M_{\rm mode}}{M}, \tag{3.46}$$

where $M_{\rm mode}$ is the *mode mass* and $\xi_r(R)$ corresponds to the radial displacement at the layer where the oscillation is measured (in this work, this corresponds to the Rosseland optical depth $\tau_{\rm rad} = 0.1$). In the following, we will always use the dimensionless mode inertia.

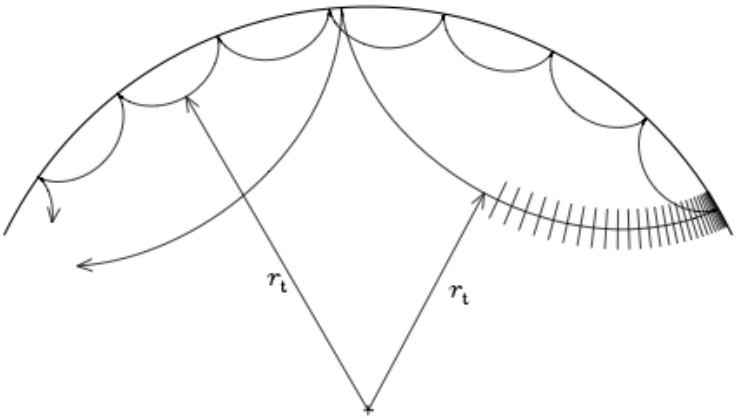

Figure 3.3: Fig. 3.16 form Aerts et al. (2010): Propagation of an acoustic wave inside the star for $\ell = 30$ and $\ell = 100$. Different modes probes different regions of the star.

Pressure modes

p modes are trapped in a resonant cavity between the surface and an inner turning point r_t determined by $L_\ell^2(r_t) = \omega^2$, which means that we have

$$\frac{\omega^2}{\ell(\ell+1)} = \frac{c_s^2(r_t)}{r_t^2}. \tag{3.47}$$

In the typical frequency domain of high-order p modes ($\omega \gg N$) we obtain from Eq. 3.42

$$K(r) \simeq \frac{1}{c_s^2}(\omega^2 - L_\ell^2) \tag{3.48}$$

The dynamic of the mode is thus determined by the variation of the sound speed inside the star. We recall that the dispersion relation of a sound wave is given by $\omega^2 = k^2 c_s^2$ for a wavenumber $|\mathbf{k}|^2 = k_r^2 + k_h^2$. Equation 3.48 is thus a dispersion relation for acoustic waves with $k_r^2 = (\omega^2 - L_\ell^2)/c_s^2$ and $k_h^2 = \ell(\ell+1)/r^2$, the restoring force being the pressure gradient. This justifies the designation p for these modes. We note that $K(r)$ increases with the frequency, hence, a larger radial-order means a higher frequency.

If we examine the propagation of a sound wave in a ray tracing view, we can easily understand that different p modes will probe different regions of the star. A mode can be viewed as a superposition of propagating sound waves. As the wave goes deeper in the star, the sound speed increases and it travels faster. It is thus refracted toward the surface[2] where the density drop sharply and thus implies the reflection of the mode (this is illustrated in Fig. 3.3 for two p modes of different angular degree). From Eq. 3.47 we see that the turning point r_t is close to the centre for small ℓ and moves closer to the surface for larger ℓ. The number of reflections on the surface thus increases with increasing ℓ and the lower the degree, the deeper the mode penetrates inside the star. The frequency of a p mode depends on the sound speed inside the star; more precisely, on the integral of the sound speed in the propagation cavity. Observation of a large number of

[2]It is similar to what happens to a light ray when entering materials with higher index of refraction, as reflected by the Snell-Descartes' law.

p modes (i.e. penetrating the star at different depths) allows one to determine the sound speed profile inside the star (and eventually, the temperature, density and pressure profiles).

Assuming that the oscillation wavelengths are much smaller than the typical (pressure, density, temperature) scale heights of the stellar interior we can make the WKB approximation (see e.g. Unno et al. 1989) to have an analytical expression for the oscillation eigenfunctions.

The asymptotic theory of oscillations, as developed by Tassoul (1980), predicts some regularities in the frequency pattern for high-order modes. It is very useful for solar-like oscillators, for it predicts a comb-like pattern in the power spectra (see e.g. Fig. 1.2) and allows one to derive easily, information of prime interest about the main structure of the star (see Sect. 3.5.1). We present here the principal results given by this theory for high-order p modes ($\omega^2 \gg N^2$). The asymptotic expression for the frequency of such a mode of angular degree ℓ and radial order n is in first approximation given by

$$\nu_{\mathrm{n,l}} \simeq \Delta\nu_0 \left(n + \frac{l}{2} + \epsilon \right), \tag{3.49}$$

where ϵ is a function of the frequency determined by the properties of the near-surface region (Christensen-Dalsgaard, Perez Hernandez 1992). The asymptotic large separation $\Delta\nu_0$ is the inverse of twice the time required for a sound wave to travel from the surface to the core of the star:

$$\Delta\nu_0 = \left(2 \int_0^R \frac{dr}{c} \right)^{-1} \simeq \sqrt{\frac{GM}{R^3}}. \tag{3.50}$$

From the asymptotic expression of the frequencies (Eq. 3.49) a characteristic spacing directly appears:

- **the large separation**

$$\Delta\nu_{\mathrm{n,l}} \equiv \nu_{\mathrm{n+1,l}} - \nu_{\mathrm{n,l}}, \tag{3.51}$$

  which provides an estimate on the mean density of the star and tends to $\Delta\nu_0$ for high radial orders.

A development of the asymptotic mode frequencies to a higher order shows that modes separated by two angular degree and one radial order are separated by

- **the small separation**

$$\delta\nu_{\mathrm{n,l}} \equiv \nu_{\mathrm{n,l}} - \nu_{\mathrm{n-1,l+2}}, \tag{3.52}$$

  which depends on the gradient of the sound speed, especially near the centre of the star. It is thus sensitive to the core structure of the star and so provides information about the evolutionary state of the star.

Gravity modes

g modes are trapped in a cavity bounded by two turning points (r_1, r_2) determined by $\omega^2 = N^2$ and/or $\omega^2 = L_\ell^2$. This generally corresponds to a cavity in the central layers of the star. For the typical g modes with low frequencies ($\omega^2 \ll L_\ell^2$), Eq. 3.42 can be approximated by

$$K(r) \simeq \frac{\ell(\ell+1)}{r^2\omega^2}(N^2 - \omega^2). \tag{3.53}$$

The dynamic of the mode is determined by the variations of the Brunt-Vaisälä frequency inside the star. Eq. 3.53 corresponds to the dispersion relation of internal gravity waves. This justifies the appellation g for these modes, the restoring force being buoyancy: gravity acting on density perturbations. We note that $K(r)$ increases with decreasing ω, hence larger radial order means lower frequency. We also remark that, in a given star, the g modes frequency range cannot excess the maximum of the Brunt-Vaisälä frequency.

Asymptotic developments for gravity modes (Tassoul 1980) for high order, low degree g modes give the period of the modes:

$$\Pi_{\mathrm{n,l}} = \frac{1}{\nu_{\mathrm{n,l}}} = \frac{2\pi^2}{\sqrt{\ell(\ell+1)}} \left(\int_{\mathrm{r_1}}^{r_2} \frac{N}{r} dr \right)^{-1} (n + \epsilon), \tag{3.54}$$

where ϵ is a constant determined by the structure of the star. As for p modes, a regular spacing appears in the asymptotic formulation, but this time in periods.

The asymptotic period spacing is given by

$$\Delta\Pi_\ell \equiv \Pi_{\mathrm{n+1},\ell} - \Pi_{\mathrm{n},\ell} = \frac{2\pi^2}{\sqrt{\ell(\ell+1)}} \left(\int_{\mathrm{r_1}}^{r_2} \frac{N}{r} dr \right)^{-1}. \tag{3.55}$$

It is very sensitive to the presence and the size of convective cores. It has recently appeared that the period spacing is of great help to determine the evolutionary stage of evolved low-mass stars (see Sect. 3.5.1).

Mixed modes

As discussed in the previous chapter (Sect. 2.5), after the main sequence, the internal structure of a low-mass star undergoes important changes. These changes will have a strong impact on the oscillation spectrum, mainly through the modifications they induce on the Brunt-Vaisälä frequency.

- the core contraction increases the local gravity, increasing the Brunt-Vaisälä frequency in the central regions.
- the presence of an hydrogen burning shell creates a large positive gradient of molecular weight ($\nabla_\mu = d\ln\mu/d\ln P > 0$). If present during the main sequence, the shrinking of a convective core also increases this gradient. This also increases the Brunt-Vaisälä frequency, specially around the bottom of the hydrogen burning shell (see Figs 3.4, right panel and 3.5, upper panel).

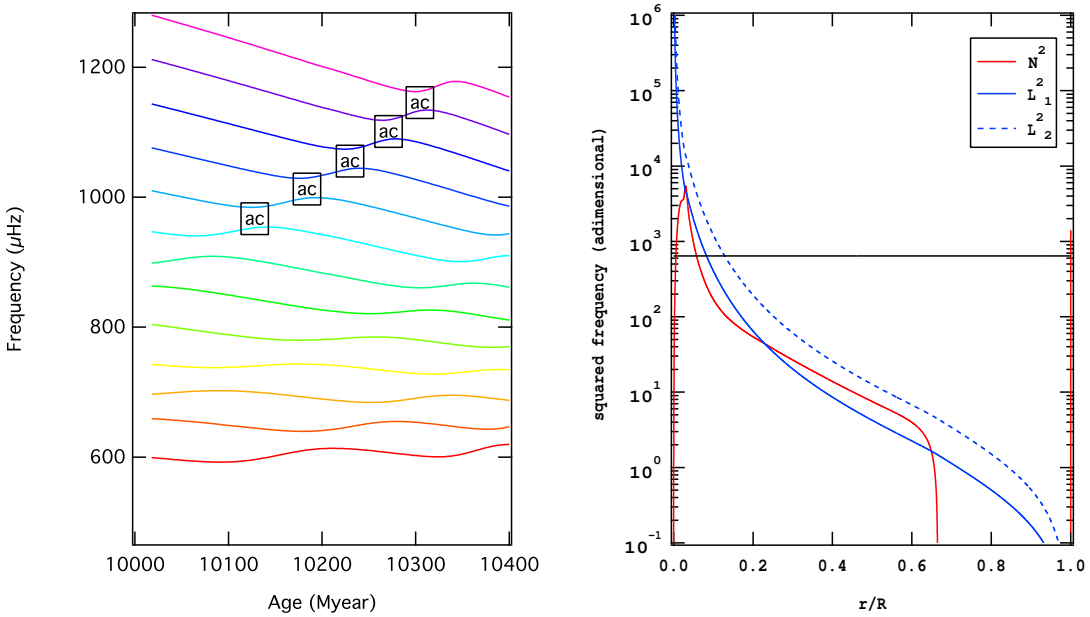

Figure 3.4: Some properties of stellar models $1.02 M_\odot$ in the subgiant phase (between 10000 and 10400 My). **Left:** variation of dipole modes frequencies of various radial orders (from bottom to top : $n = 4$ to $n = 16$) with the age of the star (ac indicate an avoided crossing). **Right:** Propagation diagram of the model of 10300 My. The frequency of the $\ell = 1$, $n = 15$ mode is represented by a black line.

The increase of the Brunt-Vaisälä frequency lifts to higher frequencies the frequency range of g-modes up to the frequency range of acoustic modes. When frequencies of two modes of same angular degree approach each other, they undergo an avoiding crossing[3] (see in Fig. 3.4, left panel, the local increase of modes frequency). At this point, the oscillation mode has a mixed nature because it can propagate in both p and g cavities (see the frequency of the mixed-mode in the propagation diagram in Fig. 3.4, right panel).

Non-radial mixed-modes are preferentially trapped in the p or g cavity, the evanescent zone between the two cavities acting like a partial reflection barrier. The first ones will be called p-dominated mixed-modes, the other ones g-dominated mixed-modes. These last modes have important amplitudes in the g cavity, leading to inertias higher than pure p modes (see Fig. 3.5). The most the mode is trapped in the g cavity, the higher the inertia. We expect that such inertia differences lead to important differences in the power spectrum (this point will be discussed in more details in the next chapters). We see in Figs. 3.4 (right panel) and 3.5 (upper panel) that the evanescent zone is larger for quadrupole modes than for dipole ones. As a result, quadrupole modes will be better trapped and their inertia will be closer to pure p or g modes one (this is illustrated for a red giant branch model in the bottom panel of Fig. 3.5).

[3] It's a phenomenon well kwnon in atomic physics

As the star evolves on the red giant branch, the Brunt-Vaisälä frequency continues to increase in the central layers. As a consequence, the period spacing between two g-dominated mixed-modes decreases (see Eq. 3.55). This leads to an increase of the density of mixed-modes (number of mixed-modes over a large separation) in a frequency power spectrum. Note that because of the mixed character of the modes, the actual period spacing between two consecutive g-dominated modes ($\Delta\Pi_\ell$) differs from the classical asymptotic one as given in Eq. 3.54.

Asymptotic developments for mixed-mode frequencies and inertias allow one to understand their main properties. In the JWKB approximation, accounting for a g cavity (between r_a and r_b), an evanescent region (r_b, r_c) and a p cavity (r_c, R), Shibahashi (1979) developed an eigenvalue condition for mixed modes:

$$\tan(\theta_p) = q\tan(\theta_g), \tag{3.56}$$

with the definitions

$$\theta_p = \int_{\mathrm{r_c}}^{R} k_r dr \simeq \frac{\pi\nu}{\Delta\nu}, \tag{3.57}$$

$$\theta_g = \int_{\mathrm{r_a}}^{r_b} k_r dr \simeq \frac{\pi}{\nu^2\Delta\Pi_1}, \tag{3.58}$$

and the coupling coefficient

$$q \simeq \frac{1}{4}(r_c/r_b)^{-2\ell}. \tag{3.59}$$

From these relations Mosser et al. (2012b) expressed the frequency of a dipole mixed-mode coupled with a pure p mode $\nu_{\mathrm{n_p},\ell=1}$ (Eq. 3.49) as

$$\nu = \nu_{\mathrm{n_p},\ell=1} + \frac{\Delta\nu}{\pi}\arctan\left[q\tan\pi\left(\frac{1}{\nu\Delta\Pi_1} - \epsilon_g\right)\right], \tag{3.60}$$

with ϵ_g a constant (see e.g. Brassard et al. 1992).
If we assume that dipole mixed modes in the range $\left[\nu_{\mathrm{n_p},\ell=1} - \Delta\nu/2\ ;\ \nu_{\mathrm{n_p},\ell=1} + \Delta\nu/2\right]$ are coupled with the pure p mode $\nu_{\mathrm{n_p},\ell=1}$, we can find $\mathcal{N}+1$ solutions to Eq. 3.60 with $\mathcal{N} \simeq \Delta\nu\Delta\Pi_1^{-1}\nu_{\mathrm{n_p},\ell=1}^{-2}$ the number of g-dominated mixed-modes in the interval.

In the asymptotic regime and neglecting the size of the evanescent zone, Goupil et al. (2013) showed that the inertia in the envelope of the star varies as $I_{\mathrm{env}} \simeq (c^2/2\pi\nu)\tau_p$ and in the core as $I_{\mathrm{core}} \simeq (a^2/2\pi\nu)\tau_g$, so we can express the total inertia as

$$I = I_{\mathrm{core}} + I_{\mathrm{env}} \simeq \frac{c^2}{2\pi\nu}(\tau_p + \frac{a^2}{c^2}\tau_g), \tag{3.61}$$

with $\tau_p = \theta_p/(\pi\nu)$, $\tau_g = \theta_g/(\pi\nu)$, c a normalisation constant and a is related to c by (see Eq. (16.49) and Eq. (16.50) from Unno et al. 1989) :

$$\frac{c}{a} = \frac{2\cos\left(arc\cot(\frac{1}{4}\cot(\pi\nu\tau_p))\right)}{cos(\pi\nu\tau_p)}. \tag{3.62}$$

$(c/a)^2$ is then a function of ν of period $1/\tau_p = \Delta\nu$ which varies between 4 (p-modes) and 1/4 (g-modes). This relation explains the periodic modulation of the inertia with a period $\Delta\nu$ observed in red giants (see Fig. 3.5 bottom panel).

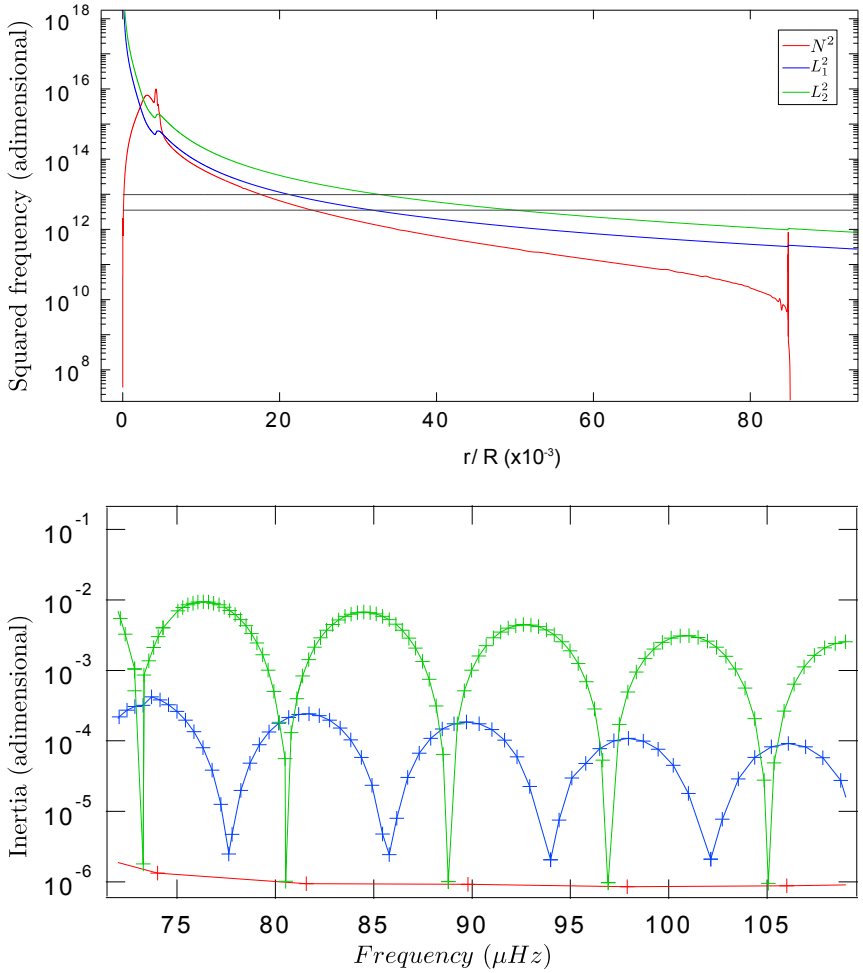

Figure 3.5: **Top:** Propagation diagram for a $1.5 M_\odot$ RGB model, the typically observed frequency range is marked with black lines. **Bottom:** $\ell = 0$ (red), $\ell = 1$ (blue), $\ell = 2$ (green) modes inertia for this model.

3.1.4 Driving and damping of oscillations.

Sect. 3.1.3 focused on the frequencies of the modes. In this section, I introduce the energetic aspects of oscillations. Thus, I will describe the damping and driving of oscillations in a radiative zone. The case of convective zones, will be detailed in Sects. 3.2 and 3.4 because they play a major role for solar-like oscillations and have to be treated in a specific way.

Using the perturbed equations obtained in Sect. 3.1.2 (hence leaving the adiabatic approximation), it is possible to write down an **integral expression for the damping rate**. To do this, one has to integrate the radial component of the equation of motion and take the imaginary part (noted $\Im$) of the result (a complete demonstration can be found in e.g Dupret et al. 2002) which reads,

$$\eta = \Im(\sigma) = \frac{1}{2\omega I_k} \int_0^M \Im \left[\frac{\delta\rho^*}{\rho} \frac{\delta P}{\rho} \right] dm = -\frac{\int_V dW}{2\omega I |\xi_r|^2 M} \tag{3.63}$$

where $*$ denotes the complex conjugate and where we assume the time dependence $\exp(i\omega t - \eta t)$. The numerator of the damping rate can be interpreted as the work W produced by the star during one oscillation period. We call it the **work integral of a mode**. The sign of the integral gives the sign of η and the sign of the integrant allows us to determine which regions of the star have a driving or damping effect on oscillations. Given the time dependence of the mode in $\exp(i\omega t - \eta t)$, the mode will be stable (or damped) if $\eta > 0$, hence if the work performed on the oscillation is negative. It immediately appears that $\eta = 0$ if variations of density are in phase with variations of pressure.

In order to better understand the physics behind the driving and damping of oscillations we rewrite the equation of the damping rate using the perturbed equations of state (Eqs. 3.11 and 3.12):

$$\eta = \Im(\sigma) = \frac{1}{2\omega I_k} \int_0^M \Im \left[\frac{\delta T^*}{T} T\delta S \right] (\Gamma_3 - 1) dm \tag{3.64}$$

For a mode to be excited, the heating due to the oscillation ($Td\delta S/dt > 0$) must occur at the hot phase of the oscillation ($\delta T^*/T > 0$). This corresponds to a heat engine (such as a Carnot cycle). Moreover, the mode should have a large amplitude in the driving region to be efficiently excited. The main contributions in $T\delta S$, having a driving effect, are $\delta\epsilon$ and $d\delta L/dm$ in Eq. 3.31. They lead to two driving mechanisms: the ϵ and κ mechanism (see Eq. 3.29 linking δL to $\delta\kappa$)[4].

- **The ϵ mechanism** has been widely studied for massive stars for which it has an important impact on the driving of the modes (Ziebarth 1970). Since the production of nuclear energy increases very quickly with the temperature, the ϵ term has always a driving effect on the oscillations. To be efficient, oscillation modes must have a significant amplitude in nuclear burning regions. Theory shows that it is most efficient in the presence of a nuclear burning shell (Noels, Scuflaire 1986).
- **The κ mechanism** in which variations of opacity permits to store energy at the hot phase. Close to the opacity peak, the work is positive and the mode is excited. Away from the peak the work is negative and the mode is damped. Whether the mode is globally excited or damped depends on the relative contribution of these different regions. To drive efficiently the mode, the opacity peak must be located in the transition region where the thermal time scale is of the order of the oscillation period.

[4]The interested reader could find in, e.g. Aerts et al. (2010) a description of the stars concerned by these different mechanisms with the associated type of modes.

When oscillations of small spatial wavelength occur in the radiative zone they undergo large variations of the temperature gradient (from $\delta T/T$ in Eq. 3.29) with a loss of heat during the hot phase of the thermal cycle (and a gain of heat during the cool phase). Therefore, they are damped. This **radiative damping** increases with the radial wavenumber k_r and with the amplitude of the oscillation in the radiative zone. For evolved low-mass stars, the very high value of the Brunt-Vaisälä frequency leads to a huge radial wavenumber of the oscillations in the g cavity ($k_r \simeq \sqrt{\ell(\ell+1)}N/(\omega r)$). Hence, these modes will undergo a strong radiative damping. It is possible to obtain a simple expression for the radiative contribution to the work integral in the asymptotic limit (see e.g. Dziembowski 1977; Van Hoolst et al. 1998; Godart et al. 2009):

$$W_{\rm rad} = -\int_{r_1}^{r_2} \frac{dW}{dr} dr \simeq \frac{K\left[\ell(\ell+1)\right]^{3/2}}{2\omega^3} \int_{r_1}^{r_2} \frac{\nabla_{\rm ad} - \nabla}{\nabla} \frac{\nabla_{\rm ad} N g L}{P r^5} dr \tag{3.65}$$

where r_1 and r_2 are the lower and upper radii of the g cavity and K is a normalisation constant. This formulation shows that the main contribution to the radiative damping occurs around the bottom of the hydrogen burning shell (see e.g. Dupret et al. 2009). When the star evolves on the red-giant branch, N/r^5 increases as a result of the contraction of the central layers, leading to an increase of the radiative damping.

3.2 Time-dependent treatment of convection

The oscillations are usually treated as a perturbation of a gas at rest. This is no longer acceptable in convective zones due to convective motions. As explained in the introduction, to model the energetic properties of solar-like oscillations, one needs to take into account the interaction between convection and oscillations. In particular, the damping rate obtained taking into account only the κ mechanism does not reproduce solar observations. Given the inherent difficulties in the treatment of convection and of its interaction with the oscillations, we study separately the damping and the excitation of the modes. In the study of the damping of oscillations by convection, we are interested in the reaction of the convective zones to an oscillation. Because for solar-like oscillations, the time scale of the most energetic eddies is of the same order as the oscillation periods, this requires a time-dependent treatment of the convection (hereafter TDC). The stochastic excitation of oscillations by turbulent motions will be treated in a specific way in Sect. 3.4.

I give here a brief presentation of the theory of convection-pulsation coupling as developed by Grigahcène et al. (2005). This theory is developed in the frame of the MLT (as presented in Sect. 2.4) based on the theory of Unno (1967) generalised by Gabriel et al. (1974); Gabriel (1996). The general procedure we follow to obtain the oscillation equations including the interaction with convection is presented in Fig. 3.6.

We start from the general equations of hydrodynamics (Sect. 3.2.1) split into a mean structure and a fluctuating part (the convective contribution). We then develop the equations of the averaged convective medium in Sect. 3.2.2 in which terms linked to the turbulence explicitly appear. The differences between the general equations and the mean structure give the equations governing the convective fluctuations (Sect. 3.2.3). These equations reduce to the classical MLT equations in the stationary case (Sect. 3.2.4). As it was done in Sect. 3.1, we obtain the oscillation equations by perturbing the equations of the average medium (Sect. 3.2.5). These new equations contain coupling terms between the convection and the oscillations. The detailed expressions of these terms are obtained by perturbing the equations for convective fluctuations

in Sect. 3.2.6. Finally, these developments will allow us to obtain a more accurate expression for the damping rate of the oscillations (Sect. 3.2.7).

We first need to make clear the difference between convective fluctuations and oscillations. A physical quantity will be separated into three contributions: its equilibrium value, a contribution of oscillations and a contribution of turbulence. The first contribution, assumed to be dominant, corresponds to the stationary term. While the oscillation contributions are periodic and modelled by the general theory of stellar oscillations (Sect. 3.1) the turbulent contribution has a stochastic nature and is difficult to model. In the following, the first and second terms (equilibrium value and oscillation contribution) are regrouped in the term called average medium.

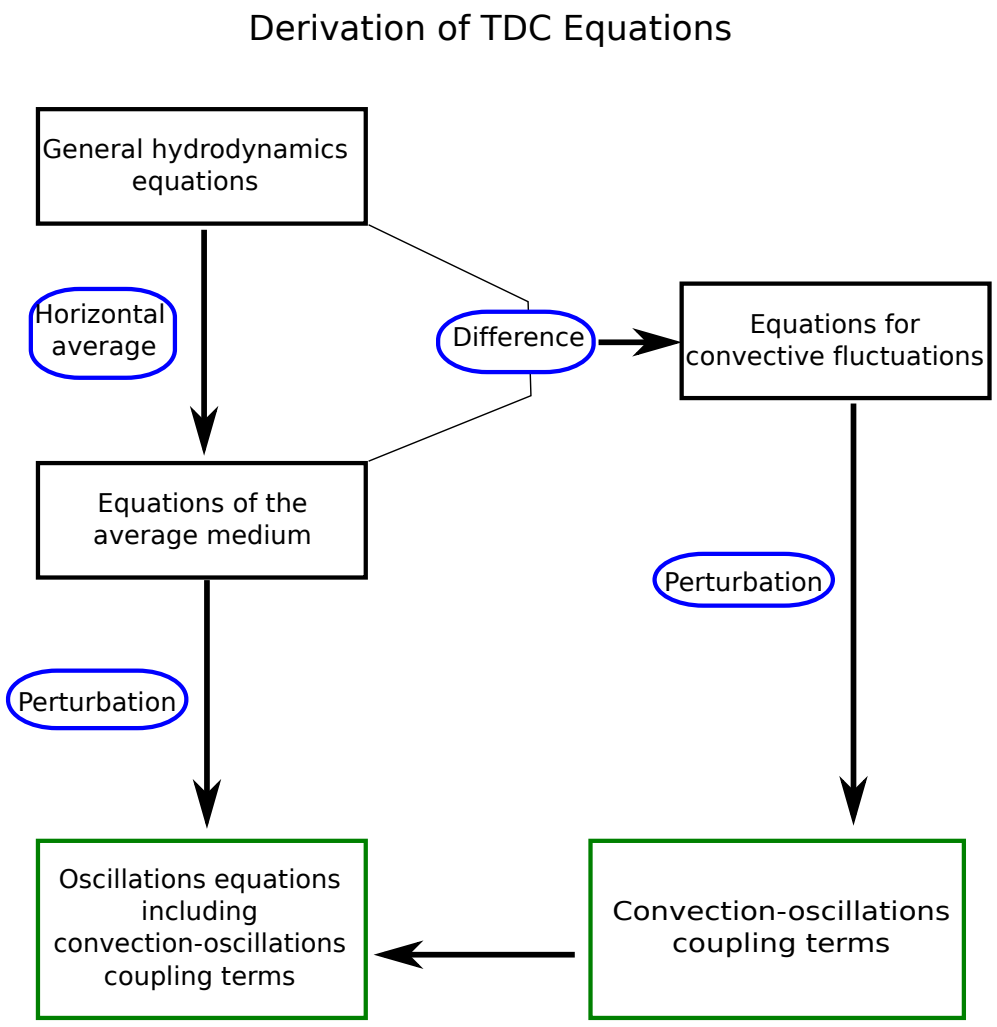

Figure 3.6: General scheme for the derivation of oscillations equations including convection-oscillations interaction.

3.2.1 General hydrodynamic equations

The general hydrodynamic equations (namely, the mass, momentum, energy conservation and the Poisson equation; Eqs. 2.5 to 2.8) are recalled here in a more convenient form:

$$\frac{\partial \rho}{\partial t} + \nabla \cdot (\rho \mathbf{v}) = 0, \tag{3.66}$$

$$\frac{\partial (\rho \mathbf{v})}{\partial t} + \nabla \cdot (\rho \mathbf{v}\mathbf{v}) = -\rho \nabla \Psi - \nabla \cdot (\mathbf{P}_g + \mathbf{P}_{\rm rad}), \tag{3.67}$$

$$\frac{\partial (\rho U)}{\partial t} + \nabla \cdot (\rho U \mathbf{v}) + (\mathbf{P}_g + \mathbf{P}_{\rm rad}) \otimes \nabla \mathbf{v} = \rho \epsilon - \nabla \cdot \mathbf{F}, \tag{3.68}$$

$$\nabla^2 \Psi = 4\pi \rho G, \tag{3.69}$$

where we have introduced the gaseous ($\mathbf{P}_g = P_g \mathbf{1} - \beta_g$) and radiative ($\mathbf{P}_{\rm rad} = P_{\rm rad}\mathbf{1} - \beta_{\rm rad}$) stress tensors, with $P_{\rm rad}$ and P_g the gas and radiative pressure (and $\mathbf{1}$ the identity tensor). The equation of energy conservation (Eq. 3.68) is given in terms of the internal energy U.

3.2.2 Equations of the average medium

Each variable in the above equations is split into an average value ($\overline{y}, \mathbf{u}$) and the convective contribution ($\Delta y, \mathbf{V}$):

$$y = \overline{y} + \Delta y \tag{3.70}$$

$$\mathbf{v} = \mathbf{u} + \mathbf{V} \tag{3.71}$$

We take horizontal averages (represented by a bar) of Eqs. 3.66 to 3.69 to obtain the equations of the average medium. Taking into account that $\overline{\Delta y} = 0$ and $\overline{\rho \mathbf{V}} = 0$ we obtain for the mass and momentum conservation:

$$\frac{\partial \overline{\rho}}{\partial t} + \nabla \cdot (\overline{\rho} \mathbf{u}) = 0, \tag{3.72}$$

$$\frac{\partial (\overline{\rho} \mathbf{u})}{\partial t} + \nabla (\overline{\rho} \mathbf{u}\mathbf{u}) + \nabla \cdot (\overline{\rho \mathbf{V}\mathbf{V}}) = -\overline{\rho} \nabla \Psi - \nabla \cdot (\mathbf{P}_g + \mathbf{P}_{\rm rad}). \tag{3.73}$$

Note the presence of the **Reynolds stress tensor** $\overline{\rho \mathbf{V}\mathbf{V}}$ which is related to the turbulent pressure $P_{\rm turb}$ through

$$\overline{\rho \mathbf{V}\mathbf{V}} = \overline{P_{\rm turb}} \mathbf{1} - \overline{\beta_t}, \qquad \text{with} \qquad \overline{P_{\rm turb}} = \overline{\rho V_r^2}, \tag{3.74}$$

The subscript r represents, as usual, the radial component (the horizontal components are represented either by the subscript h or the subscripts θ and ϕ).

We define the **anisotropy factor** A as:

$$A = \frac{1}{2} \frac{\overline{\rho V_r^2}}{\overline{\rho V_\theta^2}} = \frac{1}{2} \frac{\overline{\rho V_r^2}}{\overline{\rho V_\phi^2}} \tag{3.75}$$

which represents the square of the ratio between the vertical and horizontal velocities of convective elements.

By neglecting β_g and $\beta_{\rm rad}$ we finally obtain for the equation of momentum conservation in the average model:

$$\overline{\rho}\frac{d\mathbf{u}}{dt} = -\overline{\rho}\nabla\Psi - \nabla(\overline{P_g} + \overline{P_{\rm rad}} + \overline{P_{\rm turb}}) + \nabla\cdot\overline{\beta_t} \tag{3.76}$$

The equation of turbulent kinetic energy conservation is obtained by multiplying Eq. 3.67 by $\mathbf{v}$, Eq. 3.73 by $\mathbf{u}$, taking the difference and then averaging. It reads:

$$\begin{aligned}\overline{\rho}\frac{d}{dt}\left(\frac{1}{2}\frac{\overline{\rho V^2}}{\overline{\rho}}\right) = &\underbrace{-\overline{(\beta_g+\beta_{\rm rad})\otimes\nabla\mathbf{V}} - \overline{\mathbf{V}\cdot\nabla(P_g+P_{\rm rad})}}_{-\epsilon_{\rm k}} - \overline{\rho\mathbf{V}\mathbf{V}}\times\nabla\mathbf{u} \\ &- \frac{1}{2}\nabla\cdot(\overline{\rho\mathbf{V}^2\mathbf{V}}) + \nabla\cdot\overline{((\beta_g+\beta_{\rm rad})\cdot\mathbf{V})}.\end{aligned} \tag{3.77}$$

On the right-hand side of this equation, the terms on the second line are negligible (Grigahcène et al. 2005). We put together the first two terms of the first line of the right-hand side as ϵ_k which represents the **dissipation rate of kinetic energy into heat**. This finally gives,

$$\frac{\overline{\rho}}{2}\frac{d}{dt}\left(\frac{\overline{\rho V^2}}{\overline{\rho}}\right) = -\overline{\epsilon_k} - \overline{\rho\mathbf{V}\mathbf{V}}\times\nabla\mathbf{u}. \tag{3.78}$$

Note that ϵ_k is equal to zero in the equilibrium model.

The average of Eq. 3.68 gives the mean equation of energy conservation:

$$\overline{\rho}\frac{d\overline{U}}{dt} + (\overline{P}_g + \overline{P}_{\rm rad})\nabla\cdot\mathbf{u} = -\nabla\cdot(\overline{\mathbf{F}}_{\rm rad} + \overline{\mathbf{F}}_C) + \overline{\rho\epsilon} + \overline{\epsilon}_k. \tag{3.79}$$

The total flux of energy transported by convection is given by:

$$\overline{\mathbf{F}}_C = \overline{(P_g + P_{\rm rad} + \rho U)\mathbf{V}} = \overline{\rho\Delta H\mathbf{V}}, \tag{3.80}$$

with H the enthalpy. Using the entropy S instead of the internal energy we finally obtain:

$$\overline{\rho}\overline{T}\frac{d\overline{S}}{dt} = -\nabla\cdot(\overline{\mathbf{F}}_{\rm rad} + \overline{\mathbf{F}}_C) + \overline{\rho\epsilon} + \overline{\epsilon}_k. \tag{3.81}$$

If we neglect pressure fluctuations and third-order terms, we obtain for the convective flux:

$$\overline{\mathbf{F}}_C = \overline{\rho}\overline{T}\overline{\Delta S\mathbf{V}}. \tag{3.82}$$

3.2.3 Equations for convective fluctuations

Equations for convective fluctuations are obtained by subtracting the equations of the average medium to the general equations of hydrodynamics.

- The **continuity equation** is obtained by subtracting Eq. 3.72 to Eq. 3.66:

$$\overline{\rho}\frac{d}{dt}\left(\frac{\Delta\rho}{\overline{\rho}}\right) + \nabla\cdot(\rho\mathbf{V}) = 0 \tag{3.83}$$

With the Boussinesq approximation, it reduces to

$$\nabla \cdot \mathbf{V} = 0 \tag{3.84}$$

- The **equation of motion** for the convection is obtained by subtracting Eq. 3.73 to Eq. 3.67 and using Eq. 3.72:

$$\begin{aligned}
\overline{\rho}\frac{d}{dt}\left(\frac{\rho\mathbf{V}}{\overline{\rho}}\right) &= -\rho\mathbf{V}\cdot\nabla\mathbf{u} + \frac{\rho}{\overline{\rho}}\nabla\cdot\left(\overline{\mathbf{P_g} + \mathbf{P}_{\rm rad} + \rho\mathbf{V}\mathbf{V}}\right) - \nabla\cdot\left(\mathbf{P}_g + \mathbf{P}_{\rm rad} + \rho\mathbf{V}\mathbf{V}\right) \\
&= -\rho\mathbf{V}\cdot\nabla\mathbf{u} + \frac{\Delta\rho}{\overline{\rho}}\nabla\left(\overline{P}_g + \overline{P}_{\rm rad} + \overline{P}_{\rm turb}\right) - \nabla\Delta\left(P_g + P_{\rm rad} + P_{\rm turb}\right) \\
&\quad -\frac{\Delta\rho}{\overline{\rho}}\nabla\cdot\left(\overline{\beta}_g + \overline{\beta}_{\rm rad} + \overline{\beta}_{\rm turb}\right) + \nabla\cdot\left(\Delta\beta_g + \Delta\beta_{\rm rad} + \Delta\beta_{\rm turb}\right).
\end{aligned} \tag{3.85}$$

We have to simplify this equation in order to recover the MLT. To do this, we follow Unno (1967) by assuming

$$\Lambda\frac{\overline{\rho}\mathbf{V}}{\tau_c} = \frac{\Delta\rho}{\overline{\rho}}\nabla\cdot\left(\overline{\beta}_g + \overline{\beta}_{\rm rad} + \overline{\beta}_t\right) - \nabla\cdot\left(\delta\overline{\beta}_g + \Delta\overline{\beta}_{\rm rad} + \Delta\overline{\beta}_t\right), \tag{3.86}$$

with Λ a constant and $\tau_c = l_m/\sqrt{\overline{V_r^2}}$ the lifetime of convective elements. With this approximation and with the Boussinesq approximation, the equation of motion finally reads:

$$\overline{\rho}\frac{d\mathbf{V}}{dt} = \frac{\Delta\rho}{\overline{\rho}}\nabla\overline{P} - \nabla\Delta P - \rho\mathbf{V}\cdot\nabla\mathbf{u} - \Lambda\frac{\overline{\rho}\mathbf{V}}{\tau_c}. \tag{3.87}$$

- The **energy equation** for the turbulence is obtained by subtracting Eq. 3.81 to Eq. 3.68:

$$\overline{\rho}\frac{d}{dt}\left(\frac{\rho U}{\overline{\rho}} - \overline{U}\right) + \nabla\cdot\left(\rho H\mathbf{V} - \overline{\rho H\mathbf{V}}\right) - \mathbf{V}\cdot\nabla\left(P_g + P_{\rm rad}\right) \tag{3.88}$$

$$+\overline{\mathbf{V}\cdot\nabla\left(P_g + P_{\rm rad}\right)} + \left(\Delta P_g + \Delta P_{\rm rad}\right)\nabla\cdot\mathbf{u} - \rho\epsilon_2 + \overline{\rho\epsilon_2}$$

$$= \rho\epsilon - \overline{\rho\epsilon} - \nabla\cdot\Delta\mathbf{F}_{\rm rad}. \tag{3.89}$$

Once again, we simplify this equation to recover the MLT. We assume following Unno (1967) that

$$\overline{\rho}\overline{T}\frac{\Delta S}{\tau_c} = -\overline{\rho}\overline{T}\mathbf{V}\cdot\nabla\overline{S} - \rho\epsilon_2 + \overline{\rho\epsilon_2} + (\rho T\nabla S)\cdot\mathbf{V} - \overline{(\rho T\nabla S)\cdot\mathbf{V}}. \tag{3.90}$$

Following the MLT approach, we linearise $\nabla\cdot\Delta\mathbf{F}_{\rm rad}$ as:

$$\nabla\cdot\Delta\mathbf{F}_{\rm rad} = -\omega_{\rm rad}\Delta S\overline{\rho T}. \tag{3.91}$$

Finally, with the Boussinesq approximation, the **energy equation for convective fluctuations** reads

$$\frac{\Delta(\rho T)}{\overline{\rho T}}\frac{d\overline{S}}{dt} + \frac{d\Delta S}{dt} + \mathbf{V}\cdot\nabla\overline{S} = -\frac{\omega_{\rm rad}\tau_c + 1}{\tau_c}\Delta S. \tag{3.92}$$

- The **equations of state** become, neglecting ΔP:

$$\frac{\Delta\rho}{\overline{\rho}} = \frac{1}{Q}\frac{\Delta S}{c_p}, \tag{3.93}$$

$$\frac{\Delta T}{\overline{T}} = \frac{\Delta S}{c_p}. \tag{3.94}$$

3.2.4 Stationary case

To recover the MLT equations (see Sect. 2.4), we rewrite Eqs. 3.84, 3.87 and 3.92 in the stationary case (i.e. assuming $\mathbf{u} = 0$ and suppressing temporal derivatives):

$$\nabla \cdot \mathbf{V} = 0 \tag{3.95}$$
$$\frac{\Delta\rho}{\overline{\rho}} \nabla \overline{P} - \nabla \Delta P - \Lambda \frac{\overline{\rho}\mathbf{V}}{\tau_c} = 0 \tag{3.96}$$
$$\mathbf{V} \cdot \nabla \overline{S} = -\frac{\omega_{\rm rad}\tau_c + 1}{\tau_c} \Delta S \tag{3.97}$$

We now search for solutions of the form of plane waves:

$$\Delta y = \Delta y \exp(i\mathbf{k} \cdot \mathbf{r}) \tag{3.98}$$
$$\mathbf{V} = \mathbf{V} \exp(i\mathbf{k} \cdot \mathbf{r}) \tag{3.99}$$

The continuity equation thus gives:

$$\mathbf{V} \cdot \mathbf{k} = 0. \tag{3.100}$$

Multiplying Eq. 3.96 by $\mathbf{k}$, isolating ΔP and reintroducing this expression for ΔP in Eq. 3.96 we obtain:

$$\rho\mathbf{V} = \frac{\tau_c}{\Lambda} \frac{\Delta\rho}{\overline{\rho}} \frac{d\overline{P}}{dr} \mathbf{b} \exp(i\mathbf{k} \cdot \mathbf{r}), \tag{3.101}$$

with the notation

$$\mathbf{b} = \left(-\frac{k_r k_x}{k^2}, -\frac{k_r k_y}{k^2}, \frac{k_h^2}{k^2} \right). \tag{3.102}$$

We can also express the entropy gradient in terms of other gradients:

$$\frac{dS}{dr} = c_p \left[\nabla - \nabla_{\rm ad} \frac{d\ln P_{\rm th}}{d\ln P} \right] \frac{d\ln P}{dr}, \tag{3.103}$$

where $P_{\rm th}$ is the pressure of the gas and P the pressure of the gas and turbulence. One usually neglects the term $d\ln P_{\rm th}/d\ln P$. From Eq. 3.97, with V_r from Eq. 3.101 and with Eqs. 3.93 and 3.103, we recover the classical MLT Eq. 2.54:

$$\Gamma(\Gamma + 1) = \mathcal{A}'(\nabla - \nabla_{\rm ad}), \tag{3.104}$$

with

$$\mathcal{A}' = \frac{A}{A+1} \frac{1}{\Lambda} \frac{P_T P}{P_\rho \rho} \left[\frac{\kappa c_p \rho^3 g l_m^2}{6acT^3 P} \right]^2 , \tag{3.105}$$

which reduces to the classical MLT $\mathcal{A}$ (see Eq. 2.48) if we assume $\Lambda = 8A/(A+1)$ and an isotropic turbulence $A = 1/2$.
The other MLT equations are then obtained following the classical developments of the MLT made in Sect. 2.4.4. They read:

$$\tfrac{9}{4}\Gamma^3 + \Gamma^2 + \Gamma = \mathcal{A}'(\nabla_{\rm rad} - \nabla_{\rm ad}) \quad , \tag{3.106}$$
$$F_c = \frac{\alpha c_p \rho T}{4} \sqrt{\frac{P_T P}{2 P_\rho \rho}} \left[\frac{\Gamma(\nabla - \nabla_{\rm ad})}{\Gamma + 1} \right]^{3/2} \quad , \tag{3.107}$$
$$P_{\rm turb} = \frac{\alpha^2}{8} \frac{P_T P}{2 P_\rho} \frac{\Gamma}{\Gamma+1} (\nabla - \nabla_{\rm ad}) \quad . \tag{3.108}$$

3.2.5 Perturbation of the average structure

We now perturb the set of equations obtained in Sect. 3.2.2 to obtain the oscillation equations. The perturbative method is the same as in Sect. 3.1, the only difference being the explicit presence of coupling terms between convection and oscillations.

The perturbed continuity equation (Eq. 3.26) and the perturbed Poisson equation (Eq. 3.27) are not modified. Eq. 3.73 gives the perturbed equation of motion:

$$-\sigma^2\rho\xi = -\delta\rho\nabla\Psi - \nabla(\delta P_g + \delta P_{\rm rad} + \delta P_{\rm turb}) + \nabla\xi\cdot\nabla\cdot\beta_t - \rho\nabla\delta\Psi + \delta(\nabla\cdot\beta_t) \tag{3.109}$$

with $\nabla\cdot\beta_t$ obtained from the definition of A (Eq. 3.75) at equilibrium:

$$\nabla\cdot\beta_t = -\frac{2A-1}{A}\frac{P_{\rm turb}}{r}\mathbf{e}_r. \tag{3.110}$$

In what follows, we will use the notation:

$$\delta(\nabla\cdot\beta_t) = -\Xi_r(r)Y_\ell^m(\theta,\phi)\mathbf{e}_r - \Xi_h(r)(r\nabla_h Y_\ell^m(\theta,\phi)). \tag{3.111}$$

The radial component of the perturbed equation of motion reads,

$$\sigma^2\xi_r = \frac{d\delta\Psi}{dr} + g\frac{\delta\rho}{\rho} + \frac{1}{\rho}\left[\frac{d}{dr}\delta P + \Xi_r(r) + \left(\frac{2A-1}{A}\frac{P_{\rm turb}}{r}\right)\frac{d\xi_r}{dr}\right] \tag{3.112}$$

with $\delta P = \delta P_g + \delta P_{\rm rad} + \delta P_{\rm turb}$. Comparing this equation with Eq. 3.16 we see that taking into account the coupling between convection and oscillations makes new terms appear (in blue in this equation)[5].

The horizontal component reads

$$\sigma^2\xi_h = \frac{1}{r}\left[\delta\Psi + \frac{\delta P}{\rho} + \Xi_h(r) + \frac{2A-1}{A}\frac{P_{\rm turb}}{\rho}\left(\frac{\xi_r}{r} - \frac{\xi_h}{r}\right)\right] \tag{3.113}$$

Finally, the perturbation of the energy equation gives:

$$\begin{aligned} i\sigma T\delta S = &-\frac{d\delta(L_C + L_{\rm rad})}{dm} + \epsilon\left[\frac{\delta\epsilon}{\epsilon} + \ell(\ell+1)\frac{\xi_h}{r}\right] \\ &+ \frac{\ell(\ell+1)}{4\pi r^3\rho}\left[L_{\rm rad}\left(\frac{\delta T}{r\left(\frac{dT}{dr}\right)} - \frac{\xi_r}{r}\right) - L_C\frac{\xi_h}{r}\right] \\ &+ \frac{\ell(\ell+1)}{\rho r}\delta F_{\rm C,h} + \delta\epsilon_k \end{aligned} \tag{3.114}$$

[5] note that the perturbation of the turbulent pressure $\delta P_{\rm turb}$ is included in δP

3.2.6 Perturbation of the convection

We now look at the equations for the perturbation of convective fluctuations in order to obtain an explicit expression for the new coupling terms appearing in the oscillations equations in Sect. 3.2.5. A complete derivation of these terms is given in Grigahcène et al. (2005). We only recall here the main assumptions that will be used for the results presented in this thesis.

The perturbation of energy equation (Eq. 3.92) gives

$$\left(\frac{\Delta\rho}{\overline{\rho}}+\frac{\Delta T}{\overline{T}}\right)\frac{d\delta\overline{S}}{dt}+\frac{d(\delta\Delta S)}{dt}+\delta\mathbf{V}\cdot\nabla\overline{S}+\mathbf{V}\cdot\delta(\nabla\overline{S})=-\omega_{\rm rad}\delta\Delta S-\delta\omega_{\rm rad}\Delta S-\delta\left(\frac{\Delta S}{\tau_c}\right) \quad (3.115)$$

The term $\Delta S/\tau_c$ corresponds to the closure approximation made for the energy equation (Eq. 3.90) in our MLT treatment. This closure term extremely simplifies many complex physical processes. It is therefore clear that the major uncertainty in this theory is associated with the perturbation of this term for which we have to make some approximations.

When $\omega\tau_c \ll 1$, convection instantaneously adapts to changes due to oscillations and, following Gabriel (1996), we assume:

$$\delta\left(\frac{\Delta S}{\tau_c}\right)=\frac{\Delta S}{\tau_c}\left(\frac{\delta\Delta S}{\Delta S}-\frac{\delta\tau_c}{\tau_c}\right) \quad (3.116)$$

As discussed in Grigahcène et al. (2005) a well known problem of the TDC treatment, when using Eq. 3.116, is the occurrence of spatial oscillations of wavelength much shorter than the mixing length. This is not consistent with the basic hypotheses of the MLT. Grigahcène et al. (2005) proposed to solve this problem by modifying the perturbation of the energy closure equation as follow:

$$\boxed{\delta\left(\frac{\Delta S}{\tau_c}\right)=\frac{\Delta S}{\tau_c}\left((1+\beta\omega\tau_c)\frac{\delta\Delta S}{\Delta S}-\frac{\delta\tau_c}{\tau_c}\right)} \quad (3.117)$$

where they introduce a free complex parameter β, of the order of unity. This parameter allows phase lags between oscillations and the adaptation of the turbulent cascade to occur. The impact of this parameter will be investigated in Chap. 5.

Using the closure assumption given by Eq. 3.117 and introducing the notations

$$\begin{aligned} B &= \frac{i\omega\tau_c+\Lambda}{\Lambda}, \\ C &= \frac{\omega_{\rm rad}\tau_c+1}{(i+\beta)\omega\tau_c+\omega_{\rm rad}\tau_c+1}, \\ D &= \frac{1}{(i+\beta)\omega\tau_c+\omega_{\rm rad}\tau_c+1}, \end{aligned}$$

we can now express the perturbations of the terms linked to convection in the equations given in Sect. 3.2.5.

When we perturb the **equation of motion** (Eq. 3.73), some terms corresponding to the perturbation of the turbulent velocity appear. The explicit form for the radial turbulent velocity

perturbation is given by:

$$\begin{aligned}\frac{\overline{V_r\delta V_r}}{\overline{V_r^2}} = \frac{1}{B+((i+\beta)\omega\tau_c+1)D}\cdot\Bigg\{&-\frac{\delta c_p}{c_p}-\frac{\delta Q}{Q}-\frac{\delta\rho}{\rho}+\frac{d\delta p}{dp}-\frac{d\xi_r}{\xi_r}\\ &-i\omega\tau_c D\frac{Q+1}{Q}\frac{\delta S}{c_p}+C\left[\frac{d\delta S}{ds}-\frac{d\xi_r}{\xi_r}\right]\\ &-\frac{A}{A+1}\frac{i\omega\tau_c}{\Lambda}\left(\frac{d\xi_r}{dr}+\frac{1}{A}\frac{\xi_r}{r}-\frac{\ell(\ell+1)}{2A}\frac{\xi_h}{r}\right)\\ &-\omega_{\rm rad}\tau_c D\left(3\frac{\delta T}{T}-\frac{\delta c_p}{c_p}-\frac{\delta\kappa}{\kappa}-2\frac{\delta\rho}{\rho}\right)\\ &+((i+\beta)\omega\tau_c+3\omega_{\rm rad}\tau_c+2)D\frac{\delta l_m}{l_m}\Bigg\}.\end{aligned} \tag{3.118}$$

After some algebra, we found a simple relation for the horizontal components of $\delta\mathbf{V}$:

$$\frac{\overline{V_\theta\delta V_\theta}}{V_r^2}+\frac{\overline{V_\phi\delta V_\phi}}{V_r^2}=\frac{1}{A}\frac{\overline{\delta V_r}}{V_r}. \tag{3.119}$$

For the convective flux (Eq. 3.82) we directly obtain for the radial and horizontal components of its perturbation:

$$\begin{aligned}\frac{\delta F_{\rm c,r}}{F_{\rm c,r}} =&\frac{\delta\rho}{\rho}+\frac{\delta T}{T}-i\omega\tau_c D\frac{Q+1}{Q}\frac{\delta S}{c_p}+C\left[\frac{d\delta S}{ds}-\frac{d\xi_r}{\xi_r}\right]+(2\omega_{\rm rad}\tau_c+1)D\frac{\delta l_m}{l_m}\\ &-\omega_{\rm rad}\tau_c D\left(3\frac{\delta T}{T}-\frac{\delta c_p}{c_p}-\frac{\delta\kappa}{\kappa}-2\frac{\delta\rho}{\rho}\right)+((i+\beta)\omega\tau_c+3\omega_{\rm rad}\tau_c+2)D\frac{\overline{\delta V_r}}{V_r}\quad,\end{aligned} \tag{3.120}$$

and

$$\begin{aligned}\frac{\delta F_{\rm c,h}}{F_{\rm c,h}} =&\frac{C(B+1)}{2A(B-C)}\frac{\delta S}{dS/d\ln r}+\frac{1}{2AB}\left[\frac{C(B+1)}{B_C}+A+2\right]\frac{\delta P}{dP/d\ln r}\\ &+\left[\frac{C(B+1)(2BA+B+1)}{2BA(A+1)(B-C)}+\frac{B-1}{2B(A+1)}+\frac{A+2}{2AB}\right]\cdot\left(\frac{\xi_h}{r}-\frac{\xi_r}{r}\right)\\ &-\frac{B-1}{2B(A+1)}\left[\frac{C(B+1)}{B-C}+A+2\right]\frac{d\xi_h}{dr}\quad.\end{aligned} \tag{3.121}$$

The perturbation of the turbulent pressure (Eq. 3.74) gives:

$$\frac{\delta P_{\rm turb}}{P_{\rm turb}}=\frac{\delta\rho}{\rho}+2\frac{\overline{\delta V_r}}{V_r}. \tag{3.122}$$

Using the definition of the turbulent pressure (Eq. 3.74) and the equation for the radial component of the turbulent velocity perturbation (Eq. 3.118), we obtain the **perturbation of the rate of dissipation of turbulent kinetic energy into heat**:

$$\delta\epsilon_k=-i\sigma P_{\rm turb}\left[\frac{A+1}{2A}\left(\frac{\delta P_{\rm turb}}{P_{\rm turb}}-\frac{\delta\rho}{\rho}\right)+\frac{d\xi_r}{dr}+\frac{1}{2A}\left(2\frac{\xi_r}{r}-\ell(\ell+1)\frac{\xi_h}{r}\right)\right]. \tag{3.123}$$

For the **perturbation of the mixing length**, following the MLT formula $\ell_m = \alpha H_p$, we assume when $\omega\tau_c \ll 1$

$$\frac{\delta\ell_m}{\ell_m} = \frac{\delta H_p}{H_p} = \frac{\delta P}{P} - \frac{d\delta P}{dP} + \frac{d\xi_r}{\xi_r}. \tag{3.124}$$

When $\omega\tau_c \gg 1$, we expect that the perturbation of the mixing length becomes negligible. These two behaviours can be reproduced by adopting the general formula

$$\frac{\delta\ell_m}{\ell_m} = \frac{1}{1+(\omega\tau_c)^2}\frac{\delta H_p}{H_p}. \tag{3.125}$$

Both Eqs. 3.124 and 3.125 have been implemented in the non-adiabatic code used in this thesis and their effect on the damping rates is discussed in Sect. 5.2.

3.2.7 Damping rates of oscillations

With this TDC treatment, we can now rewrite the damping rate Eq. 3.63 in a more explicit form, by decomposing the different contributions to the work integral. To do this we first express $\delta P = \delta P_{\rm turb} + \delta P_g$ and we use Eq. 3.12 in Eq. 3.63 (we also neglect non-diagonal components of the Reynolds stress tensor, Ξ). We finally obtain

$$\begin{aligned}\eta = &\underbrace{\frac{1}{2\omega I}\int_0^M \Im\left(\frac{\delta\rho^*}{\rho}\frac{\delta P_{\rm t}}{\rho}\right)dm}_{\text{turbulent pressure contribution}} + \underbrace{\frac{1}{2\omega I}\int_0^M \Re\left[(\Gamma_3-1)\frac{\delta\rho^*}{\rho}\frac{d\delta L_{\rm conv}}{dm}\right]dm}_{\text{convective flux contribution}} \\ &+ \underbrace{\frac{1}{2\omega I}\int_0^M \Re\left[(\Gamma_3-1)\frac{\delta\rho^*}{\rho}\frac{d\delta L_{\rm rad}}{dm}\right]dm}_{\text{radiative flux contribution}} - \underbrace{\frac{1}{2\omega I}\int_0^M \Re\left[(\Gamma_3-1)\frac{\delta\rho^*}{\rho}\delta\epsilon_k\right]dm}_{\text{dissipation of kinetic energy contribution}}\end{aligned} \tag{3.126}$$

Eq. 3.126 exhibits four contributions to the damping, considered as the dominant ones in the current state of the art (see Belkacem et al. 2012b, for a detailed investigation of these different contributions).

- The first term of Eq. 3.126 corresponds to the contribution of turbulent pressure. The phase difference between variations of density and turbulent pressure control its effect on oscillations (driving or damping). We recall that the turbulent pressure is simply linked to the Reynold stress tensor (Eq. 3.74). Its perturbation is obtained by Eq. 3.122.

- The second term of Eq. 3.126 is related to the contribution of the convective flux (through Eq. 3.30 and Eqs. 3.120, 3.121). It strongly depends on the coupling between convection and oscillations.

- The third term of Eq. 3.126 is the contribution of the radiative luminosity, already discussed in Sect. 3.1.4.

- The last term of Eq. 3.126 is associated to the perturbation of the rate of dissipation of kinetic energy into heat (Eq. 3.123). It partially compensates the effect of the turbulent pressure (there is a total compensation for an isotropic fully ionised gas).

Based on this treatment, Belkacem et al. (2012b) have shown that the contributions of turbulent pressure and entropy are of the same order of magnitude with opposite signs; the turbulent pressure has a damping effect while entropy fluctuations have a driving effect. Moreover they remark that the maximum compensation of these two contributions creates the well known plateau of damping rates of solar-like oscillations.

3.3 Non-local treatment of convection

As mentioned in Sect. 2.4, the MLT is a local theory. The TDC treatment presented here is also local. This local approximation is, in most of the cases, false when dealing with stellar convection. The state of a convective element depend of what happens to it in the previously crossed layers. 3D hydrodynamic simulations are required to model properly the non-local behaviour of convection. Such simulations are however very time consuming and cannot be easily used for the interaction between convection and oscillations. Based on the original idea of Spiegel (1963), Dupret et al. (2006b,a) proposed a non-local treatment based on the MLT approach.

The main idea of this non-local treatment is that non-local quantities can be obtained by weighted averages of local ones. Spiegel (1963) introduces this idea by analogy with the radiative transfer in stellar atmosphere. Following Balmforth (1992a), we approximate the non-local turbulent pressure and convective flux by:

$$P_{\rm t,nl}(\zeta_0) = \int_{-\infty}^{+\infty} P_{\rm t,l}\ e^{-b|\zeta-\zeta_0|} d\zeta\ , \quad F_{\rm c,nl}(\zeta_0) = \int_{-\infty}^{+\infty} F_{\rm c,l}\ e^{-a|\zeta-\zeta_0|} d\zeta, \tag{3.127}$$

where the subscript nl indicates non-local quantities, l local quantities, and $\zeta = r/\ell_m$. a and b are free non-local parameters that can be constrained with 3D simulations (see Dupret et al. 2006a). The second-order derivatives of Eqs. 3.127 give:

$$\frac{d^2 P_{\rm t,nl}}{d\zeta^2} = b^2 (P_{\rm t,nl} - P_{\rm t,l})\ , \quad \frac{d^2 F_{\rm c,nl}}{d\zeta^2} = b^2 (F_{\rm c,nl} - F_{\rm c,l}). \tag{3.128}$$

Solving these equations allows one to deduce non-local quantities from local ones. Such a treatment can be implemented in a stellar evolution code to improve the treatment of the convective zones. However, in this thesis, we use a local MLT description in the computation of the equilibrium model but we implement it, a-posteriori, in the non-adiabatic oscillation code. The perturbations of Eqs. 3.128 (neglecting perturbations of ζ) are simply added to the classical oscillation equations. The local TDC treatment (Sect. 3.2) makes the link between the local perturbations of convective flux and turbulent pressure, and the classical perturbed quantities. It allows us to obtain a better determination of the damping rates of solar-like oscillations. I will discuss the effects of the free parameters a and b on the damping rates of solar-like oscillations in Sect. 5.2.

3.4 Stochastic excitation

Solar-like oscillations are excited by turbulent motions in the upper convective layers of stars. Given the stochastic nature of turbulence, this driving process is named stochastic excitation. A lot of work has been done to develop a theory of stochastic excitation (see Sect. 1.1.1). I present in the following sections the formulation of Samadi, Goupil (2001).
The modelling of the effects of turbulence on oscillations presents some particular difficulties (for instance this is a non-linear process in which one has to describe the effect of an overwhelming process over a small one), so that we have to treat it in a specific way. One thus traditionally makes the hypothesis that damping and driving of solar-like oscillations can be treated separately. In Sect. 3.4.1, I give the relation between mode amplitudes (and mean squared surface velocity) and the power injected into the modes by the turbulence. This last quantity is quantified thanks to the stochastic excitation theory presented in Sect. 3.4.2. I finally discuss in Sect. 3.4.3 the different key elements of such a formulation.

3.4.1 The problematic of mode amplitude

We give here, the relations linking the oscillation velocity, amplitude and the power injected into the mode by the turbulence. The displacement vector of an oscillation of frequency ω is given by:

$$\delta\mathbf{r} = \frac{1}{2}\left(A(t)\xi e^{i\omega t} + cc\right), \tag{3.129}$$

where $A(t)$ is the instantaneous amplitude of the oscillation and cc represents the complex conjugate. In the excitation region, the typical frequency of turbulent eddies is of the order of the pulsation period which is much smaller than the lifetime of the modes ($\tau = 1/\eta$). The velocity of the mode $\mathbf{v}_{\rm osc} \equiv d\delta\mathbf{r}/dr$ can be approximated by:

$$\mathbf{v}_{\rm osc}(t) \simeq \frac{1}{2}\left(i\omega A(t)\xi e^{-i\omega t} + cc\right) \tag{3.130}$$

and the time averaged mode energy is given by (see Balmforth 1992b)

$$\overline{E}_{\rm osc} = \int_0^M \overline{v}^2_{\rm osc} dm = \frac{1}{2}\overline{|A|}^2 I_k \omega^2 \tag{3.131}$$

Because of the stochastic nature of the process $A(t)$ cannot be obtained in a deterministic way. We thus have to look at mean values, over an infinite set of independent realisations, denoted by the operator $\langle\cdot\rangle$. The derivation of this mean squared amplitude will be presented in Sect. 3.4.2. At a given point r_s (where the amplitude of the mode is measured), we have

$$\left\langle \overline{v}^2_{\rm osc}(r_s)\right\rangle = \frac{1}{2}\left\langle \overline{|A|}^2\right\rangle \omega^2 |\xi_r(r_s)|^2. \tag{3.132}$$

We define the mode mass as:

$$\mathcal{M}_m = \frac{I_k}{|\xi_r(r_s)|^2}, \tag{3.133}$$

and thus we obtain

$$\overline{E}_{\rm osc}(r_s) = \overline{v}^2_{\rm osc}(r_s)\mathcal{M}_m \tag{3.134}$$

Note that for $r_s = R$ we have according to Eq. 3.46, $\mathcal{M}_m = MI$.

With η the linear damping rate (such as $dv_{\rm osc}/dt = -\eta v_{\rm osc}$) and $\mathcal{P}$ the energy injected into the oscillation (per unit time), the variation of the mode energy with time is given by (using Eq. 3.131):

$$\frac{dE_{\rm osc}}{dt} = \mathcal{P} - 2\eta E_{\rm osc}. \tag{3.135}$$

Since solar-like oscillations are stable modes, a stationary solution is obtained by averaging the previous equation over a long time scale which gives:

$$\overline{E}_{\rm osc} = \frac{\overline{\mathcal{P}}}{2\eta} \tag{3.136}$$

Dropping the bar for the time average, the power injected into the oscillations is given by:

$$\mathcal{P} = 2\pi\Gamma E_{\rm osc} \tag{3.137}$$

with $\Gamma = \eta/\pi$ the mode linewidth. Inserting Eq. 3.134 in Eq. 3.137, the mean squared surface velocity of a mode is thus given by the relation (Balmforth 1992b):

$$\boxed{\left\langle v_{\rm osc}^2(R)\right\rangle = \frac{1}{2}\omega^2|\xi(R)|^2\left\langle |A|^2\right\rangle = \frac{\mathcal{P}}{2\eta MI}.} \tag{3.138}$$

3.4.2 The stochastic excitation mechanism

The main steps of the derivation of the power injected into the oscillations by the turbulence are schemed in Fig. 3.7. For sake of simplicity, I will limit this presentation to radial oscillations with a driving only coming from the turbulent Reynolds stress (see Samadi, Goupil 2001, for more complete developments.). We start by the perturbed momentum and continuity equations (Eqs. 3.139 and 3.140) in which we split the velocity into the contribution of oscillations and turbulence. This gives an inhomogeneous equation of a damped and forced oscillator (Eq. 3.142). Whithout the source term, this equation (which is now homogeneous) reduce to the classical adiabatic oscillation equation. We thus inject the solutions of the form of Eq. 3.129 (the displacement vector of an oscillation) into the inhomogeneous wave equation. This gives us a differential equation for mode amplitudes (Eq. 3.145). We solve it, assuming a stationary turbulence, and obtain the mean squared mode amplitude (Eq. 3.150). With some closure approximations and hypotheses on the kinetic energy spectrum, we write down the detailed expression for the Reynolds stress source term and the associated power injected into radial modes (Eq. 3.157).
To establish the equations describing the stochastic excitation (more specifically the forcing terms), we start from the perturbed momentum and continuity equations under the Cowling approximation:

$$\frac{\partial \rho\mathbf{v}}{\partial t} + \nabla\cdot(\rho\mathbf{v}\mathbf{v}) + \nabla P' = 0, \tag{3.139}$$

$$\frac{\partial \rho'}{\partial t} + \nabla\cdot(\rho\mathbf{v}) = 0. \tag{3.140}$$

If we limit the development to the first order, the perturbed equation of state reads:

$$P' = c_s^2\rho' + \alpha_s S', \tag{3.141}$$

with $\alpha_s = \left(\frac{\partial P}{\partial S}\right)_\rho$. Second-order terms are not necessary since we will linearise the above equations in the next step.

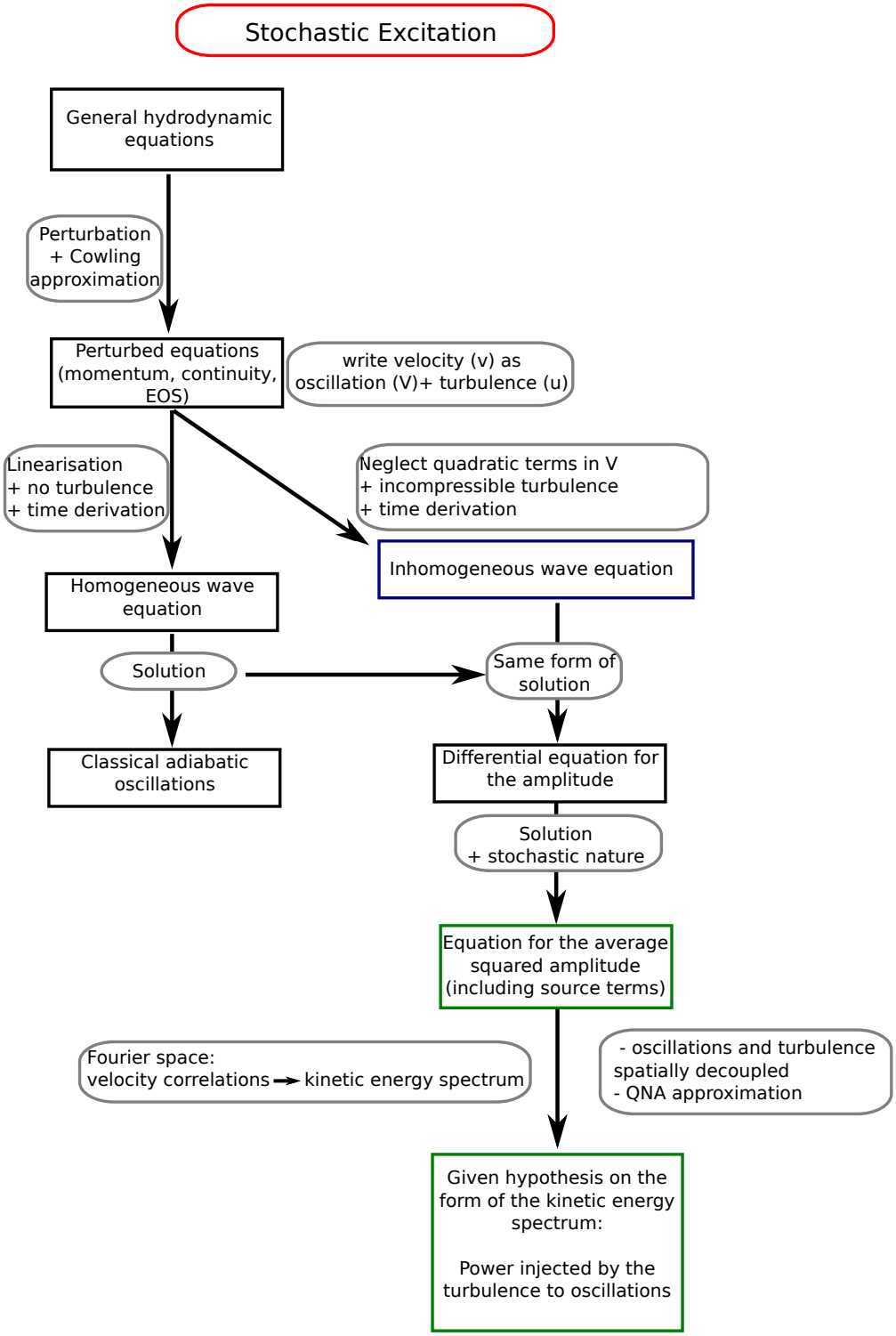

Figure 3.7: General procedure for the obtention of the power injected into the modes by turbulence.

The inhomogeneous wave equation

As done for the oscillation equations (in Sect. 3.1.2), we derive the momentum equation (Eq. 3.139) with respect to the time, and we decompose the velocity into the contributions of the oscillations and of the turbulence: $\mathbf{v} = \mathbf{v}_{\rm osc} + \mathbf{u}$. This gives us an inhomogeneous wave equation where the left-hand side comes from the oscillations and the right-hand side from the turbulence:

$$\rho \left(\frac{\partial^2}{\partial t^2} - \mathbf{L} \right) [\mathbf{v}_{\rm osc}] + \mathcal{D}(\mathbf{v}_{\rm osc}) = \frac{\partial}{\partial t} \mathcal{S} - \mathcal{C}, \tag{3.142}$$

with the operator:

$$\mathbf{L}(\mathbf{X}) = \frac{1}{\rho} \left[\nabla \left(c_s^2 \nabla \cdot (\rho \mathbf{X}) + \alpha_s \mathbf{X} \cdot \nabla S - \mathbf{g} \nabla \cdot (\rho \mathbf{X}) \right) \right], \tag{3.143}$$

and the driving source terms:

$$\mathcal{S} \equiv - \left[\nabla \cdot (\rho \mathbf{u}\mathbf{u}) + \nabla (\alpha_s S_t) \right]. \tag{3.144}$$

The first term on the right-hand side of Eq. 3.144 represents the contribution of the Reynolds stress tensor. The second one is related to the turbulent entropy fluctuations. The term $\mathcal{C}$ in Eq. 3.142 involves high-order terms and is found to be negligible (see Samadi, Goupil 2001, for a complete derivation of this term). The $\mathcal{D}$ operator involves terms linking linearly oscillations and turbulent quantities (see Samadi, Goupil 2001, for a complete derivation of this term).

The solution of the homogeneous equation (i.e. Eq. 3.142 without the right-hand side terms of Eq. 3.142) is the classical adiabatic oscillations solution (with the eigendisplacement ξ associated with the eigenfrequency ω). We thus assume that the solutions of the inhomogeneous wave equation are of the form of Eqs. 3.129 and 3.130.

In order to solve the inhomogeneous wave equation, we also have to make some approximations that will allow us to separate oscillations and turbulence. We assume that perturbations related to oscillations are small in front of the perturbations associated to turbulent motions, and that oscillations do not affect the evolution of the turbulence.
We insert Eq. 3.130 in Eq. 3.142, neglect the second temporal derivatives of the amplitude (since for typical oscillation, its period is much lower than its lifetime, $\omega \gg \eta$ and then $d \ln A/dt \ll \omega$), multiply Eq. 3.142 by $\vec{\xi}^*(r,t)$ and integrate over the star. Then, the inhomogeneous wave equation gives for the amplitude:

$$\frac{dA}{dt} + \Delta\sigma A = \frac{1}{2\omega^2 I} \int \vec{\xi}^* \cdot \frac{\partial \vec{\mathcal{S}}}{\partial t} \, d^3x, \tag{3.145}$$

where $\Delta\sigma = i\Delta\omega + \eta_D$ comes from the contribution of linear coupling between oscillations and turbulence (the $\mathcal{D}$ term in Eq. 3.142). $\Delta\omega$ corresponds to a frequency shift due to the turbulence. This shift is of the order of the one introduced by non-adiabatic effects (see e.g. Brun et al. 1998; Houdek 1996) and does not affect the estimated amplitude of the oscillations. η_D represents the dynamical damping. Following Balmforth (1992b); Goldreich et al. (1994), this term is replaced by the global linear damping rate η.

The solution of Eq. 3.145 is straightforwardly obtained:

$$A(t) = \frac{i e^{-\eta t}}{2\omega I} \int_{-\infty}^{t} dt' \int_{\mathcal{V}} e^{(\eta + i\omega)t'} \vec{\xi}^*(\vec{x}) \cdot \vec{\mathcal{S}}(\vec{x}, t) \, d^3x, \tag{3.146}$$

where the second integral is made over the whole volume $\mathcal{V}$ of the star.

The square of the amplitude thus writes,

$$|A|^2(t) = \frac{e^{-2\eta t}}{4(\omega I)^2} \int_{-\infty}^{t} dt_1 \; dt_2 \int_{\mathcal{V}} d^3r_1 d^3r_2 \; e^{\sigma(t_1,t_2)} \left(\vec{\xi}(\vec{r}_1)\cdot\vec{\mathcal{S}}(\vec{r}_1,t_1)\right)\left(\vec{\xi}(\vec{r}_2)\cdot\vec{\mathcal{S}}(\vec{r}_2,t_2)^*\right) \quad (3.147)$$

where $\sigma(t_1,t_2) = \eta(t_1+t_2)+i\omega(t_1-t_2)$. We define the new coordinates $\vec{x}_0, t_0$ corresponding to a space-time position where the integration of the stochastic excitation is made and $\vec{r}, \tau$ associated with the local turbulence.

$$\begin{aligned} \vec{x}_0 &= \frac{\vec{r}_1+\vec{r}_2}{2}, & t_0 &= \frac{t_1+t_2}{2}, \\ \vec{r} &= \vec{r}_2-\vec{r}_1, & \tau &= t_2-t_1. \end{aligned}$$

We should note that τ is associated to the lifetime of thes turbulent eddies and t_0 to the lifetimes of the modes. In these coordinates the mean squared amplitude (over an infinite set of independent realisations) writes

$$\begin{aligned} \left\langle |A|^2(t)\right\rangle = & \frac{e^{-2\eta t}}{4(\omega I)^2} \int_{-\infty}^{t} dt_0 e^{2\eta(t_0-t))} \int_{2(t_0-t)}^{2(t-t_0)} d\tau \int_{\mathcal{V}} d^3x_0 d^3r e^{-i\omega\tau} \\ & \times \left\langle \vec{\xi}\cdot\vec{\mathcal{S}}\left[\vec{x}_0-\frac{\vec{r}}{2},t_0-\frac{\tau}{2}\right]\vec{\xi}\cdot\vec{\mathcal{S}}^*\left[\vec{x}_0+\frac{\vec{r}}{2},t_0+\frac{\tau}{2}\right]\right\rangle. \end{aligned} \quad (3.148)$$

Since the eddies lifetime τ_c is much smaller than the oscillations lifetime ($\sim 1/\eta$), the term $e^{-2\eta t}$ in Eq. 3.148 is constant over the eddies time scale which allows us to extend to infinity the integration over τ. We then assume that the turbulence is stationnary such as the source term $\mathcal{S}$ is invariant by translation of time around t_0. Moreover, the source term is real since it involves quantities of turbulent origin. Finally, integrating over t_0, the mean squared amplitudes writes

$$\left\langle |A|^2(t)\right\rangle = \frac{1}{8\eta(\omega I)^2} \int_{\mathcal{V}} d^3x_0 \int_{-\infty}^{+\infty} d^3r \; d\tau \; e^{-i\omega\tau} \left\langle \left(\vec{\xi}\cdot\vec{\mathcal{S}}\right)_1 \left(\vec{\xi}\cdot\vec{\mathcal{S}}\right)_2 \right\rangle, \quad (3.149)$$

where the subscript 1 and 2 indicate that we evaluate quantities at respectively $[\vec{x_0}-\frac{\vec{r}}{2},-\frac{\tau}{2}]$ and $[\vec{x_0}+\frac{\vec{r}}{2},\frac{\tau}{2}]$. For convenience, we note the mean squared average of the amplitude:

$$\boxed{\left\langle |A|^2(t)\right\rangle = \frac{1}{8\eta(\omega I)^2}(C_R^2+C_S^2+C_{\rm RS}^2),} \quad (3.150)$$

where the detail derivation of the different source terms (the Reynolds C_R^2, entropy C_S^2, and crossing $C_{\rm RS}^2$ terms) can be found in Samadi, Goupil (2001) and the crossing term is found negligible.

The Reynolds stress contribution

In order to simplify the presentation of this theory, we will consider here only the Reynolds stress contribution. A complete derivation of the power injected into the modes by the turbulence and including the entropy source term can be found in Samadi, Goupil (2001). However, as discussed by Samadi et al. (2013a), a severe deficiency of the modelling of this entropy source term appears with non-adiabatic eigenfunctions. Thus, in the following and in the results presented in the second part of this thesis, we will not take the entropy contribution into account.

The Reynolds stress contribution in Eq. 3.150 is given by (see Samadi, Goupil 2001, for a detailed derivation):

$$C_R^2 = \int_{\mathcal{V}} d^3x_0 \int d\tau dr^3 \, e^{-i\omega\tau} (\rho\nabla_i \xi_j^*)_1 \left\langle (u_i u_j)_1 (u_k u_m)_2 \right\rangle (\rho\nabla_k \xi_m)_2. \tag{3.151}$$

If we assume that oscillations and turbulence act on well separated spatial scales (i.e. we assume that ξ varies on a scale larger that the characteristic spatial scale of turbulence) then, $(\rho\nabla_i\xi_j)$ is almost constant over the eddies length scale. This allows us to simplify Eq. 3.151 as:

$$C_R^2 = \int_{\mathcal{V}} d^3x_0 \, \rho^2 \nabla_i \xi_j^* \nabla_k \xi_m \int_{-\infty}^{+\infty} d^3r \, d\tau \, e^{-i\omega\tau} \left\langle (u_i u_j)_1 (u_k u_m)_2 \right\rangle . \tag{3.152}$$

This equation involves a fourth-order velocity correlation ($\langle (u_i u_j)_1 (u_k u_m)_2 \rangle$). There is no theoretical expression for correlations of this order (fourth-order moments are expressed in terms of fifth-order moments themselves expressed in terms of sixth-order moments ...). A simple closure model for this problem is the **Quasi Normal Approximation** which allows us to express fourth order moments in terms of second-order moments as (see details in Lesieur et al. 1997):

$$\begin{aligned} \left\langle (u_i u_j)_1 (u_k u_m)_2 \right\rangle = \left\langle (u_i u_j)_1 \right\rangle \left\langle (u_k u_m)_2 \right\rangle + \left\langle (u_i)_1 (u_m)_2 \right\rangle \left\langle (u_j)_1 (u_k)_2 \right\rangle \\ + \left\langle (u_i)_1 (u_k)_2 \right\rangle \left\langle (u_j)_1 (u_m)_2 \right\rangle \quad . \end{aligned} \tag{3.153}$$

Such approximation is formally valid only when the velocities are normally distributed. Some improvements for the closure model have been proposed by Belkacem et al. (2006a,b) but it appears that the final differences in the power injected into the modes for the Sun, between the QNA and the new model, is of the order of the differences between the seismic constraints from different instruments (see Fig. 9 of Samadi 2011).

Such expression in terms of velocities correlations is not convenient to use. If we assume an inhomogeneous, incompressible, isotropic and stationary turbulence, $\phi_{\rm ij}$ the Fourier transform of the second order velocity correlations $\langle (u_i)_1 (u_j)_2 \rangle$ is related to the kinetic energy spectrum E by (Batchelor 1953):

$$\phi_{\rm ij}(\mathbf{k}, \omega_t) = \frac{E(\mathbf{k}, \omega_t)}{4\pi k^2} \left(\delta_{\rm ij} - \frac{k_i k_j}{k^2} \right) \tag{3.154}$$

with k the wavenumber and ω_t the frequency associated with turbulent elements, and $\delta_{\rm ij}$ is the Kronecker symbol. Following Stein (1967) we decompose $E(\mathbf{k}, \omega_t)$ into the time average kinetic energy spectrum $E(k)$ and a frequency dependent component $\chi_k(\omega_t)$ as:

$$E(\mathbf{k}, \omega_t) = E(k) \chi_k(\omega_t) \tag{3.155}$$

χ_k is linked to the temporal correlation between eddies. Both components satisfy the normalisation conditions:

$$\int_{-\infty}^{+\infty} d\omega_t \chi_k(\omega_t) = 1 \qquad \text{and} \qquad \int_0^{\infty} dk E(k) = \frac{1}{2} \left\langle \mathbf{u}^2 \right\rangle = \frac{\phi}{2} \left\langle u_z^2 \right\rangle = \frac{3}{2} u_0^2, \tag{3.156}$$

with u_z the vertical component of the velocity, $\phi \equiv \left\langle u^2 \right\rangle / \left\langle u_z^2 \right\rangle$ the anisotropy factor as introduced by Gough (1977)[6] and u_0 the characteristic velocity of the eddies at the injection length

[6] One can easily link this anistropy factor with the one used in the TDC treatment (see Eq. 3.75) as $\phi = 1 + 1/A$.

scale k_0^{-1} We discuss the specific forms that can be adopted for these components in Sect. 3.4.3.

Finally, using the QNA approximation and in the Fourier space, Eqs. 3.138 and 3.152 give **the power injected by the turbulent Reynold stress into radial modes**:

$$\mathcal{P} = \frac{\pi^3}{2I}\mathcal{G}\int_0^M dm \frac{\rho u_0^3}{k_0^4}\left|\frac{d\xi_r}{dr}\right|^2 \tilde{\mathcal{S}}_R(m,\omega), \tag{3.157}$$

with $\mathcal{G}$ linked to the anistoropy factor as defined by Samadi, Goupil (2001) and $\tilde{\mathcal{S}}_R$ the dimensionless source function

$$\tilde{\mathcal{S}}_R = \frac{k_0^4}{u_0^3}\int_0^\infty dk \frac{E^2(k,m)}{k^2}\int_{-\infty}^{+\infty} d\omega_t \; \chi_k(\omega+\omega_t,m)\chi_k(\omega_t,m). \tag{3.158}$$

We have introduced the characteristic wavenumber of turbulent elements k_0 related to the mixing length by $k_0 = 2\pi/\beta_t\ell$ with β_t a free parameter introduced to gauge the definition of k_0 (the impact of this parameter will be discussed in the next section).

A similar source term can be found for the contribution of entropy fluctuations, as it is done by Samadi, Goupil (2001). This formalism has also been extended to non-radial modes (Belkacem et al. 2008). Calculations for the Sun are in overall good agreement with the seismic observations (see e.g. Samadi 2011).

3.4.3 Physical key quantities for stochastic excitation

We now discuss the different physical elements and prescriptions that can affect theoretical predictions of the power injected into the modes (see also Samadi 2011; Belkacem, Samadi 2013). To illustrate the discussion, we reproduce in Fig. 3.8 the solar excitation rates for pressure modes. The estimate of the power injected into the mode depends on the MLT treatment applied (it affects the amount of kinetic energy of the turbulent eddies) and obviously on the physical properties of the oscillation mode.

- The mode inertia decreases with increasing frequency. If we assume that the same amount of energy is available for all modes, it is more difficult to drive modes with high inertia (at low frequency) than modes with small inertia (at high frequency). This explains the decrease of the power at low frequency in Fig. 3.8
- The term $d\xi_r/dr$ in Eq. 3.157 corresponds to the mode compressibility. It has been shown that mode compressibility is maximum in the transition layers between the convective and radiative regions and increases with mode frequency. This enhances the effect of the inertia, favouring the excitation of high frequency modes.
- The way the convection is modelled has also a direct influence through the term u_0. Indeed, for isotropic turbulence, one can write the kinetic energy flux as $F_{\rm kin} = 3/2\rho_0 u_0^3$ which in the MLT framework is roughly proportional to the convective flux.

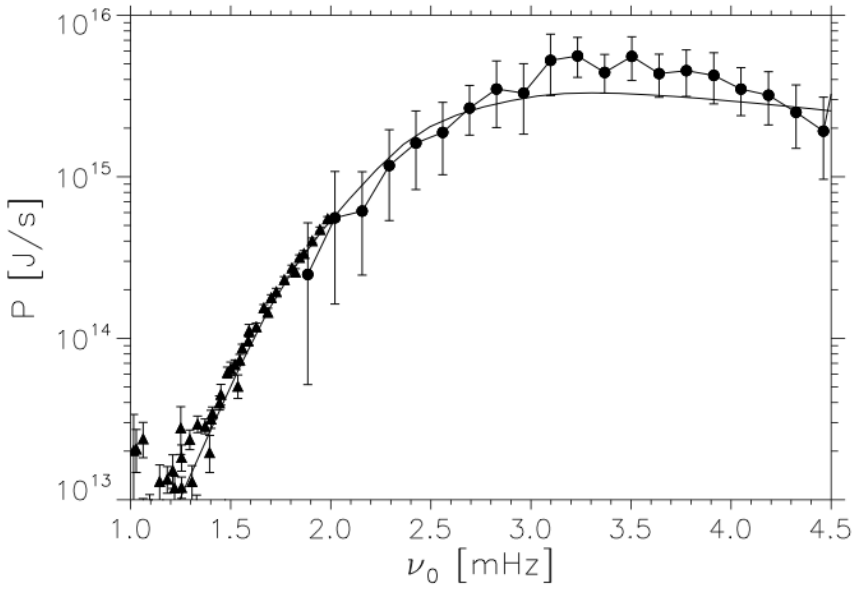

Figure 3.8: Theoretical power injected to the solar acoustic modes by turbulence as a function of the frequency compared to GONG observation [from Belkacem, Samadi (2013)].

The power injected to the modes also strongly depends on the description of the turbulence through:

- $E(k)$ which can be modelled either with analytical formulations or directly from 3D simulations. Different shapes of this spectrum can be adopted. The most currently used formulations are the Kolmogorov Spectrum, the Raised Kolmogorov Spectrum, the Broad Kolmogorov Spectrum and the Extended Kolmogorov Spectrum (see e.g. Musielak et al. 1994). 3D simulations of the solar convective envelope suggest that the EKS is the best candidate (Samadi et al. 2003a).

- The choice of the characteristic wavenumber k_0 is more important, for $\mathcal{P}$ is very sensitive to the choice of k_0. 3D simulations of the Sun allow one to calibrate this wavenumber. In such calibration, the value of β_t depends on the value of the mixing-length parameter used in the equilibrium model. Extension of such calibration to other stars is still an open question.

- $\chi_k(\omega)$ represents the resonance between oscillations and turbulent eddies. This function is often modelled by a gaussian function. However, 3D simulations of the Sun show that a Lorentzian function is better suited. Belkacem et al. (2010) have recently improved the analytical description of χ_k by using a modified Lorentzian function (see also Sect. 4.4).

3.5 Asteroseismic techniques for solar-like oscillations.

We have seen in this chapter how one can compute the oscillation properties (frequencies, damping rates, amplitudes) of an equilibrium stellar model. In this section, I discuss how one can obtain information on stars from the observation of their oscillations.
A general discussion on the use of these different techniques and the results obtained for solar-like oscillations can be found in e.g. Chaplin, Miglio (2013). This discussion will mainly focus on the inferences on stellar global properties and structure one can derives from observed frequencies.

The use of the energetic properties of solar-like oscillations (linewidths and amplitude) is more recent and still at its beginning, for it presents both observational and theoretical challenges to interpret such asteroseismic constraints. We will briefly see in this section and in more details in the following chapters that the observed mode linewidths can help to constrain the modelling of the time-dependent treatment of convection. These constraints can come from scaling relations or from fit of theoretical linewidths to observed ones (as discussed in Chap. 5).

3.5.1 Global asteroseismic quantities and scaling relations

Thanks to the space-borne telescopes CoRoT and *Kepler*, asteroseismology of solar-like oscillations allows astronomers to derive global information (such as the mass, radius, evolutionary state) for a large number of field stars. This is mainly done with empirical scaling relations, linking some average asteroseismic observables to global stellar parameters. A detailed study of these scaling relations can be found in e.g. Belkacem (2012). Because the obtention of average seismic quantities can be done quickly and with a good precision, even when observations are not precise enough to extract individual frequencies, scaling relations are useful to study large groups of observed stars. This is the basis of a new field of study called "ensemble asteroseismology" (see e.g. Miglio 2013). The main hypothesis underlying all these relations is the assumption that scalings between solar global parameters and helioseismic quantities are applicable for all stars exhibiting solar-like oscillations whatever their mass or evolutionary stage.

Stellar mass and radius

As we have shown in Sect. 3.1, asymptotic developments (Eq. 3.51) link the large separation to the mass and radius of the star. Scaled to the solar large separation it gives

$$\frac{\langle \Delta\nu \rangle}{\langle \Delta\nu \rangle_\odot} \simeq \left(\frac{M}{M_\odot}\right)^{1/2} \left(\frac{R}{R_\odot}\right)^{-3/2}, \tag{3.159}$$

where $\langle\rangle$ indicates the mean observed value which differ from the asymptotic one. In the following we will use $\langle \Delta\nu \rangle_\odot = 135.5 \mu Hz$ as given in Mosser et al. (2010a).

Solar-like oscillations are characterised by a bell-shape power spectra. Brown et al. (1991) proposed that the frequency of maximum power ($\nu_{\max}$) scales as the acoustic cut-off frequency. This frequency characterises the stellar atmosphere and represents a maximum frequency for oscillations beyond which acoustic waves from the stellar interior are no longer reflected by the atmosphere. For an isothermal atmosphere, it is theoretically given by (see e.g. Balmforth, Gough 1990): $\nu_c = c_s/2H_\rho \propto MR^{-2}T_{\rm eff}^{-1/2}$ (with H_ρ the density scale height at the photosphere).

Assuming that $\nu_{\rm max} \propto \nu_{\rm c}$ one can write the scaling relation for $\nu_{\rm max}$:

$$\frac{\nu_{\rm max}}{\nu_{\rm max,\odot}} \simeq \left(\frac{M}{M_\odot}\right)\left(\frac{R}{R_\odot}\right)^{-2}\left(\frac{T_{\rm eff}}{T_{\rm eff,\odot}}\right)^{1/2} \tag{3.160}$$

In the following we will use $\nu_{\rm max,\odot} = 3050\mu Hz$ (as given in Mosser et al. 2010a). Belkacem et al. (2011) have theoretically investigated this scaling relation and showed that $\nu_{\rm max}$ and $\nu_{\rm c}$ are linked together through their relation to the local thermal time-scale. Moreover, they showed that a more precise scaling relation for $\nu_{\rm max}$ should take into account the stellar Mach number.

From Eqs. 3.159 and 3.160, and assuming that the effective temperature of the star is known, one can easily obtain the mass and radius, and subsequently the mean density and surface gravity, of any observed star exhibiting solar-like oscillations.

Stellar evolutionary stage

In Sect. 3.1.3, we have seen that the evolution of the star inner structure leads to the appearance of mixed-modes in the power spectra. The density of mixed-modes (i.e. their number over a large separation) is controlled by the Brunt-Vaisälä frequency and hence is a good indicator of the stellar evolutionary stage. Moreover, observations and theoretical adiabatic computations (see e.g. Montalbán, Noels 2013) have shown that red-giant branch and horizontal branch stars with almost the same surface properties (i.e. almost same location in the HR diagram) have similar $\Delta\nu$ but different period spacing $\Delta\Pi$ (calculated from observed dipole mixed-modes frequencies). Due to the expansion of the core, and the apparition of a convective core after the He-flash, the Brunt-Vaisälä frequency decreases in the central layers leading to an increase of the period spacing (see the asymptotic relation given by Eq. 3.55) We thus have in a $\Delta\nu$, $\Delta\Pi$ diagram two distinct regions. Such a diagram can even lead to a more precise insight into the evolutionary stage of the star (see Fig. 3.9 reproduced from Mosser et al. 2014). The relation between the period spacing and the evolutionary stage is still qualitative but very promising for the knowledge of stellar cores.

Scaling relations for the energetic properties of solar-like oscillations

In addition to these two largely used relations, a lot of work have been done to relate the energetic properties of modes (typically for the radial modes close to $\nu_{\rm max}$) and stellar properties (see e.g. Belkacem 2012).

Based on theoretical computations (and the hypothesis of equipartition of energy between modes and most energetic eddies), Kjeldsen, Bedding (1995) have proposed that the maximum mode surface velocity $V_{\rm max}$ scales as L/M. More recently, focusing on red giants, and thanks to the large amount of CoRoT and *Kepler* observations, 3D simulations and theoretical developments, Samadi et al. (2012) have found that:

$$V_{\rm max} \propto \Gamma_{\rm max}^{1/2}\left(\frac{L}{M}\right)^{1.3}\left(\frac{M}{R^3}\right)^{0.525}, \tag{3.161}$$

where $\Gamma_{\rm max}$ is the linewdith of radial modes at $\nu_{\rm max}$. They also derived for the intensity variations

$$\left(\frac{\delta L}{L}\right)_{\rm max} \propto \Gamma_{\rm max}^{1/2}\left(\frac{L}{M}\right)^{1.55}\left(\frac{M}{R^3}\right)^{0.5}. \tag{3.162}$$

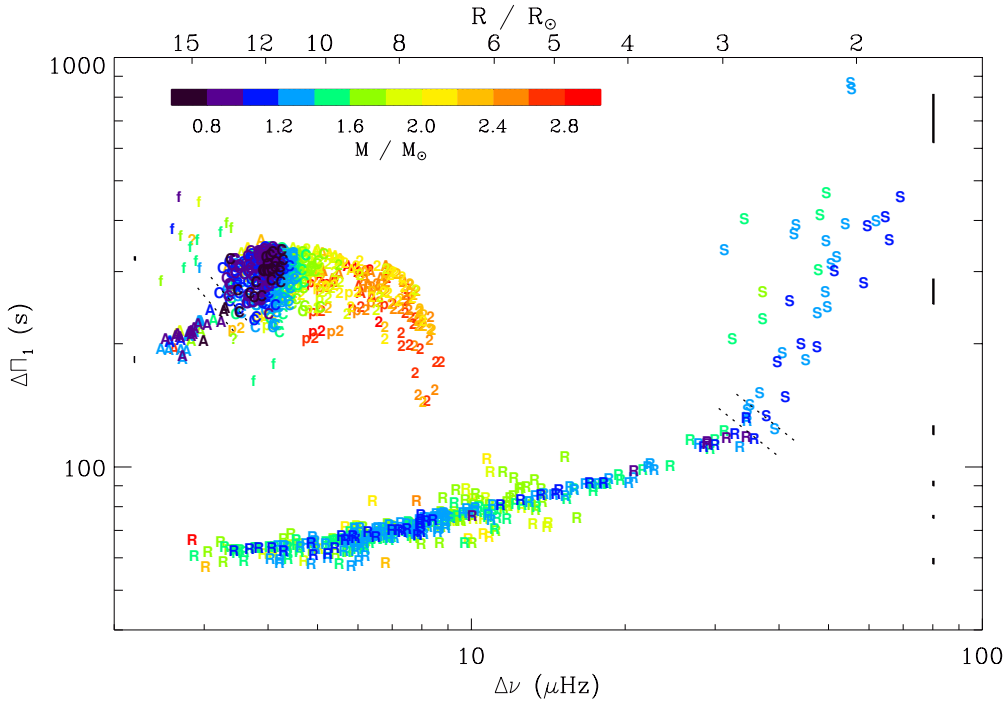

Figure 3.9: From Mosser et al. (2014): Period spacing of dipole modes as a function of the large frequency separation. The color indicate the mass of the star, the letter the evolutionary status (S = Subgiant, R = Red-giant branch, f = Helium subflash stage, C = Red clump, and more evolved stages toward A= Asymptotic giant branch). Stars of different evolutionary states occupy different regions of this diagram.

They however note the importance of leaving the adiabatic approximation for the relation between mode velocity and intensity variation. These scalings (Eqs. 3.161 and 3.162) present systematic differences for red giant observations thought to be due to non-adiabatic effects.

A relation between modes linewidths (or damping rates) and the effective temperature have been investigated from both observational and theoretical point of view. Belkacem et al. (2012) derived a theoretical scaling relation for the linewidth of acoustic modes at $\nu_{\max}$:

$$\Gamma_{\max} \propto T_{\rm eff}^{10.8} g^{-0.3} \tag{3.163}$$

which shows that damping rates strongly depends on the effective temperature. This relation is found in good agreement with *Kepler* observations (see Belkacem et al. 2012).

These scaling relations for $V_{\max}$ and $\Gamma_{\max}$ are still investigated and may be promising for a better understanding of the energy exchanges between oscillations and the turbulent convection. I will present in Sect. 5.1.2, in a study of the impact of TDC parameters on modes linewidths, how the observed $\Gamma_{\max} - T_{\rm eff}$ relation can help to constrain these parameters.

3.5.2 Individual mode frequencies

The traditional way to investigate stars inner structure is to make direct comparisons between the frequencies of stellar equilibrium models and the observed ones.
Two approaches are generally used to find the model that best reproduces the observations. The first way is to compute grids of stellar models and search inside, the one that best fit the observations. The second way is to use a Levenberg-Marquardt algorithm that searches in the parameter space the set of parameters for which the resulting stellar model gives the best fit to the observations (see e.g. Miglio, Montalbán 2005). This search is automated and sensitive to local minima of the merit function used to characterise the fit. Because of this limitation, global minimisation methods are also often used. However, it does not require to compute an entire grid and automatically adjust the step between two tested values of a parameter to obtain the best one. I will present in Chap. 7 a practical use of this method, with some particularities for the modelling of an observed *Kepler* subgiant.
In most cases, one compares the observed frequencies with theoretical adiabatic ones. As a result, a shift appears between the observed and computed frequencies. This shift is due to the poor modelling of the surface layers and is found to increase with frequency. These "surface effects" come from the non-adiabaticity of the modes in these layers and the effects of the turbulent pressure. In Chap. 7 I will discuss the use of non-adiabatic frequencies in the search of a best fit model. An important work is done on the understanding of these surface effects and on the possibility to correct adiabatic frequencies to improve the fitting process. Empirical relations (such as the one proposed by Kjeldsen et al. 2008) are generally used to correct the adiabatic frequencies but their validity (for stars other than the Sun) is still subject to discussion. 3D simulations coupled with non-adiabatic computations may bring a new light on this issue (see e.g. T. Sonoi contribution in KASC/TASC 2015 meeting). Another possibility to avoid surface effects in the fitting process is to use some frequency separation ratios, independent of these surface effects (Roxburgh, Vorontsov 2013). The use of some specific frequency ratios allows one to constrain particular features of the stellar structure such as glitches and rapid variations of physical quantities. The presence of mixed-modes in observed power spectra bring additional constraints since their frequencies strongly depend on the age of the star (see e.g. Deheuvels, Michel 2011).
We should note that, to be efficient, these methods also require the knowledge of non-seismic parameters of the star (such as its effective temperature, metallicity, ...).

3.5.3 Perspectives

Use of energetic properties of individual modes

The recent possibility brought by the high quality of *Kepler* observations to measure the frequencies, linewidths and amplitudes of individual modes opens the way to new asteroseismic constraints. As I will present in Chap. 5, observed mode linewidths can be used to constrain the TDC treatment.
From the measure of mixed-mode linewidths and amplitudes in subgiant stars, Benomar et al. (2014) have derived observed inertia ratios between non-radial and radial modes. Such ratios bring important constraints on mode trapping and can be used in the search of a best fit model (Tian et al. 2015). I will discuss in Sect. 7.4 the inertia ratios of quadrupole mixed-modes of an observed *Kepler* subgiant in order to understand differences between observed and theoretical mode energetic properties. Since mixed-modes bring very strong constraints on the star inner structure, the use of inertia ratios is a promising way toward a better understanding of evolved low-mass stars.

Inversion techniques

A technique widely used for the Sun to overcome the limitations of standard equilibrium models is to perform seismic inversions. The main idea is to measure the differences between the frequencies of a reference standard model and the observed ones in order to correct the structure of the reference model. This technique as the advantage to not be based on restrictive hypotheses on stellar physics. It produces a corrected model outside the reach of standard modelling. However, to obtain the detailed density or sound-speed profile of a star (like it was done for the Sun) it requires a huge number of frequencies measured with a very high precision. Given observation limitations for other stars, the current outcomes of inversions on other solar-like stars mainly concern global quantities, such as the mean density (Reese et al. 2012), the acoustic radius and evolutionary stages indicators (Buldgen et al. 2015a) and an indicator of mixing processes (Buldgen et al. 2015b). The estimation of a star inner rotation profile can however be obtained by inversion techniques (Deheuvels et al. 2014) since for rotation we have additional information brought by the frequency rotational splitting. This is particularly true for evolved low-mass stars, for which the difference between the rotational splitting of g-dominated mixed-modes and p-dominated ones gives a direct information on the difference of the rotation rate between the core and the envelope of the star.

Part II

New results on the energetic properties of solar-like oscillations

Chapter 4

Models and methods for computing theoretical power spectra

In this chapter, I present the models and methods I used to compute the different properties of solar-like oscillations and theoretical power spectra.
The general theories of stellar structure, evolution and oscillations have been presented in Chaps. 2 and 3. Thus, this chapter details the practical path we follow for the computation of a theoretical power spectrum, as schemed on Fig. 4.1. Particular attention will be paid to red giants structure and oscillation spectra.
The first step (Sect. 4.1) is the obtaining of the equilibrium structure of stellar models with an evolutionary code. A particular attention has also to be put on the precise computation of some specific features of red-giant models (such as numerical noise, discontinuities, ...).
Once the equilibrium model is obtained, we can compute the oscillation properties (frequencies, damping rates, inertias,...) thanks to an oscillation code. Our non-adiabatic oscillation code uses an non-local, time-dependent treatment of the convection. These formalisms (see Sects. 3.2 and 3.3) require to choose between different assumptions and to fix some free parameters. The effects of these assumptions and parameters will be discussed in Chap 5. I give in Sect. 4.2 the standard choices made for the oscillation computations presented in the next chapters. Since the main free parameter of the TDC treatment is the complex β parameter (see Eq. 3.117), which affects a lot the theoretical predictions, I detail in Sect. 4.3 the procedure adopted to constrain this parameter.
After having obtained the equilibrium model and the non-adiabatic oscillation properties, we use a stochastic excitation code to determine the power injected into the modes by the turbulence. This will be described in Sect 4.4.
Finally, mode frequencies, lifetimes, and powers will be combined to obtain mode amplitudes and the theoretical power spectrum. In this last procedure, we have to take into account the duration of observations to account for the resolution of the modes and the heights of the corresponding peaks in the power spectrum.

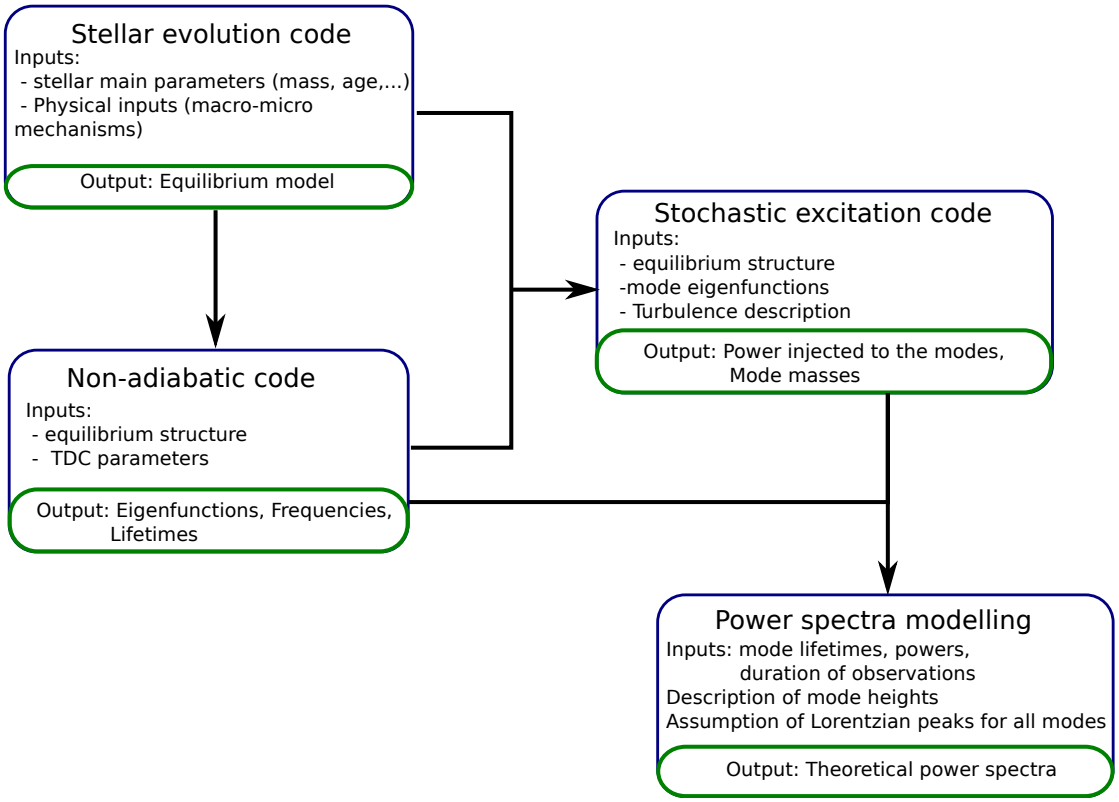

Figure 4.1: Scheme of the computation process to obtain a theoretical power spectrum.

4.1 Equilibrium models

I provide in this section the main physical ingredients we used to compute our models with two evolutionary codes. In both cases, we do no take into account rotation and magnetic field. I then discuss some difficulties encountered in the computation of red-giant equilibrium models especially for asteroseismic use in Sect. 4.1.2.

4.1.1 The stellar evolutionary codes

ATON

We used the ATON code (Ventura et al. 2008) for red-giant branch (hereafter RGB) and helium burning models. This code is able to evolve a model through the helium flash. Mass loss on the RGB is not taken into account. The convection is described by the classical mixing-length theory (see Sect. 2.4). The radiative opacities come from OPAL (Iglesias, Rogers 1996) for the metal mixture of Grevesse, Noels (1993) completed with Alexander, Ferguson (1994) at low temperatures. The conductive opacities correspond to the Potekhin et al. (1999) treatment corrected following the improvement of the treatment of the e-e scattering contribution (Cassisi et al. 2007). Thermodynamic quantities are derived from OPAL (Rogers, Nayfonov 2002), Saumon et al. (1995) for the pressure ionisation regime and Stolzmann, Bloecker (1996) treatment for the He/C/O mixtures. Finally, the nuclear cross-sections are from NACRE compilation (Angulo et al. 1999), and the surface boundary conditions are provided by a grey atmosphere following the treatment by Henyey et al. (1965).

CESTAM

The CESTAM code (Marques et al. 2013) has also been used to study models from the main sequence phase to the bottom of the red-giant branch.
The convection is also described by the classical mixing-length theory. Our models are computed with the OPAL05 equation of state (Rogers, Nayfonov 2002) and OPAL96 radiative opacities (Iglesias, Rogers 1996) completed with Ferguson et al. (2005) at low temperatures. The metal mixture can be chosen between GN93, AGN05 and AGSS09 (see the paragraph on the chemical composition in Sect. 2.2.2). The nuclear reaction rates are from NACRE compilation (Angulo et al. 1999) with the revised LUNA rate (Formicola et al. 2004) for the $^{14}N(p,\gamma)^{15}O$ reaction. When a convective core appears during the main sequence, it is possible to consider overshooting. The core overshoot distance is given by $l_{\rm ov} = \alpha_{\rm ov} \times \min(R_{\rm cc}, H_P)$ with $\alpha_{\rm ov}$ a free parameter ($R_{\rm cc}$ the radius of the convective core and H_P the pressure scale height). We can also include convective penetration ("undershooting" below the convective envelope) following the model of Zahn (1991) in which the distance of convective penetration L_p is given by $L_p = \zeta_{\rm pc}/\chi_P H_P$, where $\zeta_{\rm pc}$ is a free parameter and χ_P the adiabatic derivative of the radiative conductivity with respect to the pressure. The surface boundary conditions are provided with an Eddington's grey atmosphere.

Turbulent pressure

As presented in Sect. 3.2, an estimate of the turbulent pressure is needed to compute the damping rates, but it is not generally included in stellar evolutionary codes. The equilibrium value of the turbulent pressure is thus included a-posteriori in the equilibrium models (Eq. 3.74) without modifying the hydrostatic equilibrium (this leads to a small inconsistency in the equation of state).

4.1.2 Specificities of red-giant equilibrium models

I will discuss here two particularities of red-giant models that impact oscillation computations.

Discontinuities

Due to the evolution of convective zones inside the star, discontinuities of the chemical composition or of the density can appear in red-giant models. It is necessary to give a specific attention to such features when addressing numerical aspects because oscillation computations are very sensitive to such rapid variations of physical quantities. Moreover discontinuities are problematic when computing numerical derivatives. Solving differential equations (such as the oscillation equations) needs to account for the presence of these discontinuities.
In practice, we use a double mesch point at each discontinuity (marked by its position at the radius r_d). Physical quantities (X) are splitted between values under and above the discontinuity. Thus, at the discontinuity, the considered physical quantities have two distinct values: $X_{\rm under}(r_d)$ and $X_{\rm above}(r_d)$. Interpolation is then made separately for each side of the discontinuity (it prevents from adding points inside the discontinuity). Finally, the solution of the oscillation equations are obtained by ensuring the continuity of the Lagrangian perturbations of pressure, gravitational potential and its gradient (see also Reese et al. 2014).
These discontinuities play an important role in mixed-modes trapping. The amplitudes of the eigenfunctions at each side of the discontinuities strongly change from one mode to another.
In the different red-giant models studied, we have spotted up to three discontinuities. The first one is located at the upper limit of the convective core in horizontal-branch stars; the others are linked to chemical composition discontinuities (of hydrogen and helium) that can appear in any red-giant models.

Brunt-Vaisälä frequency

The second point requiring a particular attention is the computation of the Brunt-Vaisälä frequency. Since the Brunt-Vaisälä frequency controls the behaviour of mixed-modes, we have to ensure that it has been computed with high enough precision, especially in the central layers. Usually, numerical derivatives of the density (as it appears in Eq. 3.39) are subject to numerical noise while temperature and pressure gradients are computed more carefully. Thus, we use in the central, homogeneous ($\nabla\mu = 0$) layers of red-giant models the expression given by (see the detailed derivation in e.g. Kippenhahn et al. 2012)

$$N^2 = \frac{-g}{QH_P}(\nabla_{\rm ad} - \nabla) \tag{4.1}$$

where Q is defined by the equation of state (Eq. 2.34).

4.2 Non-adiabatic computations

Non-adiabatic oscillation computations are made with the non-adiabatic code developed by M.A. Dupret (Dupret 2001) including a non-local, time-dependent treatment of the convection (see Sects. 3.2 and 3.3).

4.2.1 Non-local, time-dependent treatment of convection

Except when specified, we use the following parameters for the treatment of the convection-oscillations interaction. The effects of changes of these parameters on theoretical damping rates will be discussed in Chap. 5 for main-sequence stars and in Chap. 6 for RGB stars.
The non-local parameters (Eq. 3.127) are those derived by Dupret et al. (2006a) from a 3D solar simulation ($a = 10$ and $b = 3$ with Balmforth (1992b) notations). We assume an isotropic turbulence ($A = 1/2$ and $\Lambda = 8/3$ in Eq. 3.105). For the perturbation of the mixing-length, we choose to model it by using Eq. 3.125. In the interaction between convection and oscillations, we take into account the perturbation of the turbulent pressure as well as the dissipation of kinetic energy into heat (see Sect. 3.2.7).
The main uncertainty in the TDC treatment comes from the closure approximation made for the closure term in the perturbation of the energy equation. This is represented by the free parameter β in Eq. 3.90. To adjust this parameter we follow Belkacem et al. (2012a) who proposed to constrain it in such a way that the radial mode damping rates present a plateau at the frequency of maximum power $\nu_{\rm max}$ given by the scaling relation 3.160. The existence of such a plateau is well known in solar observations and is also detected in other solar-like oscillators (Appourchaux et al. 2014). It is linked with the existence of a maximum in the power spectrum (Belkacem et al. 2012a). In this procedure we assume that the canonical scaling relation for $\nu_{\rm max}$ is valid. However, we know this relation is incomplete because, for example, the dependence to the Mach number is missing. Nevertheless, for red-giant stars, the dependence of $\nu_{\rm max}$ to the surface gravity dominates, making the variation of the Mach number disappears during the evolution on the red-giant branch (see Belkacem et al. 2013). I have also noted that in all the models computed during my thesis, the maximum in the theoretical power spectrum always appears around the plateau of the damping rates or equivalently around the frequency of the minimum of the product of the damping rate by the inertia (Belkacem et al. 2011). From a practical and numerical point of view, looking at a minimum of ηI is easier than searching a plateau of η. Since this parameter has a very strong impact on theoretical damping rates, I detailed how we fix its value in Sect. 4.3.

4.2.2 Specificities of mixed-modes in red giants

I have already mentioned in Sect. 4.1.2 the issue of discontinuities in red giants equilibrium models and how we solved it for oscillation computations. We also take care of the precise computation of the Brunt-Vaisälä frequency in the equilibrium models. Two additional numerical difficulties are present in the computations of mixed-mode properties, linked to the computation of the work integral in the core of the star and to the high density of mixed-modes in red giants (the very high number of g-dominated mixed-modes in a small frequency interval between two p-dominated modes).
The computation of the work integral of the modes in a red-giant core presents some numerical difficulties due to the very high number of nodes of the eigenfunctions in the g-cavity. However, this high number of nodes allows us to use an asymptotic formulation for the radiative damping described by Eq. 3.65.

Mixed-modes density

Another significant difficulty arises from the high density of non-radial modes over a large separation. It leads to modes with very close angular frequencies (real part of mode eigenvalues) but with very different damping rates (imaginary part of the eigenvalues). The algorithm solving the non-adiabatic equations searches the eigenvalues by the inverse iteration method. Thus, it converges towards the closest eigenvalue to the initial guess in the complex plane. Using only the adiabatic frequency (obtained in a previous step) as an initial guess for the real part of the eigenvalue, the convergence to the correct mode (i.e. the one with the frequency and trapping corresponding to the adiabatic case) of the algorithm is not easily ensured. Initial adiabatic frequencies of different modes could lead to the same eigenvalue in the non-adiabatic algorithm. As a remedy, we have to find an initial guess for the imaginary part of the frequency to be sure to obtain all the modes with different trappings. To do this, we use the inertia ratio between radial and non-radial modes derived from previous adiabatic computations. We scale the initial guess for the imaginary part (noted $\Im$) of the eigenvalues to the damping rates of radial modes with this inertia ratio:

$$\Im(\sigma)_{\text{guess},\ell} = \Im(\sigma)_{\ell=0} \frac{I_{\ell=0,\text{ad}}}{I_{\ell,\text{ad}}} \tag{4.2}$$

Without radiative damping (i.e. neglecting the work in the radiative core), this choice gives a very good approximation of the non-radial damping rates (see Eq. 3.63, since the work integral in the envelope does not depend on the angular degree and trapping). In the presence of radiative damping, our initial guess underestimate the true value of $\Im(\sigma)_\ell$. However, it allows us to reproduce the damping rates of p-dominated modes and modes closed to these ones when the radiative damping is small. These, are the modes which are the most difficult to obtain with the inverse iteration method.

4.3 Constraining the main TDC parameter β

We have explained in Sect. 3.2.3 that the β parameter has originally been introduced to avoid the occurrence of non-physical short-wavelength spatial oscillations in the eigenfunctions, in particular for luminosity variations (Grigahcène et al. 2005). Such oscillations are easily visible when looking at the work integral of a mode (see Fig. 4.3) which is directly linked to luminosity variations (see Eq. 3.126). Thus, to restrain the range of acceptable values for β we choose to introduce the quantity C_W allowing us to estimate the presence and importance of these spurious oscillations. We define it as:

$$C_W = \left| \frac{\int dW}{\int |dW|} \right|, \tag{4.3}$$

where W is the work and the integrals are made over the whole stellar radius. This quantity is close to 1 in the absence of non-physical oscillations. Indeed, for any function $f(x)$, we have $\left|\int f\ dx / \int |f|\ dx\right| \ll 1$ when f presents a lot of oscillations around 0. The absolute value is here to also take into account the case of a negative work integral (i.e. unstable mode) to have a clear view on which values of β in the complex plane lead to non-physical oscillations. Fig 4.3 represents typical work integrals near the surface of a red-giant model for different values of this quantity (obtained with different values of β). The lower C_W, the more the work present short wavelength oscillations around 0.

As discussed in the previous chapter, solar-like oscillations are damped. Thus, starting from the acceptable values of β obtained with the first criterium, we can exclude all values leading to a

negative work integral. Moreover, observations of solar-like oscillations across the HR diagram show a limited range of linewidths for radial modes (see e.g. Fig. 2 of Belkacem et al. 2012). We thus restrain our search to values of β giving a linewidth of radial modes of the order of the observed ones (e.g. following the scaling relation given in Eq. 3.163).
Finally, we also want to obtain a frequency of maximum power in our theoretical power spectrum in agreement with the observed $\nu_{\max}$. We adopt here the strategy proposed by Belkacem et al. (2012) which consists in searching values of β for which the theoretical damping rates present a plateau around $\nu_{\max}$ obtained by the scaling relation given in Eq. 3.160. Searching a plateau of the damping rates is equivalent to search a (local) minimum of the product between the damping rates and the inertia (Belkacem et al. 2011). A minimum of ηI corresponds to a maximum in the power spectrum. A minimum being easier to find in an automatic way, we have adjusted the code to search, for each value of the β parameter, the minimum interpolated value of ηI for mode frequencies in the range $[\nu_{\max} - 5\Delta\nu; \nu_{\max} + 5\Delta\nu]$ (which corresponds to the typical frequency range of observed solar-like oscillations). We select as good values of β, the ones giving the frequency of the minimum at $\nu_{\max} \pm 0.5\Delta\nu$ (thus we take into account scattering and uncertainties in the $\nu_{\max}$ scaling relation).

These constraints allow us to strongly reduce the range(s) of acceptable values of β for each stellar model. As an example, we present in Figs. 4.3, 4.4 and 4.5 maps of each criterion obtained for a scan of values of the complex parameter $\beta \in [-2; 0] \times [-2; 0]$ with a 0.01 step for a $1.5 M_{\odot}$ red giant model (model A in Tab. 6.1). From these maps, we see that to select the good value of β we have to find a compromise between the above criteria. Thus, our choice of β is first made by ensuring that a minimum of ηI is close to the predicted $\nu_{\max}$. To obtain long lifetimes, we have to take values of β with lower C_W, i.e. with more short wavelength oscillations (see Figs. 4.3 and 4.4, zones of higher lifetimes are obtained in zones of lower C_W). This represents the main compromise that we have to make. It appears that a value of $C_W \sim 5.10^{-2}$ (see Fig. 4.3) is a good compromise allowing us to have almost no short-wavelength oscillations and lifetimes of the order of the observed ones.
For this model, $C_W \sim 5.10^{-2}$ is obtained in the orange regions in Fig. 4.3. This region corresponds to lifetimes around 10 days (Fig. 4.4, dark red regions). The corresponding regions of these two criteria do not overlap completely and thus reduce the range of acceptable values of β. They have to be compared with the regions giving a minimum of ηI around the frequency of maximum power obtained from scaling relation (in green in Fig. 4.5). Finally, we obtain a large region of acceptable values of β around $\beta = -1.7 - 0.7i$. and few much smaller regions (as example for $\beta = -0.106 - 0.945i$, corresponding to the little circular region in Figs 4.3 and 4.4) where the criterion for $\nu_{\max}$ is much more sensitive to the value of β. The impact of these two values of β, taken as example, on a theoretical power spectrum will be discussed in Sect 6.3.2.

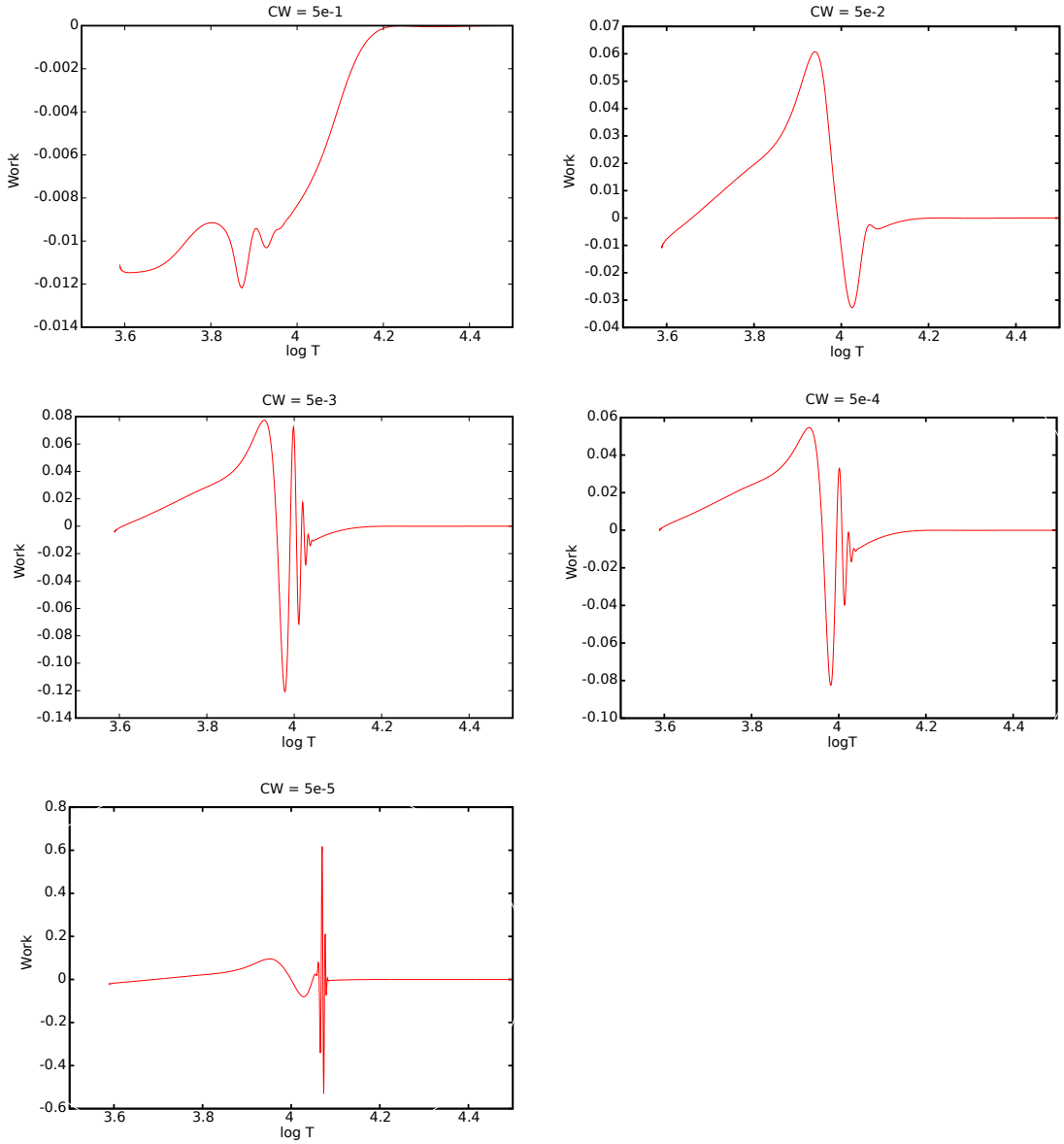

Figure 4.2: Typical work integral for different values of C_W for a radial mode in a RGB model.

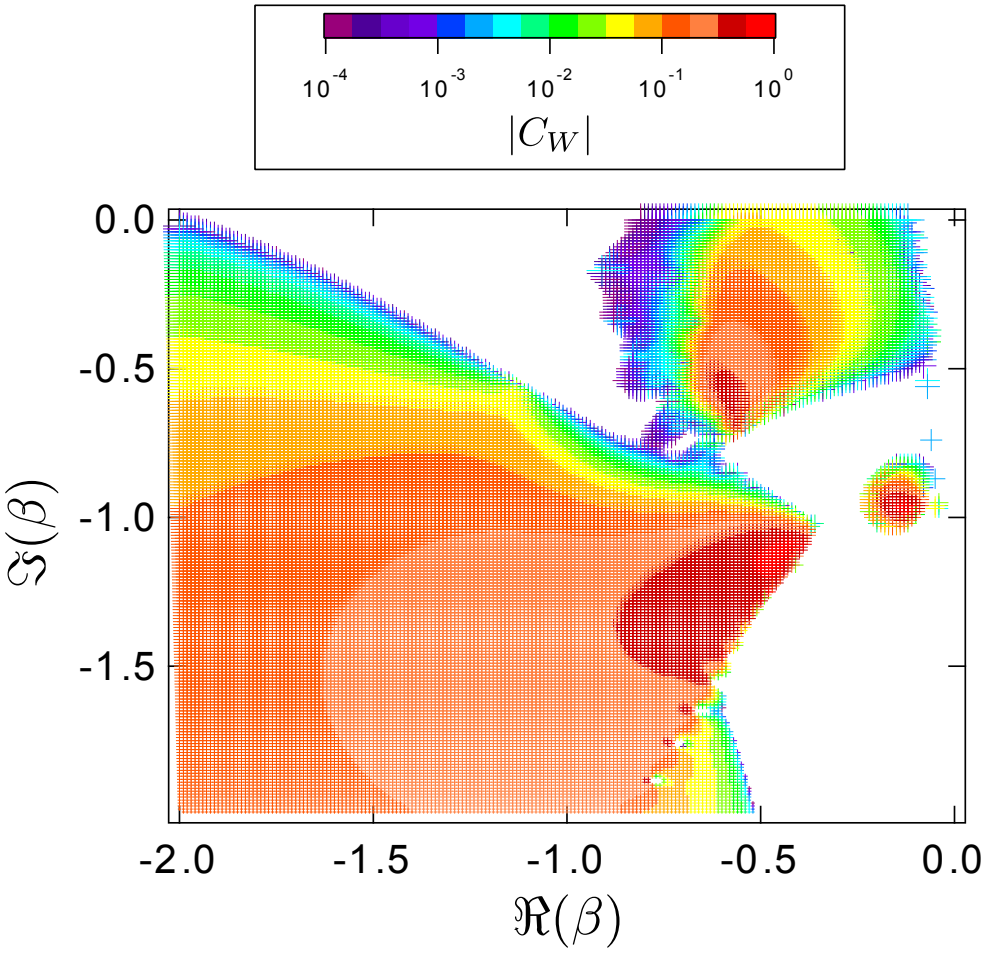

Figure 4.3: Spurious oscillations criterion C_W for a radial mode close to $\nu_{\max}$ as a function of β. Points leading to unstable oscillations are in white.

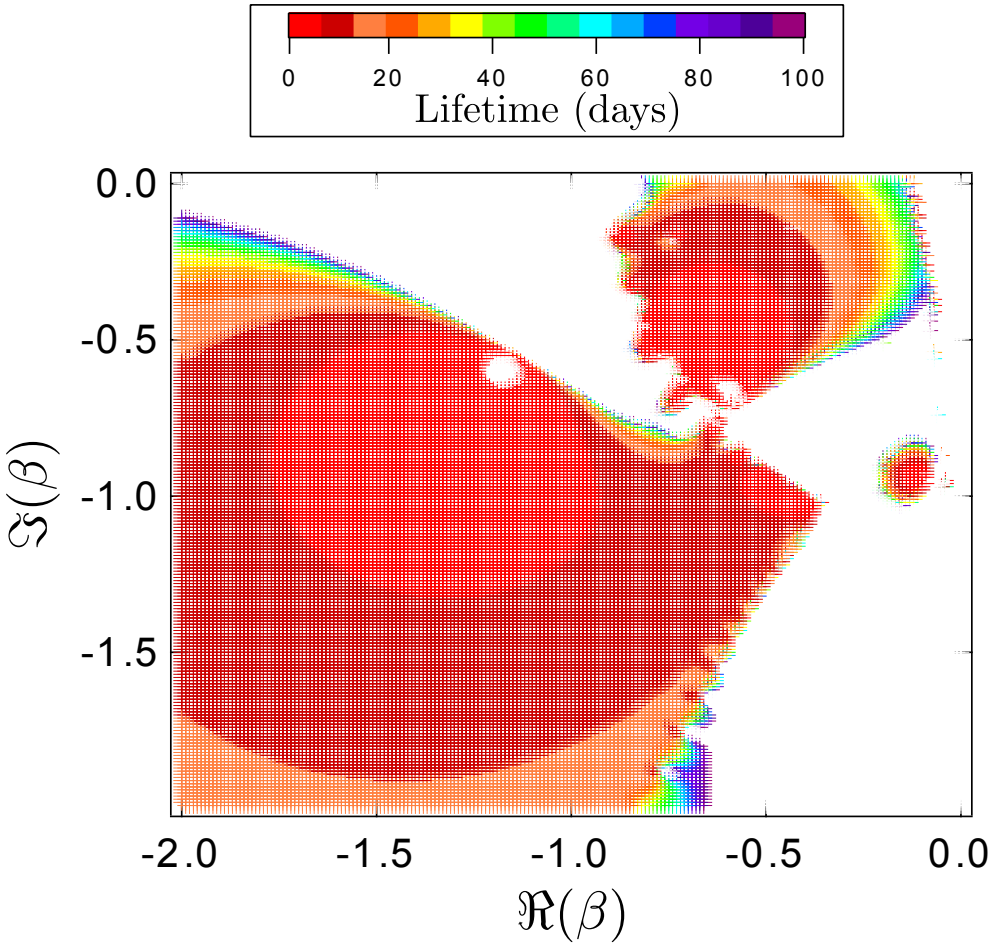

Figure 4.4: Lifetime of a radial mode close to $\nu_{\max}$ as a function of β. Points outside the colorscale are in white

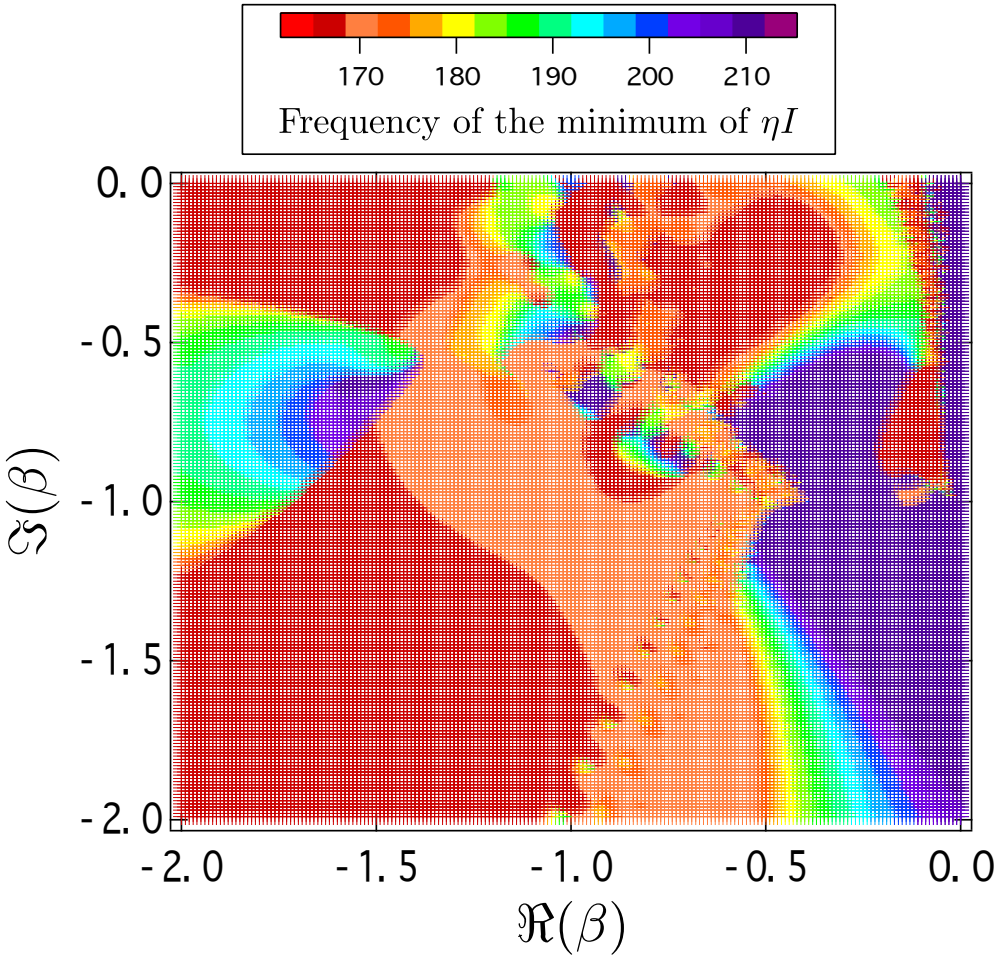

Figure 4.5: Position of the minimum of ηI as a function of β. For this model, we have $\nu_{\max} \simeq 190\ \mu Hz$ from scaling relations.

4.4 Stochastic excitation and peak properties in a power spectrum

4.4.1 Mode amplitudes

Mode amplitudes (Eq 3.138) are obtained using their damping rates (from the non-adiabatic oscillation computations), mode masses and the power injected into the modes by turbulence. This power is modelled with the stochastic excitation code developed by R. Samadi (Samadi, Goupil 2001), following the formalism presented in Sect. 3.4.2. We consider the turbulent Reynolds stress as the dominant driving source. We do not take the entropy contribution into account (thermal source of driving) for which a severe deficiency in the modelling with non-adiabatic eigenfunctions appears (as discussed in Samadi et al. 2013b).

The stochastic excitation code

We use solar parameters to describe the turbulence in the upper convective layers (constrained with a 3D hydrodynamics simulation by Samadi et al. 2003b). They found that the k dependency of the kinetic energy spectrum (k is the eddies wavenumber in the Fourrier space of turbulence) is best reproduced with the analytical Extended Kolmogorov Spectrum (EKS, Musielak et al. 1994). The eddy time-correlation function from 3D simulations seems to be almost Lorentzian. We use here a Lorentzian profile with a high frequency cut-off as prescribed by Belkacem et al. (2010) in order to also reproduce the observed solar low-frequency excitation rates. This is based on the sweeping assumption (see e.g. Kaneda et al. 1999) which consists in assuming that advection by energy-bearing eddies dominates in the inertial subrange (between the scale of energy-bearing eddies and the viscous dissipation scale in the turbulent cascade, where inertial effects dominate in front of viscous effects). The free parameter β_t introduced in the characteristic wavenumber of turbulence is assumed proportional to the pressure scale height (Samadi et al. 2008) and scaled to the solar value derived by Samadi et al. (2003b). The anisotropy parameter Φ (Eq. 3.156) is fixed at 2, in agreement with the Böhm-Vitense description of the MLT and with 3D solar simulations (Samadi et al. 2003b).

Mode velocity vs bolometric variations

The outcome of the stochastic excitation code gives the power injected by the turbulence into the modes in cgs units and consequently, the amplitude A of the oscillation is given in radial velocity (i.e. in cm/s) while observations in photometry gives bolometric intensity variations ($\delta L/L$ in ppm.) A bolometric corrections that considers the instrumental response of the $CoRoT$ space-borne telescope was originally proposed by Michel et al. (2009). Kjeldsen, Bedding (1995) proposed an intensity to velocity conversion factor but their approach is made in the adiabatic hypothesis. From our non-adiabatic code, a conversion factor from radial velocities to bolometric amplitudes can be obtained. When the non-adiabatic phase-lag is neglected, the intensity-velocity relation is given by:

$$\frac{\delta L}{L} = \frac{4 f_T - 2}{2\pi\omega R} A \tag{4.4}$$

with $f_T = \mid \delta T_{\rm eff}/T_{\rm eff} \mid / \mid \xi_r/R \mid$. Using non-adiabatic computations, Samadi et al. (2013b) proposed a scaling relation for the intensity-velocity relation. However, while they found theoretical velocities in agreement with observations, intensity variations presented systematic differences.

We thus decided to present our results in radial velocity because the conversion to bolometric intensity introduces additional uncertainties which have still to be understood.

Moreover, to make direct comparisons with observations, the visibilities of the modes should also be accounted for (i.e. for geometrical and limb-darkening effects). Ballot et al. (2011) have computed a grid of values for mode visibilities as a function of the effective temperature, surface gravity and metallicity in the range of the observed *Kepler* stars and considering the *Kepler* instrumental response. Mode visibilities will be used in the comparisons of our theoretical predictions with the observed power spectrum of a subgiant star in Chap. 7.

4.4.2 The shape of a mode peak

Lorentzian shape and temporal resolution

As discussed in Sect. 1.1.1, mode peaks in the solar power spectrum follow, when resolved, a Lorentzian shape (thus characterised by a frequency, a linewidth and an height). This is a direct consequence of the intrinsic damping the oscillations. When non-resolved, peaks follow a $\sin^2$ function.

The resolution criterion is the direct application of the Fourier theorem. To resolve a mode in an observed power spectrum, the observation time ($T_{\rm obs}$) needs to be greater than, in principle, two times the lifetime of the mode ($\tau = 1/\eta$). Actually, $T_{\rm obs} = 2\tau$ means that there is two observation points within the linewidth of the peak. Thus, in practice, $T_{\rm obs} \gtrsim 10\tau$ is required to clearly resolve a mode. In this case, one can measure the mode linewidth and hence obtain the observational value of the mode damping rate.

For sake of simplicity, we model all modes by Lorentzian profiles in ours theoretical power spectra. The parameters of the Lorentzian (the height H, the full-width at half maximum Γ and the frequency of the peak) and their link to the oscillation mode properties are presented in Fig. 4.6 and discussed hereafter.

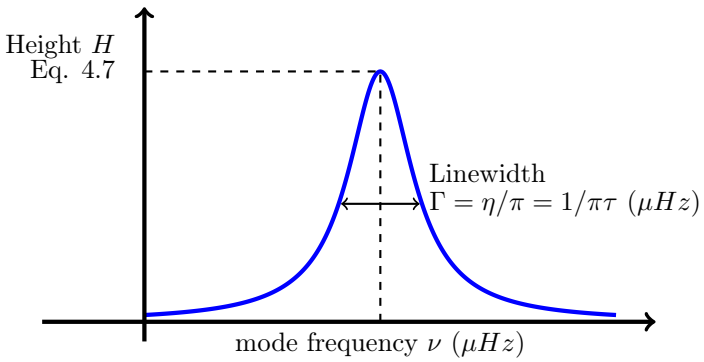

Figure 4.6: Lorentzian profile of a resolved solar-like oscillation mode. The area under the peak gives the amplitude of the mode.

Height of a mode

Assuming that a mode is resolved if its lifetime (τ) is much shorter than half the duration of observation, i.e. $\tau \ll T_{\rm obs}/2$, the height of this mode is given by (e.g. Lochard et al. 2005)

$$H = A^2(R)\tau, \tag{4.5}$$

and for unresolved modes $\tau \gg T_{\rm obs}/2$

$$H_\infty = A^2(R)T_{\rm obs}/2, \tag{4.6}$$

where $A(R)$ is the amplitude of the oscillation (given by Eq. 3.138), not including the disk integration factor. These formulae are strictly correct in the limit cases, when the lifetimes are much longer or shorter than the duration of observations. Both formulae give the same value for the height in $\tau = T_{\rm obs}/2$. If we use directly these two formulae (for $T_{\rm obs} \geq 2\tau$ and $T_{\rm obs} \leq 2\tau$) the resulting function $H(T_{\rm obs})$ present an angular point in $T_{\rm obs}/2$.

An alternative formulation for the heights of the modes have been proposed by Fletcher et al. (2006) (see also Chaplin et al. 2009a). It reads,

$$H = \frac{A^2(R)T_{\rm obs}}{T_{\rm obs}/\tau + 2}, \tag{4.7}$$

which tends to the same value of Eqs. 4.5 and 4.6 when $\tau \ll T_{\rm obs}/2$ and $\tau \gg T_{\rm obs}/2$, respectively, and interpolate the heights smoothly between these two extreme cases. The main difference between Eq. 4.7 and Eqs. 4.5, 4.6 concerns the region where the observation time is of the order of the mode lifetime. With Eq. 4.7 the height of the mode is only half its maximal height if $\tau = T_{\rm obs}/2$. More observational times is thus required to fully resolve a mode and, for it, to reach its maximal height. All our power spectra are computed using this latest description of the height (i.e. Eq. 4.7).

Before comparing observational and theoretical power spectra, it is worth mentioning that the relation between amplitudes and heights depends on whether we deal with a two-sided or a single-sided power spectrum. In the first case, the normalisation is such that the integral of the spectrum from $-\infty$ to $+\infty$ gives,

$$A = \sqrt{\pi\Gamma H}. \tag{4.8}$$

With a single-sided power spectrum we have

$$A = \sqrt{\pi\Gamma H/2}. \tag{4.9}$$

Here we consider a two-sided power spectrum, which is a different convention from the one used in Chaplin et al. (2009a).

Computation of theoretical power spectra

For sake of simplicity, we model all our theoretical power spectra with a Lorentzian for each mode (whether or not they are resolved). To have a clear view on the different types of modes, we have represented each mode individually in the power spectrum in the top panel of Fig. 4.4.2. A more realistic power spectrum is the result of the sum of the contributions of all the modes at a given frequency and is presented in the bottom panel of Fig. 4.4.2.

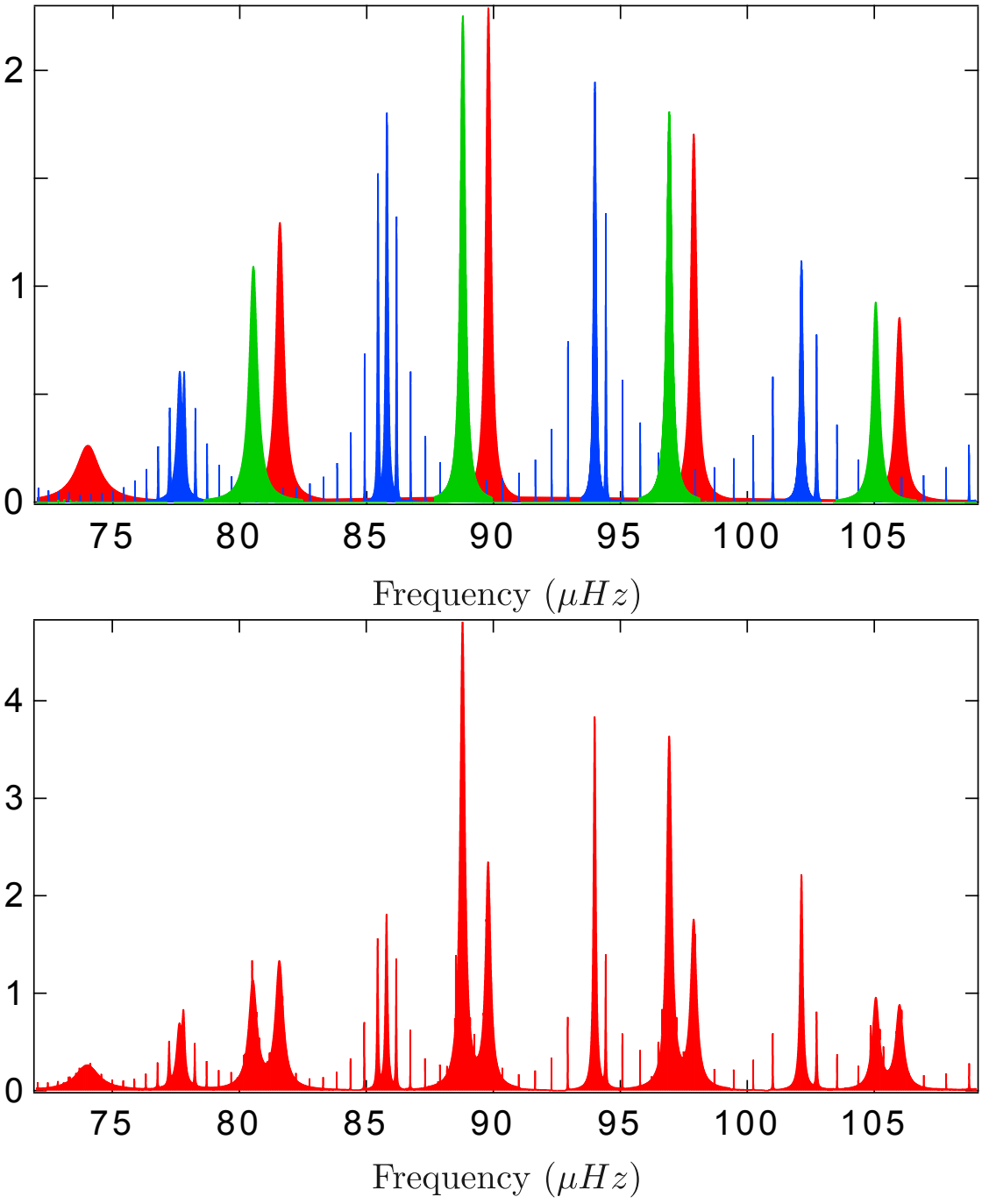

Figure 4.7: Theoretical power spectra obtained for a $1.5M_{\odot}$ RGB model assuming $T_{\rm obs} = 1$ year. **Top:** Each mode is represented individually. **Bottom:** Sum of the contribution of all the modes at a given frequency. The heights of the peaks are given in $(m/s)^2/\mu Hz$.

Chapter 5

Impact of the TDC treatment on main sequence linewidths

In this chapter, I discuss the effects of the time-dependent treatment of convection on the theoretical mode linewidths. The first section (Sect. 5.1) focus on the main parameter of the TDC treatment: the complex free parameter β. I will discuss its effect on mode linewidths and how it is constrained from observed linewidths. In the second section (Sect. 5.2), I present the effect of the other parameters and hypotheses of the TDC treatment on mode linewidths. This is necessary, since the tuning of the free parameter β is not enough to reproduce all the observations (as we will see in this chapter).

5.1 Constraints on the TDC β parameter

As shown in Sect. 4.3, the three criteria we use to constrain β (i.e. the absence of non-physical oscillations, the frequency of maximum power and the radial mode linewidth at this frequency) can provide a large zone of acceptable values for this parameter. However, small changes of β can lead to non negligible changes in the theoretical linewidths (e.g. in the position, values and shape of the plateau of the damping rates). To some extent, these changes can be predicted, following a local behaviour of the damping rates with β (see Sect. 5.1.1). Such local behaviour will help us to search for optimised value of β in order to reproduce the observed $\Gamma_{\rm max}$ - $T_{\rm eff}$ relation (in Sect. 5.1.2) and to fit the observed linewidths of *Kepler* main-sequence stars (in Sect. 5.1.3). The study of the local behaviour of the damping rate is necessary for an efficient search of optimised values of β. Indeed, given the non-linearity of the problem and the presence of local minima, automated search of an optimised value of β (e.g. with a merit function) could be not efficient enough and/or very time consuming.

5.1.1 Local behavior of the damping rates around the optimized value of β

By studying the effects of small changes of β in the area of acceptable values, it is possible to predict how the damping rates will change. It thus allows us to reduce the time spent in the search of β for various stellar models. Starting with a given β, the impact of changing β with a small step can be described (in most cases) as follows:

- Change of the real part of β (Fig. 5.1 left panel): a small increase of $\Re(\beta)$ shifts the position of the minimum of ηI toward higher frequencies and the damping rates around this minimum to higher values (the stability of these modes is increased).
- Change of the imaginary part of β (Fig. 5.1 right panel): a small increase of $\Im(\beta)$ tends to decrease the damping rates of the plateau (these modes become less stable) without change of the position of the minimum of ηI.

We note that the damping rates, away from the plateau, are just a bit affected by these changes of β. We have obtained these general trends in all the models studied during this thesis. We also note that the sensitivity of the damping rates to a modification of β depends on the evolutionary status of the model. Red-giant theoretical damping rates are more sensitive to β than the ones of main-sequence stars (see the effect of small changes of β on RGB lifetimes in Fig. 6.10).

With this local behaviour of the damping rates with β, we can finely adjust the shape of the plateau around $\nu_{\max}$. When the frequency of the plateau is obtained at the desired value (the value of $\nu_{\max}$ derived from the scaling relation) by adjusting the real part of β, we can adjust the value of the linewidth at $\nu_{\max}$ with the imaginary part of β by changing the depth of the plateau. These results also show the limit of theoretical computations. For a given frequency of the plateau, changes of β do not allow us to obtain a deep plateau with a high value of the damping rates (and reciprocally).

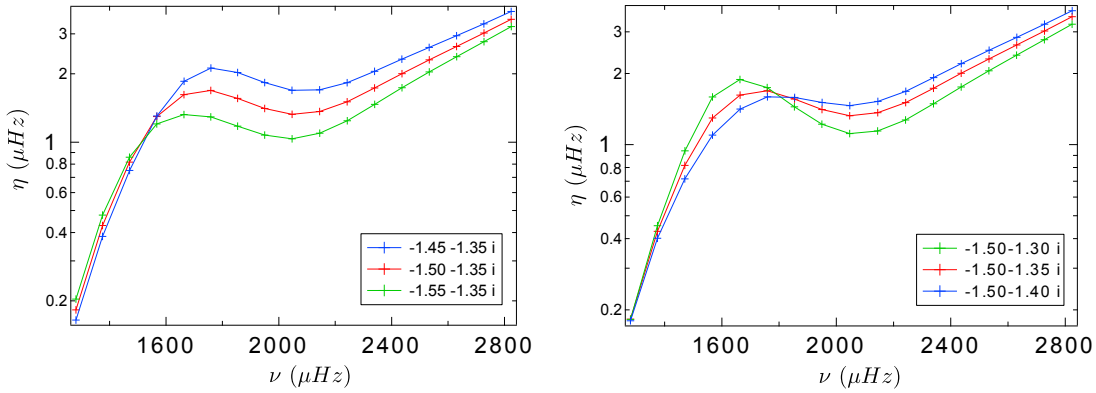

Figure 5.1: Effect of small changes of β on the damping rates of a main sequence model ($M = 1.2 M_{\odot}$, $\nu_{\max} \simeq 2004\ \mu Hz$). **Left:** change of the real part of β. **Right:** change of the imaginary part of β. Values of β are given in the legend.

5.1.2 The $\Gamma_{\max}$ - $T_{\rm eff}$ scaling relation

The effect of β (Sect. 5.1.1) on the damping rates shows that for a given $\nu_{\max}$ we can obtain a range of values for the damping rate at $\nu_{\max}$. To better constrain this parameter we thus need, at least, the value of the damping rate at $\nu_{\max}$. We have already mentioned (in Sect. 3.5.1) that this value follows a scaling relation with the effective temperature. This relation was deduced from CoRoT and *Kepler* observations (Baudin et al. 2011; Appourchaux et al. 2012) as reproduced in Fig. 5.2.

I have searched to reproduce this relation for stellar equilibrium models on evolutionary tracks. First, I searched, for models of $1M_{\odot}$, values of β that gave $\Gamma_{\max}$ around the observed ones (red circle on Fig. 5.2) for main-sequence and early subgiant stars. The resulting values of β are given in Fig. 5.3 and seem to follow two linear relations with $\nu_{\max}$ in the main-sequence and in the subgiant phase. To test the impact of the mass on theoretical linewidths and on the $\beta - \nu_{\max}$ relations, I have also searched values of β for a $1.2M_{\odot}$ evolutionary sequence laying in the observed linewidths range (green circles in Fig. 5.2). The values of β obtained do not follow the relation found for the $1M_{\odot}$ sequence in the $\beta - \nu_{\max}$ plane. Nonetheless, they still follow a tight relation between β and $\nu_{\max}$ (see Fig. 5.3) so it is again possible to find good values of β for additional models on this sequence by extrapolation from the β obtained for the first models of the corresponding evolutionary phase.

We see in Fig. 5.2 that we have been able to reproduce the typical observed linewidths of main-sequence and subgiant stars adjusting only β. The situation is a little more complex for red-giant stars (see Sect. 6.3.2). The dispersion of the linewidths in this figure is linked to the evolutionary stage and the mass of the stars.
From these results (see Fig. 5.3), we see that it does not seem to exist a simple formula that can give directly an optimised value of β. However, for a given evolutionary phase, it is possible to extrapolate values of β on an evolutionary sequence. It will be interesting to extend this study to other masses and to test the impact of other stellar parameters (such as the metallicity, ...) in order to see if it is possible to obtain a grid of values of β which could be used in future theoretical computations. Such computations may also help us to better understand the physics hidden behind this free parameter.
Finally, adjusting only β is a valid approach for studying large samples of main-sequence and subgiant stars since it allows us to reproduce the $\Gamma_{\max} - T_{\rm eff}$ scaling relation. In these evolutionary stages, we can also use some $\beta - \nu_{\max}$ relations to study a given evolutionary sequence. For the study of specific stars for which the linewidths of all observed modes are available, we have to search more carefully the optimised value of β (and maybe of other TDC parameters) in order to reproduce the observations. This will be discussed in the next sections.

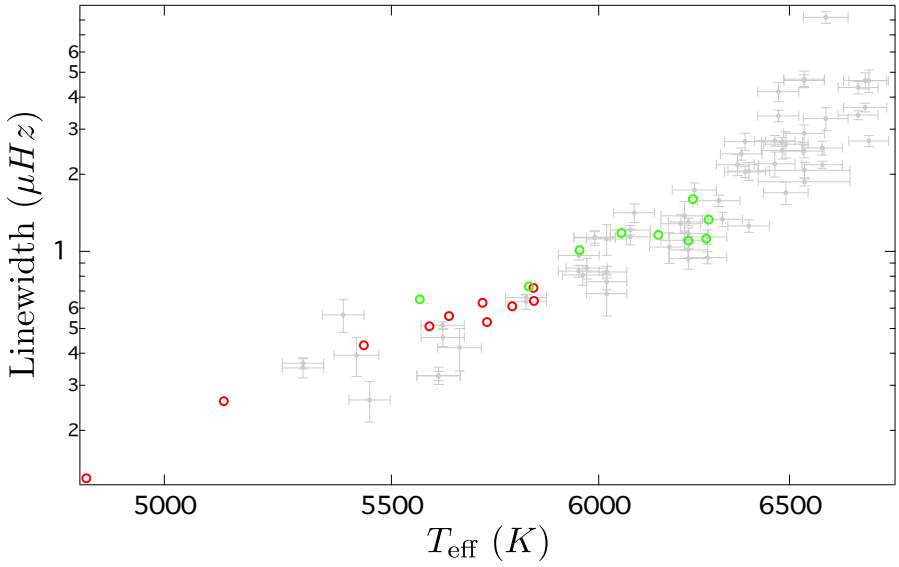

Figure 5.2: Theoretical linewidth for $1M_{\odot}$ (red) and $1.2M_{\odot}$ (green), MS to RGB stars. Observed linewidths from Appourchaux et al. (2012).

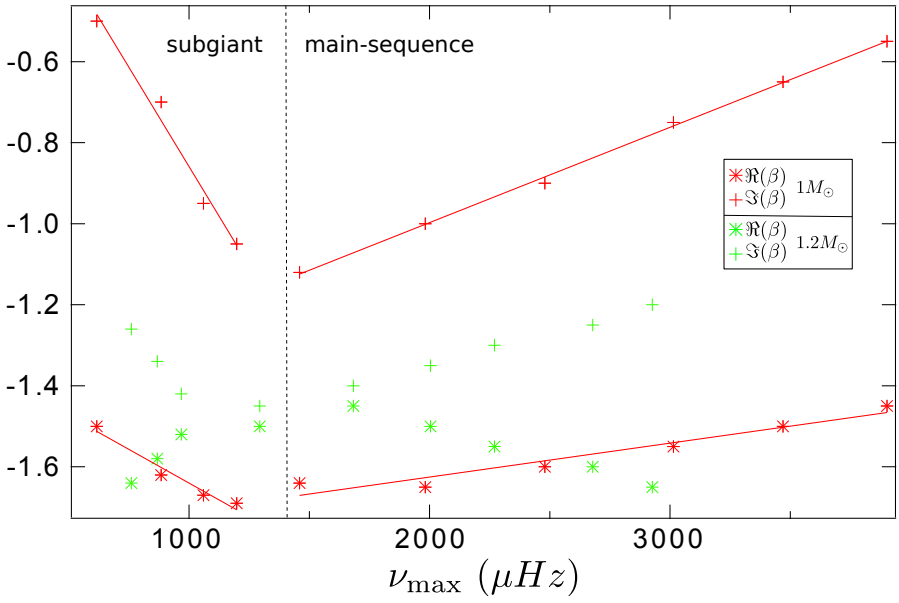

Figure 5.3: Values of the real part and imaginary part of β found for models of $1M_{\odot}$ (in red) and $1.2M_{\odot}$ (in green). Red lines indicate the fits obtained for the $1M_{\odot}$ models in the main-sequence and in the subgiant phase.

5.1.3 Fit of four *Kepler* main-sequence star linewidths

In Sect. 5.1.2, the only constraint for the search of the optimised value of β was the typical linewidth of the radial mode at $\nu_{\max}$. In this section, we search optimised value of β when more constraints are available. Our goal is to make a quantitative comparison between theoretical and observed linewidths in order to test and constrain even more the TDC treatment.
Appourchaux et al. (2012, 2014) have measured the linewidths of radial modes for various main sequence stars observed by *Kepler*. The equilibrium structure of some of these stars have been modelled by S. Deheuvels (private communication). The main parameters of the equilibrium models of these stars, as well as, the values of β are listed in Tab. 5.1. We present here the results of our search of β to fit the observed linewidths of four of these stars. Since we have not only the value of the linewidth around $\nu_{\max}$ but also the shape of the plateau, the optimised value of β is much more constrained that it was in Sect. 5.1.2.

The theoretical and observed linewidths are presented in Fig. 5.4. We see that, adjusting only β, we have been able to reproduce pretty well the observed linewidths. Differences between theoretical and observed linewidths can appear away from $\nu_{\max}$. Smaller error bars, as well as more values of observed linewidths at lower frequencies should give us a more precise view on these differences. For KIC 8694723, discrepancies between observed and theoretical linewidths appear. The reason of such differences is still unclear and an extended study, with a larger sample of stars is needed. We could only note that this star is the less metallic and the one with the lower $\nu_{\max}$ of the four studied stars. Such study could also allow us to investigate which stellar characteristic and/or physical process could be at the origin of this difficulty in the modelling of these linewidths. This would give us more insight on the interaction between convection and oscillations.

Even with all these constraints, and a precise search of an optimised value of β, the observed linewidths are not perfectly reproduced by our theoretical computations. We will thus test the effects of others TDC parameters on theoretical linewidths in the next section.

KIC number	Mass ($M_\odot$)	Radius ($R_\odot$)	$T_{\rm eff}(K)$	$\log L/L_\odot$	Z/X	$\nu_{\rm max}(\mu Hz)$	β
6116048	1.06	1.2392	6030.2	0.2606	0.015	2062	$-1.75 - 1.18i$
8694723	1.12	1.5154	6488.5	0.5626	0.008	1402	$-1.79 - 1.98i$
9139151	1.06	1.1145	6114.2	0.1926	0.025	2519	$-1.64 - 1.25i$
10454113	1.22	1.2628	6141.0	0.3087	0.018	2268	$-1.55 - 1.25i$

Table 5.1: Models parameters of 4 MS Kepler stars

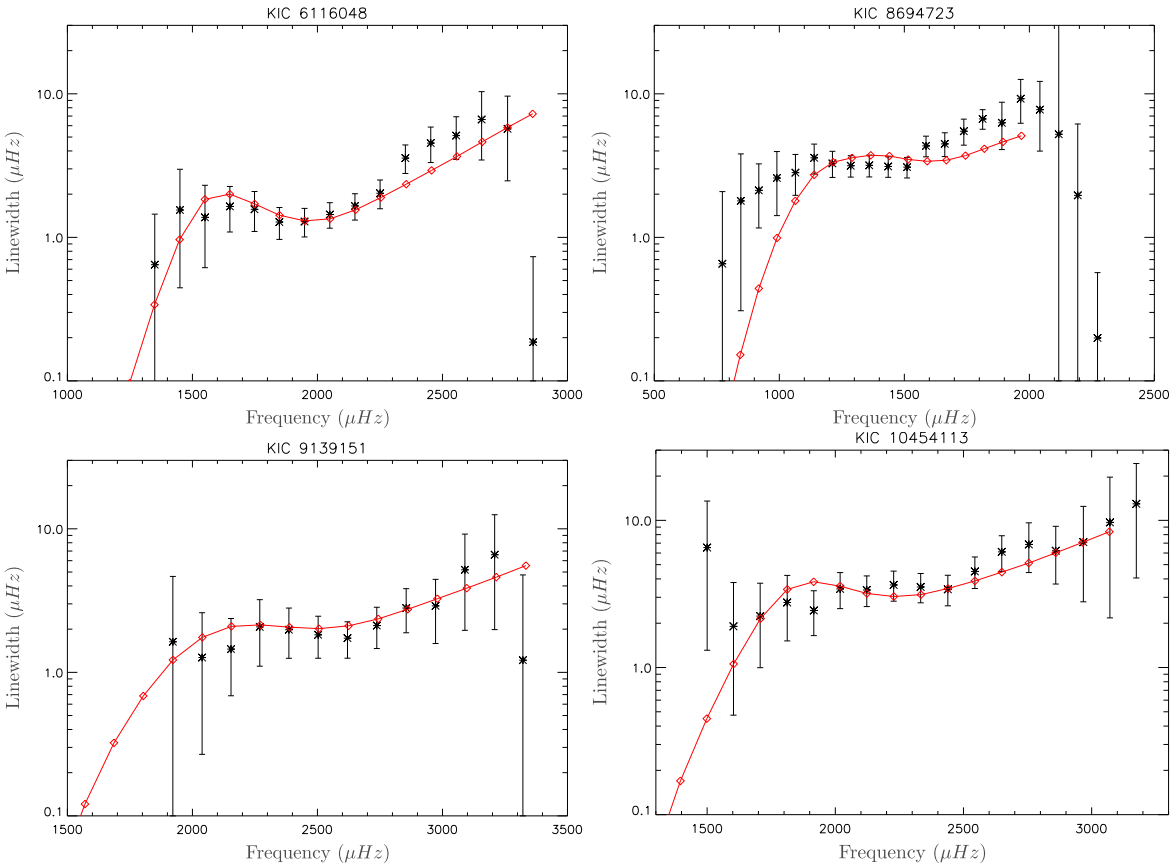

Figure 5.4: Observed and theoretical linewidths for 4 *Kepler* main-sequence stars. The characteristc of the equilibrium models are given in Tab. 5.1. The theoretical linewidths are fitted to the observed ones by adjusting the free complex parameter β.

5.2 Additional changes in the TDC parameters and hypothesis

Based on the results obtain for the MS *Kepler* star KIC 9139151 in the previous section, I have performed tests on the impact of the other parameters and hypotheses involved in the treatment of the interaction between convection and oscillations. This will allow us to determine, beside β, which TDC hypotheses can have an impact on the theoretical linewidths and if observational constraints can help us to discriminate between different hypotheses; and to better understand some physical processes and the proper way to model them.

5.2.1 Non-local parameters

As seen in Sect. 4.2, our non-adiabatic code uses a non-local treatment of the convection with two parameters a and b (linked respectively to the description of the convective flux and of the turbulent pressure, see Eq. 3.127). By default those parameters are obtained from a 3D solar simulation as performed by Dupret et al. (2006a). In this section, I test the impact of a change of these parameters. Hydrodynamic simulations for solar-like and red-giant stars seem to favour an almost constant value of b (R. Samadi, private communication). We thus test the impact of a change of a and then of a change of both a and b. The tests are performed by doubling the default value for these parameters (i.e. tending to a more local description).

When changing the non-local parameters a and b, we have to find a new value for β. The one obtain in Sect. 5.1.3 does not allow us to reproduce a plateau of the damping rates at $\nu_{\max}$ and can even lead to unstable modes. The new values of β found are far from the original ones. They allow us to obtain a minimum of ηI around $\nu_{\max}$ but the eigenfunctions of the modes present non-physical short-wavelength spatial oscillations (C_W is smaller than the original one). The resulting linewidhts are presented in Fig. 5.5.

These results show the important effect of the non-local parameters on theoretical linewidths and eigenfunctions. When we double only a (Fig. 5.5, top panel), we tend to a more local description of the convective flux while not changing the description of the turbulent pressure. Even with the change of β the theoretical linewidths do not reproduce correctly the observed ones. They are globally smaller than the observed ones. When we double both a and b (Fig. 5.5, bottom panel), we find smaller linewidths away from $\nu_{\max}$, but in good agreement with the observed ones.

This shows the importance of the ratio between these two parameters for theoretical linewidths. However, these more local descriptions also lead to more spurious oscillations in the eigenfunctions and thus strengthen the use of the values of a and b derived from 3D simulations (i.e. $a = 10$ and $b = 3$).

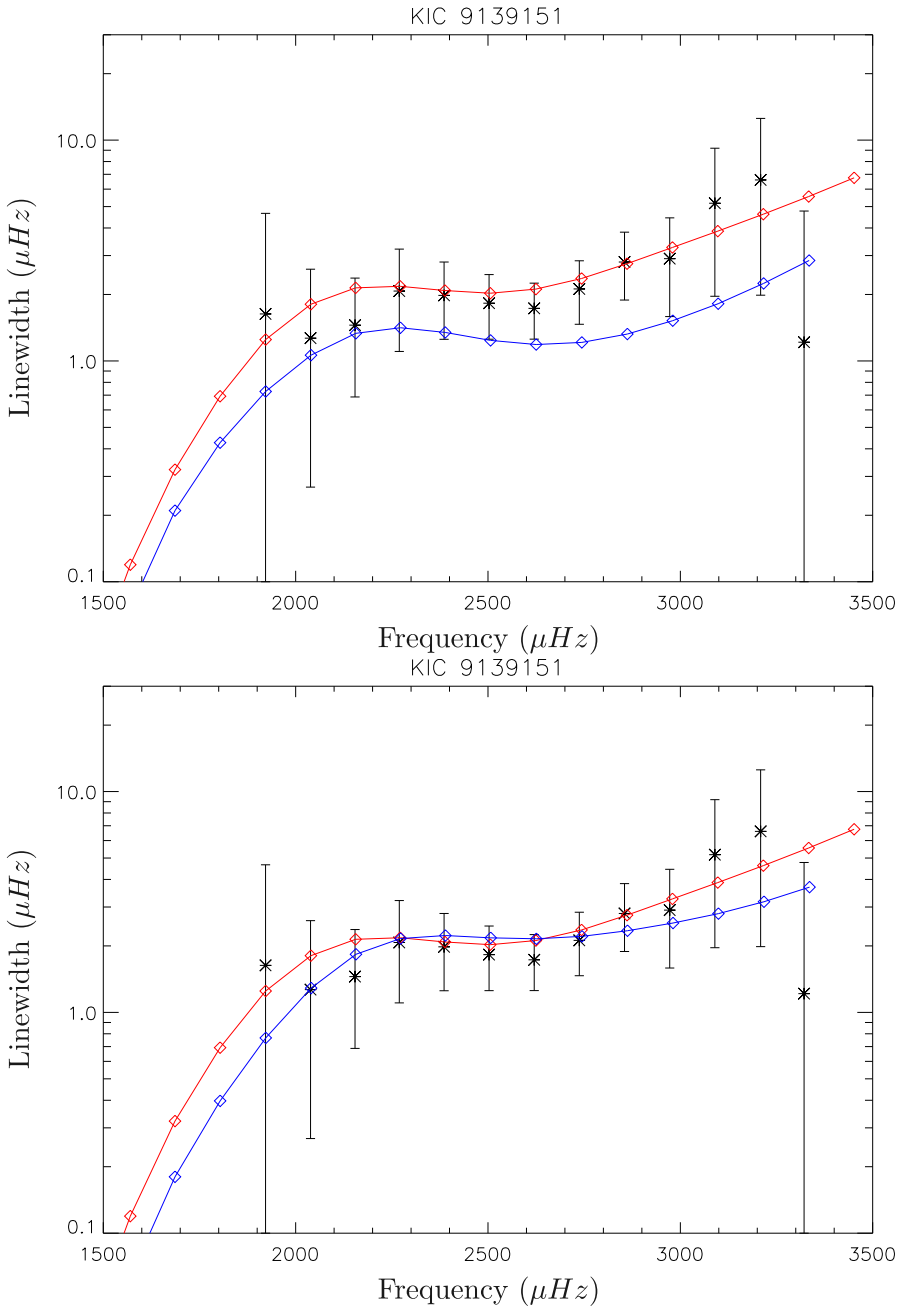

Figure 5.5: Theoretical linewidths for KIC 913915. Red curves correspond to $a = 10$,$b = 3$ (corresponding to the results presented in Sect. 5.1.3). The blue curves are obtained by varying the non-local parameters.
Top: $a = 20$, $b = 3$, $\beta = -2.60 - 0.80i$ gives $C_W = 1.5 \cdot 10^{-2}$ at $\nu_{\max}$
Bottom: $a = 20$, $b = 6$, $\beta = -2.50 - 0.80i$ gives $C_W = 1.9 \cdot 10^{-2}$ at $\nu_{\max}$

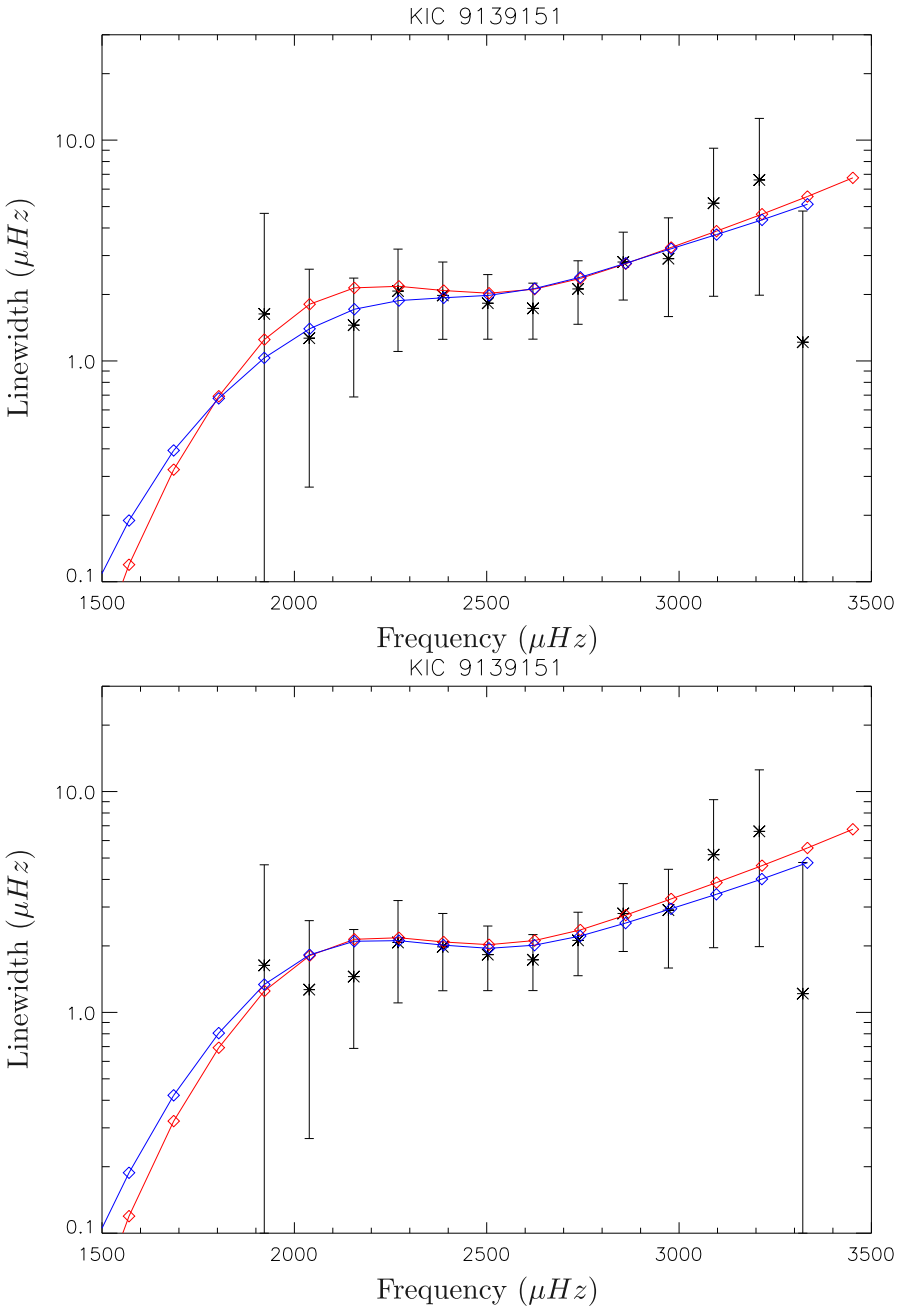

Figure 5.6: Theoretical linewidths for KIC 9139151 (the red curves correspond to the TDC treatment described in Sect. 4.2.1). The blue curves are obtained with $\delta\ell_m/\ell_m = dH_P/H_P$.
Top: $\beta = -1.64 - 1.25i$ gives $C_W = 9.3 \cdot 10^{-2}$ at $\nu_{\max}$
Bottom: $\beta = -1.60 - 1.15i$ gives $C_W = 7.3 \cdot 10^{-2}$ at $\nu_{\max}$

5.2.2 Perturbation of the mixing-length

As stated in Sect. 3.2.6 there is already two equations for the perturbation of the mixing length implemented in our code. We test here the impact of these formulae on theoretical linewidths. One simply relates the perturbation of the mixing length to the perturbation of the pressure scale height (Eq. 3.124, blue curves in Fig. 5.6). The other (Eq. 3.125, the standard one used in this thesis) introduces a factor $1/(1+(\omega\tau_c)^2$. This represents the assumption that the perturbation of the mixing length becomes negligible when mode periods are much smaller than the lifetime of convective eddies.

We see in Fig. 5.6 that it is not possible to discriminate between the two forms of the perturbation of the mixing length used. Indeed, a small change of β is sufficient to recover the linewidths obtained previously (see Fig. 5.6, bottom panel). It will be interesting to look if this small effect can be generalised to other observed stars, as well as to test other formulations for the perturbation of the mixing length (e.g. the ones proposed by Cowling 1935; Boury et al. 1964; Unno 1967; Unno et al. 1989).

5.2.3 The anisotropy factor

I recall that the anisotropy factor is defined by:

$$A = \frac{< v_r^2 >}{< v_\theta^2 + v_\phi^2 >}, \tag{5.1}$$

where v_r, v_θ, v_ϕ are the radial, longitudinal and azimuthal components of the velocity of the convective elements. Usually, we assume an isotropic turbulence such as $A = 1/2$.
To test the effect of the anisotropy on theoretical linewidths, we try $A = 1/4$ and $A = 1$ (see Fig. 5.7). For main-sequence stars, we find theoretical linewidths inside the error bars in both case without changing β and keeping a good value for $C_{\rm W}$ (i.e. avoiding non-physical spatial oscillations). At constant β, an increase (respectively a decrease) of the anisotropy factor leads to a global increase (respectively a decrease) of the theoretical linewidths. We can also find theoretical linewidths closer to the original ones with only a small adjustment of the β parameter. We will see in Chap. 6 that the anisotropy effect is more marked for red-giant stars. For main-sequence stars, given the error bars and the combined effects of the anisotropy and β, it is difficult to conclude on the value one should adopt for this parameter. 3D hydrodynamic simulations of main-sequence and red-giant stars show that this parameter varies approximately between 2.5 and 0.10 from the bottom to the top of these simulations. It is thus unclear if it is reasonable to keep a constant A in the TDC treatment; and even if kept constant if we should use a mean value of A or the value of A given by 3D simulations in the region where the convective damping is the most efficient.

For main-sequence stars, we are able to fit the observed linewidths with different values of the anisotropy factor. Thus, for these evolutionary stages, we cannot conclude on the best value to use. For the red-giant models, we will find in Chap. 6 that $A = 1/4$ allows us to better reproduce the typical observed linewidths of red-giant stars. A specific study, including various prescriptions for the anisotropy and comparisons to 3D simulations and observations, is needed for a better modelling of the anisotropy effect on solar-like oscillations.

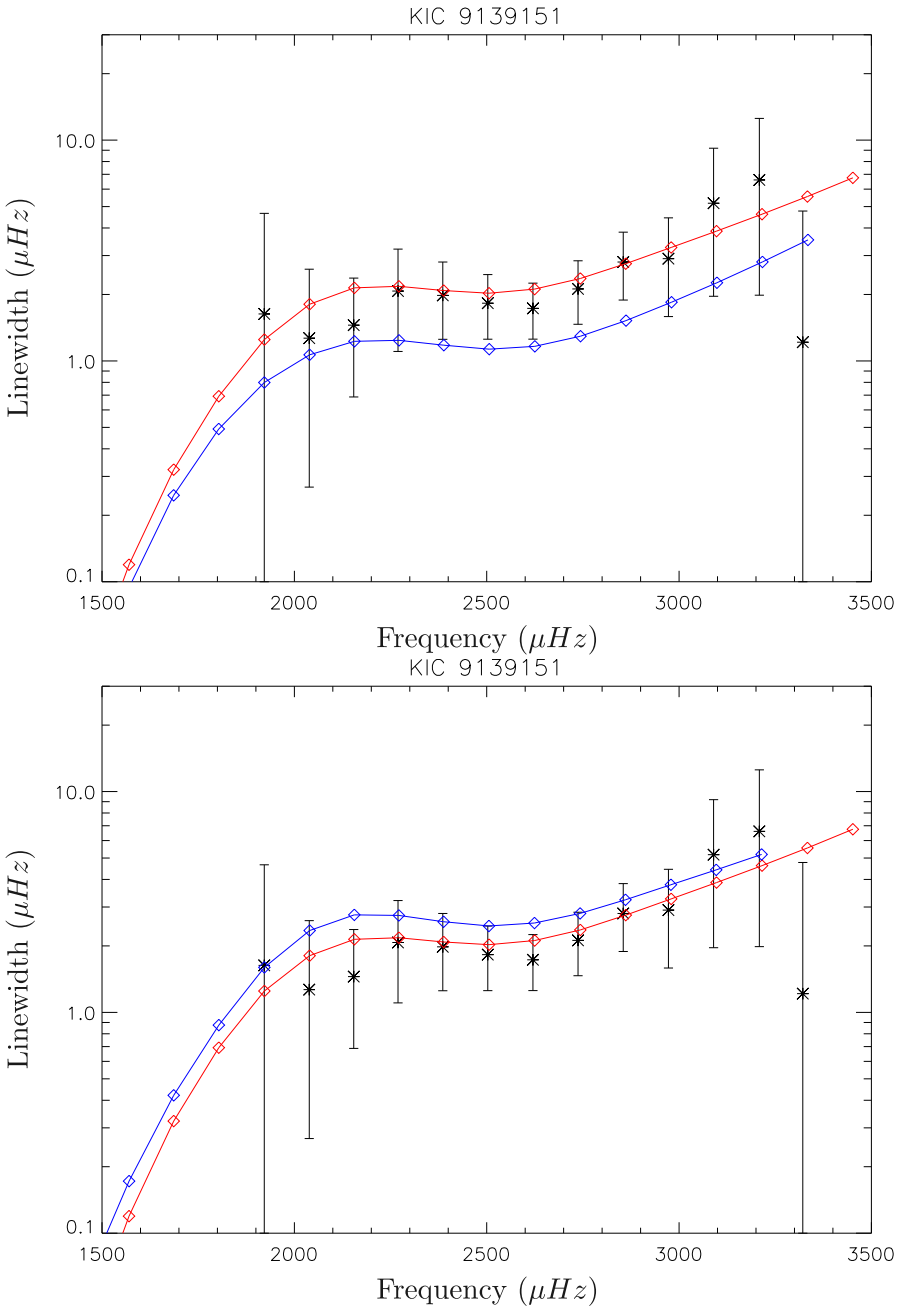

Figure 5.7: Theoretical linewidths for KIC 9139151 (the red curve correspond to the TDC treatment describe in Sect. 4.2.1). The blue curves are obtained by varying the anisotropy factor.
Top: $A = 1/4$, $\beta = -1.64 - 1.25i$ gives $C_W = 8.3 \cdot 10^{-2}$ at $\nu_{\max}$
Bottom: $A = 1$, $\beta = -1.64 - 1.25i$ gives $C_W = 8.5 \cdot 10^{-2}$ at $\nu_{\max}$

Conclusion

The complex parameter β is the main free parameter in the time-dependent treatment of the convection that significantly affects theoretical linewidths. From comparisons to observations and with tests of the impact of other TDC parameters, we have seen that, for main-sequence stars, adjusting β individually for each stellar model (or extrapolating it for models in an evolutionary sequence) is enough to reproduce the observed linewidths. We have strengthened the use of non-local parameters derived from 3D simulations, for it allows us to fit the observed linewidths. Since the effect of the description of the different formalisms implemented for the perturbation of the mixing-length is small, we cannot conclude on the one that should be adopted. The effect of the anisotropy factor is more important but remains in the error bars for the main-sequence star studied here. Detailed studies including a larger sample of stars (at different evolutionary stages) with observed linewidths (with small error bars), as well as various formulations of these parameters, are needed to better understand and constrain these parameters and the interaction between convection and oscillations. In the small sample of main-sequence stars studied here, it appears one case where significant differences between observed and theoretical linewidths appear away from $\nu_{\rm max}$ (a similar result is also found for the subgiant star studied in Chap. 7). The origin of such discrepancies is still unclear and investigations on theoretical and observed linewidths for a larger sample of observed stars (including more evolved stars) may help to understand them. Such studies could bring more information on the convection-oscillations interaction process.

Chapter 6

Theoretical power spectra of mixed-modes in low-mass red-giant stars

Observed red-giant power spectra display a wide range of morphologies and complexities. In some power spectra, we observe a lot of mixed-modes between two radial modes and in other only few are detectable (see e.g. Chaplin, Miglio 2013). In some cases, the heights of the mixed-modes are of the order of the radial ones while in other cases they cover a range between the height of radial modes and the noise level. Mosser et al. (2012a) have also remarked a family of stars in which the dipole modes (acoustic- and gravity-dominated) have all very small heights compared to radial modes. We denote them as depressed dipole modes.

In this chapter, we study the impact of stellar evolution on solar-like oscillation properties, and consequently on the power spectrum. This will allow us to understand, from a theoretical point of view, various morphologies of red-giant power spectra through the evolution of the linewidths, amplitudes and heights of the mixed-modes. First, we will follow the evolution of a 1.5 $M_{\odot}$ star from the red-giant branch to the helium-burning phase and the resulting changes in theoretical power spectra. We will then consider models of different masses to extend to the typical mass range of observed red giants the results obtained for the previous evolutionary sequence. Finally, we will have a closer look at some particular features present in power spectra of stellar models close to the helium-flash.

6.1 Power spectrum evolution from the bottom of the RGB to the horizontal branch

Motivated by the results of Dupret et al. (2009) and the contribution of CoRoT and *Kepler* observations (see e.g. Chaplin, Miglio 2013, and references within), our objective is to have a closer and more detailed look at the evolution of power spectra on the red-giant branch. I am particularly interested by the evolution of the detectability of mixed-modes in theoretical power spectra. Determining theoretical detectability limits is interesting for the preparation of observation programs and the targets selection to predict the observation time needed to detect mixed-modes and thus to obtain information on the stellar core.

Dupret et al. (2009) have already shown the impact of the radiative damping on mixed-mode heights. While Dupret et al. (2009) studied models of 2 and 3 $M_\odot$, we will consider here models of lower masses (around 1.5 $M_\odot$) more representative of the CoRoT and *Kepler* observed red giants. Moreover, Dupret et al. (2009) computations did not reproduce the bell shape of the power spectra, mainly due to their choice for the TDC parameter β. The more careful approach developed in Chap. 4 will thus give more accurate results for theoretical power spectra.

6.1.1 Non-adiabatic effects on mixed-mode heights

The shape of a power spectrum is mainly determined by two contributions: the modulation of inertia through mode trapping and the radiative damping. To discuss this shape, we describe the behaviour of the ratio between the height of a g-type mode (H_g) and of a p-type mode (H_p). From Eqs. 3.138 and 4.7, we have

$$\left(\frac{H_g}{H_p}\right) = \frac{(P_R I)_g}{(P_R I)_p} \frac{\eta_p I_p^2}{\eta_g I_g^2} \frac{f_g}{f_p}, \tag{6.1}$$

where, according to Chaplin et al. (2009a), we could take $f_{\rm g,p} = (T_{\rm obs}\eta_{\rm g,p} + 2)^{-1}$. In the following, we derive this height ratio in the two asymptotic cases, when $\tau \ll T_{\rm obs}/2$ and $\tau \gg T_{\rm obs}/2$, to discuss the main physical properties of the modes that can affect this ratio and to help the interpretation of numerical results (see Sect. 6.1.3).

Assuming that the modes are resolved (i.e. $\Gamma \ll T_{\rm obs}/2$), f_g/f_p in Eq. 6.1 tends to η_p/η_g and the height ratio is given by

$$\left(\frac{H_g}{H_p}\right)_{\rm res} = \frac{(P_R I)_g}{(P_R I)_p} \left(\frac{(\eta I)_p}{(\eta I)_g}\right)^2, \tag{6.2}$$

where $P_R I$ only depends on the eigenfunction of the mode near the surface, and thus does not depend on the type of modes at a given frequency (see Samadi, Goupil 2001), because the stochastic excitation is only efficient close to the surface (so for a p and g mode of the same frequency we have $(P_R I)_g \simeq (P_R I)_p$). Taking into account the equation of the damping rate (Eq. 3.63) and the decomposition of the work integral into the contribution of the core (W_c) and of the envelope (W_e) in Eq. 3.63, we can rewrite the height ratio as

$$\left(\frac{H_g}{H_p}\right)_{\rm res} \simeq \left(\frac{(\eta I)_p}{(\eta I)_g}\right)^2 \simeq \left(\frac{(\int dW)_p}{(\int dW)_g}\right)^2 \simeq \left(1 + \left[\frac{W_c}{W_e}\right]_g\right)^{-2}, \tag{6.3}$$

where we have used $(W_{\rm e})_g \simeq (W_e)_p$ since the eigenfunctions of p-type and g-type modes are very similar in the envelope. We also neglect the core contribution in the work integral of a p-type mode. We note from this formula that, when the radiative damping of g-type modes is negligible compared to the convective damping, the heights of g-type modes are the same as the height of p-type modes if they are resolved. Increasing the radiative damping clearly decreases the height ratio.

If we assume now that the p-type mode is resolved and the g-type mode is not resolved (which is often the case in observed power spectra), the situation is different, and f_g/f_p in Eq. 6.1 tends to $\eta_p T_{\rm obs}/2$ so

$$\left(\frac{H_g^{unres}}{H_p}\right) = \frac{(P_r I)_g}{(P_R I)_p} \frac{(\eta_p I_p)^2}{\eta_g I_g^2} \frac{T_{\rm obs}}{2} = \left(\frac{(\eta I)_p}{(\eta I)_g}\right)^2 \eta_g \frac{T_{\rm obs}}{2}, \tag{6.4}$$

following the same development as in Eq. 6.3, we find

$$\left(\frac{H_g^{unres}}{H_p}\right) \simeq \left(\frac{H_g}{H_p}\right)_{\rm res} \eta_p \frac{I_p}{I_g} \left(1 + \left[\frac{W_{\rm c}}{W_{\rm e}}\right]_g\right) \frac{T_{\rm obs}}{2}. \tag{6.5}$$

We see from this formula that the height ratio of unresolved modes depends on both their inertia and radiative damping, and on the duration of observations.

We see from Eq. 6.3, that there are clearly two contributions, the inertia and the non-adiabatic effects (i.e. the ratio between the work in the core and the work in the envelope), that determine the shape of the power spectrum. For unresolved modes, the duration of observation also plays an important role in the morphology of the power spectrum. How the inertia depends on the models is explained in several other studies (e.g. Montalbán, Noels 2013) and can be understood through simple asymptotic derivations (see e.g. Goupil et al. 2013, and Eq. 3.61). The work due to non-adiabatic effects for p-type modes can be estimated with scaling relations (Belkacem et al. 2013). The only remaining unknown is the ratio of the work integrals, which will be discussed in the following sections. This shows the importance of non-adiabatic computations to fully understand the links between the different power spectra morphologies (power spectra rich or poor in mixed-modes) and the inner properties of the stars.

6.1.2 Red-giant models and general tendencies

We first consider 1.5 $M_\odot$ models that are typical of CoRoT and *Kepler* observed red-giant stars from the bottom of the red-giant branch to the helium core-burning phase (see models A to D in Table 6.1 and Fig. 6.1). All these models are computed with the ATON code as described in Sect. 4.1.1. For each model we give the global seismic parameters: the large frequency separation ($\Delta\nu$), the frequency of maximum oscillation power ($\nu_{\rm max}$), and the asymptotic period spacing ($\Delta\Pi$). An adiabatic analysis of these models is presented in Montalbán, Noels (2013). In addition, we have selected models between 1 and 2.1 $M_\odot$ (see models E to G in Table. 6.1 and Fig. 6.1) at an evolutionary stage similar to model B but with different masses. The criteria for choosing these models, as well as the consequences for theoretical power spectra are discussed in Sect. 6.2.

Model	Mass $[M_\odot]$	Radius $[R_\odot]$	$\Delta\Pi_1$ [s]	$\Delta\nu\,[\mu Hz]$	$\nu_{\rm max}\,[\mu Hz]$
A	1.5	5.17	79.7	14.1	190
B	1.5	7.31	70.5	8.4	97
C	1.5	11.9	57.2	4	37
D	1.5	11.9	242.5	4	37
E	1.0	6.3	76.7	8.5	88
F	1.7	8.1	68.6	7.7	90
G	2.1	10.5	88.0	5.7	66

Table 6.1: Global parameters of our models: the large separation $\Delta\nu$ and the frequency of maximum power $\nu_{\rm max}$ are computed using the seismic scaling relations (e.g. Mosser et al. 2010b; Belkacem 2012). The period spacing $\Delta\Pi_1$ is computed using the asymptotic expansion (e.g. Tassoul 1980).

With the objective to produce theoretical power spectra compatible with the observed ones, we want first to obtain a maximum of mode amplitudes in agreement with $\nu_{\rm max}$ given by the scaling relation (Eq. 3.160). We have explained in Sect. 4.3 that the main TDC parameter affecting our theoretical predictions is the free complex parameter β. In order to reproduce the bell-shape of the power spectra, we have to ensure the presence of a minimum of the product of the damping rate by the inertia at $\nu_{\rm max}$ (by adjusting β, as prescribed by Belkacem et al. 2011). We see in Fig 6.2, that with a unique value $\beta_{\rm RGB} = -0.106 - 0.945i$, we can reproduce a minimum of ηI around the frequency $\nu_{\rm max}$ predicted by the scaling relation for all our RGB models (see also Sect. 4.3). For the helium-burning model, we have to take another value $\beta_{\rm RC} = -0.130 - 0.950i$. We also assume an isotropic turbulence. We thus use these values in the non-adiabatic computations for the models we present here. We will discuss the effect of the choices made in the TDC parameters for a qualitative comparison with observed power spectra in Sect. 6.3.2. The synthetic power spectra are modelled following the procedure detailed in Sect. 4.4. They are computed assuming 1 year of observations. Even if longer duration of observations are now accessible from *Kepler* data, we use this value because it allows us to clearly distinguish and discuss the different type of modes (fully resolved or not). We do not consider the noise background (which can limit the detectability of mixed modes). We will nonetheless discuss the effects of an increase of the duration of observations for each model in Sect. 6.1.3. We therefore consider that the detectability of mixed modes can be derived from the appearance of peaks in our synthetic power spectra.

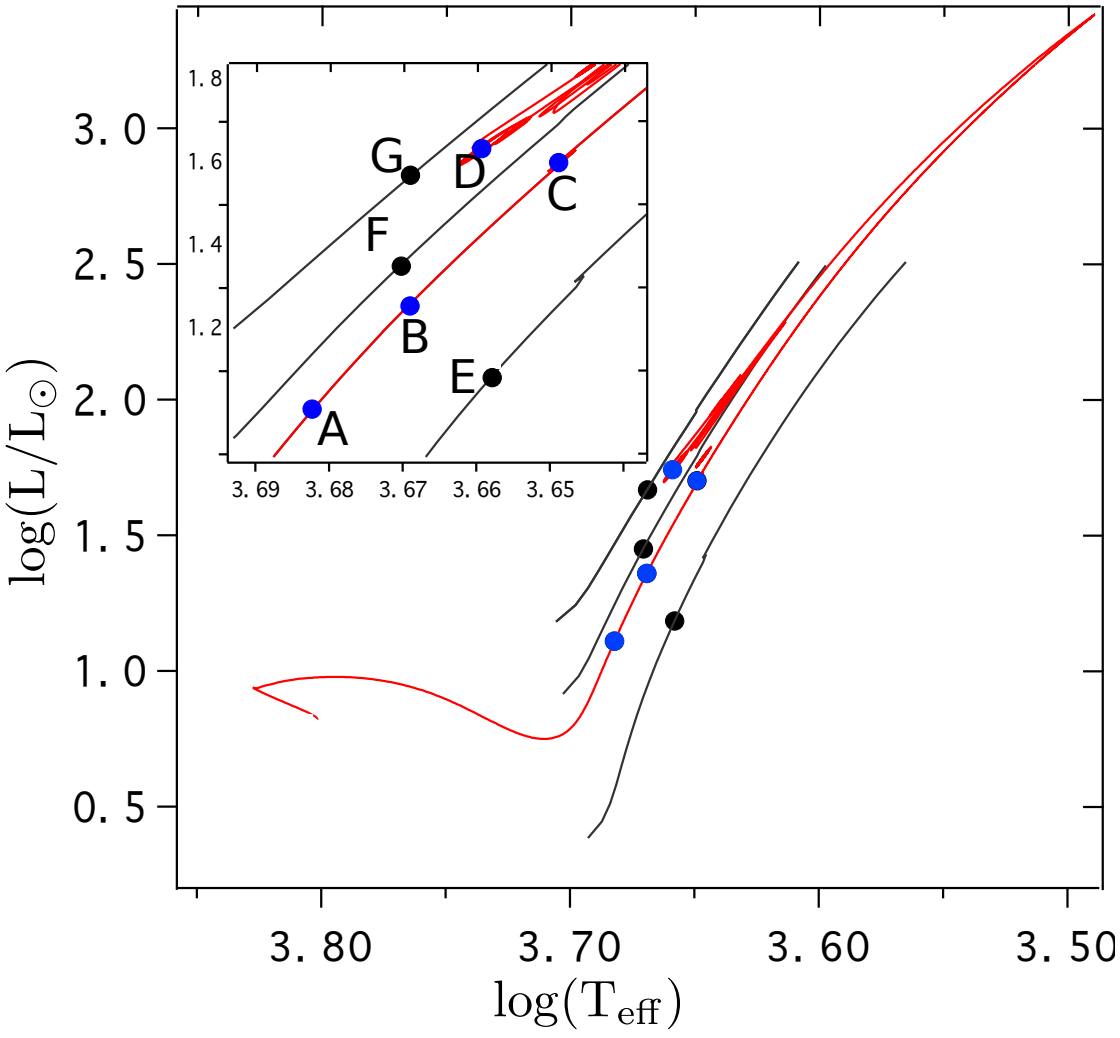

Figure 6.1: Evolutionary tracks in the Hertzsprung-Russell diagram of our models. Selected models are represented by dots. Blue dots correspond to models of a 1.5 $M_{\odot}$ star at different ages (on the red-giant branch and on the horizontal branch). Black dots correspond to models with the same number of mixed modes over a large separation as model B.

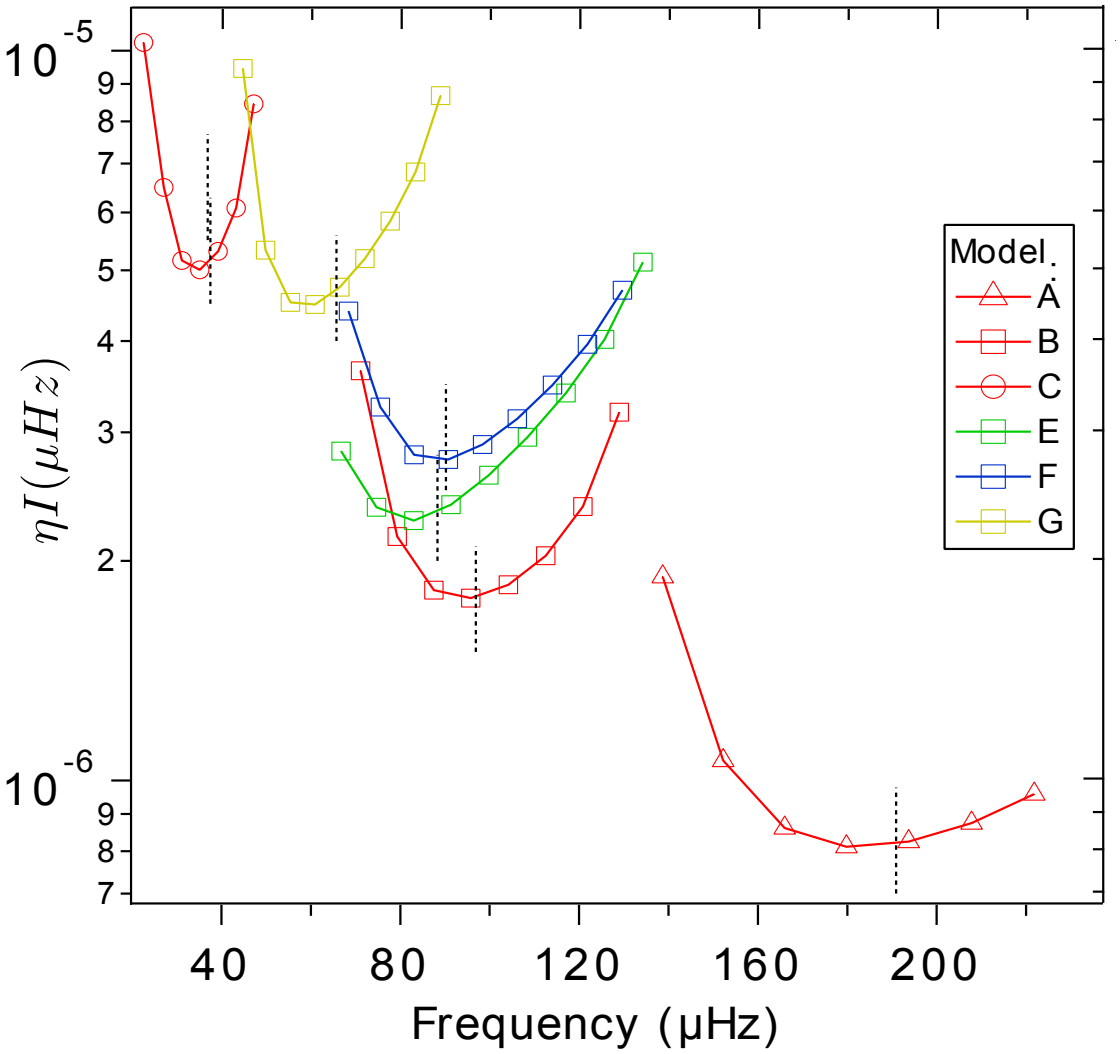

Figure 6.2: A unique value of β ($\beta_{\rm RGB} = -0.106 - 0.945i$) can reproduce the minimum of ηI at $\nu_{\rm max}$ (in dashed line) for various RGB models.

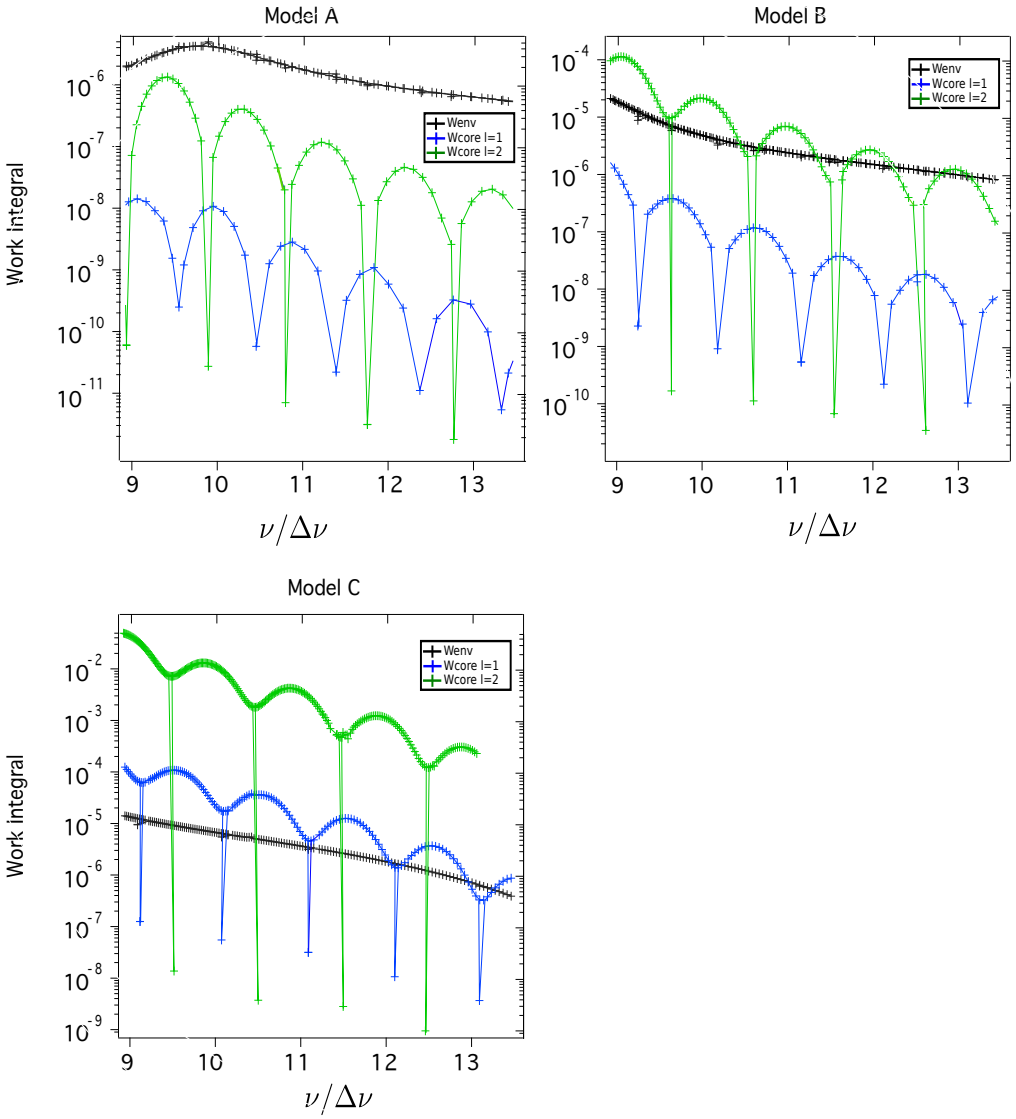

Figure 6.3: Core and envelope contributions to the work integral for the three RGB models of $1.5M_{\odot}$. The work is normalised by GM^2/R. Unlike the envelope contribution, the core contribution depends on the trapping and on the angular degree of the mode.

As discussed in Sect. 6.1.1, the shape of the power spectra is mainly determined by the inertia and the ratio between the convective and radiative contributions to the work integral. This ratio strongly affects the lifetimes and the heights of mixed-modes. The core and envelope contributions to the work integral of Models A to C are presented in Fig. 6.3, while the corresponding mode lifetimes and theoretical power spectra are displayed in Fig. 6.5. When the star evolves on the RGB, the radiative contribution to the work integral increases up to overcome the convective contribution. This corresponds to the increase of the radiative damping, which is expected to occur due to the increase of the core density.
As we will detail in the next section, these different behaviours of the damping rates will have a strong impact on the theoretical power spectra. As can be seen in Fig. 6.4, our theoretical predictions succeed in reproducing the main tendencies of power spectra along the evolution on the red-giant branch: the frequency range of solar-like oscillations goes to lower frequency, the large separation and the period spacing decrease, and the height of the modes in the power spectrum increases. Fig. 6.4 also summarises different types of power spectra we will discuss: from power spectra with few mixed-modes at the bottom of the RGB, to power spectra with numerous mixed-modes and finally without any visible g-type mixed-modes. We have mentioned before that among the large diversity of observed red-giant power spectra some show depressed dipole modes. We should note that in all the models we have studied, we never found such behaviour of the mixed-modes.

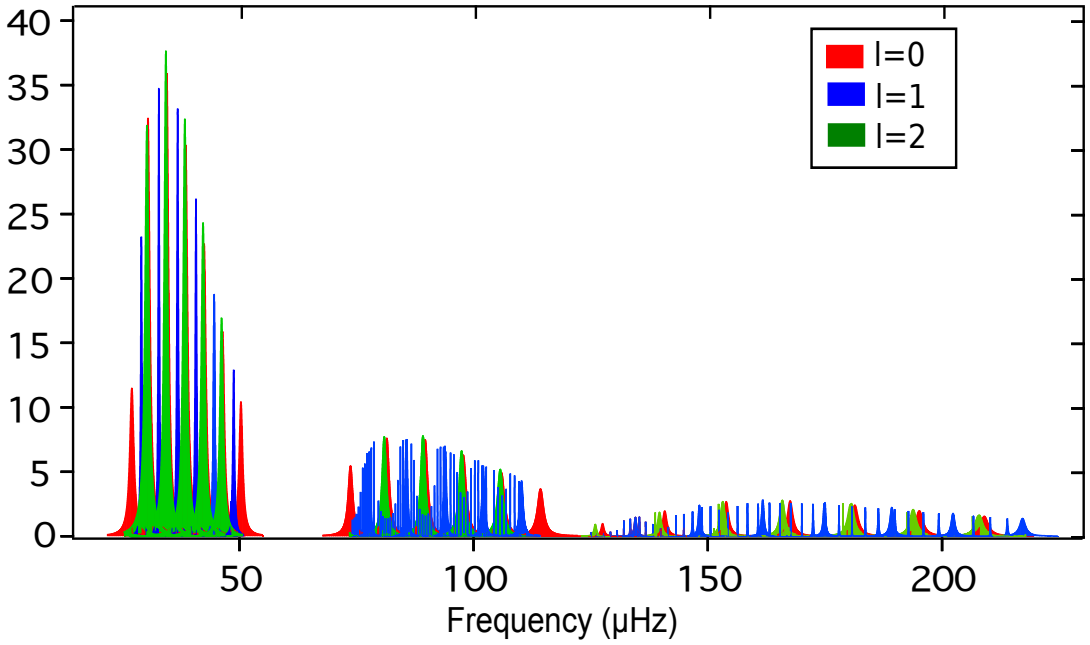

Figure 6.4: Power spectra of the three RGB models (A, B, and C from right to left) of $1.5M_{\odot}$, summarising the global evolutionary tendencies on power spectra. The heights of the peaks are given in $(m/s)^2/\mu Hz$.

6.1.3 Detailed description of the evolution of a theoretical power spectrum

In this section, we discuss the changes in the power spectrum along with the stellar evolution. We focus on the changes in the damping rates and on the height of mixed modes, as well as the effect of increasing the duration of observation. We consider the $1.5M_{\odot}$ models as described in Sect. 6.1.2.

Model A: At the bottom of the red-giant branch, the radiative contribution to the work integral (Eq. 3.65) is small for all modes in comparison with the convective one (Fig. 6.3). In addition, the convective work is a smooth function of the frequency and thus, as already pointed out, is independent of the mode trapping. From the damping rate equation (see Eq. 3.63), we see that only the inertia is responsible for the observed modulation of dipole and quadrupole mode lifetimes (Fig. 6.5, first panel).
In this model, all dipole mixed modes are resolved (except for low frequencies) and have amplitudes that are high enough to be detected. Since the radiative damping is always negligible, their heights are close to those of p-dominated modes (see Eq. 6.3). This spectrum is more regular than the spectrum corresponding to Model A in Dupret et al. (2009). Some quadrupole mixed-modes, close to the p-dominated ones, are also visible in the synthetic power spectrum (Fig 6.5, first panel).
Increasing the duration of observations would not change the dipole mode profiles. Indeed, since those modes are resolved, their heights no longer depend on the duration of the observations. Thus, at this early stage on the red-giant branch, we already find a clear structure in the power spectrum for dipole modes, allowing us to derive a period spacing. Conversely, as the observation duration increases, the number of visible quadrupole modes increases, too. With four years of observation, some quadrupole modes are resolved (more precisely quadrupole modes with lifetimes lower than 700 days) with heights comparable to the p-dominated modes. Moreover, the height of some quadrupole unresolved modes increases so as to become visible in the synthetic power spectrum. Finally, a very long time of observations (typically about 27.5 years) is required to have all quadrupole modes resolved, with all heights similar to the heights of the radial ones.
In this model, we also consider the behaviour of the $\ell = 3$ modes (not shown in the figures). At this early stage on the RGB, they already undergo a strong radiative damping so that only the modes trapped in the envelope are visible in the power spectrum (observations longer than a hundred years would be required to see some g-dominated ones). The increase in the radiative damping during the ascension of the red-giant branch will prevent from detecting $\ell = 3$ g-types modes higher on the RGB. We thus predict that the detectable $\ell = 3$ modes in red giants are all p-type modes.

Model B: Higher on the red-giant branch, the radiative contribution to the work integral is similar to the convective contribution for quadrupole modes (Fig. 6.3). This explains why the lifetimes for low-frequency quadrupole modes level off (Fig. 6.5, second panel). Moreover, the coupling between the two cavities decreases due to the contraction of the core and the expansion of the envelope. Indeed, when the star evolves, the number of mixed-modes by large separation increases, leading to an increase in the inertia ratio between a p-type and a g-type mode. Because of these two effects, $\ell = 2$ mixed modes are no longer visible in our synthetic power spectrum. Even when increasing the duration of observation above twice the lifetime of quadrupole modes (corresponding to approximately 10 years of observation), they would still not be detectable due to their significant radiative damping in the core.

For dipole modes, the convective contribution is still the dominant part of the work integral so that their lifetimes are still clearly modulated by the inertia. Dipole modes strongly trapped in the core are not resolved and have smaller amplitudes. Moreover, as shown in Fig. 6.5 (second panel), their detection would be made difficult by the overlapping with radial modes and p-type quadrupole modes that exhibit large linewidths. In Sect. 6.3.2, we detail the effect of the TDC parameter β on the lifetimes of the p-type modes (see also Chap. 5). Other values of this parameter could lead to longer lifetimes, hence to narrower peaks (see Fig. 6.12). Nevertheless, increasing the duration of observations will increase the heights of dipole modes. Taking four years of observation would allow us to have almost all $\ell = 1$ modes resolved, and in this case, their heights are very similar to the p-dominated non-radial modes.

Model C: For a more evolved model, the radiative damping continues to increase and the coupling between the two cavities becomes very small owing to the expansion of the envelope and contraction of the core. This implies that the lifetimes of all modes, except modes strongly trapped in the envelope, are dominated by the radiative damping (Fig. 6.5, third panel). This damping is high enough to obtain lifetimes of g-dominated quadrupole mixed-modes lower than the dipole ones. Consequently, only p-dominated modes are detectable (Fig. 6.5, third panel). In this model, increasing the duration of the observation even more (even with $T_{\rm obs} > 2\tau$ for all modes) does not lead to detectable mixed-modes, because of the strong radiative damping (much more important than the convective one, see Fig. 6.3).

Model D: Further along in the evolution, after the helium-flash, the star begins to burn helium in its core. This model presents lifetimes similar to those of model B (Fig. 6.5, fourth panel). After the helium flash, the core has expanded and the envelope contracted leading to a decrease in the radiative damping of mixed-modes and a stronger coupling between the p and g cavities. The appearance of a convective core also contributes to this decrease. The detectability of mixed modes (Fig. 6.5, fourth panel) is very similar to the case of model B . After the He-flash, the radiative damping of the $\ell = 3$ modes is still too high to observe g-type modes in our synthetic power spectrum.

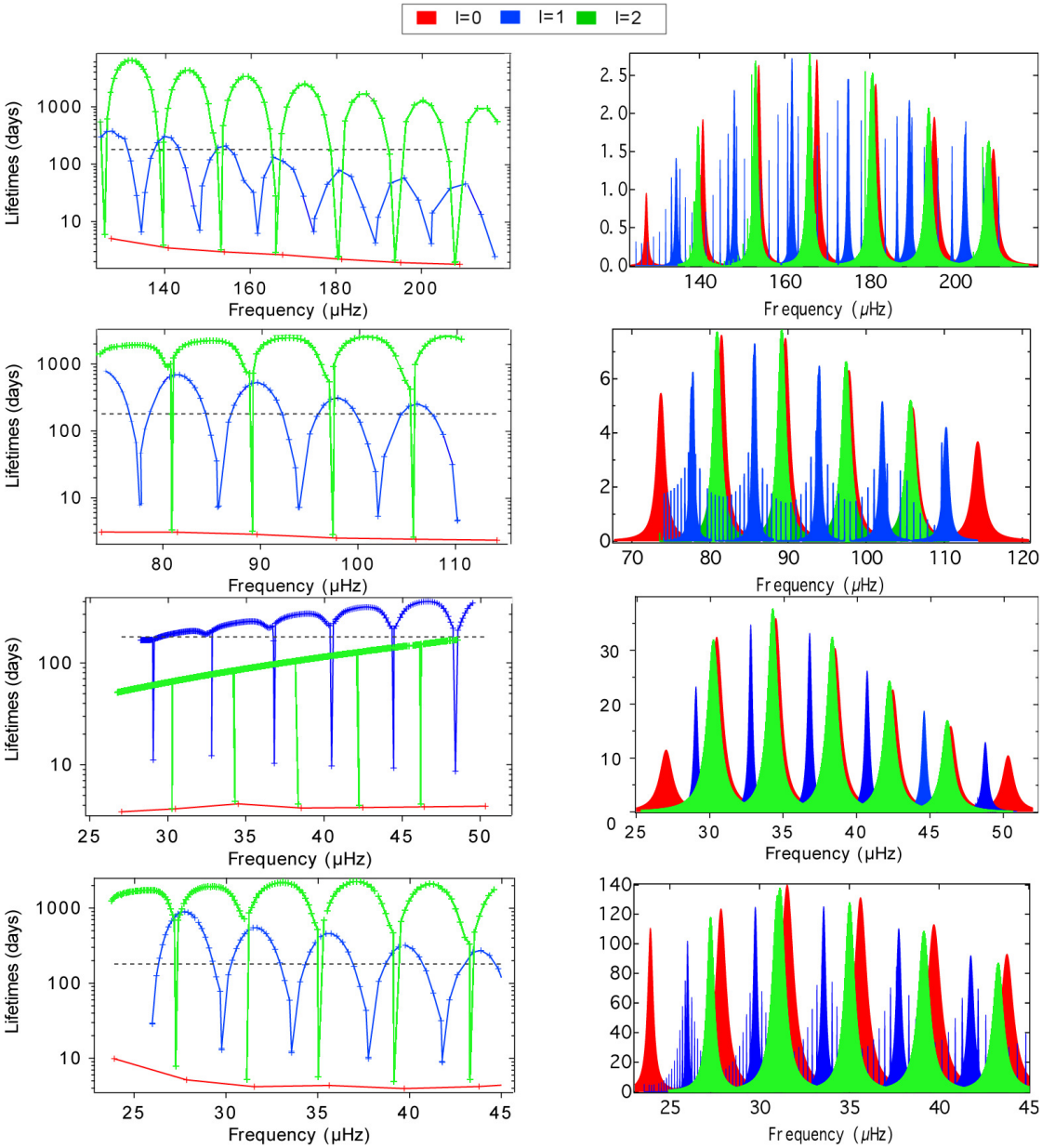

Figure 6.5: **Left :** Lifetimes of $\ell = 0$ (red), $\ell = 1$ (blue), and $\ell = 2$ (green) modes in models A, B, C, and D (from top panel to bottom). The dashed line represents $T_{\rm obs}/2$ (with $T_{\rm obs} = 1\ year$. **Right:** Corresponding power spectra. The heights in power spectra are given in $(m/s)^2/\mu$Hz.

6.2 Generalisation of the results on mixed-modes detectability

In the previous section, we have seen that when the stars climb the red-giant branch, the mixed modes become more difficult to detect until their heights are too low to be visible in our synthetic power spectra (even if we consider a longer duration of observation to resolve all modes). In the following lines, we denote n_g and n_p as the number of nodes of a dipole mode in the g- and p-cavities, respectively. Our analysis of models with the same number of mixed-modes over a large separation (models E to G in Table 6.1) or, equivalently, a given ratio n_g/n_p shows that they all exhibit the same behaviour of the lifetimes (Fig. 6.7, left panel). They also present very similar power spectra (Fig. 6.7, right panel) with the same height ratios of mixed modes. Using the heights computed in the previous sections (i.e. from the calculations of the damping rates and of the power injected into the modes by turbulence), we show in Fig. 6.6 a relation between the height ratio of g- and p-type modes around $\nu_{\max}$ on the one side and n_g/n_p on the other side, for fully resolved and partially resolved modes. This relation is more marked in the case of fully resolved modes. More computations for a larger number of models will be needed to derive a more precise relation for the relative heights of the modes. There is a higher dispersion between the models with the same n_g/n_p with only one year for the duration of observations, because these modes are only partially resolved. In Sect. 6.1.3 we have seen that there is a theoretical limit on the RGB above which mixed-modes are no longer detectable. The results obtained here for models with the same number of mixed modes over a large separation allow us to extend the previous results to other masses. Moreover, we note that the inertia ratio can also be expressed as a function of n_g/n_p (Goupil et al. 2013). We thus conclude that this ratio is a good proxy for the shape of power spectra.

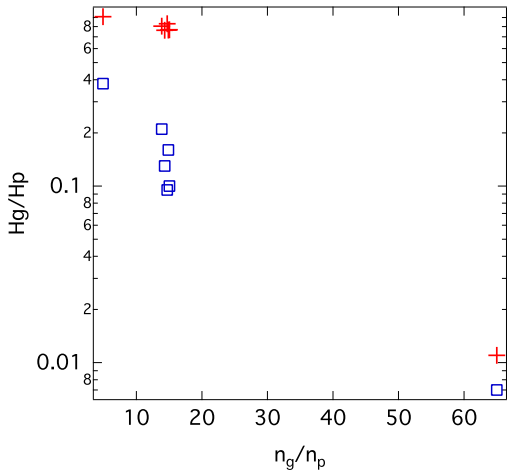

Figure 6.6: Height ratio between a g-type (the $\ell = 1$ with the highest inertia close to $\nu_{\max}$) mode and a p-type mode around $\nu_{\max}$ as a function of n_g/n_p for all our models. Red crosses represent the ideal case where all the modes are resolved. Blue squares are for observation durations of one year.

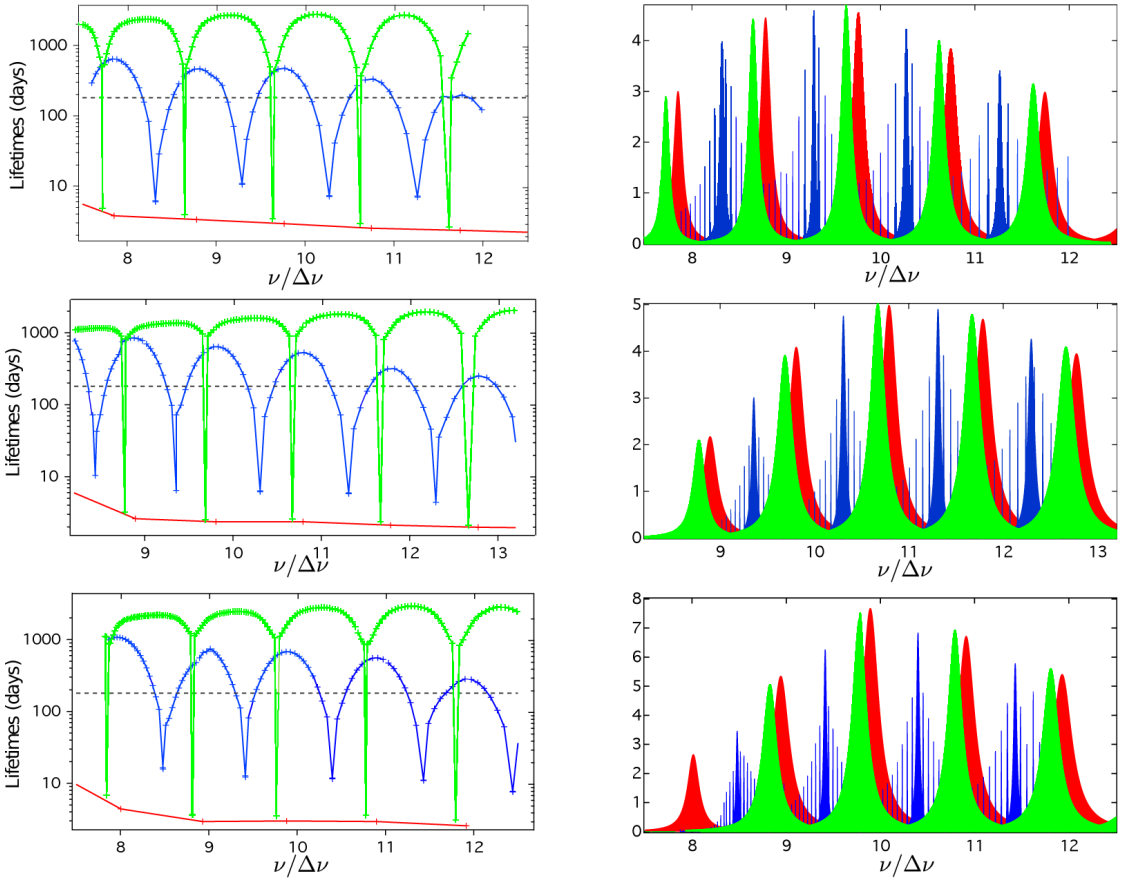

Figure 6.7: **Left:** Lifetimes of $\ell = 0$ (red), $\ell = 1$ (blue) and $\ell = 2$ (green) modes in models E, F, and G (from top panel to bottom). The dashed line represents $T_{\rm obs}/2$ ($T_{\rm obs} = 1\ year$) . **Right:** Corresponding power spectra. The heights in power spectra are given in $(m/s)^2/\mu$Hz.

Our results on the theoretical power spectra for models along the red giant branch and of different masses shows that the number of mixed mode over a large separation is a good proxy for the theoretical detectability of mixed modes. A theoretical evaluation of this proxy is easily obtained through asymptotic relations. Indeed, from Eq. 3.49 we can express the n_p close to $\nu_{\max}$ as $n_p \simeq \nu_{\max}/\Delta\nu$, from Eq. 3.54 $n_g \simeq 1/(\Delta\Pi\nu_{\max})$ and thus $n_g/n_p \simeq \Delta\nu/(\Delta\Pi\nu^2_{\max})$. Taking then the background noise into account, it becomes possible to estimate the detectability of mixed modes along the red-giant branch. Using this relation, we present in Fig. 6.8 the theoretical limit for mixed modes detectability (corresponding to $n_g/n_p \simeq 60$), which is the level on the red-giant branch where we are no longer able to see any dipole mixed modes in the synthetic power spectra even by increasing the time of observation to more than ten years (so that all modes are resolved).

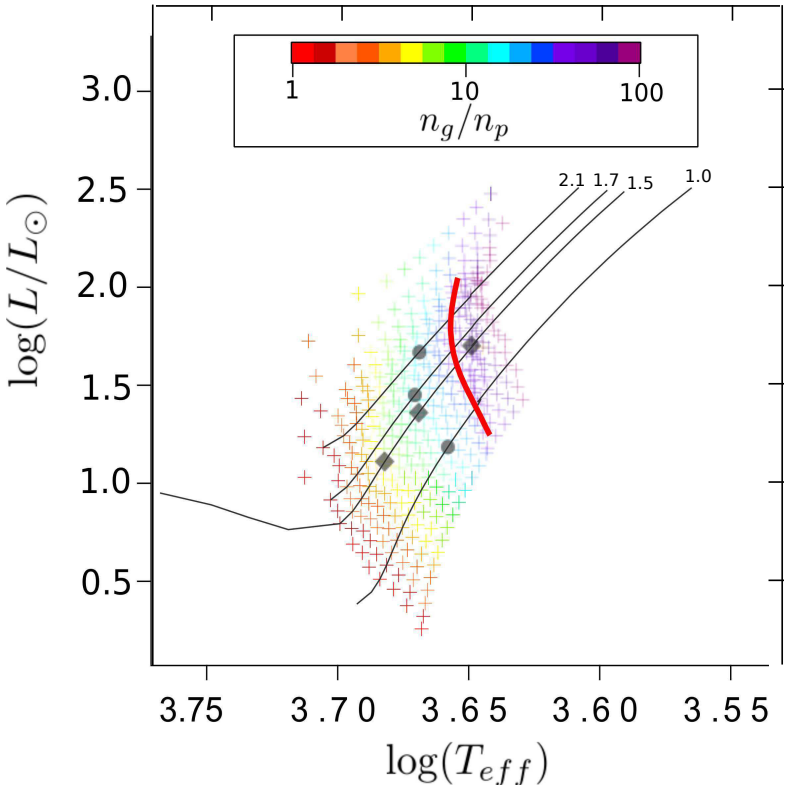

Figure 6.8: Evolutionary tracks in the HR diagram of all our red-giant branch models. Numbers on the top of the tracks indicate the mass of the star (in $M_\odot$). The color scale indicates models with the same number of mixed modes by large separation. The red line represents the detectability limit we have found for the dipole modes (assuming that all modes are fully resolved).

6.3 Comparison to Kepler power spectra

6.3.1 The detectability of mixed modes

We present in Figure 6.9 some power spectra obtained with Kepler along with our $1.5M_{\odot}$ RGB theoretical power spectra to show the main tendencies discussed in this paper. Concerning the height ratios and the limit for the detectability of mixed-modes, we found the same tendencies as the observed ones. At the beginning of the red-giant branch, dipole mixed modes have heights that are comparable to the p-type mode heights. It seems, however, that the observed heights of the mixed-modes (especially for the ones the most trapped in the core) are smaller than our predictions. A modulation of the heights of dipole mixed-modes appears for the star at the level of model A. Higher on the RGB, dipole mixed modes are partially resolved, and their heights present a clear modulation compared to the heights of p-type modes. At the level of model C, only the p-type modes have significant heights. There are more visible mixed-modes in the observed spectra, owing to the presence of rotational multiplets, but without any consequence for their heights and widths.

This confrontation of ours theoretical results to the observations shows that we reproduce pretty well the different shapes of the power spectra. However, it appears that our p-dominated mode theoretical linewidths are much larger than the observed ones. This will be discussed in Sect. 6.3.2.

For comparison, we give in Table 6.2 the conversion factor to obtain the height for the radial mode at $\nu_{\rm max}$ in ppm$^2/\mu$Hz. When the non-adiabatic phase lag is neglected here, it is obtained using the relation

$$\frac{\delta L}{L} = \frac{4f_T - 2}{2\pi\nu R} V = C_f V \tag{6.6}$$

with $f_T = \mid \delta T_{\rm eff}/T_{\rm eff} \mid / \mid \xi_r/R \mid$. We decided to present our results in radial velocity because the conversion to bolometric intensity introduces additional uncertainties. Observations (as presented in Fig. 6.9) show that the typical maximal heights for radial modes on the part of the RGB studied here are between more or less 9000 and 120000 $ppm^2/\mu Hz$, thus in overall agreement with our theoretical results.

Model	$\nu_{\rm max}[\mu Hz]$	$C_f^2[ppm^2/(m/s)^2]$	H $[ppm^2/\mu Hz]$
A	190	3.6×10^3	9×10^3
B	97	2.9×10^3	2×10^4
C	37	2.4×10^3	8×10^4
D	37	3.2×10^3	4×10^5
E	88	8.8×10^3	4×10^4
F	90	12.7×10^3	6×10^4
G	66	39.1×10^3	3×10^5

Table 6.2: Conversion factor C_f^2 from radial velocities to intensity variations for heights around $\nu_{\rm max}$

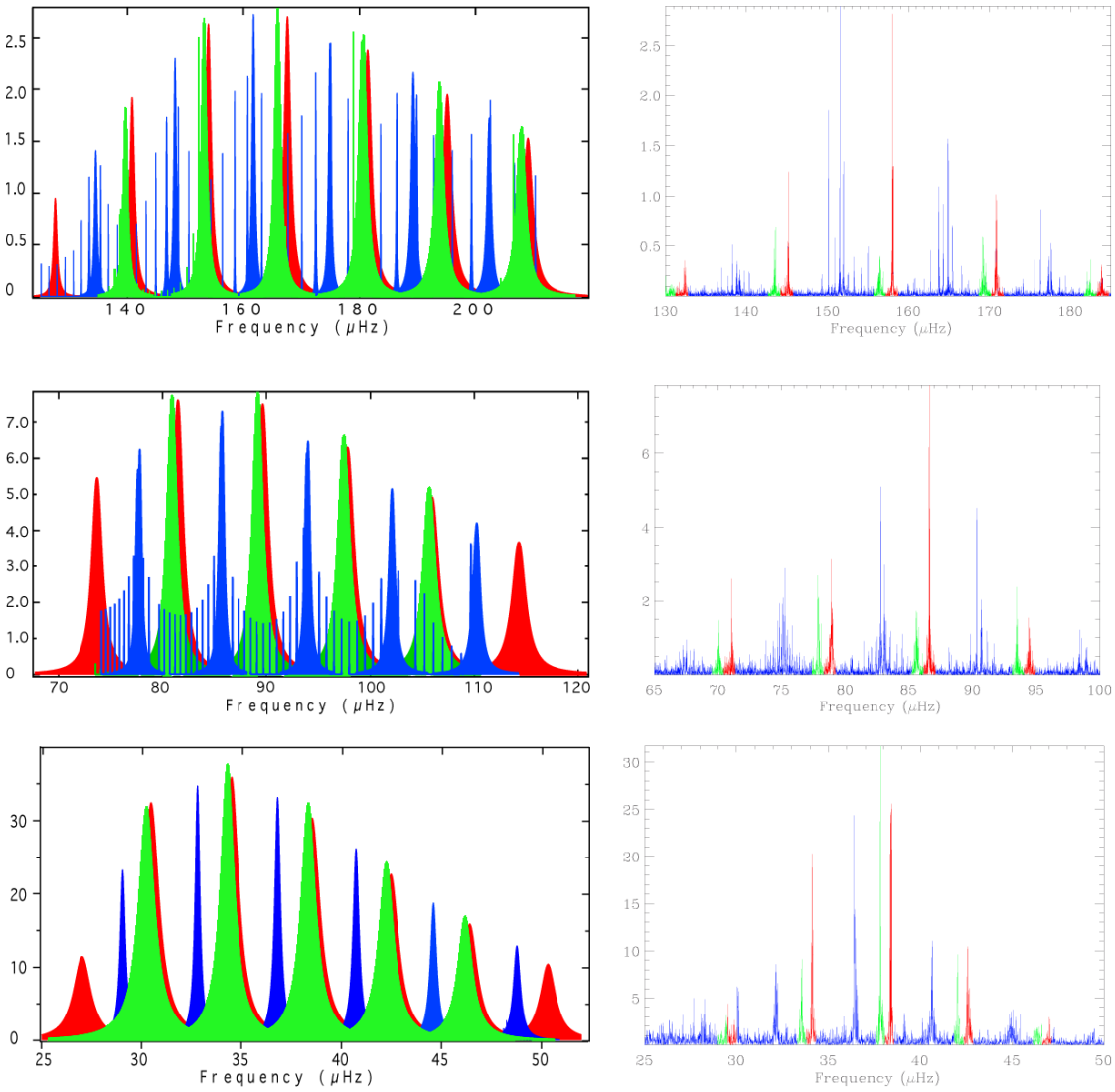

Figure 6.9: Theoretical and observed power spectra of *Kepler* stars with similar masses (from top to bottom: 1.44, 1.48, 1.47 $M_{\odot}$), $\Delta\nu$, and $\nu_{\max}$. The heights in theoretical power spectra are in $(m/s)^2/\mu Hz$. The heights for observed spectra are given in $ppm^2/\mu Hz$ divided by a factor 6000 to have scales similar as the theoretical spectra.

6.3.2 Lifetimes of radial modes on the red giant branch

The main differences between the observed and theoretical power spectra are the widths of the p-type modes. As discussed in the previous chapter, we often underestimate the lifetimes of red-giant p modes in our computations. Guided by the various tests on the TDC treatments made in Sect. 4.3, we search to obtain longer lifetimes, first with a change of β, then with a change of the anisotropy factor. Indeed, the free parameter β has a strong impact on the theoretical linewidths (as it can be seen in Fig. 6.10) but this may not be enough to reach lifetimes of the order of the observed ones.

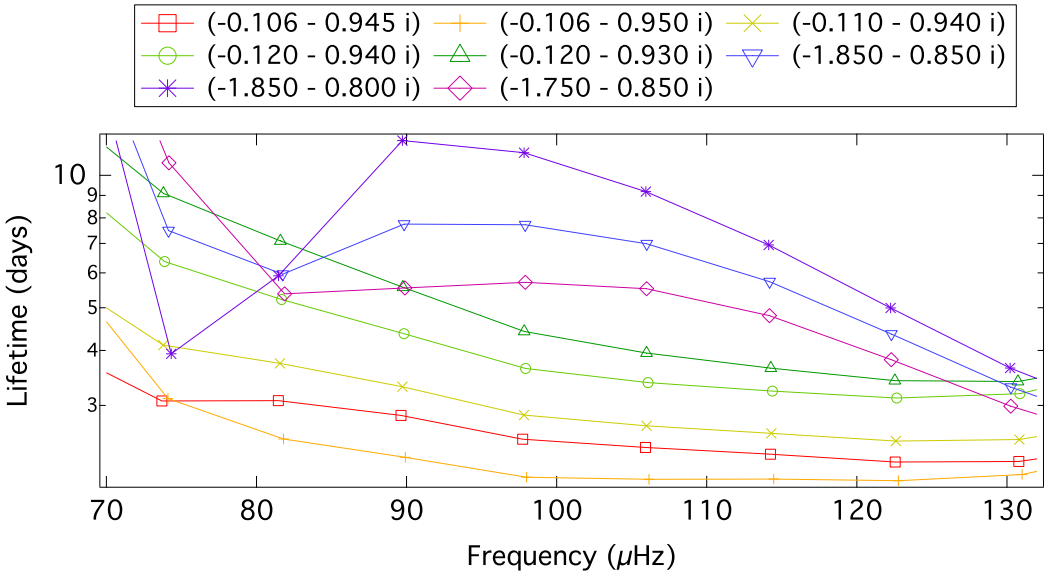

Figure 6.10: Theoretical lifetimes of radial modes of model B for different values of β. The lifetimes corresponding to β used in this paper are denoted by red squares. For this model, the $\Gamma_{\max}$ - $T_{\rm eff}$ scaling relation (see Sect. 5.1.2) gives lifetimes of the order of 20 days.

We see in Fig. 6.11 (in blue), that we have been able to obtain longer lifetimes, by changing the value of β between each model. We use respectively for models A, B and C: $\beta_A = 1.700 - 0.700i$, $\beta_B = -1.940 - 0.800i$, $\beta_C = -1.780 - 0.920i$. These lifetimes are however a little smaller than the typical observed ones The test made on the anisotropy factor (see Sect. 3.75) suggest that $A = 1/4$ may give a better agreement between theoretical and observed lifetimes. Using this value for the anisotropy factor and the values of $\beta_A, \beta_B, \beta_C$ given here-above, we obtain lifetimes (see Fig. 6.11 in green) of the order of the observed ones and in good agreement with the scaling relation between $\Gamma_{\max}$ and $T_{\rm eff}$ (see Eq. 3.163).
As an example, we present in Fig. 6.12 the resulting power spectra for these changes (of β and of the anisotropy factor) for model B. Such modifications in the TDC parameters affect the linewidths of the modes (mainly the p-type modes) but does not change considerably the general aspect of the power spectra and, in particular, the detectability of g-type mixed-modes.

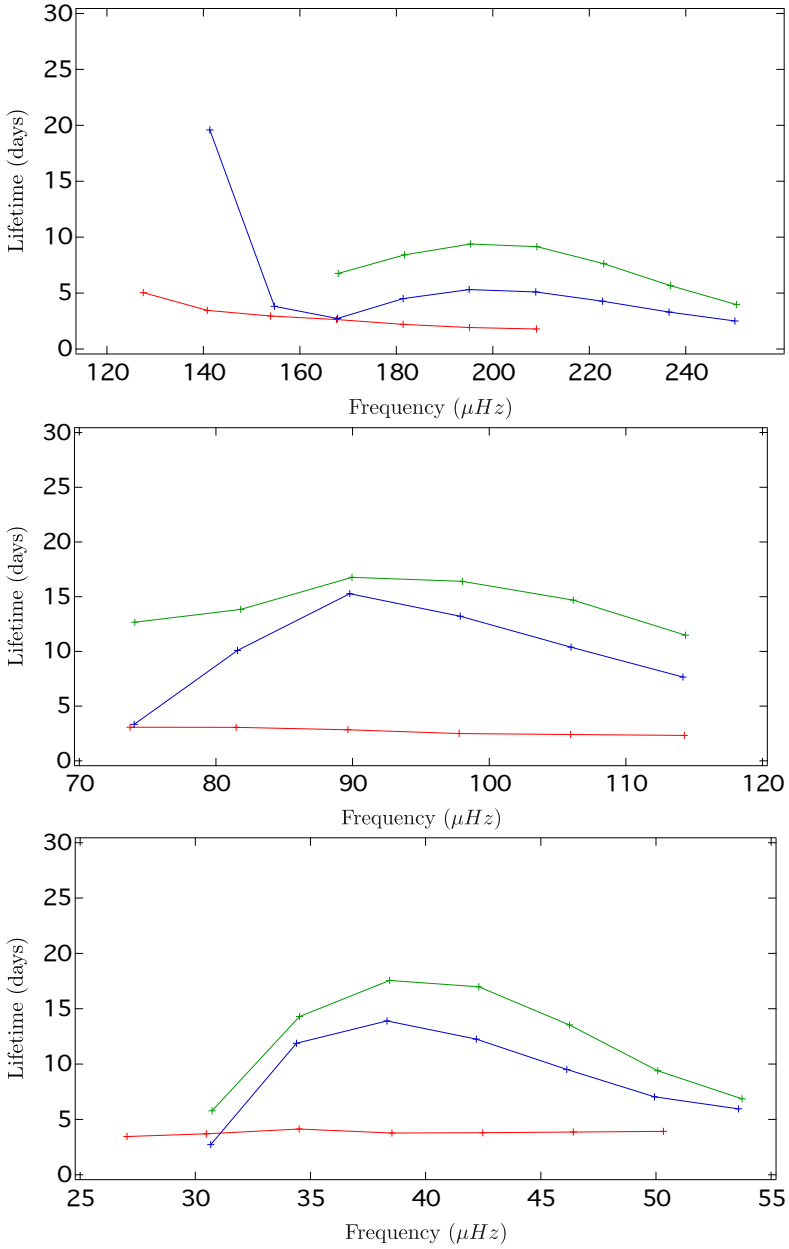

Figure 6.11: Lifetimes of radial modes for models A, B and C (from left to right). The lifetimes from β used in Sect. 6.1 are in red. The blue curves represent the change of β. The green curves give the lifetimes with the change of the anisotropy factor.

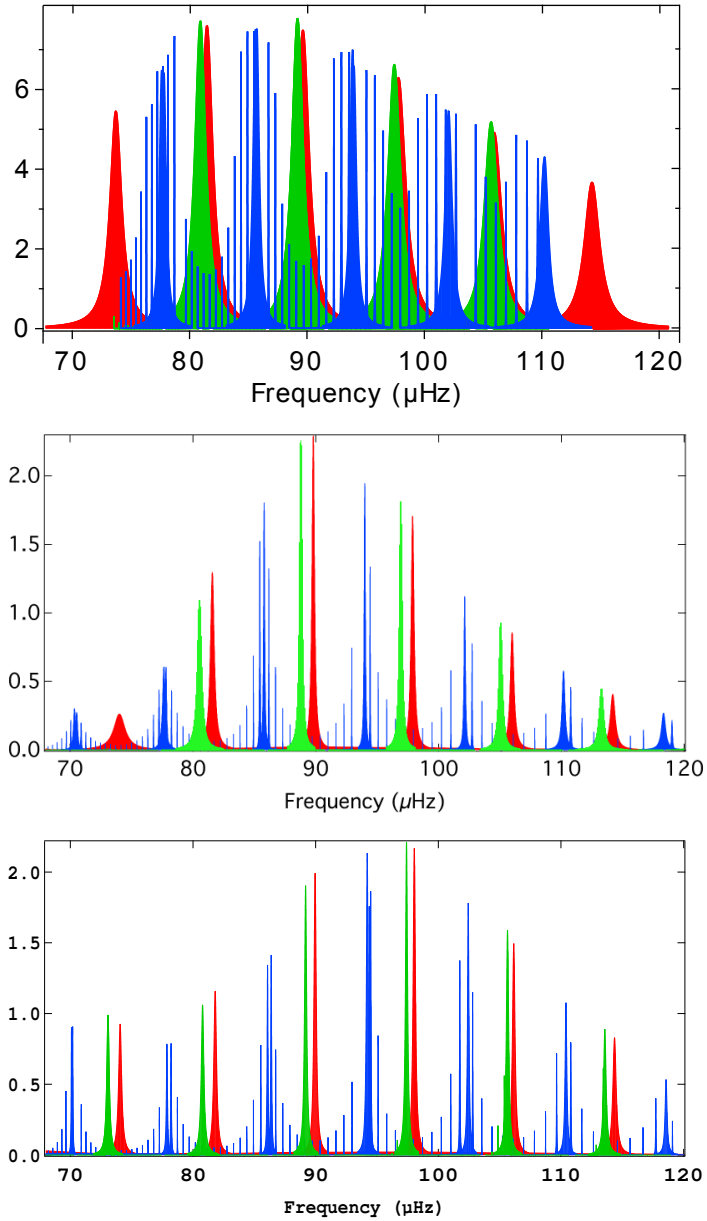

Figure 6.12: Power spectrum of model B for the TDC parameters $\beta = -0.106 - 0.945i, A = 1/2$ (top panel), $\beta = -1.940 - 0.800i, A = 1/2$ (middle panel), $\beta = -1.940 - 0.800i, A = 1/4$ (bottom panel).

6.4 Particular signature in the theoretical power spectrum shortly after the helium flash

Shortly after the He-flash, the stellar structure presents remnants of the multiple small flashes. These remnants will finally disappear, being smoothed, during the evolution on the horizontal branch. We illustrate such a behaviour with a stellar model, computed with the ATON evolutionary code. It corresponds to a 1.4 $M_\odot$ model with a radius of 11.4 $R_\odot$ and an effective temperature of 4563 K. For this model, we obtain from scaling relations $\nu_{\max} = 37.8\ \mu Hz$, and from Eq. 3.55 the asymptotic period spacing $\Delta\Pi_1 = 252\ s$.

In Fig. 6.13, we see some discontinuities of the chemical composition left by the flash. These discontinuities produce peaks in the Brunt-Vaisälä frequency. The most important discontinuity, at the bottom of the hydrogen burning shell, also produces a discontinuity in the Lamb frequency (around $\log T = 7.42$). This chemical discontinuity acts like a partial reflection barrier for non-radial modes. This is clearly visible when looking at the inertia of the modes. In Fig. 6.14, we distinguish two types of inertia ranges for dipole modes. This double trapping is also present in a less extent for quadrupole modes. As expected, this special feature impacts the lifetimes of the modes. Approximately one over three g-type dipole modes have a small lifetime. The impact is less marked for the quadrupole modes because of the radiative damping.

The direct consequence of this double trapping is that in the power spectra the visible dipole mixed modes do not follow the regular pattern presented in the previous section. Only the modes with small inertia appear in the power spectrum (see Fig. 6.15). Thus, between two visible g-type dipole modes there is a gap in the power spectrum due to missing modes (the modes with higher inertias). Such a situation can create a misinterpretation of the observed power spectrum. Indeed, if we observe a star shortly after the helium-flash we will only see the modes with low inertia. We thus have to be very careful in the use of such period spacing for which the asymptotic interpretation is no longer valid.

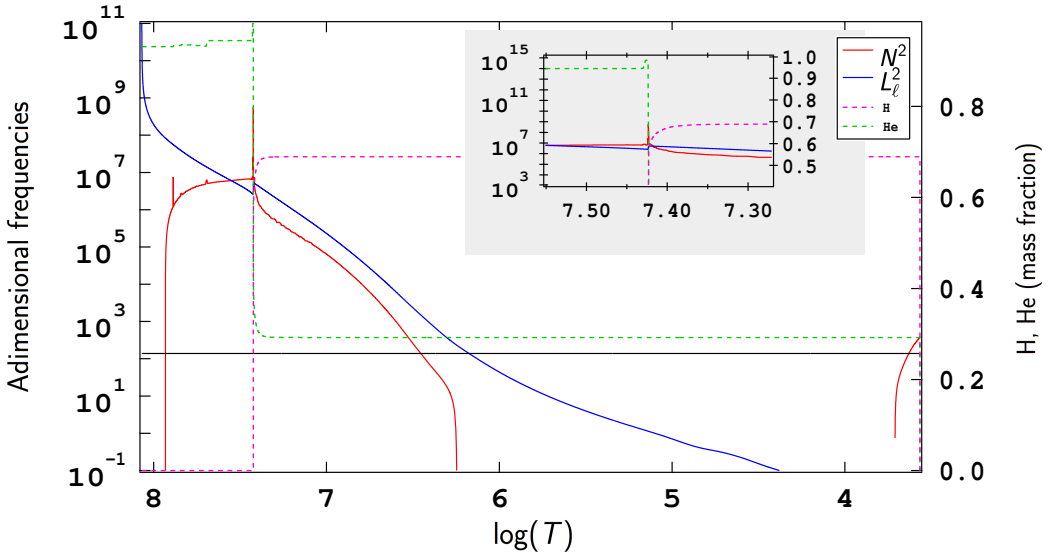

Figure 6.13: Propagation diagram of a $1.4 M_\odot$ model shortly after the Helium Flash. The horizontal black line represents $\nu_{\max}$

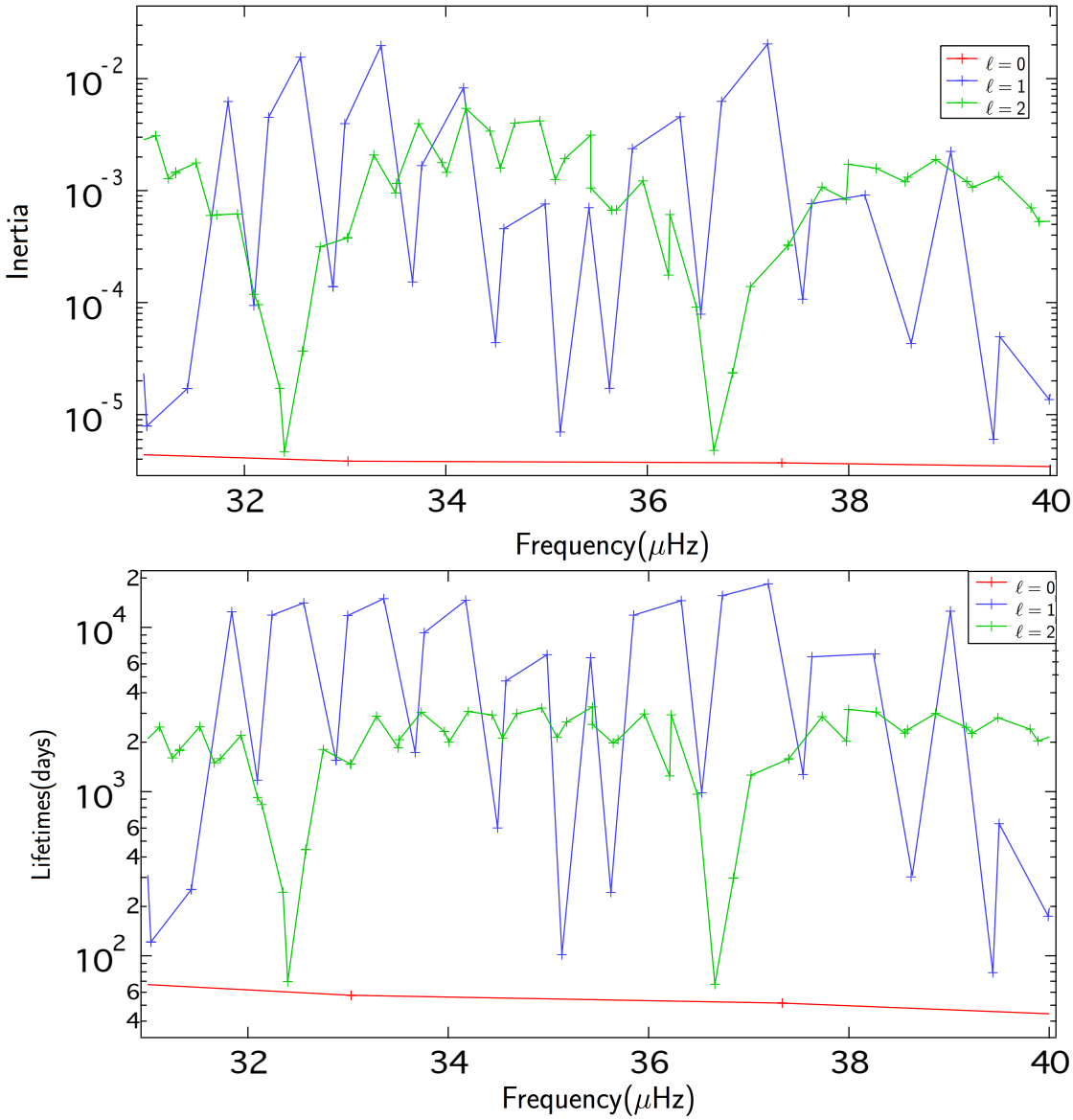

Figure 6.14: **Top:** Inertia of radial and non-radial modes for a model shortly after the helium flash. g-type mixed-modes are trapped in two different regions. **Bottom:** Corresponding lifetimes, which are also sensitive to the two modes trapping. We note the impact of the radiative damping for quadrupole modes.

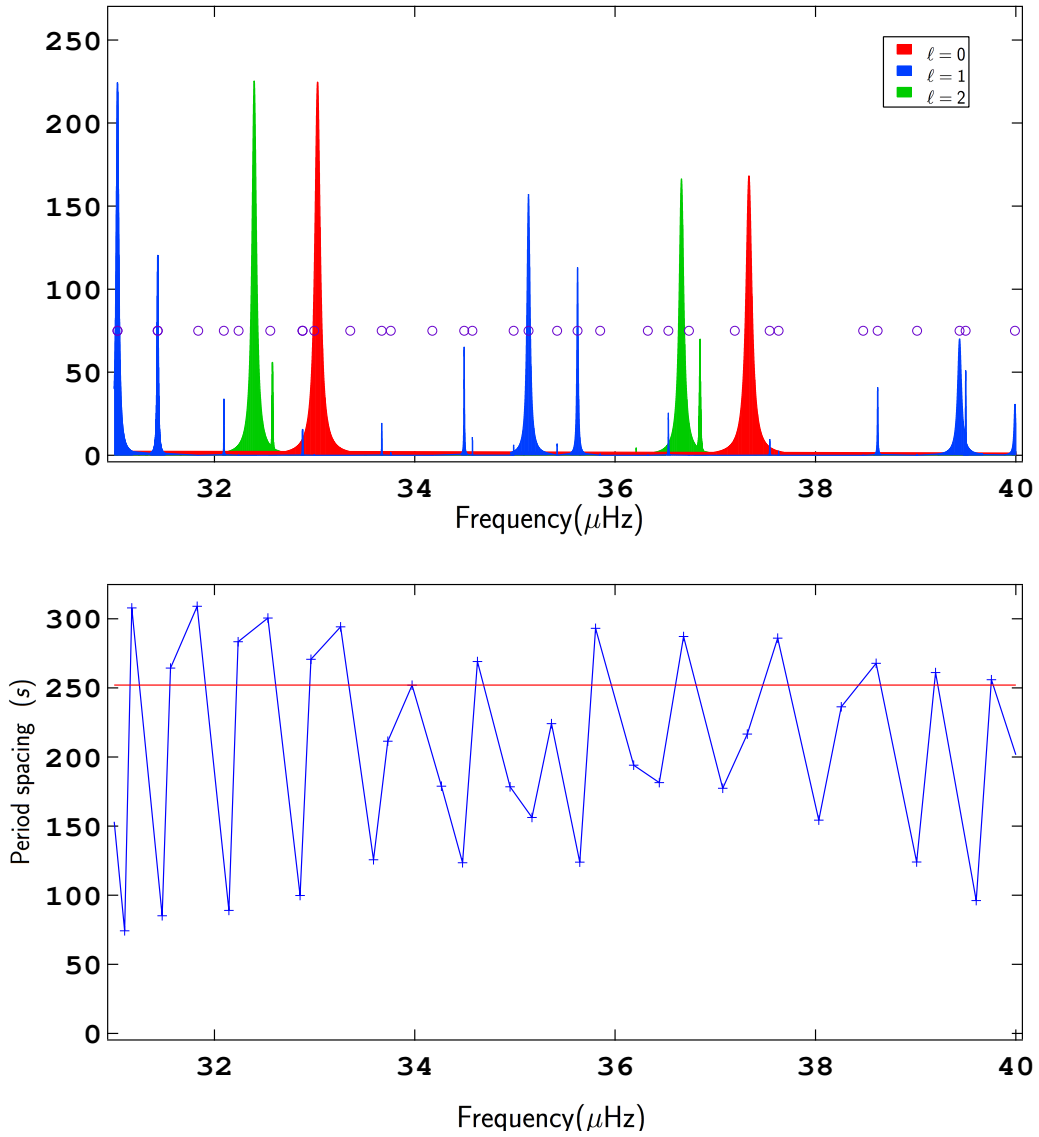

Figure 6.15: **Top:** Resulting power spectra, for an helium burning model shortly after the Helium flash. Only the g-type mixed-modes with low inertia are visible. The purple circles represent the frequencies of all dipole modes. **Bottom:** Computed (blue) and asymptotic (red) period spacing for dipole modes. Accounting for only the visible modes in the power spectrum gives a period spacing smaller than the asymptotic one.

Conclusion

Theoretical power spectra of red giants are in good agreement with the observed ones. In particular, the detectability of mixed-modes seems to correspond to the typical observed power spectra in this evolutionary phase. A more detailed and extended analysis of this result is needed to precise the detectability limit, as well as the relation between the height ratios of mixed-modes and the number of mixed-modes over a large separation. This should be done from both the observational and theoretical point of view, and for various stellar properties (e.g. to test the impact of other parameters such as the metallicity, ...).
For the p-type mode linewidths, we have shown that an adjustment of the main TDC free parameter β is not enough to reach the typical observed red-giant linewidths. However, we have been able to recover the observed linewidths with a change of the anisotropy factor. Quantitative comparisons between theoretical and observed linewidths for red-giant stars should help us to better understand the properties of the interaction between convection and oscillations on the red-giant branch.
Finally, we have exhibited a particular behaviour of the mixed-modes shortly after the He-flash that could lead to a misinterpretation of the observed power spectra. It would be very interesting to observe (and properly identify) such a particular situation which could bring new constraint on the characteristics of post He-flash stellar interiors.

Chapter 7

Non-adiabatic analysis of a *Kepler* subgiant: KIC 6442183

In this chapter, we intend to perform a full seismic analysis, using non-adiabatic computations, of an evolved low-mass star, the *Kepler* subgiant KIC 6442183. Our objective is to provide a first quantitative test for theoretical predictions on mixed-modes linewidths and amplitudes. We also want to investigate to which extent these observations can provide additional constraints on the stellar structure and on the oscillations-convection interaction processes (more precisely on the damping and driving of mixed-modes).
We present in Sect. 7.1 the different information we already have on this star: the spectroscopic data, and the oscillation mode parameters (frequencies, linewidths, heights) extracted from photometric data (from 9 months of *Kepler* observations). We will also shortly present the previous studies on this star, made with adiabatic computations.
Given the presence of mixed-modes in the power spectra, we have to adapt the way we search for the equilibrium models that best fit the observations. The method we have adopted is presented in Sect. 7.2 with the resulting best fit models. A particularity of our equilibrium models is the use of computed non-adiabatic frequencies in the fitting process. We will see in Sect. 7.3.1 the impact of the use of non-adiabatic frequencies. In Sects. 7.3.2 and 7.3.3 we compare the theoretical and observed linewidths and amplitudes. From these comparisons, we can draw conclusions on the energetic modelling of the modes as well as predictions on the detectability of mixed-modes. Finally, in Sect 7.4, we will test these predictions by confronting them to the power spectra obtained with four years of *Kepler* observations, which will also bring us additional constraints on the models.

7.1 State of the Art (Observations and first models)

The *Kepler* light-curves of KIC 6442183 have been analysed by Benomar et al. (2013) using Quarters 5 to 7 (9 months) of *Kepler* observations. They extracted the frequencies, lifetimes and amplitudes of all the modes (corresponding to $\ell = 0, 1, 2$) in the power spectrum using a Markov Chain Monte Carlo fitting algorithm. The star is in the subgiant phase and its main characteristics are given in Table 7.1. Scaling relations show that the mass and radius of the star are approximately 0.94 $M_\odot$ and 1.60 $R_\odot$, respectively. We use the values of mode frequencies, linewidths, and amplitudes as provided by Benomar et al. (2013) to search the corresponding theoretical equilibrium model.

Additional constraints are given by spectroscopic observations (Bruntt et al. 2012; Molenda-Żakowicz et al. 2013). We used the values of $T_{\rm eff}$, $\log g$ and $[Fe/H]$ provided by Molenda-Żakowicz et al. (2013) as constraints for our models. This choice does not really impact our fitting, since the effective temperature and metallicity obtained in both studies are very similar (see Tab. 7.1). The main difference between these two spectroscopic studies is the value of the surface gravity which is not used as a constraint in our fitting (the value of the large separation is much more constraining for the fit).

From this first analysis of the power spectra, Benomar et al. (2014) derived observed inertia ratios between radial and dipole modes (including mixed-modes). They stress that such ratios can give additional constraints for the modelling and the understanding of the internal structure of the star. They also provided a first modelling of this star (based on adiabatic computations) and find that theoretical inertia ratios are in agreement with the observed ones.
Tian et al. (2015), using the same set of observations as Benomar et al. (2013), provided an independent measure of KIC 6442183 mode frequencies, consistent with the previous determination. With these frequencies and the spectroscopic observations by Bruntt et al. (2012), Tian et al. (2015) used a grid based approach to search for theoretical models fitting the observations. Then, they used inertia ratios between dipole and radial modes (with a particular interest for mixed-modes) as an additional constraint to discriminate between the different good fit models. They indeed found that the inertia ratios allow one to more precisely determined the fundamental parameters of the star. They have also shown that a well chosen frequency combination can play a similar role as inertia ratio, allowing them to identify the modes with the most g-mode characteristic.

These theoretical works were based on an adiabatic approach for computing the oscillations. These works showed that models that fit the frequencies of the mixed-modes also reproduce their trapping. This comforts us on the validity of mixed-modes modelling.
An additional analysis of this star with 4 years of Kepler observation was also made (Benomar, private communication). We will discuss in Sect. 7.4 the new asteroseismic constraints brought by a longer observation duration.

	Observations	
$\Delta\nu$ (μHz)	$65.07 \pm 0.09^{(a)}$	$64.9 \pm 0.2^{(c)}$
$\nu_{\rm max}$ (μHz)	$1160 \pm 4^{(a)}$	$1225 \pm 17^{(c)}$
$T_{\rm eff}$ (K)	$5738 \pm 62^{(b)}$	$5740 \pm 70^{(d)}$
$\log g(dex)$	$4.14 \pm 0.10^{(b)}$	$4.03 \pm 0.03^{(d)}$
$[Fe/H]$	$-0.120 \pm 0.050^{(b)}$	$-0.11 \pm 0.06^{(d)}$

Table 7.1: Global parameters of KIC 6442183 used in our study (a) Benomar et al. (2013), (b) Molenda-Żakowicz et al. (2013). Alternative values by (c) Tian et al. (2015), (d) Bruntt et al. (2012).

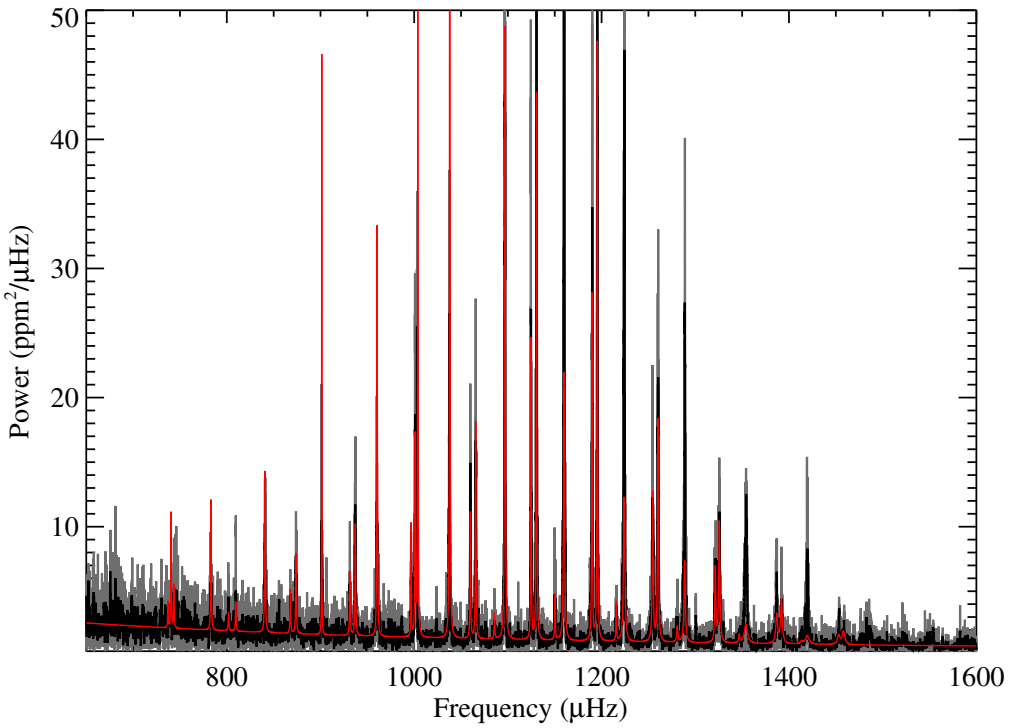

Figure 7.1: Observed power spectrum of KIC 6442183 obtained with 9 months of *Kepler* observations. The Lorentzian fit of oscillation modes by Benomar (private communication) is presented in red.

7.2 Finding the equilibrium model of a star with mixed-modes

Our goal in this section is to find a theoretical model that matches the observational constraints (i.e. mode frequencies and spectroscopic constraints). This will lead us to make quantitative and precise comparisons between theoretical and observed linewidths and amplitudes (see Sects. 7.3 and 7.4). These comparisons will give us new insights on the damping and driving mechanisms in evolved low-mass stars. The equilibrium model is obtained following the procedure detailed in Sect. 7.2.1 with the CESTAM evolutionary code (see Sect. 4.1). Oscillation computations are made with the MAD code (see Sect. 4.2).

The presence of mixed-modes in the power spectrum creates particular conditions for the search of a best-fit model. Standard fitting methods are not useful when mixed-modes are present. Indeed, avoided crossings occur on a short time-scale compared to the usual time steps in evolutionary codes. Thus, for a grid approach it would require to compute an enormous number of models, given that we have to produce models spanning a large range of stellar parameters with a very small time step between each other. A direct Levenberg-Marquardt approach is also problematic because it is difficult to find an appropriate time step. The presence of mixed-modes makes also

the classical technics, using large and small frequency separations (or any frequency combination or ratio), inadequate. Moreover, when dealing with mixed-modes, one should be aware that it is highly probable that all the oscillation modes of a star, of a given angular degree, may not lead to an observable peak in the power spectrum. Thus, we can expect to have, in a given frequency range, more theoretical modes than observed ones.

7.2.1 Fitting process

Mass and age: Deheuvels, Michel (2011) proposed a solution for the search of the best-fit model of a star with mixed-modes by constraining the stellar age and mass in the fit. Considering only one mixed-mode, for a given set of parameters, there is only one value for the mass and age that allows one to simultaneously fit the mean large separation and the frequency of the mixed-mode. This search for the mass and age can be rapidly done for various sets of stellar parameters (such as the mixing-length parameter α, the initial helium abundance Y_0, ...) and physical prescription (metal mixture, overshooting, diffusion ...) allowing one to finally obtain series of models fitting the large separation and the frequency of the mixed-mode. We adopt this method to obtain first constraints on the mass and the age of the star.

Levenberg-Marquardt: We then use a Levenberg-Marquardt algorithm (developed by R. Samadi) to fit the other parameters. An important aspect of our method is to use non-adiabatic frequencies in the Levenberg-Marquardt algorithm. We discuss here-below (see the paragraph on the constraints, and Sect. 7.3.1) the interest and specificities of using non-adiabatic frequencies for the fit. The preliminary results on the mass and age allow us to determine the range of values allowed for these parameters as well as the sensitivity of the mixed-mode frequency to these parameters. As a starting point for the Levenberg-Marquardt algorithm, we choose the model obtained in the previous step that presents the best χ^2 when accounting for all the observational constraints (or at least the same set of constraints that will be used in the Levenberg-Marquardt algorithm).

Free parameters and physical prescriptions: Using the same physical prescriptions as in step 1, we select a set of free parameters (mass, age, ...). We first perform searches of the best fit model for subsets of these parameters. We then add progressively more parameters and constraints. This is done to ensure that the starting point of the algorithm is not too far from the best fit model, as well as to avoid numerical issues. This procedure allows us to finally adjust the different free parameters taking into account all the constraints and in particular the frequencies of all the observed mixed-modes

Constraints: For the fit, we define a χ^2 with a weight parameter that allows us to give more importance to some specific frequencies in the fit. The values of this weight parameter can vary depending on how many constraints we use. The fit is thus made using a merit function defined as

$$\chi^2 = \sum_S \left(\frac{S_{\rm obs} - S_{\rm th}}{\sigma(S_{\rm obs})} \right)^2 + \sum_\nu \left(W_\nu \frac{\nu_{\rm obs} - \nu_{\rm th}}{\sigma(\nu_{\rm obs})} \right)^2 \tag{7.1}$$

where the subscript "*th*" indicates theoretical value, "*obs*" the observed ones and σ the corresponding error. The first sum (over S) represents the contribution to the χ^2 of the spectroscopic constraints. The second sum (over ν) represents the contribution of the asteroseismic constraints (the individual frequencies) with a weight parameter W_ν.
Since mixed-modes bring very strong constraints on the stellar structure and are only weakly affected by surface effects, we increase their weight in our fitting procedure to be sure that the

final model will reproduce the frequency and trapping of these modes with a good precision (see also Sect. 7.4). We also increase, to a lesser extent, the weight of low-frequency p modes (typically below 1200 μHz) compared to high-frequency p modes, in order to account for the uncertainties in the modelling of high-frequency modes due to surface effects. Since we use non-adiabatic frequencies and due to the uncertainties of current empirical methods to correct theoretical frequencies (see Kjeldsen et al. 2008; Sonoi et al. 2015), we do not apply a-posteriori corrections on the theoretical frequencies. This explains our choice to grant different weights for the p-type mode frequencies in the fitting process. To avoid numerical issues, the final model is obtained at the end of series of fits increasing step by step the number of constraints (up to finally take into account all observed constraints with different weights).

7.2.2 Best fit model

The fit was made by given an important weight to the mixed-mode frequency ($W_\nu = 100$ for the mixed-mode at $\nu = 1002.93$ μHz) and limiting the fit of p-type modes to the low-frequency ones ($\nu < 1000$ μHz, to avoid surface effects). I fixed the metallicity and metal mixture of the model and let the mass, the age, the mixing-length parameter and the initial helium abundance as free parameters. The main parameters of the resulting model (SUBG1) are given in Tab. 7.2.2. The parameters of this model are in agreement with the best candidate models found by Benomar et al. (2014) and Tian et al. (2015).

Model	Free parameters output				Input parameters		Additional outputs			
	M	Age	α	Y_0	$[Fe/H]$	Metal mixture	$T_{\rm eff}$	R	log g	$\Delta\nu$
	($M_\odot$)	(Gyr)			(dex)		(K)	($R_\odot$)	(dex)	(μHz)
SUBG1	1.02	10.368	1.61	0.267	-0.120	GN93	5624	1.65	4.01	65.03

Table 7.2: Global parameters of a model fitting the observations of KIC 6442183

During our search for a best model, we have encountered several issues at different steps of the fitting process. In the first step, for some values of M, α, Y_0, our attempts to obtain the age that gives a mixed-mode at the desired frequency were not always successful. It appears sometimes that the model computed for a given age, could be located outside the evolutionary track computed with the same input parameters up to an older age. Even if the difference is small, mixed-mode properties strongly depend on the inner structure of the equilibrium models which could affect the convergence toward a best fit model. Some models seem to present inconsistencies in the central layers. The final interpolation made (at the end of the evolutionary code) to provide a model with enough points for further computations can give near the centre values of the luminosity and mass that are not in full agreement with the energy generation equation ($dL/dm = \epsilon$). As a consequence, the computed radiative gradient could be incorrect and become greater than the adiabatic gradient. When such a situation happens, it leads to a misinterpretation of the region as a convective zone in our oscillation code, while in the point of view of the evolutionary code the region is not mixed (i.e. a radiative zone). The hydrostatic equilibrium in the central layers may be not always ensured which strongly impacts the oscillation properties. I think that these are the main reasons why, sometimes we can not find a mixed-mode at the desired frequency by adjusting the age of the model and sometimes mode identification (radial order n) is incorrect and prevents the Levenberg-Marquardt algorithm from working properly (the same radial order is assigned to two consecutive modes of the same angular degree, or an additional mode with the same radial order and a very close frequency appears).

Searches of an equilibrium model using other weights (such as the same weight for all the modes, an even more important weight for the mixed-modes, ... see also Sect. 7.4) have been made but did not produce an equilibrium model that fit properly the observed echelle-diagram. This could come from some numerical difficulties (such as mode identifications in theoretical computations, consistency of the equilibrium models, ...) and more investigations, including testing the impact of other parameters (such as the metal mixture, diffusion, ...) are needed to better describe this star (see e.g. Tian et al. 2015).

7.3 Comparisons between theory and observations

In these sections, we compare theoretical oscillations properties with the observed ones. We first look at the frequency of the modes in Sect. 7.3.1. Then, Sect. 7.3.2 and 7.3.3 focus on the energetic properties of the modes, respectively their linewidth and amplitude. We then present the theoretical power spectra obtained with model SUBG1 (Fig. 7.5) for comparison with the observed ones (in Fig. 7.1).

7.3.1 Frequencies

We present in Fig. 7.2 an echelle-diagram combining the observed frequencies as well as the theoretical adiabatic and non-adiabatic ones. The impact of the so-called surface effects is clearly visible in this echelle-diagram. The difference between observed and theoretical frequencies increases with the frequency. This is due to the poor modelling of the superficial layers of the stars. The two main processes expected to be responsible for these differences, and not usually included in theoretical computations, are the non-adiabaticity of the modes and the impact of turbulent pressure in the superficial layers of the star. Since we used non-adiabatic computations, we took into account the first one. As a consequence, the differences between observed and theoretical frequencies are smaller for the non-adiabatic frequencies than for the adiabatic ones. This strengthens our non-adiabatic modelling. The remaining discrepancies between observed and non-adiabatic frequencies are believed to be due to the effect of the turbulent pressure. However, it is unlikely that the two processes (non-adiabaticity and turbulent pressure) simply add, the problem being non-linear. Thus, non-adiabatic computations on a model including turbulent pressure are needed to go further in the modelling of these surface effects. The use of 3D hydrodynamic simulation to describe the near surface layers of the star, coupled with a non-adiabatic code (see e.g. Sonoi et al. 2015) is a promising way to improve our modelling of the oscillations.

We remark in this echelle-diagram (Fig. 7.2), in the observed frequency range, three quadrupole modes appearing in the theoretical computations without any equivalent in the observed frequencies. These modes are located away from the quadrupole p-modes ridge because of their mixed nature. As mentioned earlier, this represents an important issue in the modelling of evolved low-mass stars, because we cannot be sure that all mixed-modes can actually be observed. So, it is probable that in a given frequency range, we could find more theoretical frequencies than the observed ones. A first indication of the actual presence of these modes, is given by the distortions in the quadrupole p-modes ridge. We are thus confident that these modes could be detected in KIC 6442183. In the following sections, we will have a closer look on the energetic properties of these additional modes. We will determine, from a theoretical point of view, if longer observations could allow us to resolve these modes.

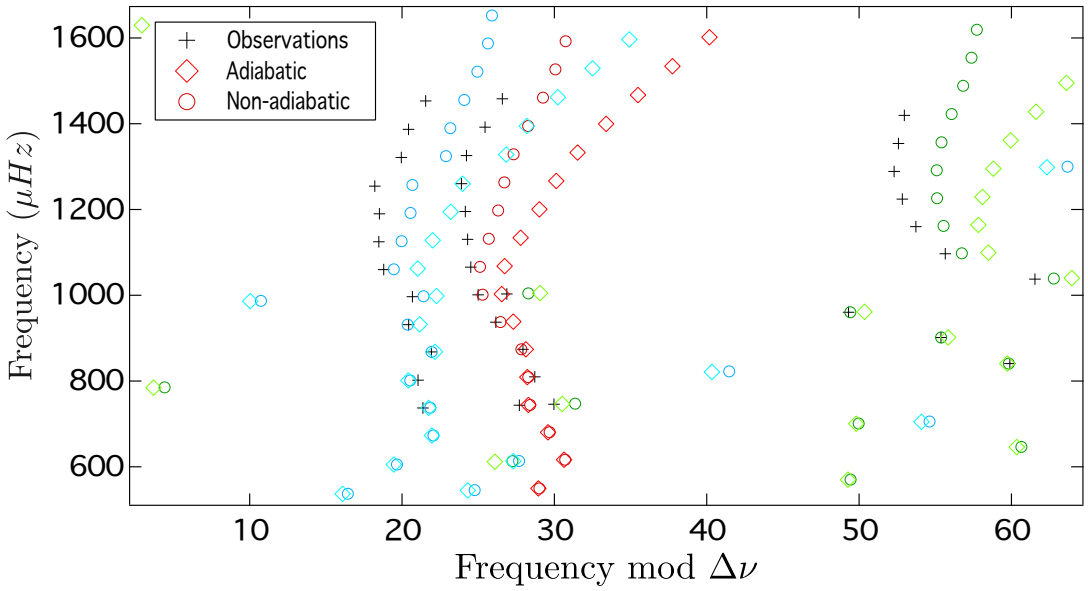

Figure 7.2: echelle-diagram of the observed and theoretical frequencies for modes $\ell = 0$ (red), $\ell = 1$ (green), $\ell = 2$ (blue).

7.3.2 Linewidths

The key parameter for the theoretical mode linewidths is the TDC free parameter β. According to the method detailed in Sect. 4.3 we tune this parameter in order to fit the observed radial mode linewidths. We find that $\beta = -1.78 - 1.12i$, with the perturbation of the mixing-length given by Eq. 3.125 gives the best fit, while assuming an isotropic turbulence, and using non-local parameters from 3D simulations. The resulting linewdiths are presented in Fig. 7.3. Our fit of the β parameter leads to theoretical linewidths in good agreement with the observed ones especially around $\nu_{\max}$. Given the observed error bars, the modes around $\nu_{\max}$ have more importance in the fit. Some discrepancies appear for low-frequency modes were it seems that our theoretical results underestimate the linewidths.
As expected, the dipole g-type modes theoretical linewidths also fit the observed ones. Our theoretical computations also confirm that the radiative damping of dipole modes is negligible in this star. As a consequence, the ratio between radial and non-radial mode linewidths is mainly determined by the ratio of their inertia (see Eq. 7.3). For these mixed-modes, theoretical computations thus reproduce the frequency of the modes as well as their trapping (see also Fig. 7.9).

Concerning the additional quadrupole g-type modes, theoretical computations show that they have small linewidths. If we compare these predicted linewidths with the duration of observations (horizontal lines in Fig. 7.3), it appears that with only 9 months of observations these modes are not, or poorly, resolved. However, 4 years of observations should be enough to resolve these modes.

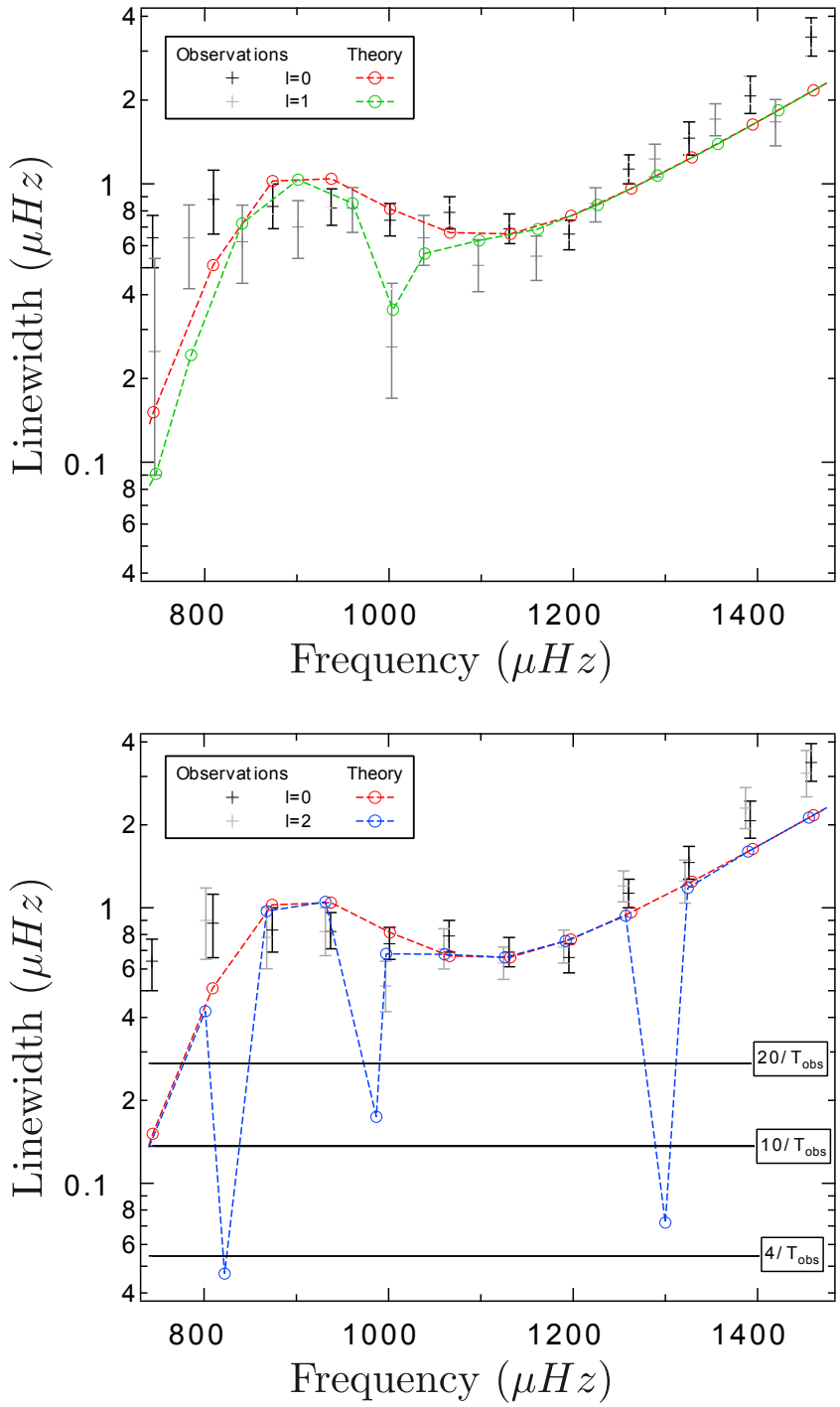

Figure 7.3: Observed and theoretical mode linewidths. **Up:** radial and dipole modes. **Bottom:** radial and quadrupole modes. The horizontal bars indicate the resolution limits ($T_{\rm obs}$ = 9 months). $X/T_{\rm obs}$ indicate that above this line we have at least X points in the linewidth of a mode.

7.3.3 Amplitudes

The direct comparison of observed and theoretical amplitudes presents several issues. The stochastic excitation code provides radial velocity amplitudes (in m/s) while observations provide the amplitudes of bolometric intensity variations (in ppm). As discussed in Sect. 4.4, the conversion from one to another is not easy and will introduce additional uncertainties. Moreover, measured amplitudes may not be accurate because of the complex *Kepler* instrumental response and of the necessary data preprocessing, prior to the power spectrum analysis. On the contrary, amplitude ratios are independent of the radial velocity to bolometric amplitudes conversion and of the instrumental response. Indeed, the conversion factor from radial velocities to bolometric variations is determined by the physics of the modes close to the surface of the star. It thus only depends on the frequency and not on the angular degree or trapping of the modes. Amplitude ratios between radial and non-radial modes thus give the same results either the amplitude are measured in radial velocity or in bolometric variations. We thus choose to compare the theoretical and observed amplitude ratios between radial and non-radial modes to test our theoretical predictions (see Fig. 7.4).

The parameters of the stochastic excitation code, are given in Sect. 4.4. We recall that we consider only the Reynolds stress contribution to the amplitudes. We take into account the visibilities of the modes using the values derived from Ballot et al. (2011). While absolute amplitudes give information on the interaction between convection and oscillations, amplitude ratios allow one to investigate the visibilities of the modes. For mixed-modes, amplitude ratios also reflect the trapping of the modes and the damping processes occurring in the stellar core (see e.g. Eq. 7.2). This is because the work of a mode in the envelope is the same for radial and non-radial modes (see Sect. 6.1).

With the help of the conversion factor given in Eq. 4.4 (a direct output of our non-adiabatic code) we have found that theoretical amplitudes (converted into bolometric variations) are of the order of the observed ones. However, theoretical individual mode amplitudes (and thus the precise bell-shape of the amplitudes) differ from the observed ones. It will need a much more accurate equilibrium model, especially for the description of the superficial layers, to better reproduce individual mode amplitudes.
The amplitude ratios for the p-type non-radial modes reflect their visibilities. The theoretical visibilities (from Ballot et al. 2011) fit the observed ones although smaller error bars may bring better constraints. Concerning the g-type dipole mixed-mode, the theoretical amplitude ratio is also in the observed error bars. As mentioned in the previous section, longer observations may also help us to test our predictions for the three quadrupole g-type mixed-modes present in our theoretical spectrum. Their predicted amplitude ratios are small but when looking at their predicted heights (see the theoretical power spectrum in Fig. 7.5) they should emerge from the noise once resolved.

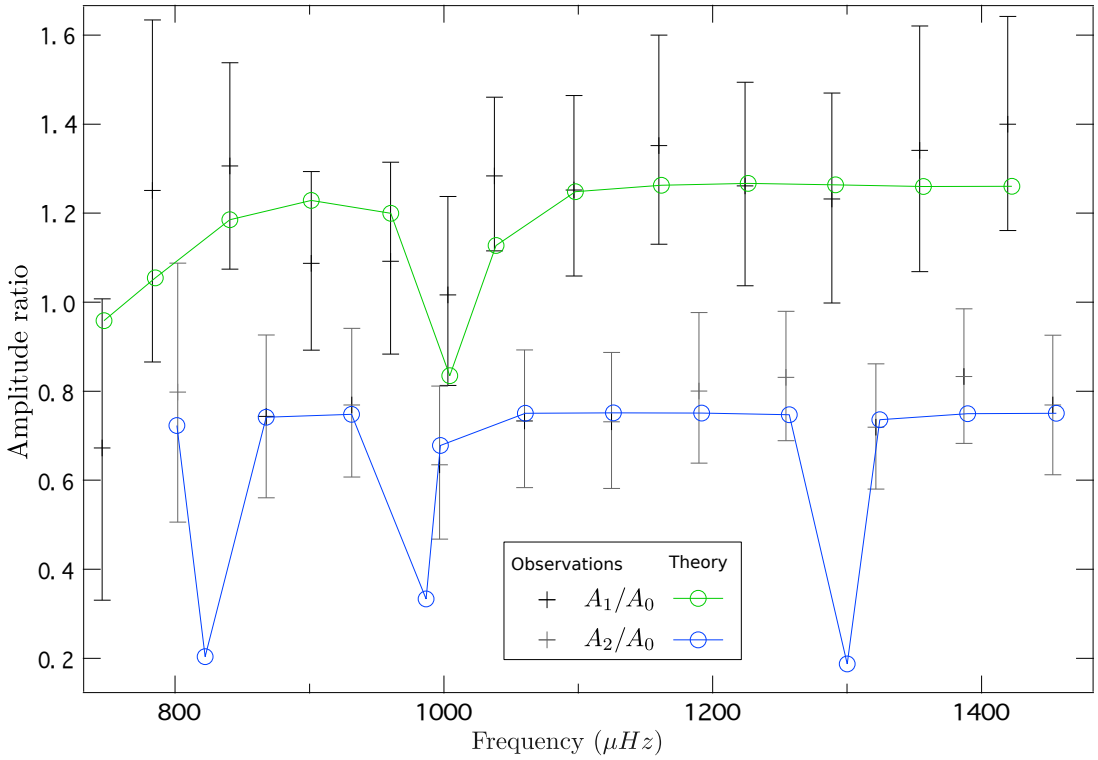

Figure 7.4: Observed and theoretical amplitude ratios between radial and non-radial modes.

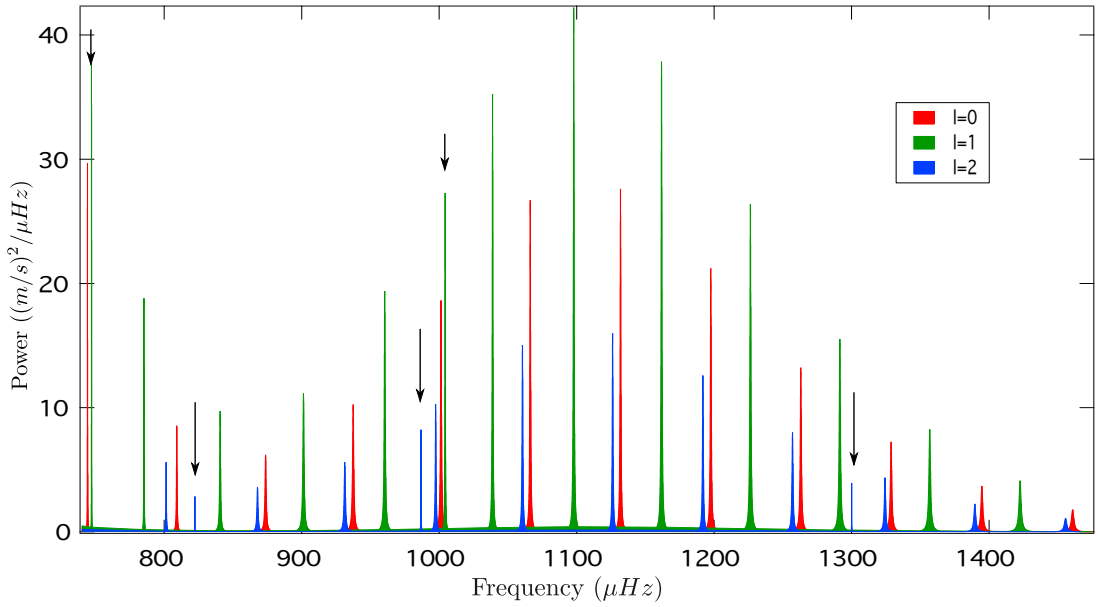

Figure 7.5: Theoretical power spectrum of KIC 6442183 (model SUBG1) for 4 years of observations. Mixed-modes are indicated with black arrows.

7.4 From 9 months to 4 years of observations

Benomar (private communication) have reanalysed this star using the full length of Kepler observations (4 years). The resulting echelle diagram is given in Fig. 7.6. It is very interesting to see that quadrupole mixed-modes are present in this power spectrum approximately at the frequencies predicted by our theoretical model.
We can also note that their heights, in the observed power spectrum, are much lower (by approximately a factor 3) than the height of the closest quadrupole acoustic mode, while our theoretical computations predicted mixed-mode heights of the order of the acoustic ones (see Fig. 7.5). We will look at these differences in more details in Sect. 7.4.2.
Using these new observed frequencies, we looked for improvement of the stellar model. First, we used the same method and weight as for SUBG1, to test the change in the parameters by adding quadripole mixed-modes to the fit (model SUBG2a). Second, we used all the observed frequencies with $W_\nu = 100$ for the mixed-modes (and $W_\nu = 1$ for the other modes) and add undershooting below the convective envelope as a free parameter (model SUBG2b). The characteristics of the new equilibrium models are given in Tab. 7.3. We include convective penetration ("undershooting" below the convective envelope) following the model of Zahn (1991) in which the distance of convective penetration L_p is given by $L_p = \zeta_{\rm pc}/\chi_P H_P$, where $\zeta_{\rm pc}$ is a free parameter and χ_P the adiabatic derivative of the radiative conductivity with respect to the pressure. We recall that classical seismic indicators such as the small separations or frequency ratios are not adapted for stars with mixed-modes. Thus, we can not use such ratios to constrain the undershooting as it was done by e.g. Lebreton, Goupil (2012).
We find that model SUBG2b fits very well the frequencies of the mixed-modes (as required) but presents a systematic shift for the frequencies of the acoustic modes (see Fig. 7.6). The shift for the acoustic modes seems to indicate a small difference between the theoretical and observed ϵ term in Eq.3.49. However, this term is more sensitive to the envelope while the mixed-modes are more sensitive to the core of the star. Thus, we can use this model to discuss the physics of mixed-modes inside the core of the star. It is interesting to note that this model, that best fits the frequencies of the two high frequency quadrupole mixed-modes also gives the best fit of their inertia ratios (see Fig. 7.12). This illustrates the difficulties to fit simultaneously and with high precision the frequencies of mixed-modes and acoustic modes.

The energetic mode properties (linewidths, amplitudes, heights) of models SUBG1 and SUBG2a are similar. I will thus discuss, in the next sections, the comparison between the 4 years of observations and model SUBG1 (to test the prediction made with only 9 months of observations) and model SUBG2b (to test the effect of a better fit of mixed-modes frequencies).
Given that models SUBG1 and SUBG2b do not present important differences in the absolute value of acoustic modes linewidths and amplitudes, I present in the following ratios of energetic properties between radial and non-radial modes. This will allow us to have a clearer view on mixed-modes properties by avoiding the systematic discrepancies between observed and theoretical linewidths away from $\nu_{\rm max}$ (as already noted from the comparison with 9 months of observations).

Model	Free parameters output					Input parameters		Additional outputs			
	M ($M_\odot$)	Age (Gyr)	$\alpha_{\rm MLT}$	Y_0	$\alpha_{\rm under}$	$[Fe/H]$ (dex)	Metal mixture	$T_{\rm eff}$ (K)	R ($R_\odot$)	log g (dex)	$\Delta\nu$ (μHz)
SUBG1	1.02	10.368	1.61	0.267	No	-0.120	GN93	5624	1.6514	4.0114	65.03
SUBG2a	1.02	10.368	1.60	0.262	No	-0.120	GN93	5620.5	1.6917	4.0014	65.02
SUBG2b	1.02	10.388	1.60	0.261	0.26	-0.120	GN93	5620.5	1.6563	4.0089	64.79

Table 7.3: Global parameters of the models fitting the observations for KIC 6442183

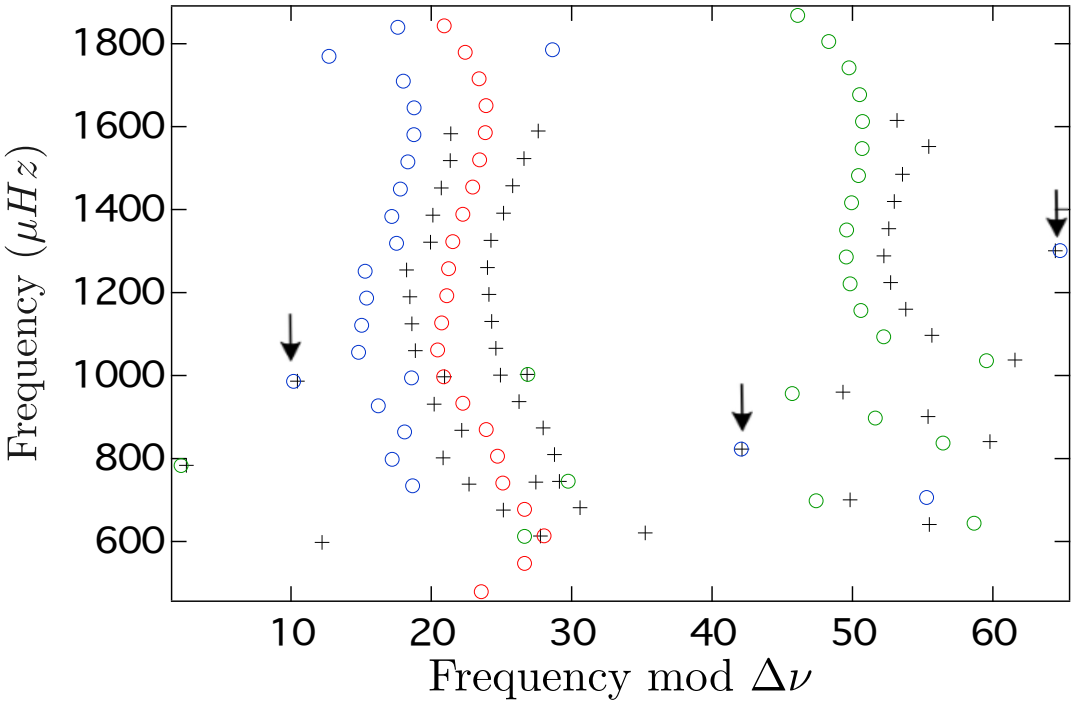

Figure 7.6: Echelle-diagram from the 4 years of *Kepler* observations of KIC 6442183 (in black) along with the non-adiabatic frequencies from model SUBG2b ($l = 0$ in red, $l = 1$ in green, $l = 2$ in blue). Additional quadrupole mixed-modes are marked by black arrows

7.4.1 Dipole modes

Concerning the dipole modes, additional observations give smaller error bars and confirm our first theoretical results for the linewidth ratios (Fig 7.7) and amplitude ratios (Fig. 7.8). We can also note that for dipole modes there is no significant differences between the ratios derived from model SUBG1 and model SUBG2b even if this last one fits better the mixed-mode frequencies. It appears that two dipole modes (at 840 and 1400 μHz) identified as acoustic modes (from the echelle-diagram) present linewidth ratios of the order of mixed-mode ones (in conflict with our predictions) but amplitude ratios of the order of the acoustic mode ones (in agreement with our predictions). It seems that these modes exhibit an inconsistency in their energetic properties, with linewidths of mixed-modes and amplitudes of acoustic modes. In the computations of models close to the ones presented here, we never found mixed-modes at these frequencies. From a theoretical point of view, we do not see a simple way to solve this problem (i.e. decreasing the linewidths of the modes without changing their amplitudes). It is however interesting to note that, to exhibit such a behaviour of the modes, it requires to study the energetic aspects of the modes. Hence linewidths and amplitudes (and from them inertias), give additional information from the ones derived from mode frequencies alone.

From observed amplitudes and linewidths we can compute observed inertia ratios as suggested by Benomar et al. (2014). They showed that, for resolved modes, if we assume (as made in Sect. 6.1.1), that the product PI does not depend on the trapping, the inertia ratio (between a non-radial and a radial mode at a given frequency) is given by:

$$\frac{I_\ell}{I_0} \simeq V_\ell \frac{A_0}{A_\ell} \sqrt{\frac{\Gamma_0}{\Gamma_\ell}} \tag{7.2}$$

where V_ℓ is the mode visibility. Fig. 7.9 shows that theoretical inertia ratios are in good agreement with the observed ones, except for the two modes that present an inconsistency between their linewidth and amplitude ratios. The inertia ratio being derived from linewidth and amplitude ratios, it is expected that our theoretical computations are not fully in agreement with the observed inertia ratios. Further investigations are required to understand this issue.

Nonetheless these results strengthen the conclusions found based on the 9 months of observations: our predictions for dipole mixed-modes are still not contradicted by observations.

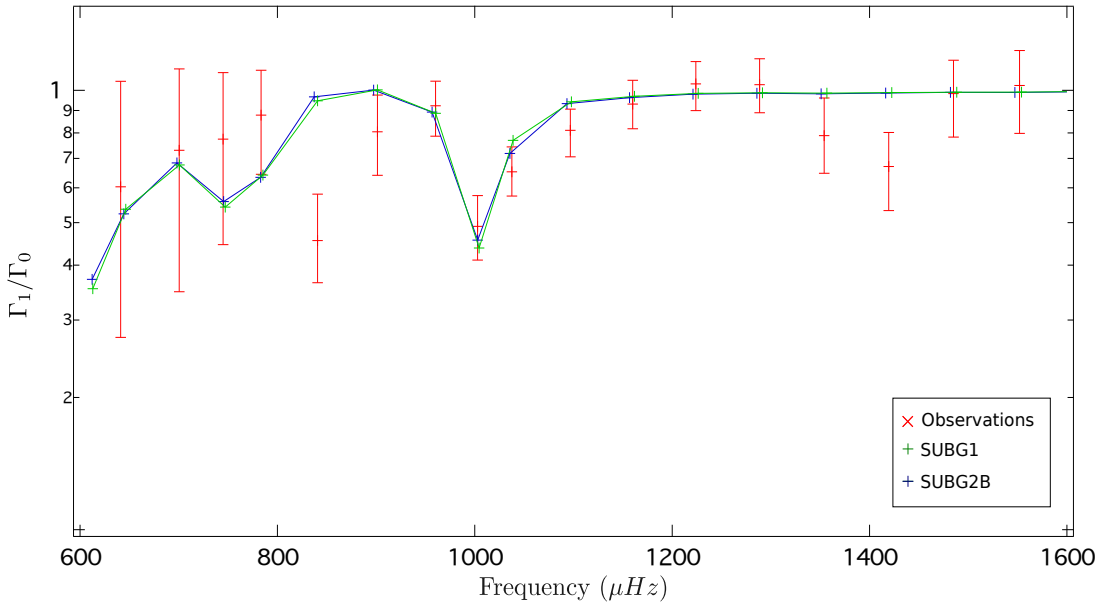

Figure 7.7: Observed and theoretical linewidth ratios of dipole modes of KIC 6442183.

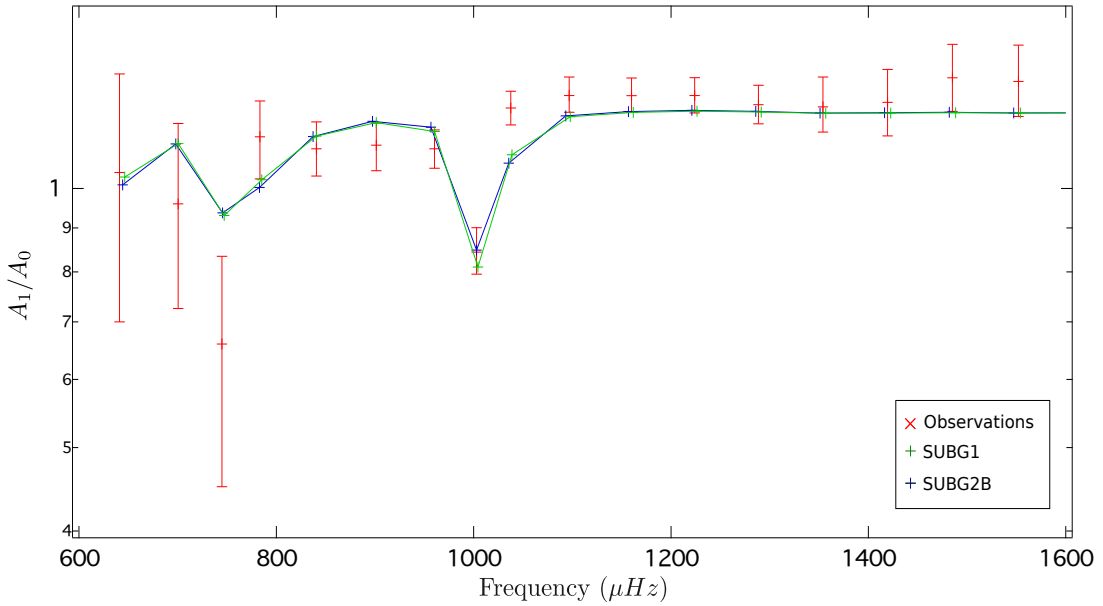

Figure 7.8: Observed and theoretical amplitude ratios of dipole modes of KIC 6442183.

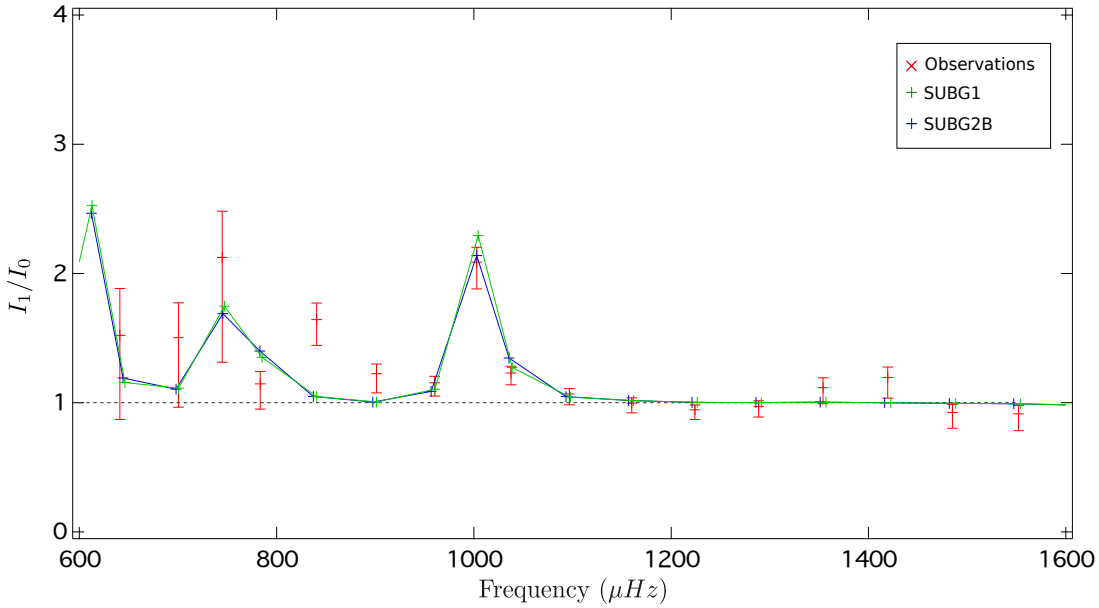

Figure 7.9: Observed and theoretical inertia ratios of dipole modes of KIC 6442183. The observed inertia ratio are computed with Eq. 7.2.

7.4.2 Quadrupole modes

For quadrupole mixed-modes, the theoretical energetic properties of these modes are not always in agreement with the observed ones. The linewidth ratios of mixed-modes predicted for model SUBG1 are lower than the observed ones (see Fig. 7.10), mainly for the mixed-mode at $1002\mu Hz$. The differences for the other quadrupole mixed-modes are less marked thus, we will focus on this mode in the following. For model SUBG2b (which better fits the mixed-mode frequencies), the linewidth ratio of this mode is a little higher but still too low to fit the observed one.

For model SUBG1 the theoretical amplitude ratio of this mixed-mode is within the observed error bars. For model SUBG2b, the linewidth ratio of this mode is closer to the observed ones but its amplitude ratio is further from the observations. This is quite surprising since the linewidth of a mode directly affects its amplitude. This appears as an inconsistency between the linewidth and amplitude ratio of this mixed-mode. It presents a linewidth ratio of an acoustic mode (in conflict with our predictions) while its amplitude ratio corresponds to the one of a mixed-mode (in agreement with our predictions).

From a theoretical point of view, when radiative damping is negligible (as it appears to be the case in our different equilibrium models), we expect from Eq. 6.3 (neglecting the work in the core W_c) that once resolved, mixed-mode heights should be of the order of acoustic mode heights. As we can see in Fig. 7.13 the observed linewidths show that quadrupole mixed-modes are resolved but their heights in Fig. 7.15 are smaller than the nearest quadrupole acoustic modes by approximately a factor 3, which is not consistent with theoretical predictions.
Moreover, without damping in the core (i.e. neglecting W_c) we can rewrite the linewidth and amplitude ratios between quadrupole and radial modes as (following the same developments made in Sect. 6.1.1):

$$\frac{\Gamma_2}{\Gamma_0} = \frac{(W_c + W_e)_2}{I_2}\frac{I_0}{W_{\mathrm{e},0}} = \frac{I_0}{I_2}, \tag{7.3}$$

$$\left(\frac{A_2}{A_0}\right)^2 = V_2\frac{\Gamma_0}{\Gamma_2}\left(\frac{I_0}{I_2}\right)^2 = V_2\frac{I_0}{I_2}, \tag{7.4}$$

with V_2 the modes visibility (which is a constant). Amplitude and linewidth ratios should thus be a measure of inertia ratios when core damping is negligible. We should thus expect that models that best fit the linewidth ratios also fit the amplitude ratios and reciprocally, which is not the case here.
Contrary to linewidths and amplitudes, inertias are not significantly affected by energetic effects since they are mostly determined by the part of the star where the oscillations are quasi-adiabatic. To go a little further we can thus compare the theoretical inertia ratios and those derived from observed amplitudes and linewidths (either with Eq. 7.2 or Eq. 7.3). We see that for our two models there is no significant differences between the observed and theoretical inertia ratios (see Fig. 7.12). However, deriving observed inertia ratios from Eq. 7.2 and Eq. 7.3 (or Eq. 7.4) does not give compatible results for quadrupole mixed-modes, which is an observational evidence of a damping process in the core (see Fig. 7.12).

All these results lead us to conclude in the presence of an additional damping (other than radiative damping) in the core of the star. This seems clear for the quadrupole mixed-mode at 1002 μHz. An additional damping will indeed increase the work in the core and thus the linewidth of the mode and decrease its amplitude. This will reconcile theoretical results and observations. In order to have height ratios between the mixed-mode and the nearest quadrupole acoustic mode $H_{2,\mathrm{mixed}}/H_{2,\mathrm{p}} \simeq 3$, Eq. 6.3 suggests that the ratio between the work in the core and in the envelope should be $W_c/W_e \simeq 0.7$, which is quite significant.
This damping affects only the quadrupole mixed-modes since for dipole ones our theoretical results provide a good fit of all the energetic properties of the mixed-modes and derivations of inertia ratios from Eq. 7.2 and Eq. 7.3 give the same results, compatible with the absence of core damping for dipole modes.

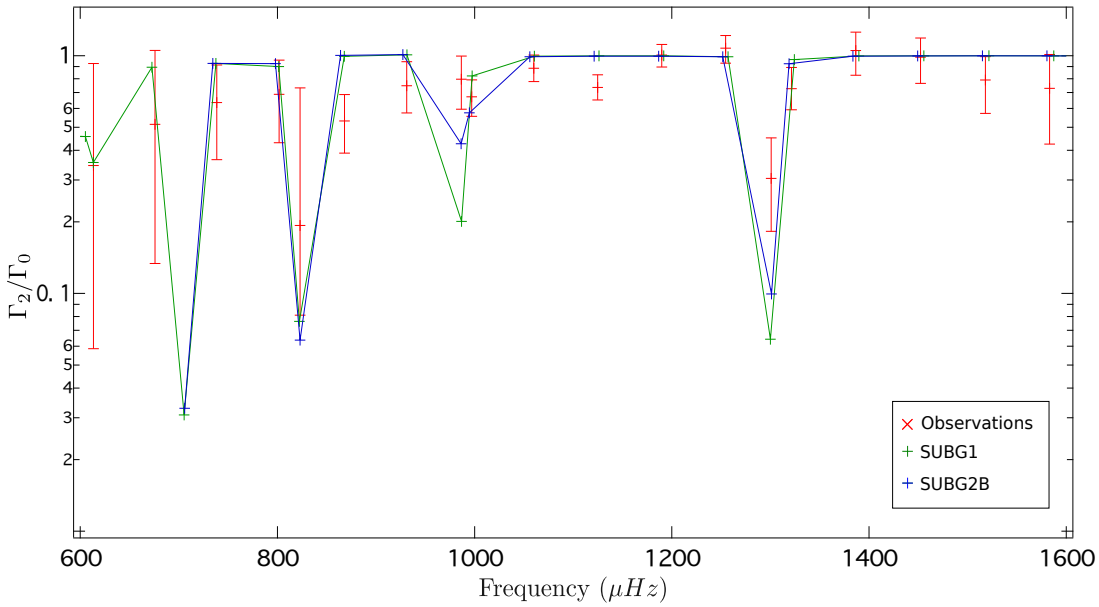

Figure 7.10: Observed and theoretical linewidth ratios of quadrupole modes of KIC 6442183.

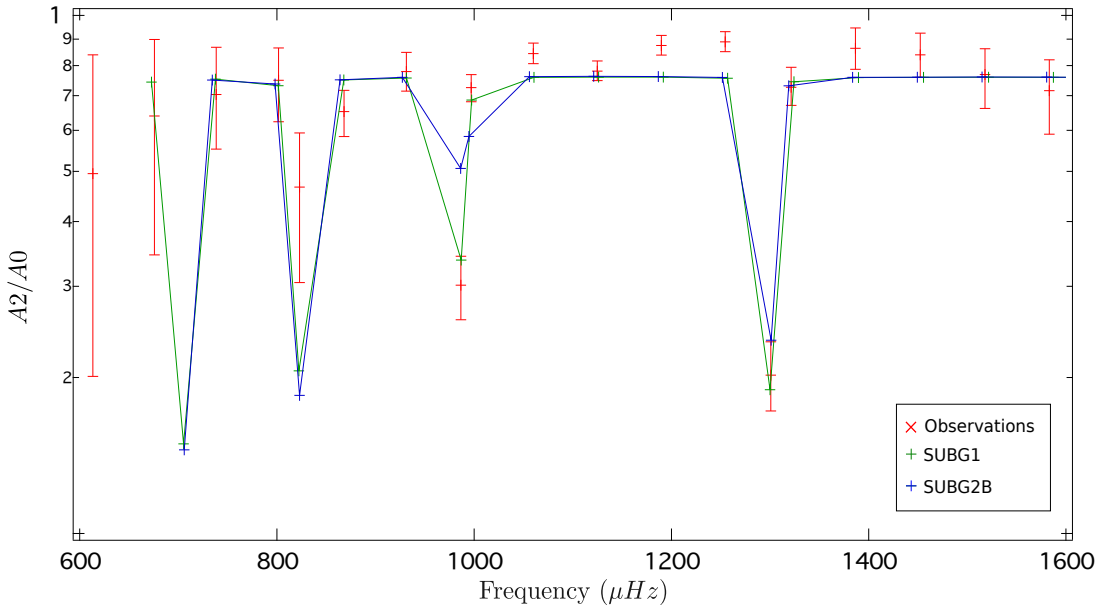

Figure 7.11: Observed and theoretical amplitude ratios of quadrupole modes of KIC 6442183.

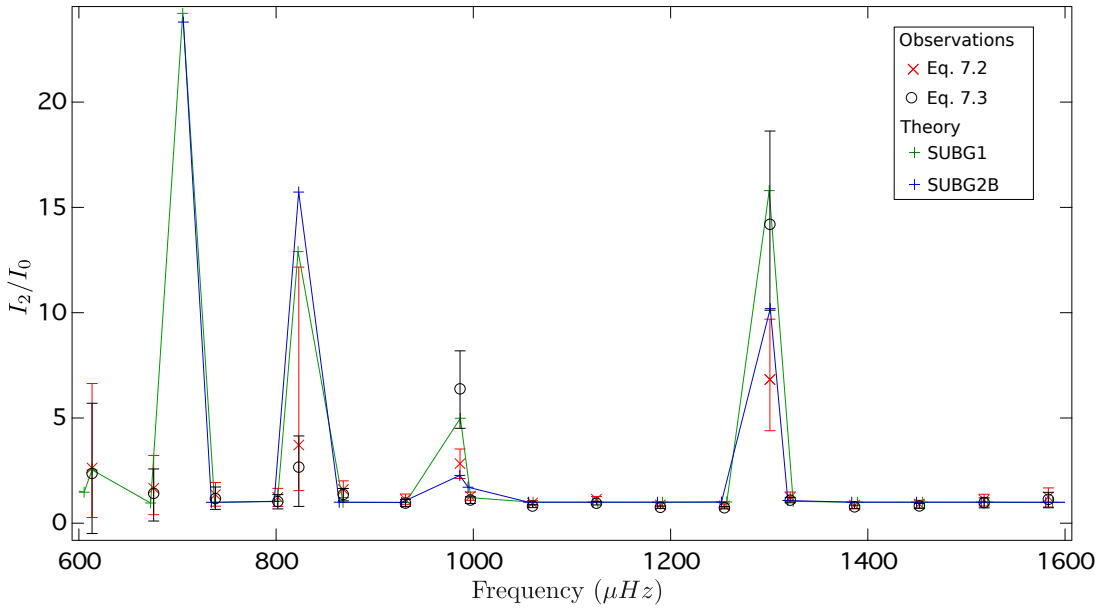

Figure 7.12: Observed and theoretical inertia ratios of quadrupole modes of KIC 6442183.

Conclusion

The use of non-adiabatic frequencies to model an observed star, has allowed us to strongly reduce the impact of surface effects on the fitting process. We have found theoretical results on the energetic aspects of observed modes (including mixed-modes) in overall agreement with the observations. We have however exhibited that at least one quadrupole mixed-mode theoretical energetic properties do not coincide with the observed ones. This calls for an additional damping mechanism, acting in the core of the star that can affect quadrupole mixed-modes.

It is interesting to note that some observations of red-giant stars also point toward the presence of an additional damping mechanism. This concerns the particular subset of stars displaying low-amplitudes dipole modes (for both p-dominated and g-dominated modes). Indeed, such stars also present dipole modes of small amplitudes (even for the p-dominated ones) while their linewidths are of the order of the radial ones (see e.g. García et al. 2014). This situation is thus similar to the one we have encountered for the subgiant presented in this chapter. The origin of the additional damping needed to explain this phenomenon is still under investigation. García et al. (2014) suggested that a fossil magnetic field in the core could explain why only the dipole modes are affected. However, for the star they had investigated (KIC 8561221) they do not find evidence of magnetic effects on dipole modes frequencies. This reduces the possibility that this star has a strong magnetic field in its core. Cantiello, Fuller (2015) also suggested that a strong magnetic field in the core can suppress the amplitude of the dipole modes. Moreover, they identified the 10% of stars on the RGB exhibiting depressed dipole modes as stars with strongly magnetised cores, possible descendants of the family of magnetic Ap stars.

Whether the damping mechanism, which seems to be missing in our modelling has the same origin than the one responsible for depressed dipole modes in more evolved star has still to be investigated. Observations of other subgiant stars presenting this effect and their non-adiabatic modelling should bring more insight on the characteristics of a possible additional damping process.

Appendix: Observed mode properties of KIC 6442183 with 4 years of *Kepler* observations.

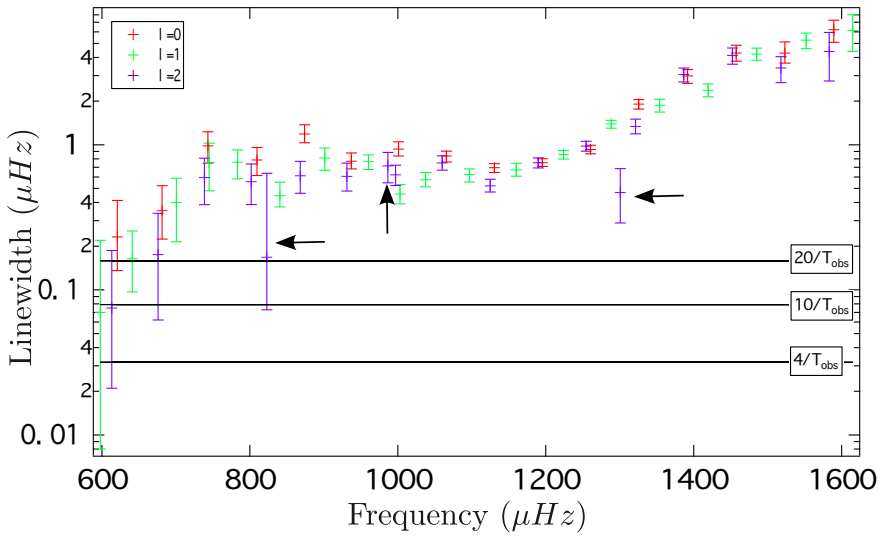

Figure 7.13: Observed modes linewidths of KIC 6442183 (with 4 years of *Kepler* observations, Benomar private comm.), quadrupole mixed-modes are marked by black arrows

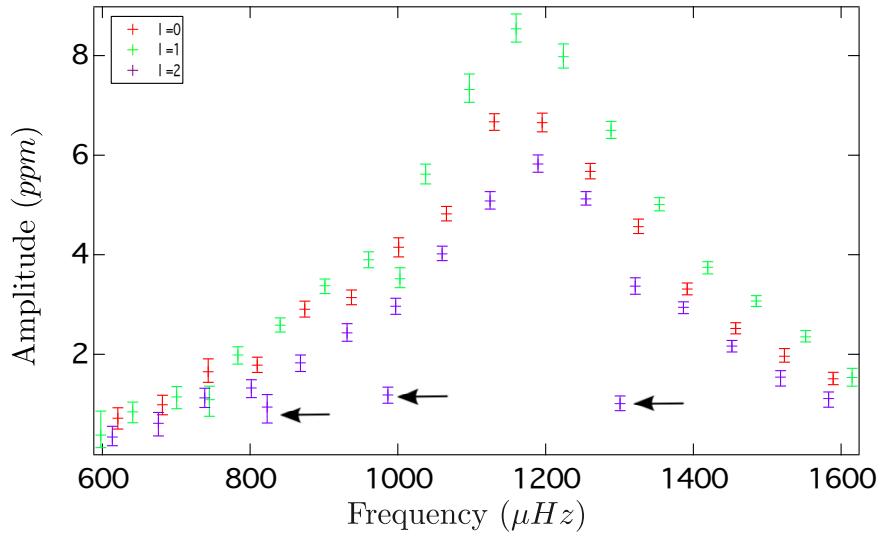

Figure 7.14: Observed modes amplitudes of KIC 6442183 (with 4 years of *Kepler* observations, Benomar private comm.), quadrupole mixed-modes are marked by black arrows.

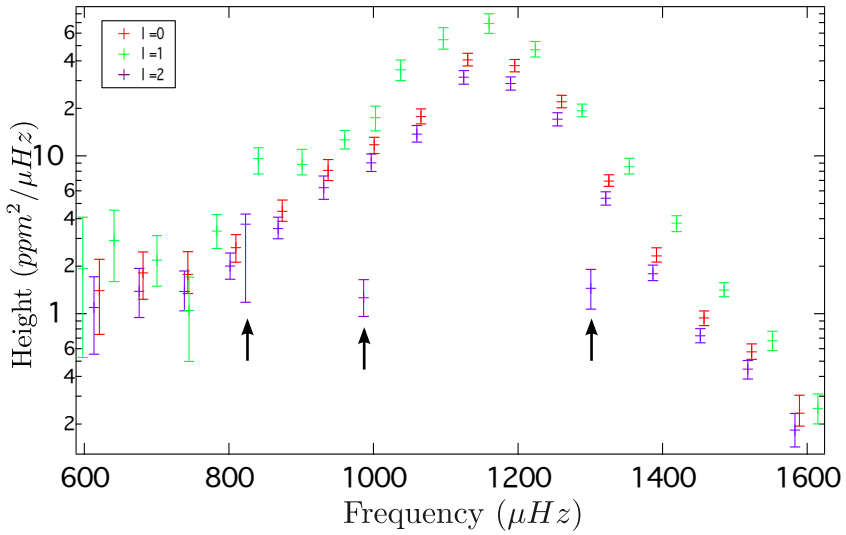

Figure 7.15: Observed modes heights of KIC 6442183 (with 4 years of *Kepler* observations, Benomar private comm.), quadrupole mixed-modes are marked by black arrows

Chapter 8

Conclusions and perspectives

The main questions behind this thesis were linked to the physical processes that give their energetic properties to solar-like oscillations. We were interested to search constraints on the proper way to model these processes. But beyond all, we wanted to study the links between the stellar structure, the properties of the physical processes within, and the different morphologies exhibited in observed power spectra. We have searched which are the characteristics of the modes that could be detected in observations and which information they could give us.

Original contributions to the thesis problematic

The aim of this thesis was to investigate the energetic properties of solar-like oscillations in evolved low-mass stars. In particular, we have been interested by the interactions between convection and oscillations. We have studied the damping and driving processes governing solar-like oscillations to understand the links between the stellar properties and the different morphologies of red-giant power spectra. At this end, we have performed non-adiabatic analyses, of radial and non-radial modes (including mixed-modes), of stellar models representative of CoRoT and *Kepler* observations. An important goal of this thesis was to reproduce the general characteristics of observed power spectra. We have succeeded to reproduce the typical bell-shape of power spectra of solar-like oscillations, with a maximum amplitude at the frequency $\nu_{\rm max}$ predicted by scaling relations. This was done by ensuring the existence of a plateau of the damping rates at $\nu_{\rm max}$, following the prescriptions of Belkacem et al. (2011) for the adjustment of the main free parameter of our time-dependent treatment of convection.

We have begun our studies of the interaction between convection and oscillations by comparing the theoretical and observed linewidths, either from scaling relations or from fit of some specific stars. Scaling relations were used for models from the main-sequence to the red-giant phase to obtain theoretical radial mode linewidths in agreement with the observations. The fit of individual mode linewidths for main-sequence and subgiant stars have exhibited the validity of the theoretical linewidth around $\nu_{\rm max}$ and the difficulties to properly reproduce the linewidths, for the stars with the lower $\nu_{\rm max}$, especially at low frequency. This has allowed us to obtain strong constraints on the modelling of the time-dependent convection and to open new perspectives for a better modelling mainly through the impact of the anisotropy on solar-like oscillations linewidths.

We have then studied the changes in the morphology of theoretical power spectra following the evolution of a red-giant star. This study clearly exhibits the impact of the radiative damping

on mixed-modes detectability. It has allowed us to derive a theoretical detectability limit for mixed-modes on the red-giant branch. The study of models of different masses exhibiting similar power spectra has allowed us to extend this limit across the typical mass range of observed red giants. We have concluded that the number of mixed-modes over a large separation is a good indicator of the final morphology of the power spectra. For star with more than approximately 60 dipole mixed-modes over a large separation, we predicts that only the modes strongly trapped in the envelope could be detected, whatever the duration of observations. This could give some limits for target selections in observation campaigns, and to predict the duration of observations required to extract information on the core of the stars.

We have also exhibited a specific behaviour of mixed-mode properties of a stellar model, shortly after the helium-flash, for which one have to be very careful in the interpretation of the corresponding power spectrum. The consecutive helium sub-flashes leave regions of partial trapping inside the core of the star. As a consequence, only the mixed-modes trapped in the outer cavity of the core reach high enough amplitude at the surface of the star. In the power spectrum, between two p-type modes, approximately only one mixed-mode over three can be detected. In such case, the period spacing that could be derived from these modes does not correspond, by far, to the asymptotic period spacing.

Finally, we have performed a full seismic analysis of an observed *Kepler* subgiant using non-adiabatic computations. For this study, we have used two sets of observations (of 9 months and 4 years) to obtain additional information on the processes behind mixed-mode energetic properties and test our theoretical predictions. This star is very challenging, for some theoretical mode properties (frequency, linewidth, amplitude) are in good agreement with the observations while others (mainly the quadrupole mixed-modes) present important differences and bring new questions on mode damping.

Theoretical predictions vs Observations

The confrontation of our theoretical computations to observations have allowed us to conclude on the strengths and limits of our modelling of the damping and driving processes.

By adjusting the main free parameter of the time dependent treatment of the convection (TDC), the complex free parameter β, we have been able to reproduce the observed scaling relation between the effective temperature and the linewidth of the modes at $\nu_{\max}$ for main-sequence and subgiant stars. Adjustment of this parameter also allows us to fit the observed linewidths of *Kepler* main-sequence stars. In this study, we have strengthened the use of non-local parameters derived from 3D hydrodynamical simulations. However, these fits were not perfects, and for some specific stars important discrepancies appear between observed and theoretical mode linewidths away from $\nu_{\max}$. For red-giant branch stars, adjustment of the free parameter β is not enough to reproduce the typical observed linewidths. In order to obtain theoretical linewidths in agreement with the observed $\Gamma_{\max} - T_{\rm eff}$ relation we had to also adjust the anisotropy factor in the TDC treatment.

For red-giant branch stars, our modelling of the driving and damping processes (including radiative damping in the core) has allowed us to reproduce different morphologies of observed power spectra, following the evolution of the star. In particular, the detectability of mixed-modes derived from theoretical computations is in good agreement with the observations. Stars with

similar masses, large separation and frequency of maximum power as our equilibrium models exhibit behaviours of mixed-modes similar to the ones found following the evolution of power spectra along the red-giant branch: from dipole mixed-modes with high heights, to heights clearly modulated by the inertia and finally with only p-dominated modes visible in the power spectrum. It seems however that theoretical heights of g-dominated dipole mixed-modes are a little higher than the observed ones, especially for models at the base of the red-giant branch for which a modulation by the inertia seems to be present in the observed power spectrum. Concerning the specific behaviour of mixed-modes observed in the stellar model shortly after the helium flash, we need to search for observed stars around this evolutionary stage to test our theoretical predictions.

The non-adiabatic results for the subgiant model of KIC 6442183 are in overall good agreement with the observations. In particular theoretical linewidths and amplitudes of g-dominated dipole mixed-modes have been confirmed by the increase of the duration of observations (from 9 months to 4 years). For some dipole acoustic modes, we found inconsistency between the linewidth and amplitude ratios that we can not explain. It is not clear if an unknown mechanism or some uncertainties in the fit of individual peaks in the observed power spectrum could be at the origin of this issue. However, we exhibit significant differences between the theoretical and observed linewidths of quadrupole g-dominated mixed-modes. Our theoretical predictions underestimate quadrupole mixed-mode linewidths while they give amplitudes and inertias in agreement with the observations. These modes present amplitudes and inertias of g-dominated mixed-modes with linewidths of acoustic modes. This is not compatible with the theoretical modelling of core damping based only on radiative damping.

Possible origins of the disagreements between observations and theoretical results

The TDC treatment is certainly one of the major source of uncertainty that could lead to differences between theoretical and observed linewidths. Indeed, this treatment involves strong assumptions for the closure terms and the perturbation of convective fluctuations. The main approximation of the TDC treatment is made for the closure term of the perturbed energy equation, and is represented by the free complex parameter β. Adjusting only this parameter is not enough to accurately reproduce the observations. Another source of uncertainty comes from the anisotropy factor. While the linewidths of main-sequence stellar models seem to hardly depend on the anisotropy factor, red-giant ones are much more affected by this parameter. Moreover, this factor varies a lot between the top and the bottom of 3D hydrodynamical simulations. This leads to an uncertainty in the value we should use in non-adiabatic computations, and if it is possible to find one value that will be in agreement with 3D simulations and with the observed linewidths. The description of the perturbation of the mixing-length could also explain the discrepancies between observed and theoretical linewidths. Several formulations for the perturbation of the mixing-length have been proposed and should be tested (we only tested two formulations).

We have mentioned some difficulties for the direct comparison of theoretical and observed amplitudes and heights of solar-like oscillations. Theoretical amplitudes are obtained in radial velocities while the observations are made in intensity fluctuations. The conversion factor between radial velocities and intensity fluctuations is certainly a source of uncertainties in the study of mode amplitudes and heights. The inaccuracy of the conversion factor derived from non-adiabatic computations is probably caused by the poor description of the upper layers of the convective envelope. Moreover, the evolution of the height of mixed-modes with the duration of observations

is described following simple relations that have still to be confronted to observations. A precise observational determination of mixed-mode linewidths and amplitudes on the red-giant branch is needed to constrain core damping and to investigate why our theoretical predictions seem to not exactly reproduce the inertia modulation of dipole g-dominated mixed-mode heights at the base of the red-giant branch.

For the issue of the quadrupole mixed-mode linewidths in the subgiant star studied here, it appears that a new damping process should be added to theoretical computations. This damping should affect only quadrupole mixed-modes at this early stage in the subgiant phase and should represent a significant contribution to the total damping (around 40% of the total work integral of the mode). This new damping could be related to the issue of depleted dipole modes observed in some red-giant stars. The question of the exact origin of this damping is currently open (some studies invoke the impact of core magnetic field).

Perspectives

Improvements of the TDC treatment are needed to go further in the study of the energetic properties of solar-like oscillations. Confrontations of theoretical predictions to observations would bring us strong constraints on the properties of the interactions between convection and oscillations. This would allow one to precise the treatment and the choice of parameters to apply. In particular, precise comparisons between observed and computed mode linewidths would allow one to discriminate between different formulations for the closure terms of the perturbations of convective fluctuations.
When we would obtain very accurate linewidths, the comparisons of observed and theoretical amplitudes could constrain the stochastic excitation treatment (because the amplitudes strongly depend on the linewidths). Strong constraints on observed amplitudes would also help us to improve the treatment of the interaction between convection and oscillations. Indeed, the conversion factor from radial velocity to intensity variations, a direct output of our non-adiabatic code, is affected by the TDC treatment. Precise comparisons between theoretical and observed linewidths and amplitudes will thus give us the opportunity to test and improve the time-dependent treatment of convection and then the stochastic excitation model.
When treated, we should have with the full length of *Kepler* observations, a lot of useful date to perform extended and detailed comparisons between observations and theoretical predictions.

An important opportunity for understanding the interaction between convection and oscillations is now open due to 3D hydrodynamical simulations. First, one could preform non-adiabatic computations on patched models to obtain more accurate results. Patched models are obtained by replacing the upper layers of standard evolutionary models by the stratification coming from 3D simulations. Studies of the energetic properties of modes from these more realistic models (e.g. accounting for the turbulent pressure) would give us an insight on the effect of a more accurate description of the convection on oscillation properties. Second, eigenmodes directly appear in 3D hydrodynamical simulations. One can thus compare the properties of these modes with the ones computed from standard or patched models. In particular, we could directly extract from 3D simulations the work of these modes. This would give us a more realistic description of the interaction between the convection and the oscillations. Comparing these results from the one of the TDC treatment should allows one to improve the theoretical description of the convection-oscillations interaction.

Bibliography

Aerts C., Christensen-Dalsgaard J., Kurtz D. W. Asteroseismology. 2010.

Aizenman M., Smeyers P., Weigert A. Avoided Crossing of Modes of Non-radial Stellar Oscillations // A&A. VI 1977. 58. 41.

Alexander D. R., Ferguson J. W. Low-temperature Rosseland opacities // ApJ. XII 1994. 437. 879–891.

Ando H., Osaki Y. Nonadiabatic nonradial oscillations - an application to the five-minute oscillation of the sun // Astronomical Society of Japan, Publications. 1975. 27. 581–603.

Ando H., Osaki Y. The Influence of the Chromosphere and Corona on the Solar Atmospheric Oscillations // Astronomical Society of Japan, Publications. 1977. 29. 221–234.

Angulo C., Arnould M., Rayet M., Descouvemont P., Baye D., Leclercq-Willain C., Coc A., Barhoumi S., Aguer P., Rolfs C., Kunz R., Hammer J. W., Mayer A., Paradellis T., Kossionides S., Chronidou C., Spyrou K., degl'Innocenti S., Fiorentini G., Ricci B., Zavatarelli S., Providencia C., Wolters H., Soares J., Grama C., Rahighi J., Shotter A., Lamehi Rachti M. A compilation of charged-particle induced thermonuclear reaction rates // Nuclear Physics A. VIII 1999. 656. 3–183.

Antia H. M., Basu S. Measuring the helium abundance in the solar envelope: The role of the equation of state // ApJ. V 1994. 426. 801–811.

Appourchaux T., Antia H. M., Benomar O., Campante T. L., Davies G. R., Handberg R., Howe R., Régulo C., Belkacem K., Houdek G., García R. A., Chaplin W. J. Oscillation mode linewidths and heights of 23 main-sequence stars observed by Kepler // A&A. VI 2014. 566. A20.

Appourchaux T., Belkacem K., Broomhall A.-M., Chaplin W. J., Gough D. O., Houdek G., Provost J., Baudin F., Boumier P., Elsworth Y., García R. A., Andersen B. N., Finsterle W., Fröhlich C., Gabriel A., Grec G., Jiménez A., Kosovichev A., Sekii T., Toutain T., Turck-Chièze S. The quest for the solar g modes // A&A Rev.. II 2010. 18. 197–277.

Appourchaux T., Benomar O., Gruberbauer M., Chaplin W. J., García R. A., Handberg R., Verner G. A., Antia H. M., Campante T. L., Davies G. R., Deheuvels S., Hekker S., Howe R., Salabert D., Bedding T. R., White T. R., Houdek G., Silva Aguirre V., Elsworth Y. P., van Cleve J., Clarke B. D., Hall J. R., Kjeldsen H. Oscillation mode linewidths of main-sequence and subgiant stars observed by Kepler // A&A. I 2012. 537. A134.

Asplund M., Grevesse N., Sauval A. J. The Solar Chemical Composition // Cosmic Abundances as Records of Stellar Evolution and Nucleosynthesis. 336. IX 2005. 25. (Astronomical Society of the Pacific Conference Series).

Asplund M., Grevesse N., Sauval A. J., Scott P. The Chemical Composition of the Sun // ARA&A. IX 2009. 47. 481–522.

Baglin A., Michel E., Auvergne M., COROT Team . The seismology programme of the CoRoT space mission // Proceedings of SOHO 18/GONG 2006/HELAS I, Beyond the spherical Sun. 624. X 2006. 34. (ESA Special Publication).

Ballot J., Barban C., van't Veer-Menneret C. Visibilities and bolometric corrections for stellar oscillation modes observed by Kepler // A&A. VII 2011. 531. A124.

Balmforth N. J. Solar Pulsational Stability - Part Three - Acoustical Excitation by Turbulent Convection // MNRAS. IV 1992a. 255. 639.

Balmforth N. J. Solar pulsational stability. I - Pulsation-mode thermodynamics. // MNRAS. IV 1992b. 255. 603–649.

Balmforth N. J., Gough D. O. Mixing-length theory and the excitation of solar acoustic oscillations // Sol. Phys.. VII 1990. 128. 161–193.

Barban C., Michel E., Martic M., Schmitt J., Bouchy F., Lebrun J. C., Connes P., Bertaux J. L., Baglin A. Possible Detection of P-Mode Oscillations on Procyon // IAU Colloq. 170: Precise Stellar Radial Velocities. 185. 1999. 177. (Astronomical Society of the Pacific Conference Series).

Batchelor G. K. The Theory of Homogeneous Turbulence. 1953.

Baudin F., Barban C., Belkacem K., Hekker S., Morel T., Samadi R., Benomar O., Goupil M.-J., Carrier F., Ballot J., Deheuvels S., De Ridder J., Hatzes A. P., Kallinger T., Weiss W. W. Amplitudes and lifetimes of solar-like oscillations observed by CoRoT. Red-giant versus main-sequence stars // A&A. V 2011. 529. A84.

Beck P. G., Montalban J., Kallinger T., De Ridder J., Aerts C., García R. A., Hekker S., Dupret M.-A., Mosser B., Eggenberger P., Stello D., Elsworth Y., Frandsen S., Carrier F., Hillen M., Gruberbauer M., Christensen-Dalsgaard J., Miglio A., Valentini M., Bedding T. R., Kjeldsen H., Girouard F. R., Hall J. R., Ibrahim K. A. Fast core rotation in red-giant stars as revealed by gravity-dominated mixed modes // Nature. I 2012. 481. 55–57.

Bedding T. R., Butler R. P., Kjeldsen H., Baldry I. K., O'Toole S. J., Tinney C. G., Marcy G. W., Kienzle F., Carrier F. Evidence for Solar-like Oscillations in β Hydri // ApJ. III 2001. 549. L105–L108.

Bedding Timothy R, Mosser Benoit, Huber Daniel, Montalbán Josefina, Beck Paul, Christensen-Dalsgaard Jø rgen, Elsworth Yvonne P, García Rafael a, Miglio Andrea, Stello Dennis, White Timothy R, De Ridder Joris, Hekker Saskia, Aerts Conny, Barban Caroline, Belkacem Kevin, Broomhall Anne-Marie, Brown Timothy M, Buzasi Derek L, Carrier Fabien, Chaplin William J, Di Mauro Maria Pia, Dupret Marc-Antoine, Frandsen Sø ren, Gilliland Ronald L, Goupil Marie-Jo, Jenkins Jon M, Kallinger Thomas, Kawaler Steven, Kjeldsen Hans, Mathur Savita, Noels Arlette, Aguirre Victor Silva, Ventura Paolo. Gravity modes as a way to distinguish between hydrogen- and helium-burning red giant stars. // Nature. III 2011. 471, 7340. 608–611.

Belkacem K. Determination of the stars fundamental parameters using seismic scaling relations // SF2A-2012: Proceedings of the Annual meeting of the French Society of Astronomy and Astrophysics. XII 2012. 173–188.

Belkacem K. Determination of the stars fundamental parameters using seismic scaling relations // SF2A-2012: Proceedings of the Annual meeting of the French Society of Astronomy and Astrophysics. Eds.: S. Boissier. X 2012. 173.

Belkacem K., Appourchaux T., Baudin F., Dupret M. A., Goupil M. J., Marques J. P., Noels A., Samadi R. Mode lifetime and associated scaling relations // European Physical Journal Web of Conferences. 43. III 2013. 3009. (European Physical Journal Web of Conferences).

Belkacem K., Dupret M. A., Baudin F., Appourchaux T., Marques J. P., Samadi R. Damping rates of solar-like oscillations across the HR diagram. Theoretical calculations confronted to CoRoT and Kepler observations // A&A. IV 2012a. 540. L7.

Belkacem K., Dupret M. A., Baudin F., Appourchaux T., Marques J. P., Samadi R. Damping rates of solar-like oscillations across the HR diagram. Theoretical calculations confronted to CoRoT and Kepler observations // A&A. IV 2012b. 540. L7.

Belkacem K., Dupret M. a., Baudin F., Appourchaux T., Marques J. P., Samadi R. Damping rates of solar-like oscillations across the HR diagram // Astronomy & Astrophysics. III 2012. 540. L7.

Belkacem K., Goupil M. J., Dupret M. A., Samadi R., Baudin F., Noels A., Mosser B. The underlying physical meaning of the numax nuc relation // A&A. VI 2011. 530. A142.

Belkacem K., Marques J. P., Goupil M. J., Mosser B., Sonoi T., Ouazzani R. M., Dupret M. A., Mathis S., Grosjean M. Angular momentum redistribution by mixed modes in evolved low-mass stars. II. Spin-down of the core of red giants induced by mixed modes // ArXiv e-prints. V 2015a.

Belkacem K., Marques J. P., Goupil M. J., Sonoi T., Ouazzani R. M., Dupret M. A., Mathis S., Mosser B., Grosjean M. Angular momentum redistribution by mixed modes in evolved low-mass stars. I. Theoretical formalism // ArXiv e-prints. V 2015b.

Belkacem K., Samadi R. Connections Between Stellar Oscillations and Turbulent Convection // Lecture Notes in Physics, Berlin Springer Verlag. 865. 2013. 179. (Lecture Notes in Physics, Berlin Springer Verlag).

Belkacem K, Samadi R, Goupil M J. Amplitudes of non-radial oscillations driven by turbulence // Journal of Physics: Conference Series. X 2008. 118. 012028.

Belkacem K., Samadi R., Goupil M. J., Baudin F., Salabert D., Appourchaux T. Turbulent eddy-time-correlation in the solar convective zone // A&A. XI 2010. 522. L2.

Belkacem K., Samadi R., Goupil M.-J., Dupret M.-A. Stochastic excitation of non-radial modes. I. High-angular-degree p modes // A&A. I 2008. 478. 163–174.

Belkacem K., Samadi R., Goupil M. J., Kupka F. A closure model with plumes. I. The solar convection // A&A. XII 2006a. 460. 173–182.

Belkacem K., Samadi R., Goupil M. J., Kupka F., Baudin F. A closure model with plumes. II. Application to the stochastic excitation of solar p modes // A&A. XII 2006b. 460. 183–190.

Benomar O., Belkacem K., Bedding T. R., Stello D., Di Mauro M. P., Ventura R., Mosser B., Goupil M. J., Samadi R., Garcia R. A. Asteroseismology of Evolved Stars with Kepler: A New Way to Constrain Stellar Interiors Using Mode Inertias // ApJ. II 2014. 781. L29.

Benomar Othman, Bedding Timothy R., Mosser Benoît, Stello Dennis, Belkacem Kevin, García Rafael a., White Timothy R., Kuehn C. a., Deheuvels S., Christensen-dalsgaard Jø rgen. Properties of Oscillation Modes in Subgiant Stars Observed By Kepler // The Astrophysical Journal. 2013. 767, 2. 158.

Böhm-Vitense E. Über die Wasserstoffkonvektionszone in Sternen verschiedener Effektivtemperaturen und Leuchtkräfte. Mit 5 Textabbildungen // Zeitschrift fuer Astrophysik. 1958. 46. 108.

Böhm-Vitense E. Introduction to stellar astrophysics. Volume 3. Stellar structure and evolution. I 1992.

Borucki W., Koch D., Basri G., Batalha N., Brown T., Caldwell D., Christensen-Dalsgaard J., Cochran W., Dunham E., Gautier T. N., Geary J., Gilliland R., Jenkins J., Kondo Y., Latham D., Lissauer J. J., Monet D. Finding Earth-size planets in the habitable zone: the Kepler Mission // IAU Symposium. 249. V 2008. 17–24. (IAU Symposium).

Bouchy F., Carrier F. P-mode observations on α Cen A // A&A. VII 2001. 374. L5–L8.

Boury A., Gabriel M., Ledoux P. Effets de la convection sur la stabilité vibrationnelle des étoiles massives // Annales d'Astrophysique. II 1964. 27. 92.

Brassard P., Fontaine G., Wesemael F., Hansen C. J. Adiabatic properties of pulsating DA white dwarfs. II - Mode trapping in compositionally stratified models // ApJS. V 1992. 80. 369–401.

Brown T. M. Solar rotation as a function of depth and latitude // Nature. X 1985. 317. 591–594.

Brown T. M., Gilliland R. L., Noyes R. W., Ramsey L. W. Detection of possible p-mode oscillations on Procyon // ApJ. II 1991. 368. 599–609.

Brown T. M., Kennelly E. J., Korzennik S. G., Nisenson P., Noyes R. W., Horner S. D. A Radial Velocity Search for p-Mode Pulsations in η Bootis // ApJ. I 1997. 475. 322–327.

Brun A. S., Turck-Chièze S., Zahn J. P. Macroscopic Processes in the Solar Interior // Structure and Dynamics of the Interior of the Sun and Sun-like Stars. 418. 1998. 439. (ESA Special Publication).

Bruntt H., Basu S., Smalley B., Chaplin W. J., Verner G. a., Bedding T. R., Catala C., Gazzano J. C., Molenda-Zakowicz J., Thygesen a. O., Uytterhoeven K., Hekker S., Huber D., Karoff C., Mathur S., Mosser B., Appourchaux T., Campante T. L., Elsworth Y., García R. a., Handberg R., Metcalfe T. S., Quirion P. O., Régulo C., Roxburgh I. W., Stello D., Christensen-Dalsgaard J., Kawaler S. D., Kjeldsen H., Morris R. L., Quintana E. V., Sanderfer D. T. Accurate fundamental parameters and detailed abundance patterns from spectroscopy of 93 solar-type Kepler targets // Monthly Notices of the Royal Astronomical Society. VI 2012. 423, 1. 122–131.

Buldgen G., Reese D. R., Dupret M. A. Using seismic inversions to obtain an internal mixing processes indicator for main-sequence solar-like stars // ArXiv e-prints. VII 2015a.

Buldgen G., Reese D. R., Dupret M. A., Samadi R. Stellar acoustic radii, mean densities, and ages from seismic inversion techniques // A&A. I 2015b. 574. A42.

Buzasi D., Catanzarite J., Laher R., Conrow T., Shupe D., Gautier T. N. III, Kreidl T., Everett D. The Detection of Multimodal Oscillations on α Ursae Majoris // ApJ. IV 2000. 532. L133–L136.

Cantiello M., Fuller J. The Asteroseismic Signature of Magnetic Red Giant Cores // IAU General Assembly. VIII 2015. 22. 58552.

Cantiello M., Mankovich C., Bildsten L., Christensen-Dalsgaard J., Paxton B. Angular Momentum Transport within Evolved Low-mass Stars // ApJ. VI 2014. 788. 93.

Canuto V. M., Mazzitelli I. Stellar turbulent convection - A new model and applications // ApJ. III 1991. 370. 295–311.

Carrier F., Eggenberger P., Bouchy F. New seismological results on the G0 IV η Bootis // A&A. V 2005. 434. 1085–1095.

Cassisi S., Potekhin A. Y., Pietrinferni A., Catelan M., Salaris M. Updated Electron-Conduction Opacities: The Impact on Low-Mass Stellar Models // ApJ. VI 2007. 661. 1094–1104.

Ceillier T., Eggenberger P., García R. A., Mathis S. Understanding angular momentum transport in red giants: the case of KIC 7341231 // A&A. VII 2013. 555. A54.

Chaplin W. J., Elsworth Y., Isaak G. R., Lines R., McLeod C. P., Miller B. A., New R. Solar p-mode excitation: further insight from recent low-l BiSON helioseismological data // MNRAS. VII 1998. 298. L7–L12.

Chaplin W. J., Houdek G., Elsworth Y., New R., Bedding T. R., Kjeldsen H. Excitation and Damping of p-Mode Oscillations of α Cen B // ApJ. II 2009a. 692. 531–537.

Chaplin W. J., Houdek G., Karoff C., Elsworth Y., New R. Mode lifetimes of stellar oscillations. Implications for asteroseismology // A&A. VI 2009b. 500. L21–L24.

Chaplin William J., Miglio Andrea. Asteroseismology of Solar-Type and Red-Giant Stars // Annual Review of Astronomy and Astrophysics. VIII 2013. 51, 1. 353–392.

Christensen-Dalsgaard J. Helioseismology // Reviews of Modern Physics. XI 2002. 74. 1073–1129.

Christensen-Dalsgaard J., Duvall T. L. Jr., Gough D. O., Harvey J. W., Rhodes E. J. Jr. Speed of sound in the solar interior // Nature. V 1985. 315. 378–382.

Christensen-Dalsgaard J., Gough D. O. Comparison of observed solar whole-disk oscillation frequencies with the predictions of a sequence of solar models // A&A. XII 1981. 104. 173–176.

Christensen-Dalsgaard J., Gough D. O., Morgan J. G. Dirty solar models // A&A. III 1979. 73. 121–128.

Christensen-Dalsgaard J., Perez Hernandez F. The phase function for stellar acoustic oscillations. I - Theory // MNRAS. VII 1992. 257. 62–88.

Claverie A., Isaak G. R., McLeod C. P., van der Raay H. B., Cortes T. R. Solar structure from global studies of the 5-minute oscillation // Nature. XII 1979. 282. 591–594.

Corsaro E., Fröhlich H.-E., Bonanno A., Huber D., Bedding T. R., Benomar O., De Ridder J., Stello D. A Bayesian approach to scaling relations for amplitudes of solar-like oscillations in Kepler stars // MNRAS. IV 2013. 430. 2313–2326.

Corsaro E., Stello D., Huber D., Bedding T. R., Bonanno A., Brogaard K., Kallinger T., Benomar O., White T. R., Mosser B., Basu S., Chaplin W. J., Christensen-Dalsgaard J., Elsworth Y. P., García R. A., Hekker S., Kjeldsen H., Mathur S., Meibom S., Hall J. R., Ibrahim K. A., Klaus T. C. Asteroseismology of the Open Clusters NGC 6791, NGC 6811, and NGC 6819 from 19 Months of Kepler Photometry // ApJ. X 2012. 757. 190.

Cowling T. G. The stability of gaseous stars (Second paper) // MNRAS. XI 1935. 96. 42.

Cowling T. G. The non-radial oscillations of polytropic stars // MNRAS. 1941. 101. 367.

Cox A. N., Guzik J. A., Kidman R. B. Oscillations of solar models with internal element diffusion // ApJ. VII 1989. 342. 1187–1206.

Cox J. P. Principles of stellar structure - Vol.1: Physical principles; Vol.2: Applications to stars. 1968.

De Meulenaer P., Carrier F., Miglio A., Bedding T. R., Campante T. L., Eggenberger P., Kjeldsen H., Montalbán J. Core properties of α Centauri A using asteroseismology // A&A. XI 2010. 523. A54.

De Ridder J., Barban C., Baudin F., Carrier F., Hatzes A. P., Hekker S., Kallinger T., Weiss W. W., Baglin A., Auvergne M., Samadi R., Barge P., Deleuil M. Non-radial oscillation modes with long lifetimes in giant stars // Nature. V 2009. 459. 398–400.

De Ridder J., Barban C., Carrier F., Mazumdar A., Eggenberger P., Aerts C., Deruyter S., Vanautgaerden J. Discovery of solar-like oscillations in the red giant \varepsilon Ophiuchi // A&A. III 2006. 448. 689–695.

Deheuvels S., Doğan G., Goupil M. J., Appourchaux T., Benomar O., Bruntt H., Campante T. L., Casagrande L., Ceillier T., Davies G. R., De Cat P., Fu J. N., García R. A., Lobel A., Mosser B., Reese D. R., Regulo C., Schou J., Stahn T., Thygesen A. O., Yang X. H., Chaplin W. J., Christensen-Dalsgaard J., Eggenberger P., Gizon L., Mathis S., Molenda-Żakowicz J., Pinsonneault M. Seismic constraints on the radial dependence of the internal rotation profiles of six Kepler subgiants and young red giants // A&A. IV 2014. 564. A27.

Deheuvels S., García R. A., Chaplin W. J., Basu S., Antia H. M., Appourchaux T., Benomar O., Davies G. R., Elsworth Y., Gizon L., Goupil M. J., Reese D. R., Regulo C., Schou J., Stahn T., Casagrande L., Christensen-Dalsgaard J., Fischer D., Hekker S., Kjeldsen H., Mathur S., Mosser B., Pinsonneault M., Valenti J., Christiansen J. L., Kinemuchi K., Mullally F. Seismic Evidence for a Rapidly Rotating Core in a Lower-giant-branch Star Observed with Kepler // ApJ. IX 2012. 756. 19.

Deheuvels S., Michel E. Constraints on the core ??-gradient of the solar-like star HD 49385 via low-degree mixed modes // Astronomische Nachrichten. XII 2010. 331, 9-10. 929–932.

Deheuvels S., Michel E. Constraints on the structure of the core of subgiants via mixed modes: the case of HD 49385 // A&A. XI 2011. 535. A91.

Deubner F.-L. Observations of low wavenumber nonradial eigenmodes of the sun // A&A. XI 1975. 44. 371–375.

Deubner F.-L., Ulrich R. K., Rhodes E. J. Jr. Solar p-mode oscillations as a tracer of radial differential rotation // A&A. II 1979. 72. 177–185.

Dupret M. A. Nonradial nonadiabatic stellar pulsations: A numerical method and its application to a beta Cephei model // A&A. I 2001. 366. 166–173.

Dupret M.-A., Belkacem K., Samadi R., Montalban J., Moreira O., Miglio A., Godart M., Ventura P., Ludwig H.-G., Grigahcène A., Goupil M.-J., Noels A., Caffau E. Theoretical amplitudes and lifetimes of non-radial solar-like oscillations in red giants // A&A. X 2009. 506. 57–67.

Dupret M.-A., De Ridder J., Neuforge C., Aerts C., Scuflaire R. Influence of non-adiabatic temperature variations on line profile variations of slowly rotating beta Cep stars and SPBs. I. Non-adiabatic eigenfunctions in the atmosphere of a pulsating star // A&A. IV 2002. 385. 563–571.

Dupret M.-A., Goupil M.-J., Samadi R., Grigahcène A., Gabriel M. A non-local MLT treatment fitting 3D simulations // Proceedings of SOHO 18/GONG 2006/HELAS I, Beyond the spherical Sun. 624. X 2006a. (ESA Special Publication).

Dupret M.-A., Samadi R., Grigahcene A., Goupil M.-J., Gabriel M. Non-local time-dependent treatments of convection in A-G type stars // Communications in Asteroseismology. I 2006b. 147. 85–88.

Duvall T. Solar Interior: Local Helioseismology // Encyclopedia of Astronomy and Astrophysics. XI 2000. 2250.

Dziembowski W. Oscillations of giants and supergiants // Acta Astronomica. 1977. 27. 95–126.

Dziembowski W. A., Gough D. O., Houdek G., Sienkiewicz R. Oscillations of α UMa and other red giants // MNRAS. XII 2001. 328. 601–610.

Eggenberger P., Montalbán J., Miglio A. Angular momentum transport in stellar interiors constrained by rotational splittings of mixed modes in red giants // A&A. VIII 2012. 544. L4.

Ferguson J. W., Alexander D. R., Allard F., Barman T., Bodnarik J. G., Hauschildt P. H., Heffner-Wong A., Tamanai A. Low-Temperature Opacities // ApJ. IV 2005. 623. 585–596.

Fletcher S. T., Chaplin W. J., Elsworth Y., Schou J., Buzasi D. Frequency, splitting, linewidth and amplitude estimates of low-l p modes of α Cen A: analysis of Wide-Field Infrared Explorer photometry // MNRAS. IX 2006. 371. 935–944.

Formicola A., Imbriani G., Costantini H., Angulo C., Bemmerer D., Bonetti R., Broggini C., Corvisiero P., Cruz J., Descouvemont P., Fülöp Z., Gervino G., Guglielmetti A., Gustavino C., Gyürky G., Jesus A. P., Junker M., Lemut A., Menegazzo R., Prati P., Roca V., Rolfs C., Romano M., Rossi Alvarez C., Schümann F., Somorjai E., Straniero O., Strieder F., Terrasi F., Trautvetter H. P., Vomiero A., Zavatarelli S. Astrophysical S-factor of ^{14}N(p,γ)^{15}O // Physics Letters B. VII 2004. 591. 61–68.

Frandsen S., Carrier F., Aerts C., Stello D., Maas T., Burnet M., Bruntt H., Teixeira T. C., de Medeiros J. R., Bouchy F., Kjeldsen H., Pijpers F., Christensen-Dalsgaard J. Detection of Solar-like oscillations in the G7 giant star xi Hya // A&A. X 2002. 394. L5–L8.

Fuller J., Lecoanet D., Cantiello M., Brown B. Angular Momentum Transport via Internal Gravity Waves in Evolving Stars // ApJ. XI 2014. 796. 17.

Gabriel M. Solar oscillations : theory // Bulletin of the Astronomical Society of India. VI 1996. 24. 233.

Gabriel M., Carlier F. Influence of hydrogen diffusion on the solar p-mode spectrum. // A&A. I 1997. 317. 580–585.

Gabriel M., Noels A., Montalbán J., Miglio A. Proper use of Schwarzschild Ledoux criteria in stellar evolution computations // A&A. IX 2014. 569. A63.

Gabriel M., Scuflaire R. Properties of non-radial stellar oscillations // Acta Astronomica. 1979. 29. 135–149.

Gabriel M., Scuflaire R., Noels A., Boury A. Influence de la Convection sur la Stabilité des Oscillations Nonradiales des Etoiles // Bulletin de l'Academie Royale de Belgique. 1974. 60. 866–887.

García R. A., Pérez Hernández F., Benomar O., Silva Aguirre V., Ballot J., Davies G. R., Doğan G., Stello D., Christensen-Dalsgaard J., Houdek G., Lignières F., Mathur S., Takata M., Ceillier T., Chaplin W. J., Mathis S., Mosser B., Ouazzani R. M., Pinsonneault M. H., Reese D. R., Régulo C., Salabert D., Thompson M. J., van Saders J. L., Neiner C., De Ridder J. Study of KIC 8561221 observed by Kepler: an early red giant showing depressed dipolar modes // A&A. III 2014. 563. A84.

Gilliland R. L., Brown T. M., Christensen-Dalsgaard J., Kjeldsen H., Aerts C., Appourchaux T., Basu S., Bedding T. R., Chaplin W. J., Cunha M. S., De Cat P., De Ridder J., Guzik J. A., Handler G., Kawaler S., Kiss L., Kolenberg K., Kurtz D. W., Metcalfe T. S., Monteiro M. J. P. F. G., Szabó R., Arentoft T., Balona L., Debosscher J., Elsworth Y. P., Quirion P.-O., Stello D., Suárez J. C., Borucki W. J., Jenkins J. M., Koch D., Kondo Y., Latham D. W., Rowe J. F., Steffen J. H. Kepler Asteroseismology Program: Introduction and First Results // Publications of the ASP. II 2010. 122. 131–143.

Godart M., Noels A., Dupret M.-A., Lebreton Y. Can mass loss and overshooting prevent the excitation of g-modes in blue supergiants? // MNRAS. VII 2009. 396. 1833–1841.

Goldreich P., Keeley D. A. Solar seismology. II - The stochastic excitation of the solar p-modes by turbulent convection // ApJ. II 1977. 212. 243–251.

Goldreich P., Murray N., Kumar P. Excitation of solar p-modes // ApJ. III 1994. 424. 466–479.

Goode P. R. The Sun's Internal Differential Rotation from Helioseismology // IAU Colloq. 130: The Sun and Cool Stars. Activity, Magnetism, Dynamos. 380. 1991. 157. (Lecture Notes in Physics, Berlin Springer Verlag).

Gough D. O. Mixing-length theory for pulsating stars // ApJ. V 1977. 214. 196–213.

Goupil M. J., Mosser B., Marques J. P., Ouazzani R. M., Belkacem K., Lebreton Y., Samadi R. Seismic diagnostics for transport of angular momentum in stars. II. Interpreting observed rotational splittings of slowly rotating red giant stars // A&A. I 2013. 549. A75.

Grec G., Fossat E., Pomerantz M. Solar oscillations - Full disk observations from the geographic South Pole // Nature. XII 1980. 288. 541–544.

Grevesse N., Noels A. La composition chimique du Soleil. // Perfectionnement de l'Association Vaudoise des Chercheurs en Physique. 1993. 205–257.

Grigahcène A., Dupret M.-A., Gabriel M., Garrido R., Scuflaire R. Convection-pulsation coupling. I. A mixing-length perturbative theory // A&A. V 2005. 434. 1055–1062.

Haber D. A., Hindman B. W., Toomre J., Bogart R. S., Larsen R. M., Hill F. Evolving Submerged Meridional Circulation Cells within the Upper Convection Zone Revealed by Ring-Diagram Analysis // ApJ. V 2002. 570. 855–864.

Hekker S., Aerts C., De Ridder J., Carrier F. Pulsations detected in the line profile variations of red giants. Modelling of line moments, line bisector and line shape // A&A. XI 2006. 458. 931–940.

Henyey L., Vardya M. S., Bodenheimer P. Studies in Stellar Evolution. III. The Calculation of Model Envelopes. // ApJ. X 1965. 142. 841.

Houdek G. Pulsation of Solar-type stars. 1996.

Iben I. Jr. Electron Conduction in Red Giants // ApJ. XI 1968. 154. 557.

Iben I. Jr. Solar oscillations as a guide to solar structure // ApJ. III 1976. 204. L147–L150.

Iglesias C. A., Rogers F. J. Updated Opal Opacities // ApJ. VI 1996. 464. 943.

Jeans J. H. The Stability of a Spherical Nebula // Royal Society of London Philosophical Transactions Series A. 1902. 199. 1–53.

Kaneda K., Okabe Y., Kikuchi M. Shape effects of finite-size scaling functions for anisotropic three-dimensional Ising models // Journal of Physics A Mathematical General. X 1999. 32. 7263–7271.

Kippenhahn R., Weigert A., Weiss A. Stellar Structure and Evolution. 2012.

Kjeldsen H., Bedding T. R. Amplitudes of stellar oscillations: the implications for asteroseismology. // A&A. I 1995. 293. 87–106.

Kjeldsen H., Bedding T. R., Baldry I. K., Bruntt H., Butler R. P., Fischer D. A., Frandsen S., Gates E. L., Grundahl F., Lang K., Marcy G. W., Misch A., Vogt S. S. Confirmation of Solar-like Oscillations in η Bootis // Astr. J.. IX 2003. 126. 1483–1488.

Kjeldsen H., Bedding T. R., Christensen-Dalsgaard J. Correcting Stellar Oscillation Frequencies for Near-Surface Effects // ApJ. VIII 2008. 683. L175–L178.

Kjeldsen H., Bedding T. R., Viskum M., Frandsen S. Solarlike oscillations in eta Boo // Astr. J.. III 1995. 109. 1313–1319.

Kosovichev A. G. Advances in Global and Local Helioseismology: An Introductory Review // Lecture Notes in Physics, Berlin Springer Verlag. 832. 2011. 3–642. (Lecture Notes in Physics, Berlin Springer Verlag).

Kosovichev A. G., Christensen-Dalsgaard J., Daeppen W., Dziembowski W. A., Gough D. O., Thompson M. J. Sources of uncertainty in direct seismological measurements of the solar helium abundance // MNRAS. XII 1992. 259. 536–558.

Krishna Swamy K. S. Profiles of Strong Lines in K-Dwarfs // ApJ. VII 1966. 145. 174.

Landau L.D., Lifshitz E.M. Fluid Mechanics, by L.D. Landau and E.M. Lifshitz. 1959. (Teoreticheskaiĭž aĭž¡ fizika).

Lebreton Y., Goupil M. J. Seismic signature of envelope penetrative convection: the CoRoT star HD 52265 // A&A. VIII 2012. 544. L13.

Lebreton Y., Goupil M. J. Asteroseismology for "à la carte" stellar age-dating and weighing. Age and mass of the CoRoT exoplanet host HD 52265 // A&A. IX 2014. 569. A21.

Lebreton Y., Montalbán J. Stellar ages from asteroseismology // IAU Symposium. 258. VI 2009. 419–430. (IAU Symposium).

Leighton R. B. // Aerodynamic Phenomena in Stellar Atmospheres. 12. 1960. 321–325. (IAU Symposium).

Lesieur M., Comte P., Lamballais E., Metais O., Silvestrini G. Large-Eddy Simulations of Shear Flows // Journal of Engineering Mathematics. X 1997. 32. 195–215.

Libbrecht K. G. Solar p-mode phenomenology // ApJ. XI 1988. 334. 510–516.

Lighthill M. J. Predictions on the Velocity Field Coming from Acoustic Noise and a Generalized Turbulence in a Layer Overlying a Convectively Unstable Atmospheric Region // Aerodynamic Phenomena in Stellar Atmospheres. 28. 1967. 429. (IAU Symposium).

Lochard J., Samadi R., Goupil M. J. Rotation profile inversion in solar-like stars. In the COROT framework // A&A. VIII 2005. 438. 939–948.

Maeder A. Physics, Formation and Evolution of Rotating Stars. 2009.

Marques J. P., Goupil M. J., Lebreton Y., Talon S., Palacios A., Belkacem K., Ouazzani R.-M., Mosser B., Moya A., Morel P., Pichon B., Mathis S., Zahn J.-P., Turck-Chièze S., Nghiem P. A. P. Seismic diagnostics for transport of angular momentum in stars. I. Rotational splittings from the pre-main sequence to the red-giant branch // A&A. I 2013. 549. A74.

Martić M., Schmitt J., Lebrun J.-C., Barban C., Connes P., Bouchy F., Michel E., Baglin A., Appourchaux T., Bertaux J.-L. Evidence for global pressure oscillations on Procyon // A&A. XI 1999. 351. 993–1002.

Mathis S., Auclair-Desrotour P., Guenel M., Le Poncin-Lafitte C. Tidal friction in rotating turbulent convectivestellar and planetary regions // SF2A-2014: Proceedings of the Annual meeting of the French Society of Astronomy and Astrophysics. XII 2014. 251–256.

Mazumdar A., Mérand A., Demarque P., Kervella P., Barban C., Baudin F., Coudé du Foresto V., Farrington C., Goldfinger P. J., Goupil M.-J., Josselin E., Kuschnig R., McAlister H. A., Matthews J., Ridgway S. T., Sturmann J., Sturmann L., ten Brummelaar T. A., Turner N. Asteroseismology and interferometry of the red giant star ϵ Ophiuchi // A&A. VIII 2009. 503. 521–531.

McDonald I., Zijlstra A. A. Mass-loss on the red giant branch: the value and metallicity dependence of Reimers' η in globular clusters // MNRAS. III 2015. 448. 502–521.

Mein P. Champ macroscopique des vitesses dans l'atmosphère solaire d'après les mesures de déplacements des raies de Fraunhofer // Annales d'Astrophysique. II 1966. 29. 153.

Mendoza C. Atomic data from the Opacity Project (OP) // Highlights of Astronomy. 1992. 9. 563.

Michel E., Samadi R., Baudin F., Barban C., Appourchaux T., Auvergne M. Intrinsic photometric characterisation of stellar oscillations and granulation. Solar reference values and CoRoT response functions // A&A. III 2009. 495. 979–987.

Miglio A. Ensemble Asteroseismology: An Introduction // Asteroseismology of Stellar Populations in the Milky Way. VII 2013. 3.

Miglio A., Montalbán J. Constraining fundamental stellar parameters using seismology. Application to α Centauri AB // A&A. X 2005. 441. 615–629.

Molenda-Żakowicz J., Sousa S. G., Frasca A., Uytterhoeven K., Briquet M., Van Winckel H., Drobek D., Niemczura E., Lampens P., Lykke J., Bloemen S., Gameiro J. F., Jean C., Volpi D., Gorlova N., Mortier A., Tsantaki M., Raskin G. Atmospheric parameters of 169 F-, G-, K- and M-type stars in the Kepler field // MNRAS. IX 2013. 434. 1422–1434.

Montalbán J., Dupret M.-A. Effect of convective outer layers modeling on non-adiabatic seismic observables of δ Scuti stars // A&A. VIII 2007. 470. 991–1002.

Montalbán J., Noels A. Asteroseismology of red giant stars: The potential of dipole modes // European Physical Journal Web of Conferences. 43. III 2013. 3002. (European Physical Journal Web of Conferences).

Morel P., Provost J., Berthomieu G. Updated solar models. // A&A. XI 1997. 327. 349–360.

Mosser B., Barban C., Montalbán J., Beck P. G., Miglio A., Belkacem K., Goupil M. J., Hekker S., De Ridder J., Dupret M. A., Elsworth Y., Noels A., Baudin F., Michel E., Samadi R., Auvergne M., Baglin A., Catala C. Mixed modes in red-giant stars observed with CoRoT // A&A. VIII 2011. 532. A86.

Mosser B., Belkacem K., Goupil M.-J., Miglio A., Morel T., Barban C., Baudin F., Hekker S., Samadi R., De Ridder J., Weiss W., Auvergne M., Baglin A. Red-giant seismic properties analyzed with CoRoT // A&A. VII 2010a. 517. A22.

Mosser B., Belkacem K., Goupil M.-J., Miglio A., Morel T., Barban C., Baudin F., Hekker S., Samadi R., De Ridder J., Weiss W., Auvergne M., Baglin A. Red-giant seismic properties analyzed with CoRoT // A&A. VII 2010b. 517. A22.

Mosser B., Benomar O., Belkacem K., Goupil M. J., Lagarde N., Michel E., Lebreton Y., Stello D., Vrard M., Barban C., Bedding T. R., Deheuvels S., Chaplin W. J., De Ridder J., Elsworth Y., Montalban J., Noels A., Ouazzani R. M., Samadi R., White T. R., Kjeldsen H. Mixed modes in red giants: a window on stellar evolution // ArXiv e-prints. XI 2014.

Mosser B., Elsworth Y., Hekker S., Huber D., Kallinger T., Mathur S., Belkacem K., Goupil M. J., Samadi R., Barban C., Bedding T. R., Chaplin W. J., García R. A., Stello D., De Ridder J., Middour C. K., Morris R. L., Quintana E. V. Characterization of the power excess of solar-like oscillations in red giants with Kepler // A&A. I 2012a. 537. A30.

Mosser B., Goupil M. J., Belkacem K., Marques J. P., Beck P. G., Bloemen S., De Ridder J., Barban C., Deheuvels S., Elsworth Y., Hekker S., Kallinger T., Ouazzani R. M., Pinsonneault M., Samadi R., Stello D., García R. A., Klaus T. C., Li J., Mathur S., Morris R. L. Spin down of the core rotation in red giants // A&A. XII 2012b. 548. A10.

Musielak Z. E., Rosner R., Stein R. F., Ulmschneider P. On sound generation by turbulent convection: A new look at old results // ApJ. III 1994. 423. 474–487.

Noels A., Scuflaire R. Non-radial instability of WR models // A&A. VI 1986. 161. 125–129.

Noerdlinger P. D. Diffusion of helium in the sun // A&A. V 1977. 57. 407–415.

Potekhin A. Y., Baiko D. A., Haensel P., Yakovlev D. G. Transport properties of degenerate electrons in neutron star envelopes and white dwarf cores // A&A. VI 1999. 346. 345–353.

Prandtl Ludwig. Bericht über Untersuchungen zur ausgebildeten Turbulenz // Z. Angew. Math. Mech. 1925. 5, 2. 136–139.

Press W. H. Radiative and other effects from internal waves in solar and stellar interiors // ApJ. IV 1981. 245. 286–303.

Proffitt C. R. Effects of Heavy-Element Settling on Solar Neutrino Fluxes and Interior Structure // Solar Neutrinos. The First Thirty Years. 1994. 69.

Reese D. R., Lara F. E., Rieutord M. Pulsations of rapidly rotating stars with compositional discontinuities // IAU Symposium. 301. II 2014. 169–172. (IAU Symposium).

Reese D. R., Marques J. P., Goupil M. J., Thompson M. J., Deheuvels S. Estimating stellar mean density through seismic inversions // A&A. III 2012. 539. A63.

Reimers D. Circumstellar envelopes and mass loss of red giant stars // Problems in stellar atmospheres and envelopes. 1975. 229–256.

Rhodes E. J. Jr., Ulrich R. K., Deubner F.-L. A new technique for measuring solar rotation // ApJ. I 1979. 227. 629–637.

Rhodes E.J.Jr., Ulrich R.K., Simon G.W. // ApJ. 1975. 218.

Rogers F. J., Nayfonov A. Updated and Expanded OPAL Equation-of-State Tables: Implications for Helioseismology // ApJ. IX 2002. 576. 1064–1074.

Roxburgh I. W. 2-dimensional models of rapidly rotating stars. II. Hydrostatic and acoustic models with Ω=Ω(r,) // A&A. VIII 2006. 454. 883–888.

Roxburgh I. W., Vorontsov S. V. On the use of the ratio of small to large separations in asteroseismic model fitting // A&A. XII 2013. 560. A2.

Rozelot J.-P., Neiner C. The Pulsations of the Sun and the Stars. 2011.

Rüdiger G., Gellert M., Spada F., Tereshin I. The angular momentum transport by unstable toroidal magnetic fields // A&A. I 2015. 573. A80.

Samadi R. Stochastic Excitation of Acoustic Modes in Stars // Lecture Notes in Physics, Berlin Springer Verlag. 832. 2011. 305. (Lecture Notes in Physics, Berlin Springer Verlag).

Samadi R, Belkacem K, Dupret M, Ludwig H, Baudin F, Caffau E, Goupil M, Barban C. Amplitudes of solar-like oscillations in red giant stars. Evidence for non-adiabatic effects using CoRoT observations // Astronomy & Astrophysics. 2012. 543. 120.

Samadi R., Belkacem K., Dupret M.-A., Goupil M. J., Ludwig H.-G., Barban C., Baudin F., Caffau E. Amplitudes of solar-like oscillations in red giants: Departures from the quasi-adiabatic approximation // European Physical Journal Web of Conferences. 43. III 2013a. 3008. (European Physical Journal Web of Conferences).

Samadi R., Belkacem K., Dupret M.-A., Goupil M. J., Ludwig H.-G., Barban C., Baudin F., Caffau E. Amplitudes of solar-like oscillations in red giants: Departures from the quasi-adiabatic approximation // European Physical Journal Web of Conferences. 43. III 2013b. 3008. (European Physical Journal Web of Conferences).

Samadi R., Belkacem K., Goupil M.-J., Ludwig H.-G., Dupret M.-A. Modeling stochastic excitation of acoustic modes in stars: present status and perspectives // Communications in Asteroseismology. XII 2008. 157. 130–136.

Samadi R., Goupil M.-J. Excitation of stellar p-modes by turbulent convection. I. Theoretical formulation // A&A. IV 2001. 370. 136–146.

Samadi R., Nordlund Å., Stein R. F., Goupil M. J., Roxburgh I. Numerical constraints on the model of stochastic excitation of solar-type oscillations // A&A. V 2003a. 403. 303–312.

Samadi R., Nordlund Å., Stein R. F., Goupil M. J., Roxburgh I. Numerical constraints on the model of stochastic excitation of solar-type oscillations // A&A. V 2003b. 403. 303–312.

Saumon D., Chabrier G., van Horn H. M. An Equation of State for Low-Mass Stars and Giant Planets // ApJS. VIII 1995. 99. 713.

Schou J., Antia H. M., Basu S., Bogart R. S., Bush R. I., Chitre S. M., Christensen-Dalsgaard J., Di Mauro M. P., Dziembowski W. A., Eff-Darwich A., Gough D. O., Haber D. A., Hoeksema J. T., Howe R., Korzennik S. G., Kosovichev A. G., Larsen R. M., Pijpers F. P., Scherrer P. H., Sekii T., Tarbell T. D., Title A. M., Thompson M. J., Toomre J. Helioseismic Studies of Differential Rotation in the Solar Envelope by the Solar Oscillations Investigation Using the Michelson Doppler Imager // ApJ. IX 1998. 505. 390–417.

Schröder K.-P., Cuntz M. A New Version of Reimers' Law of Mass Loss Based on a Physical Approach // ApJ. IX 2005. 630. L73–L76.

Scuflaire R. The Non Radial Oscillations of Condensed Polytropes // A&A. XI 1974. 36. 107.

Shibahashi H. Modal Analysis of Stellar Nonradial Oscillations by an Asymptotic Method // Astronomical Society of Japan, Publications. 1979. 31. 87–104.

Sonoi T., Samadi R., Belkacem K., Ludwig H.-G., Caffau E., Mosser B. Surface-effect corrections for solar-like oscillations using 3D hydrodynamical simulations // ArXiv e-prints. X 2015.

Spiegel E. A. A Generalization of the Mixing-Length Theory of Turbulent Convection. // ApJ. VII 1963. 138. 216.

Spiegel E. A., Zahn J.-P. The solar tachocline // A&A. XI 1992. 265. 106–114.

Stein R. F. Generation of Acoustic and Gravity Waves by Turbulence in an Isothermal Stratified Atmosphere // Sol. Phys.. XII 1967. 2. 385–432.

Stein R. F., Leibacher J. Waves in the solar atmosphere // ARA&A. 1974. 12. 407–435.

Stello D., Kjeldsen H., Bedding T. R., Buzasi D. Oscillation mode lifetimes in ξ Hydrae: will strong mode damping limit asteroseismology of red giant stars? // A&A. III 2006. 448. 709–715.

Stolzmann W., Bloecker T. Thermodynamical properties of stellar matter. I. Equation of state for stellar interiors. // A&A. X 1996. 314. 1024–1040.

Takata M. An Approach to the Exact Classification of Adiabatic Eigenmodes of Stars // Progress in Solar/Stellar Physics with Helio- and Asteroseismology. 462. IX 2012. 412. (Astronomical Society of the Pacific Conference Series).

Talon S. Transport Processes in Stars: Diffusion, Rotation, Magnetic fields and Internal Waves // EAS Publications Series. 32. XI 2008. 81–130. (EAS Publications Series).

Tassoul M. Asymptotic approximations for stellar nonradial pulsations // ApJS. VIII 1980. 43. 469–490.

Tian Z., Bi S., Bedding T. R., Yang W. Asteroseismic analysis of solar-mass subgiants KIC 6442183 and KIC 11137075 observed by Kepler // ArXiv e-prints. VI 2015.

Ulrich R. K., Rhodes E. J. Jr., Deubner F.-L. The effect of a radial rotational velocity gradient on p-mode eigenfrequencies // ApJ. I 1979. 227. 638–644.

Unno W. Stellar Radial Pulsation Coupled with the Convection // Astronomical Society of Japan, Publications. 1967. 19. 140.

Unno W., Osaki Y., Ando H., Saio H., Shibahashi H. Nonradial oscillations of stars. 1989.

Van Hoolst T., Dziembowski W. A., Kawaler S. D. Unstable non-radial modes in radial pulsators: theory and an example // MNRAS. VI 1998. 297. 536–544.

Vandakurov Y. V. The Frequency Distribution of Stellar Oscillations. // Soviet Astronomy. II 1968. 11. 630.

Ventura P., D'Antona F., Mazzitelli I. The ATON 3.1 stellar evolutionary code. A version for asteroseismology // ApSS. VIII 2008. 316. 93–98.

Vorontsov S. V., Baturin V. A., Pamiatnykh A. A. Seismological measurement of solar helium abundance // Nature. I 1991. 349. 49–51.

Yang J. Y., Li Y. Testing Reynolds stress model in solar interior // IAU Symposium. 239. V 2007. 373–375. (IAU Symposium).

Zahn J.-P. Convective penetration in stellar interiors // A&A. XII 1991. 252. 179–188.

Ziebarth K. On the Upper Mass Limit for Main-Sequence Stars // ApJ. XII 1970. 162. 947.